


MITSUBISHI HEAVY INDUSTRIES, LTD.
16-5, KONAN 2-CHOME, MINATO-KU
TOKYO, JAPAN

December 28, 2010

Document Control Desk
U.S. Nuclear Regulatory Commission
Washington, DC 20555-0001

Attention: Mr. Jeffery A. Ciocco

Docket No. 52-021
MHI Ref: UAP-HF-10356

Subject: MHI's Outputs related to US-APWR DCD RAI No. 636-4732

Reference: 1) "Request for Additional Information No. 636-4732 Revision 0, SRP Section: 03.06.02 – Determination of Rupture Locations and Dynamic Effects Associated with the Postulated Rupture of Piping, Application Section: 3.6.2," dated 9/23/2010.
2) "MHI's Responses to US-APWR DCD RAI No. 636-4732," UAP-HF-10335, dated 12/15/2010.

With this letter, Mitsubishi Heavy Industries, Ltd. ("MHI") transmits to the U.S. Nuclear Regulatory Commission ("NRC") Outputs related to US-APWR DCD RAI No. 636-4732.

Enclosed are revised presentation material, UAP-HF-10320, entitled "Response to RAI 636-4732 for Pipe Break Hazard Analysis Revision 1 (Proprietary)", 10 out of 17 references cited in Reference 2, entitled "MHI's Responses to US-APWR DCD RAI No. 636-4732," UAP-HF-10335, dated 12/15/2010, technical report, MUAP-10017-P Revision 1, entitled "Methodology of Pipe Break Hazard Analysis (Proprietary)", and MUAP-10017-NP Revision 1, entitled "Methodology of Pipe Break Hazard Analysis (Non-Proprietary)". The Technical Reports is being submitted electronically in compact discs (CDs). These materials were prepared to reflect the discussion results at the conference call with NRC held on December 1. Additionally, Remained 7 references cited in Reference 2 will be submitted to NRC later.

The enclosed presentation material and technical report contains information that MHI considers proprietary, and therefore the material and report should be withheld from disclosure pursuant to 10 C.F.R. § 2.390 (a)(4) as trade secrets and commercial or financial information which is privileged or confidential. Accordingly, the Report is being submitted in two versions, in separate compact discs. One version (in CD 1) contains the complete proprietary version of the Report. The non-proprietary version of the Report is enclosed in CD 2. In the non-proprietary version, the proprietary information, bracketed in the proprietary version, is replaced by the designation "[]". In accordance with the NRC submittal procedures, this letter includes an Affidavit that identifies the reasons why the proprietary version of the Report should be withheld from disclosure pursuant to 10 C.F.R. § 2.390 (a)(4).

Please contact Dr. C. Keith Paulson, Senior Technical Manager, Mitsubishi Nuclear Energy Systems, Inc. if the NRC has questions concerning any aspect of this submittal. His contact information is provided below.

D081
NRO

Sincerely,

Atsushi Kumaki Cor

Yoshiki Ogata,
General Manager- APWR Promoting Department
Mitsubishi Heavy Industries, LTD.

Enclosures:

1. Affidavit of Atsushi Kumaki
2. Revised Presentation Material, UAP-HF-10320, "Response to RAI 636-4732 for Pipe Break Hazard Analysis Revision 1 (Proprietary)"
3. References cited in Response to RAI 636-4732 for Pipe Break Hazard Analysis Revision 1
4. CD 1: Technical Report, MUAP-10017-P Revision 1, "Methodology of Pipe Break Hazard Analysis (Proprietary)"
5. CD 2: Technical Report, MUAP-10017-NP Revision 1 "Methodology of Pipe Break Hazard Analysis (Non-Proprietary)"

The file contained in each CD is listed in Attachments 1 hereto.

CC: J. A. Ciocco
C. K. Paulson

Contact Information

C. Keith Paulson, Senior Technical Manager
Mitsubishi Nuclear Energy Systems, Inc.
300 Oxford Drive, Suite 301
Monroeville, PA 15146
E-mail: ck_paulson@mnes-us.com
Telephone: (412) 373-6466

Enclosure 1

Docket No. 52-021
MHI Ref: UAP-HF-10356

MITSUBISHI HEAVY INDUSTRIES, LTD.

AFFIDAVIT

I, Atsushi Kumaki, state as follows:

1. I am Group Manager, Licensing Promoting Group in Promoting Department, of Mitsubishi Heavy Industries, LTD ("MHI"), and have been delegated the function of reviewing MHI's US-APWR documentation to determine whether it contains information that should be withheld from public disclosure pursuant to 10 C.F.R. § 2.390 (a)(4) as trade secrets and commercial or financial information which is privileged or confidential.
2. In accordance with my responsibilities, I have reviewed the enclosed documents, UAP-HF-10320 and MUAP-10017 Revision 1 and have determined that portions of the document contain proprietary information that should be withheld from public disclosure. All pages contain proprietary information as identified with the label "Proprietary" on the top of the page, and the proprietary information has been bracketed with an open and closed bracket as shown here "[]". The first page of the document indicates that all information identified as "Proprietary" should be withheld from public disclosure pursuant to 10 C.F.R. § 2.390 (a)(4).
3. The information identified as proprietary in the enclosed documents has in the past been, and will continue to be, held in confidence by MHI and its disclosure outside the company is limited to regulatory bodies, customers and potential customers, and their agents, suppliers, and licensees, and others with a legitimate need for the information, and is always subject to suitable measures to protect it from unauthorized use or disclosure.
4. The basis for holding the referenced information confidential is that it describes the unique design and methodology developed by MHI for performing the plant design of protection against postulated piping failures.
5. The referenced information is being furnished to the Nuclear Regulatory Commission ("NRC") in confidence and solely for the purpose of information to the NRC staff.
6. The referenced information is not available in public sources and could not be gathered readily from other publicly available information. Other than through the provisions in paragraph 3 above, MHI knows of no way the information could be lawfully acquired by organizations or individuals outside of MHI.
7. Public disclosure of the referenced information would assist competitors of MHI in their design of new nuclear power plants without incurring the costs or risks associated with the design of the subject systems. Therefore, disclosure of the information contained in the referenced document would have the following negative impacts on the competitive position of MHI in the U.S. nuclear plant market:

- A. Loss of competitive advantage due to the costs associated with the development of the methodology related to the analysis.
- B. Loss of competitive advantage of the US-APWR created by the benefits of the approach to jet expansion modeling that maintains the desired level of conservatism.

I declare under penalty of perjury that the foregoing affidavit and the matters stated therein are true and correct to the best of my knowledge, information and belief.

Executed on this 28th day of December, 2010.



Atsushi Kumaki,
General Manager- APWR Promoting Department
Mitsubishi Heavy Industries, LTD.

Docket No. 52-021
MHI Ref: UAP-HF-10356

Enclosure 3

UAP-HF-10356
Docket No. 52-021

References cited in Response to RAI 636-4732 for Pipe Break Hazard
Analysis Revision 1

December, 2010

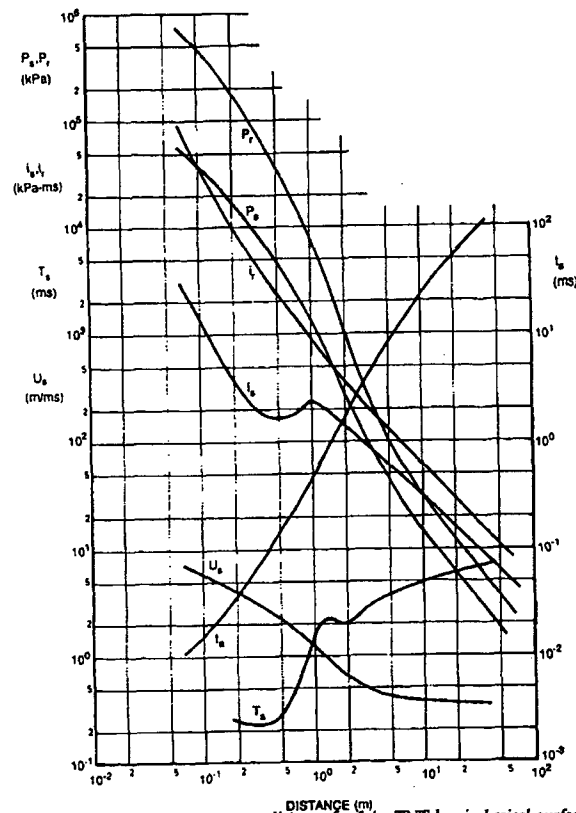


Figure 3.14 Blast wave parameters vs distance for 1 kg TNT hemispherical surface burst (after Ref. 10)

3.9 Blast wave interactions

When blast waves encounter a solid surface or an object made of a medium more dense than that transmitting the wave, they will reflect from it and, depending on its geometry and size, diffract around it. The simplest case is that of an infinitely large rigid wall on which the blast wave impinges at zero

Table 3.4

Z (m/kg ^{1/3})	b
0.4	8.50
0.6	8.60
0.8	10.00
1.0	9.00
1.5	3.50
2.0	1.90
5.0	0.65
10.0	0.20
20.0	0.12
50.0	0.24
100.0	0.50

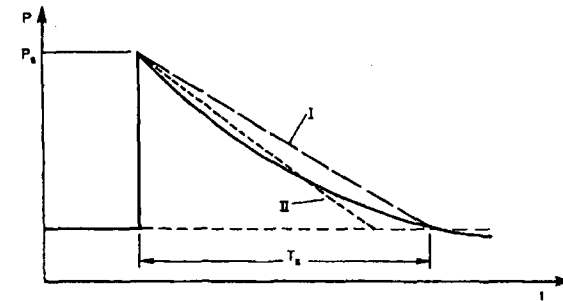


Figure 3.15 Blast wave profiles: real, conservative, impulse equality

angle of incidence. In this case the incident blast wavefront, travelling at velocity U_s into air at ambient pressure, undergoes reflection when the forward moving air molecules comprising the blast wave are brought to rest and further compressed inducing a reflected overpressure on the wall which is of higher magnitude than the incident overpressure. The situation is illustrated in Figure 3.16.

As mentioned above shock front parameters were first calculated by Rankine and Hugoniot derived from considerations of conservation of momentum and energy. From these equations, and assuming that air behaves as a real gas with specific heat ratio $C_p/C_v = \gamma$, all significant blast front parameters are obtainable.

For zero incidence, reflected peak pressure p_r is given by

$$p_r = 2p_s + (\gamma + 1)q_s \quad (3.36)$$

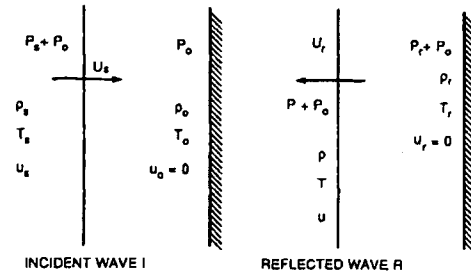


Figure 3.16 Face-on reflection

where the dynamic pressure q_s is

$$q_s = \frac{1}{2} \rho_s u_s^2 \quad (3.37)$$

Here ρ_s is the density of the air and u_s is the particle velocity behind the wavefront. It can be shown that

$$u_s = \frac{a_o p_s}{\gamma p_o} \left[1 + \left[\frac{\gamma + 1}{2\gamma} \frac{p_s}{p_o} \right] \right]^{-1} \quad (3.38)$$

where a_o is the speed of sound at ambient conditions. Substitution of Equations 3.37 and 3.38 into Equation 3.36 and rearrangement gives

$$p_r = 2p_s \left[\frac{7p_o + 4p_s}{7p_o + p_s} \right] \quad (3.39)$$

when, for air, γ is set equal to 1.4.

Inspection of this equation indicates that an upper and lower limit to p_r can be set. When the incident overpressure p_s is a lot less than ambient pressure (e.g. at long range from a small charge) the equation reduces to

$$p_r = 2p_s \quad (3.40)$$

When p_s is a lot greater than ambient pressure (e.g. at short range from a large charge) Equation 3.39 reduces to

$$p_r = 8p_s \quad (3.41)$$

If a reflection coefficient C_R is defined as the ratio of p_r to p_s then the Rankine-Hugoniot relationships predict that C_R will lie between 2 and 8. However, because of gas dissociation effects at very close range, measurements of C_R of up to 20 have been made. Figure 3.17 shows reflected overpressure and impulse i_r for normally reflected blast wave parameters plotted against scaled distance Z . It is worth noting that the lowest possible value of Z corresponds to the surface of the (spherical) TNT charge. If TNT is taken as being of density 1600 kg/m^3 , the limiting Z value is 0.053.

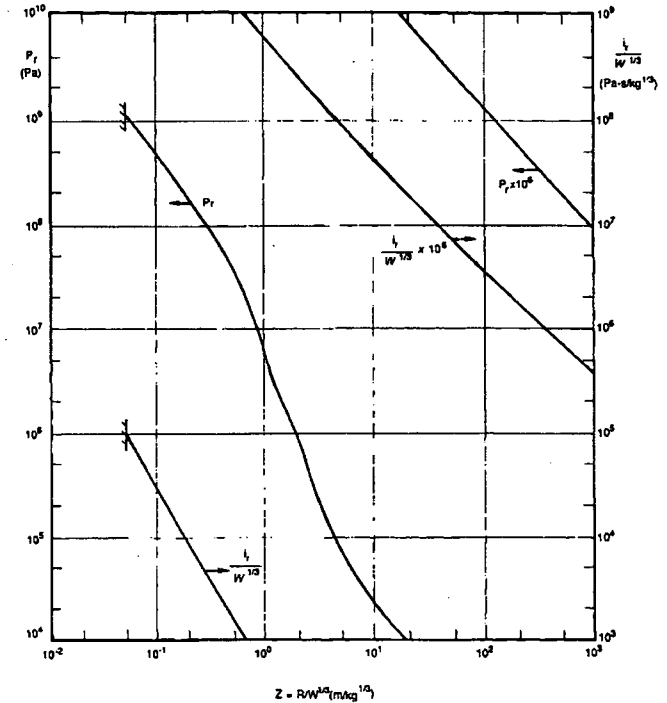


Figure 3.17 Face-on reflection: blast wave parameters vs scaled distance for spherical charges of TNT (after Ref. 6)

Reflected overpressure and impulse data are also given in the graphs of Figures 3.10 and 3.14 for 1 kilogramme spherical and hemispherical charges of TNT respectively.

3.9.1 Regular and Mach reflection

In the discussion above, the angle of incidence α_1 of the blast wave on the surface of the target structure was zero. When α_1 is 90° there is no reflection and the target surface is loaded by the peak overpressure which is sometimes referred to as 'side-on' pressure. For α_1 between these limits either regular reflection or Mach reflection occurs.

Consider firstly regular reflection which is illustrated in Figure 3.18.

To
Elizabeth, Caroline and Rachel
and
Janice, Alexander, Iona, Douglas, Amy and Alastair

Blast and Ballistic Loading of Structures

P. D. Smith

Senior Lecturer, Civil Engineering Group,
Cranfield University, Royal Military College
of Science

J. G. Hetherington

Head, Design Group, Cranfield University,
Royal Military College of Science

BUTTERWORTH
HEINEMANN

OXFORD AMSTERDAM BOSTON LONDON NEWYORK PARIS
SAN DIEGO SAN FRANCISCO SINGAPORE SYDNEY TOKYO

1442

Nuclear Engineering and Design

volume 67, No. 2, January 1982

EXPERIMENTAL STUDY ON AN IMPINGEMENT HIGH-PRESSURE STEAM JET

F. MASUDA and T. NAKATOGAWA

MAPI Engineering Center, Mitsubishi Atomic Power Industries, Inc., 1-2-1, Taito, Taito-ku, Tokyo, Japan

and

K. KAWANISHI and M. ISONO

Takasago Technical Institute, Mitsubishi Heavy Industries, Ltd., Takasago, Hyogo, Japan

pp. 273-286



NORTH-HOLLAND PUBLISHING COMPANY - AMSTERDAM

EXPERIMENTAL STUDY ON AN IMPINGEMENT HIGH-PRESSURE STEAM JET

F. MASUDA and T. NAKATOGAWA

MAPI Engineering Center, Mitsubishi Atomic Power Industries, Inc., 1-2-1, Taito, Taito-ku, Tokyo, Japan

and

K. KAWANISHI and M. ISONO

Takasago Technical Institute, Mitsubishi Heavy Industries, Ltd., Takasago, Hyogo, Japan

Received 29 September 1981

An experimental study on impingement high-pressure steam jet was performed as one of the efforts to establish evaluation methods for effects caused by a jet under the postulated pipe rupture accident in a nuclear power plant.

An ejected steam jet from a nozzle into the atmosphere is impinged vertically on the flat plate. Nozzle reaction, jet impingement force and impingement pressure distribution were measured over a wide range of impingement distances. Employed nozzles are circles and ellipses. The steam is supplied under steady state and dry saturated, and the pressure is approximately 4.56 MPa.

From the data of nozzle reaction and impingement force, these are mutually equal and are proportional to the stagnant pressure upstream of the nozzle; and from this data, the thrust coefficient for each nozzle was calculated. Based on the data of impingement pressure distribution, the jet is roughly divided into three regions on the axis according to the characteristics of distribution in both circular and elliptical nozzles. In addition, in the case of a circular nozzle, locations where the characteristics of distribution distinctly change depend on the location of Mach disk. In the case of an elliptical nozzle, expansion on the minor axis is remarkably higher than on the major axis, particularly near the nozzle exit.

1. Introduction

In the design of a nuclear power plant, it is required to secure the safety of the plant against effects caused by jet flow under the postulated pipe rupture accident. These effects include thrust forces, impingement loads, environmental changes and so on. They have a serious effect on the structural design of the building, equipment and the other components. For thrust forces and environmental changes, sufficient information or understanding seems to have been obtained. On the other hand, for the characteristics of a high-energy jet, the work up to now has not been enough to establish applicable evaluation methods in the design. Particularly, there are many unknown characteristics of a jet in the case of high-energy fluid conditions such as high-pressure steam present under the highly under-expanded condition or subcooled water behaving as a two-phase jet including moreover, the effects of nozzle geometry supposed in the design.

With these considerations, an experimental study has

been carried out to clarify the characteristics of impingement jet and incidental effects. In a previous study, the fundamental experimental study on subcooled water and steam jet was carried out and the results were reported in Paper F6/2 of 5th SMIRT [1]. At present, the experimental study of an impingement steam jet was carried out to obtain more detailed data and to further clarify the characteristics over a wide axial range, including the effects of nozzle geometry.

In this paper, representative results of the experiment are described and the characteristics of pressure distribution of a jet are discussed in relation to the internal structure of the jet.

2. Experimental apparatus and procedure

A scheme of the experimental apparatus is shown in fig. 1. A steam jet is ejected downward into the atmospheric environment and impinged vertically on the flat plate. The nozzle reaction force is measured by the load

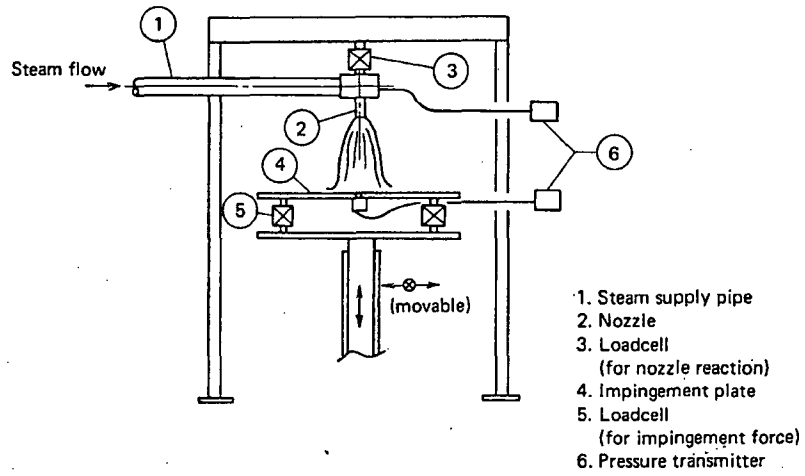


Fig. 1. Sketch of experimental apparatus.

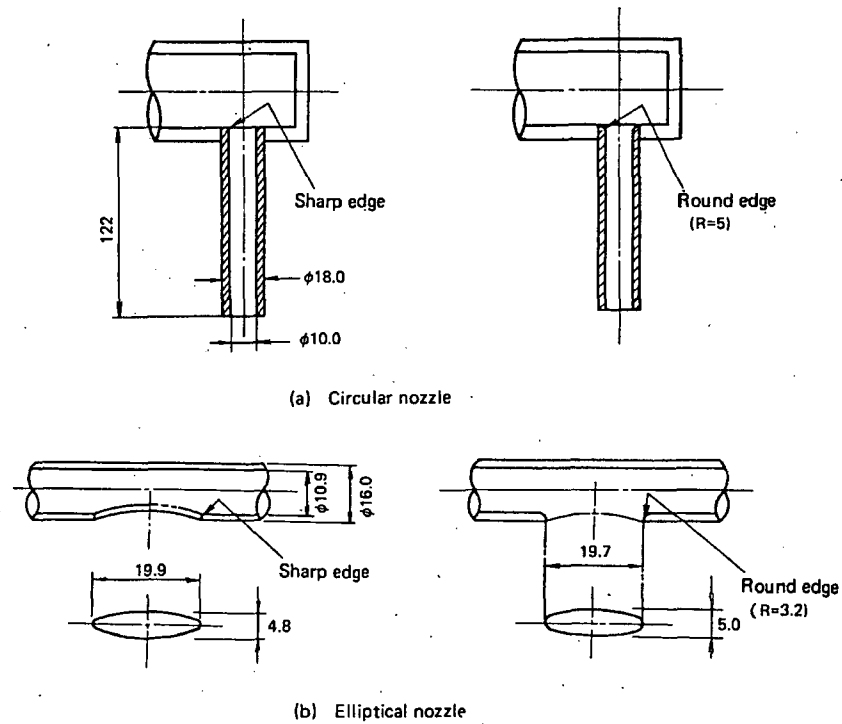


Fig. 2. Nozzle geometry.

cell in contact with the nozzle. Impingement force and impingement pressure distribution are measured by the load cells and pressure gauge attached to the impingement plate. The impingement plate is devised to be movable horizontally and vertically to permit the measurements of axial variation of impingement forces and pressure distributions.

As shown in fig. 2, two types of nozzles are employed. One is circular (short pipe) and the other elliptical opened in the longitudinal side of the pipe simulating the break geometry of which the aspects ratio is 4, postulated in the design. For surveying the effect of flow contraction, two types of edge entrances, round and sharp, are provided with each nozzle type.

The steam is supplied under steady state and dry saturated, and the pressure is approximately 4.56 MPa. Furthermore, for surveying an internal structure of the jet, pressure distributions of the free jet were also measured using the Pitot tube.

3. Experimental results and discussion

3.1. Nozzle reaction and impingement force

Measured nozzle reaction forces are plotted in fig. 3 for the circular nozzles and in fig. 4 for the elliptical nozzles. Practically no differences were observed between the impingement force data and nozzle reaction

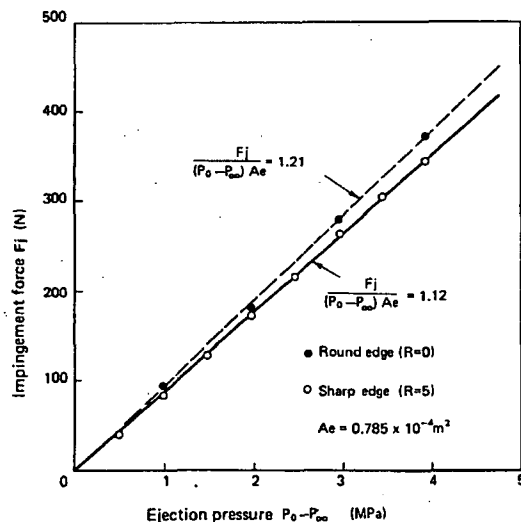


Fig. 3. Impingement jet forces for the circular nozzle.

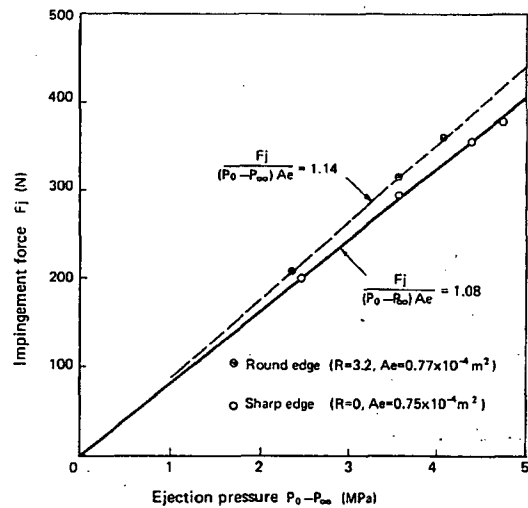


Fig. 4. Impingement jet forces for the elliptical nozzle.

force data. From the relation shown in the figures, these forces are approximated as

$$F_R = F_j = K (P_0 - P_\infty) A_e, \quad (1)$$

where F_R is nozzle reaction, F_j impingement force, K thrust coefficient, P_0 stagnation pressure upstream of nozzle, P_∞ environmental pressure ($= 101.3$ kPa) and A_e discharge area. Using experimental data the thrust coefficient K for each nozzle is obtained from eq. (1) as follows:

- $K = 1.21$, circular nozzle with round edge;
- $K = 1.12$, circular nozzle with sharp edge;
- $K = 1.14$, elliptical nozzle with round edge;
- $K = 1.08$, elliptical nozzle with sharp edge.

These values are smaller than $K = 1.24$ which is obtained from Moody's critical flow model for the ideal nozzle [2], though the value for the circular nozzle with round edge is practically equal. The value for the sharp edge is relatively smaller than for the round edge; it shows that the flow contraction causes a reduction of reaction and impingement forces. The value for the ellipse is relatively smaller than for the circle with the same edge type; it may show that an upstream pressure drop to the exit and a contraction effect at the exit cause the reduction of forces.

Variation of impingement forces and central pressures on the plate at impingement distances $H/D = 0.01-0.5$ were measured for the circular nozzle. As

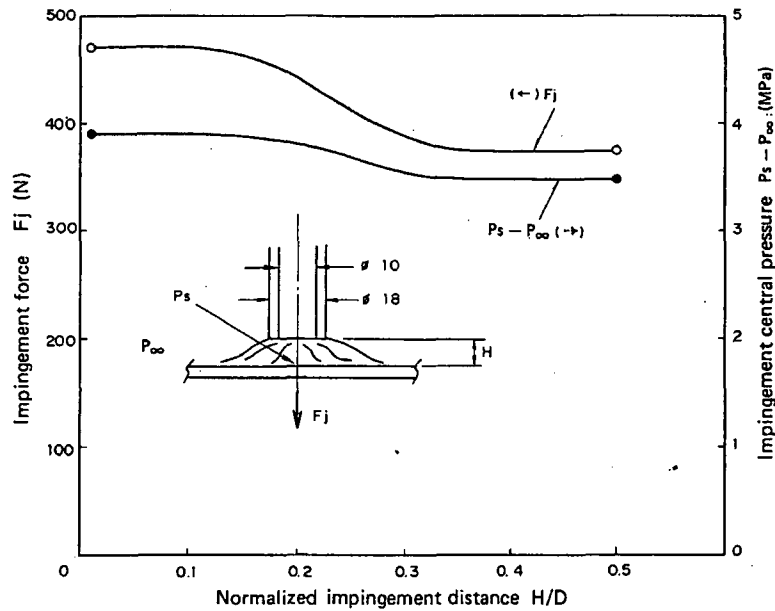


Fig. 5. Impingement jet forces and central pressures at short distances (circular nozzle $R=5$, $P_0 - P_\infty = 3.92$ MPa).

shown in fig. 5, impingement forces and pressures increase with decreasing the distance. Such a tendency is attributed to the fact that the sonic plane moves from the nozzle exit to the gap between the nozzle lip and the plate surface, namely, the flow is choked in the gap and hence the central flow becomes nearly stagnant and the high-pressure region acting on the plate surface increases.

3.2. Characteristics of impingement pressure distribution

From application to the design evaluation point of view, it is required to seize various characteristics of impingement jets, taking into consideration the initial fluid condition, nozzle geometry, impingement distance, target geometry or inclination, ambient pressure and so on.

Here, the basic experiments were carried out in order to determine the characteristics of impingement high-pressure steam jet in relation to the effects of ejection pressure, impingement distance and nozzle geometry. The pressure distributions were measured at the impingement distances $H/D = 0.5-62.5$ for the circular nozzle and $H = 5-373$ mm for the elliptical nozzle (major diameter = 20 mm, minor diameter = 5 mm).

3.2.1. Characteristics of an impingement jet from the circular nozzle

Typical structures of highly under-expanded free and impingement jet from the circular nozzle are shown in fig. 6. The Schlieren photographs in Kukita's study [3] were referred to when drawing the figure.

First, for a free jet near the nozzle exit, as flow is choked at the exit, the exit pressure is higher than the ambient pressure. Hence a discharged flow rapidly expands and is present with the structure formed by some shock waves as shown in fig. 6. As for the impingement jet, three typical flow patterns occur with increasing impingement distance. In the region near the nozzle exit, flow is supersonic and when intercepted by the plate, a detached shock wave is formed in front of the plate. In the region downstream to the Mach disk, the occurrence of a recirculation stream in front of the plate has been verified by some other studies [3,4]. In the further region, characteristics are transformed into those of a turbulent jet, which are well known.

Some of the measured pressure distributions on an impingement jet are shown in fig. 7 and the measured Pitot pressure distributions on a free jet are shown in fig. 8 for $P_0 = 4.02$ MPa. For $P_0 = 2.06, 3.04, 4.02$ MPa variations of central pressure are shown in fig. 9. In

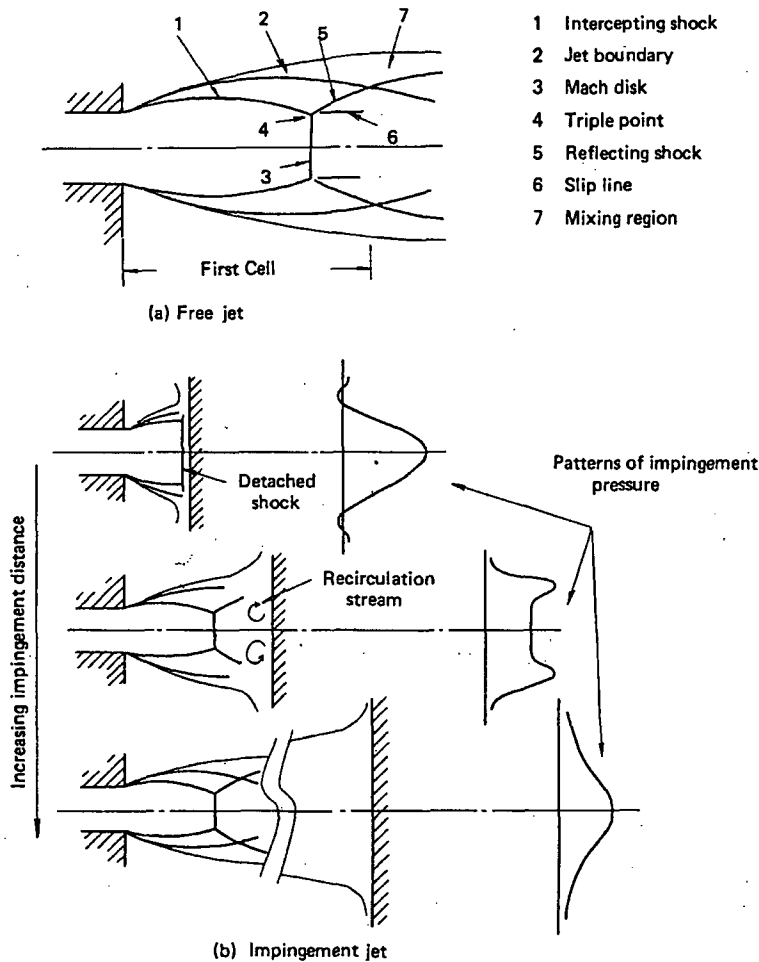


Fig. 6. Structure of highly under-expanded jet.

fig. 9, Donaldson's data [4] on an air jet ($P_0 = 0.6$ MPa) are reproduced, the measured data on a free jet ($P_0 = 4.02$ MPa) and Mach disk locations given by Love et al. [5] are also shown. An impingement jet is roughly divided into three regions on the jet axis according to the characteristics of distributions shown in fig. 7:

(1) *First region.* In the region near the nozzle exit, a rapid expansion accompanied by a reduction of impingement pressure occurs and the pressure profile changes from convex (like the hanging bell) type to the type which has shoulders. Increasing the distance further, the central peak falls and a flat pattern occurs. The

location where the flat pattern is formed is approximately equal to that of the Mach disk given by Love et al. [5], and the end of the first region may be defined by this location. (Though the location of the Mach disk in Love's study is for an air jet, the differences of characteristics between steam and air are expected to be small. As for the measured data on a free jet, the verified location of the Mach disk practically agrees with that of Love's study as shown in fig. 9 as the beginning of the flat portion.)

Considering that the detached shock wave is formed in front of the plate in this first region, the variation of

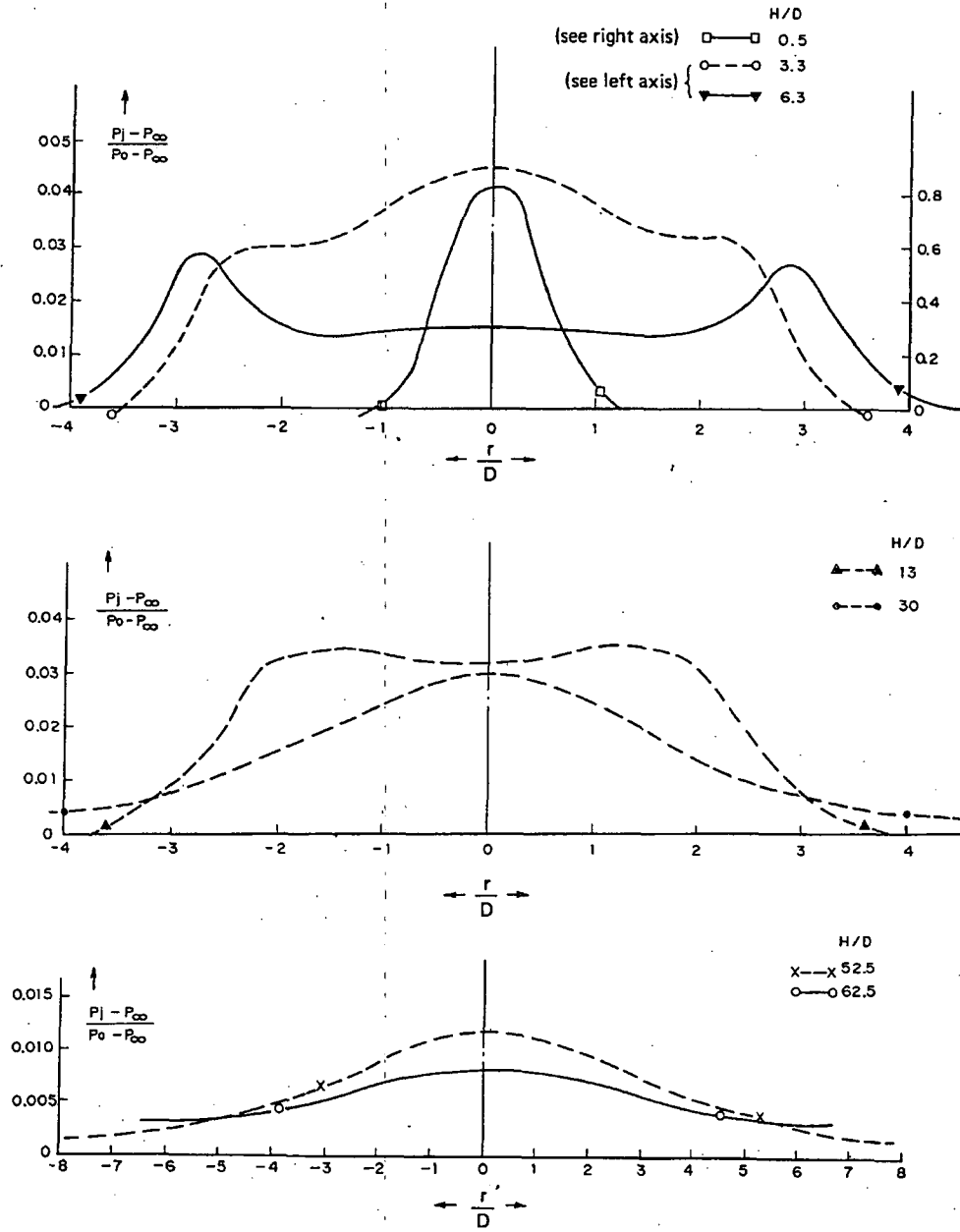


Fig. 7. Impingement pressure profiles ($P_0 = 4.02$ MPa, circular nozzle with sharp edge entrance).

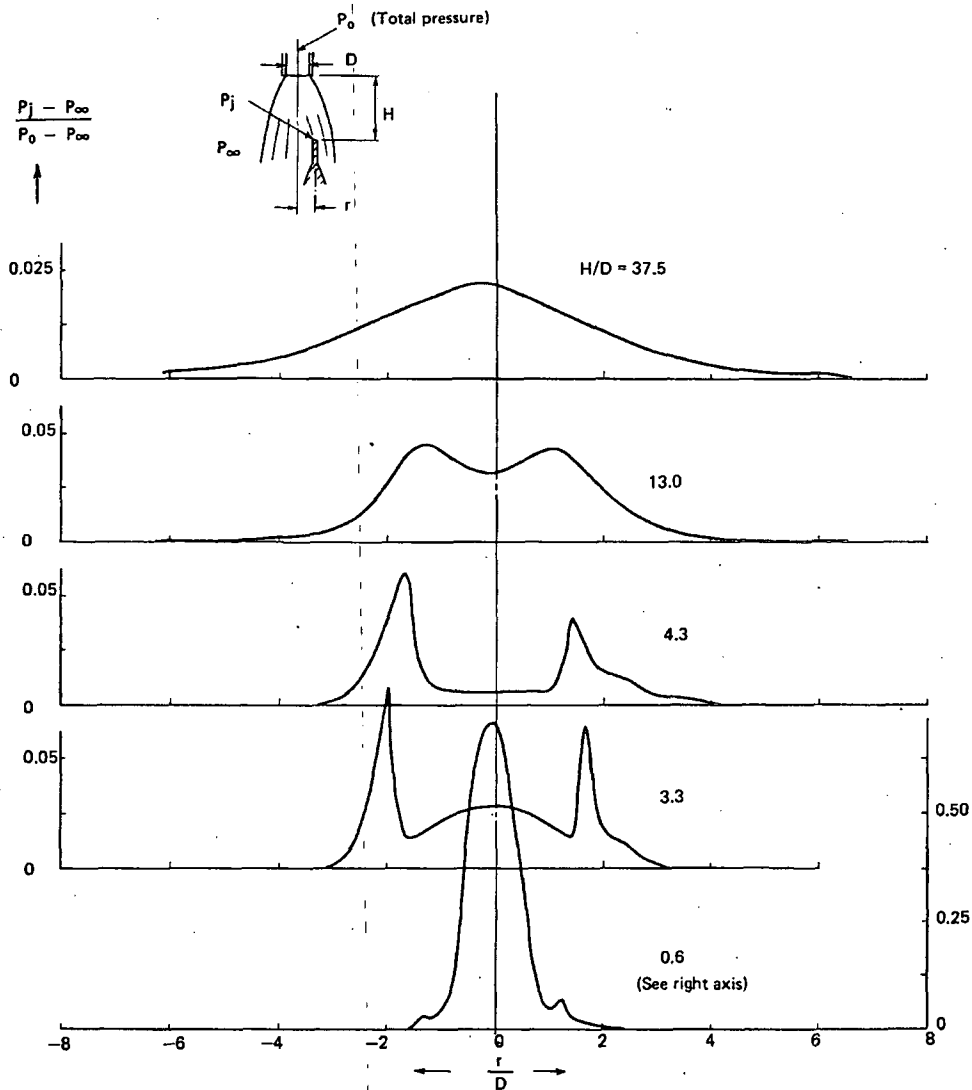


Fig. 8. Pitot pressure profiles on a free jet ($P_0 = 4.02$ MPa, circular nozzle with round edge entrance).

central pressure is approximately expressed by the normal shock wave relation for stagnation pressure ratio across the shock wave as follows:

$$\frac{P_3}{P_0} = \left[\frac{(k+1)M_1^2}{(k-1)M_1^2 + 2} \right]^{\frac{k}{k-1}} \left[\frac{k+1}{2kM_1^2 - (k-1)} \right]^{\frac{1}{k-1}} \quad (2)$$

where P_0 : total pressure upstream of shock, P_3 : total pressure downstream of shock, k : ratio of specific heats, M_1 : Mach number upstream of shock. The result calculated using eq. (2) is shown in fig. 9 as a broken line. (In the calculations, the Mach number distribution in Owen et al.'s study [6] for an ideal gas ($k = 1.4$) equivalent to air was referred to.)

Compared with the data on a free jet, the calculated

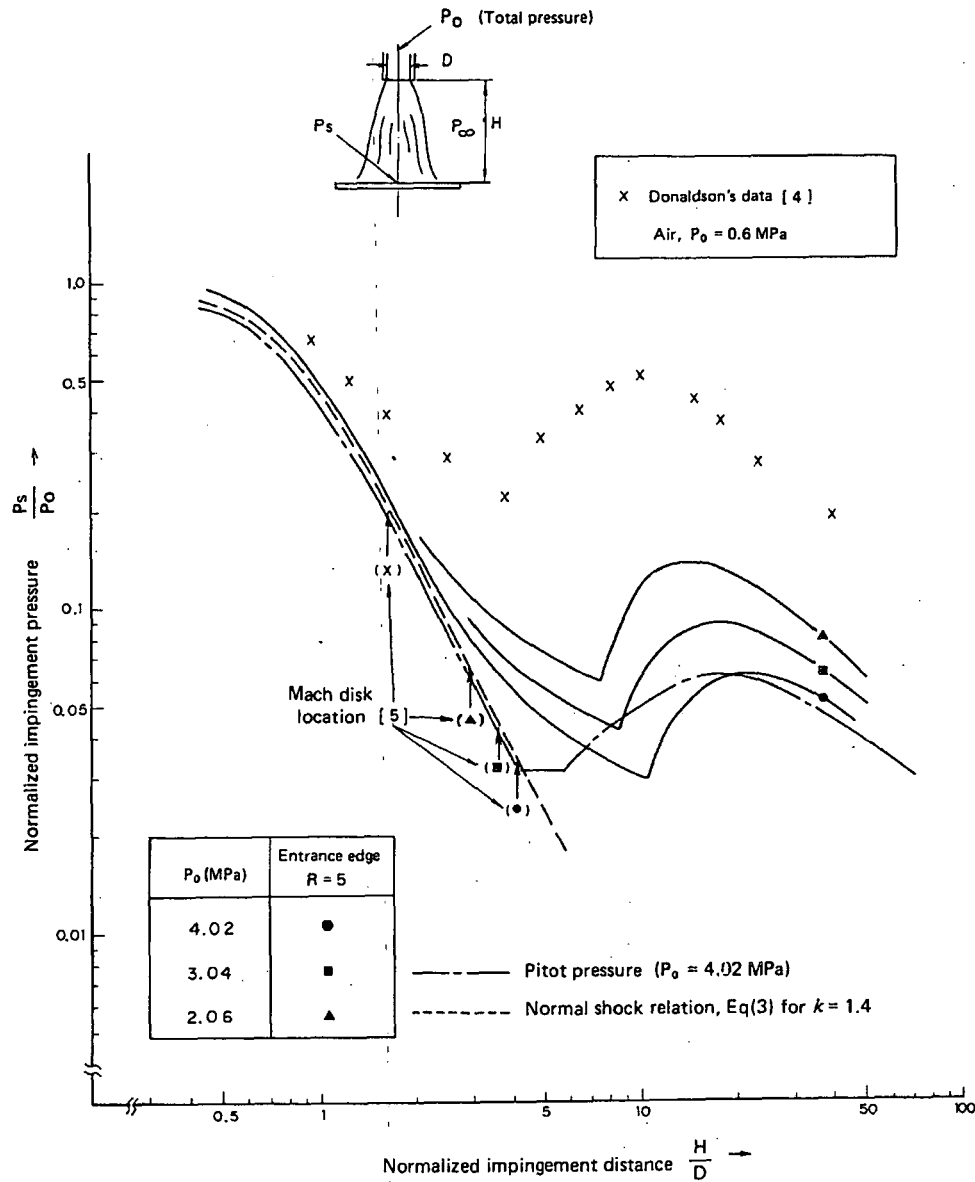


Fig. 9. Variation of central impingement pressure for the circular nozzle.

result approximately agrees, but is slightly higher. This slight shift may show the difference of characteristics between steam and ideal gas. Besides, comparing the data of an impingement jet with the calculated results

from eq. (2) (or the data on a free jet), the former is slightly higher near the nozzle exit and gradually separates on nearing the Mach disk location. These tendencies may be attributed to the reason that the detached

shock is formed away from the plate and the distance between the detached shock and the plate increases on nearing the Mach disk location. Here, noticing that the peripheral peak (corresponding to the jet boundary) on

a free jet becomes conspicuous on nearing the Mach disk location such as given in fig. 8, this condition may cause a smooth delivery of flow from the central portion to be intercepted and central pressure to be increased

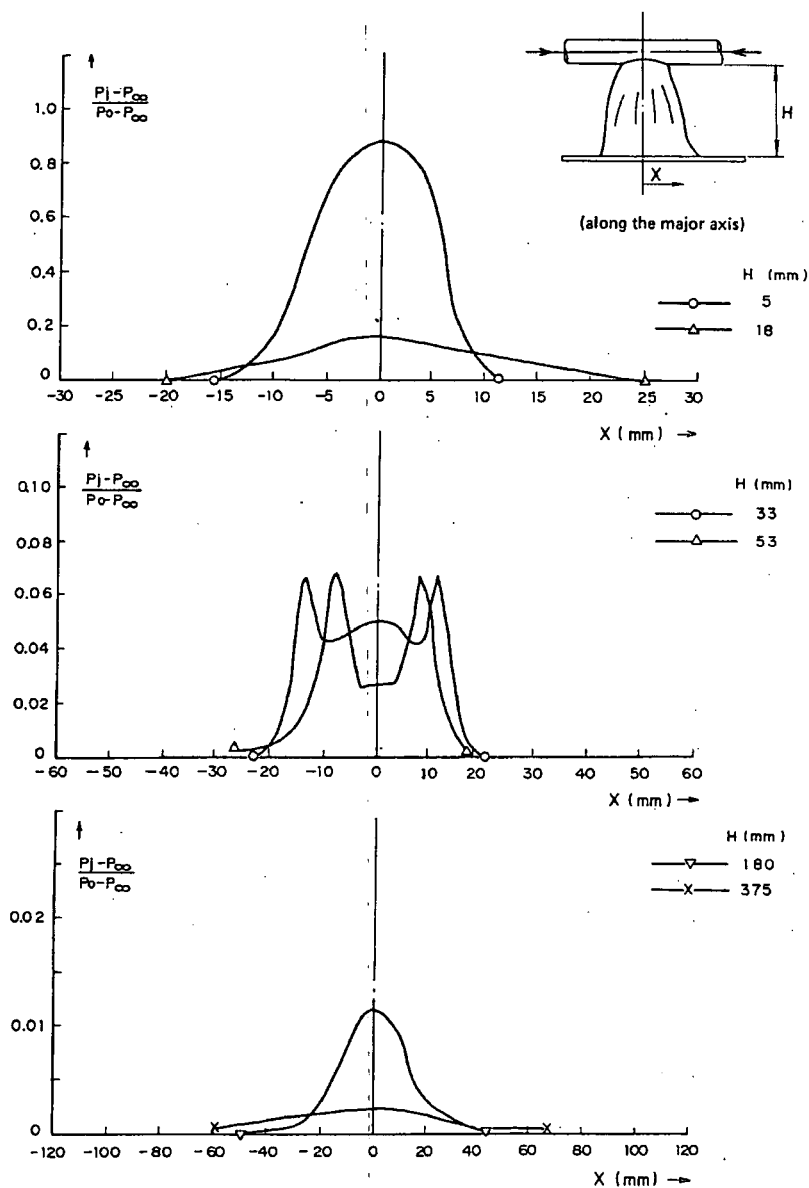


Fig. 10a. Impingement pressure profiles for the elliptical nozzle ($R=0$, $P_o = 4.56$ MPa, X direction).

when impinged on the plate, and that is why the distance between the detached shock and the plate increases.

(2) *Second region.* Marked radial expansion does not

occur in this region. However, as the central pressure reduces on increasing the impingement distance, the pressure profile changes from the flat type to the concave (like the saddle-back) type. Then the recovery of

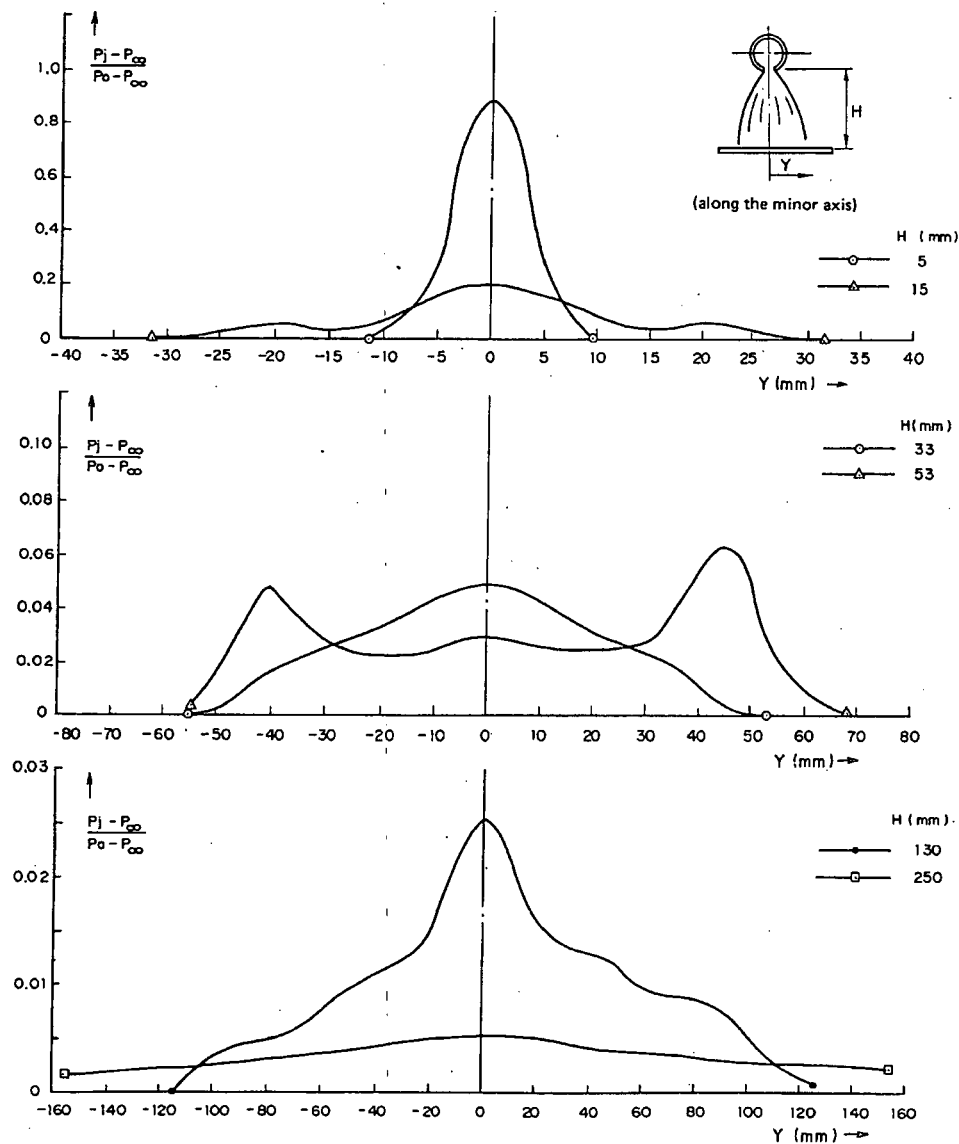


Fig. 10b. Impingement pressure profiles for the elliptical nozzle ($R=0$, $P_0=4.56$ MPa, Y direction).

pressure occurs in the center on increasing the impingement distance and a re-transition of the pattern from the flat type to the smooth type is seen. The end of the second region may be defined as the point where the

maximum recovery pressure occurs. As shown in fig. 9, the location at which the bottom pressure occurs corresponds to about 2.5 times the distance to the Mach disk, and the location at which the maximum recovery pres-

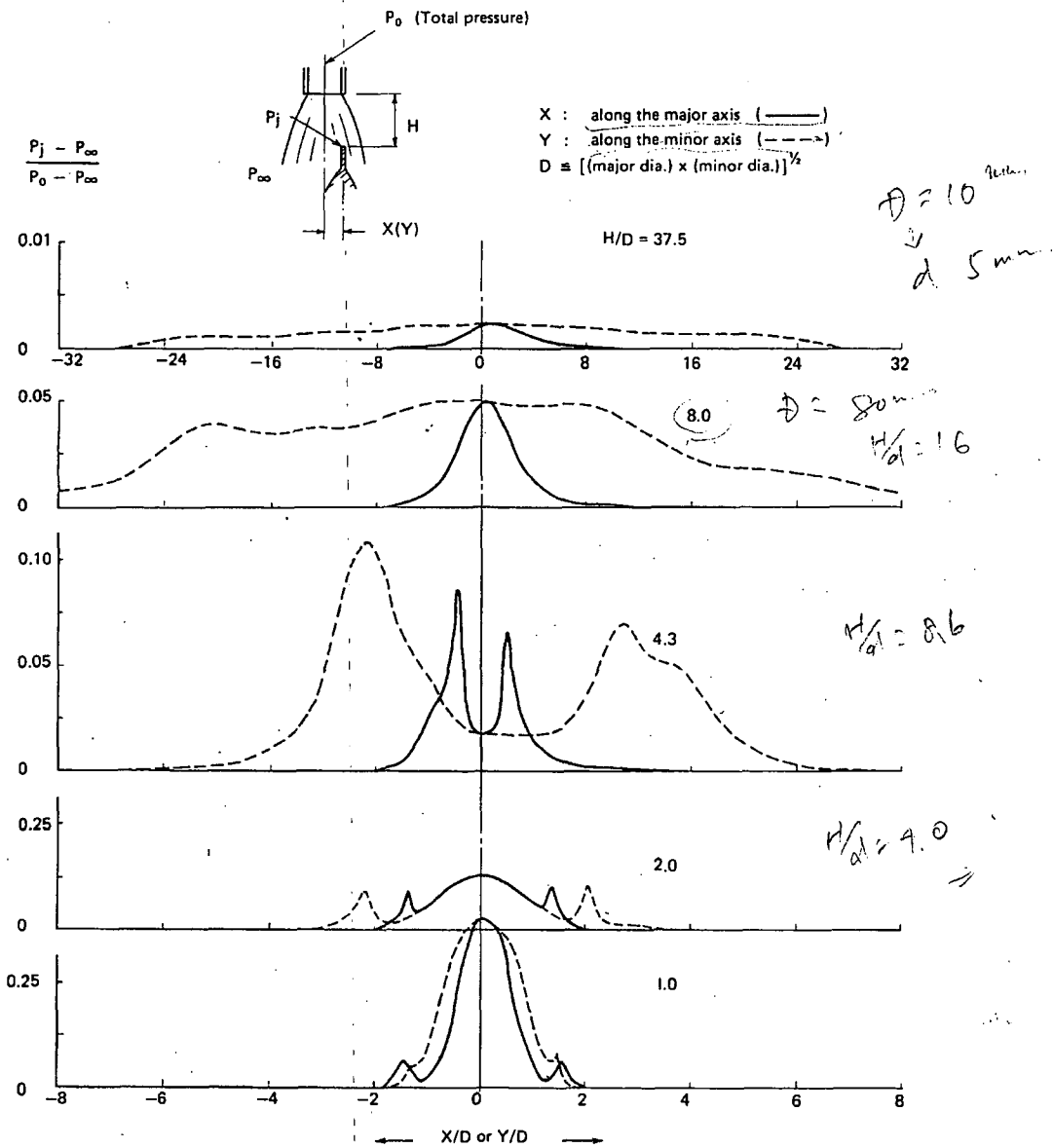


Fig. 11. Pitot pressure profiles on a free jet ($P_0 = 4.02$ MPa, elliptical nozzle with round edge entrance).

sure occurs corresponds to about 5 times that distance. The bottom pressure and the maximum recovery pressure increase slightly on decreasing the stagnation pressure P_0 . In addition to the above, it is seen that the

bottom pressure is approximately equal to that calculated with the normal shock wave relation at the Mach disk location.

(3) *Third region.* In this region, the jet expands grad-

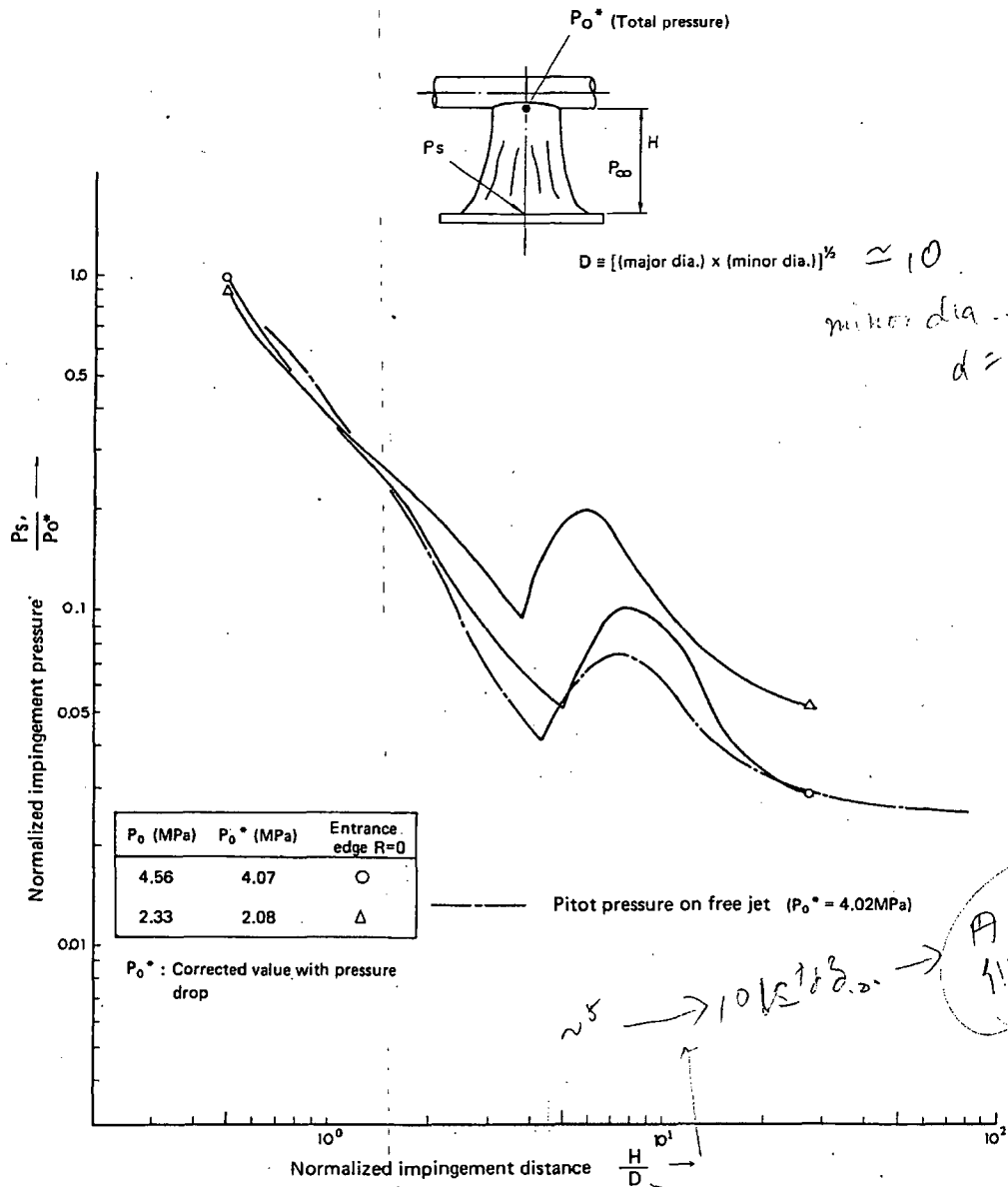


Fig. 12. Variation of central impingement pressure for the elliptical nozzle.

ually and the central pressure decays monotonically as the mixing region grows. As is well known, the characteristics of the impingement pressure distribution is given by the half-width expression once the mixing region is fully developed. Referring to fig. 9, transitional points to linear decay reflecting the characteristics of turbulent jet are equivalent to about 10 times the distance to the Mach disk location.

3.2.2. Characteristics of an impingement jet from the elliptical nozzle

Up to now, sufficient theoretical or experimental information on the highly under-expanded jet discharged from the nonaxisymmetric nozzle, such as the ellipse in this study, has not been found.

Some of the measured pressure distributions on an impingement jet for $P_0 = 4.56$ MPa are shown in fig. 10a along the major axis and in fig. 10b along the minor axis, while Pitot pressure distributions on a free jet for $P_0 = 4.02$ MPa are shown in fig. 11. For $P_0 = 2.33$ MPa ($P_0^* = 2.08$ MPa) and $P_0 = 4.56$ MPa ($P_0^* = 4.07$ MPa), the variations of central pressure are shown in fig. 12. Here, P_0^* denotes the stagnant pressure proportionally corrected with the reduction rate of thrust coefficient of the circular nozzle with a round edge entrance.

As shown in figs. 10a and 10b, the variations of patterns with increasing impingement distance are similar to the case of the circular nozzle. Therefore, impingement jet from the elliptical nozzle may be roughly divided into three regions on the jet axis, similar to the case of the circular nozzle.

In addition to the above similarity with the circular nozzle, the following particular characteristics are seen:

(1) The expansion along the minor axis is greater than that along the major axis in the measured region. This tendency is remarkable in the region near the nozzle exit.

(2) Concerning the transition of the type of pressure profile, the results of measurements show that the transition on the major axis occurs at a shorter impingement distance than that on the minor axis.

Here, considering the behavior of expansion near the nozzle exit, expansion near both the ends of the major axis is three-dimensional, and near the center nearly two-dimensional. In such a condition, a reduction of pressure near both ends of the major axis is more rapid than that near the center, and hence expansion on the major axis may be suppressed. This behavior can be verified by the variations of location of a peripheral peak (corresponding to the jet boundary) on the jet axis in fig. 11. In addition, for transition to the turbulent jet, since the expansion width on the major axis is narrower

than on the minor axis, this condition is liable to further promote the growth of a mixing region on the major axis and to cause the transition to the turbulent jet at a shorter distance.

4. Conclusion

Principal results in this study are as follows.

(1) The values of the thrust coefficient, K , for each nozzle type were obtained from measurements of nozzle reaction forces and impingement forces. Comparing these values with the value 1.24, obtained theoretically by applying Moody's critical flow model, the value for the circular nozzle with a round edge entrance is practically equal, and for other nozzle types substantial reduction exists.

(2) Impingement forces in the region near the nozzle exit ($H/D = 0.01-0.5$) for the circular nozzle were also measured. It was found that impingement forces in this region were greater than those in a further region on the jet axis.

(3) For both circular and elliptical nozzles, the pattern of impingement pressure distribution of a jet remarkably changes with increasing impingement distances and a jet is roughly divided into three regions on the jet axis according to the characteristics of distribution.

(4) For a circular jet, locations where the pattern of impingement pressure distribution distinctly changes depend on the location of the Mach disk which is determined by the stagnant pressure at the nozzle exit. These locations are approximately expressed by multiplying constants, which are common for any value of the stagnant pressure, by the distance to the Mach disk.

(5) For an elliptical jet, the expansion on the minor axis is greater than that on the major axis, particularly near the nozzle exit. The locations where the pattern of impingement pressure distribution distinctly changes depend on the stagnant pressure at the nozzle exit, similar to the case of the circular jet. Concerning the transition of the type of pressure profile, however, the transition on the major axis occurs at a shorter impingement distance than that on the minor axis.

References

- [1] K. Kitade et al., Experimental study of pipe reaction force and jet impingement load at the break. Paper F6/2 of 5th SMiRT, Berlin (August 1979).
- [2] F.J. Moody, Maximum flow rate of a single component

- two-phase mixture, *J. Heat Transfer, ASME, Series C*, Vol. 87 (1965).
- [3] Y. Kukita, Study on unstable phenomena of supersonic impinging jets, Ph. D. Thesis, University of Tokyo (December 1974).
- [4] C.D. Donaldson et al., A study of free jet impingement. Part 1: Mean properties of free and impinging jets, *J. Fluid Mech.* 45, Part 2 (1971).
- [5] E.S. Love et al., Experimental and theoretical studies of axisymmetric free jets, *NASA Technical Report R-6* (1959).
- [6] P.L. Owen et al., The flow in an axially-symmetric supersonic jet from a nearby sonic orifices into a vacuum, *Brit. A.R.C. Technical Report, R&M 2616* (1952).

Experimental and Computational Investigation of Supersonic Impinging Jets

F. S. Alvi*

Florida A&M University and Florida State University, Tallahassee, Florida 32310

and

J. A. Ladd[†] and W. W. Bower[‡]

The Boeing Company, St. Louis, Missouri 63166

The results of an experimental and computational study of a moderately underexpanded axisymmetric supersonic jet issuing from a converging nozzle and impinging on a ground plane are presented. The goal of this work is to develop a better understanding of the impinging jet flowfield, which is of significant practical interest because of its presence in short takeoff and vertical landing (STOVL) aircraft during hover as well as in other aerospace-related and industrial applications. The experimental measurements include flow visualization, surface-pressure distributions, and velocity field data obtained using particle image velocimetry (PIV). The experimental data, especially the velocity field measurements, were used to verify the accuracy of computational predictions. Computational results obtained using two different turbulence models produced almost identical results. Comparisons with experimental results reveal that both models capture the significant features of this complex flow and were in remarkably good agreement with the experimental data for the primary test case. The experiments and computations both revealed the presence of the impingement zone stagnation bubble, which contains low velocity recirculating flow. Other features, including the complex shock structure and the high-speed radial wall jet, were also found to be very similar. The ability to measure and predict accurately the impinging jet behavior, especially near the ground plane, is critical because these are regions with very high mean shear, thermal loads, and unsteady pressure forces, which contribute directly to the problem of ground erosion in STOVL applications.

Introduction

HIGH-SPEED impinging jets can occur in a variety of aerospace-related applications. These jet flows are particularly troublesome to short takeoff and vertical landing (STOVL) aircraft, such as the Harrier/AV-8 family, during hover mode. In these instances the flowfield produced by the impingement of the high-speed lift jets produces adverse local flow conditions, which can potentially lead to the degradation of aircraft performance in a number of areas during hover. These adverse effects, collectively referred to as ground effects, are the result of the highly unsteady nature of the flow generated by the impingement of the high-speed jet(s) on the ground plane and the pressure field caused by the natural entrainment by these jets. They include lift loss caused by flow entrainment associated with the lifting jets, which induces low surface pressures on the airframe resulting in a "suckdown" force opposite to lift. The lift loss typically increases in magnitude as the aircraft approaches the ground and can be greater than 60% of the total lift jet thrust when the jets are very close to the ground plane.¹ Increased noise or overall sound-pressure levels associated with high-speed impinging jets and the sonic fatigue of structural elements in the vicinity of the nozzle exhaust caused by unsteady loading is also an area of concern. In addition to higher levels, the noise spectrum is dominated by discrete tones, which, if close to the aircraft panel frequencies, can further aggravate the sonic fatigue problem. Furthermore, the impingement of hot, high-speed lift jets on the landing surface can lead

to significant erosion caused by the extremely high shear stresses and wall heat-transfer rates created in this flow. Finally, the outwash from the hot impinging jets can be drawn into the engine inlets, a phenomenon known as hot gas ingestion, thus degrading engine performance and potentially risking engine failure.

Some of the problems just outlined are known to occur for the subsonic Harrier family of aircraft. They are expected to become more acute for the future generation of the supersonic STOVL aircraft, where the environment is expected to be more severe because of the impingement of supersonic jets operating at higher temperatures. Consequently, the study of supersonic impinging jet flows is of great interest from a practical perspective. Furthermore, the complex nature of the impinging jet flowfield, which often includes multiple shock and shock/shear layer interactions, subsonic, supersonic and separated flows, makes this flow interesting from a fundamental fluid dynamics standpoint.

Impinging jet flows have been the focus of research for over three decades, where their fluid dynamic and acoustic properties have been carefully examined by a number of capable investigators. Notable among the acoustic studies are those by Neuwerth,² Powell,³ Tam and Ahuja,⁴ Henderson and Powell,⁵ and most recently Krothapalli et al.¹ One of the primary outcomes of these aeroacoustic studies is that the highly unsteady, oscillatory nature of impinging jet, which is accompanied by discrete, high-amplitude acoustic tones, referred to as impingement tones, is caused by a feedback loop. The globally oscillatory behavior of the jet and the resulting impingement tones have been explained well by a feedback mechanism derived from earlier work by Powell.⁶ Recently, Krothapalli et al.¹ demonstrated that the feedback phenomenon might also be responsible for the lift loss, described earlier, through the generation of large-scale structures in the jet shear layer. Because the focus of the present work is the mean behavior of the impinging jet, a more detailed discussion of the unsteady properties is outside the scope of this article. The interested reader is directed to the references just cited. Suffice it to say that the fluid dynamic and acoustic properties of this flow appear to be intimately related.

The structure and fluid dynamic properties of this flow have also been investigated in a number of studies. In a classic study Donaldson and Snedeker^{7,8} examined the flowfield using schlieren

Presented as Paper 2000-2224 at Fluids 2000, Denver, CO, 19-22 June 2000; received 7 August 2000; revision received 24 July 2001; accepted for publication 20 September 2001. Copyright © 2001 by the authors. Published by the American Institute of Aeronautics and Astronautics, Inc., with permission. Copies of this paper may be made for personal or internal use, on condition that the copier pay the \$10.00 per-copy fee to the Copyright Clearance Center, Inc., 222 Rosewood Drive, Danvers, MA 01923; include the code 0001-1452/02 \$10.00 in correspondence with the CCC.

* Associate Professor, Fluid Mechanics Research Laboratory, Department of Mechanical Engineering, Senior Member AIAA.

[†] Engineer/Scientist, Mailcode 1067126, P.O. Box 516, Member AIAA.

[‡] Boeing Technical Fellow, Mailcode 1067126, P.O. Box 516, Associate Fellow AIAA.

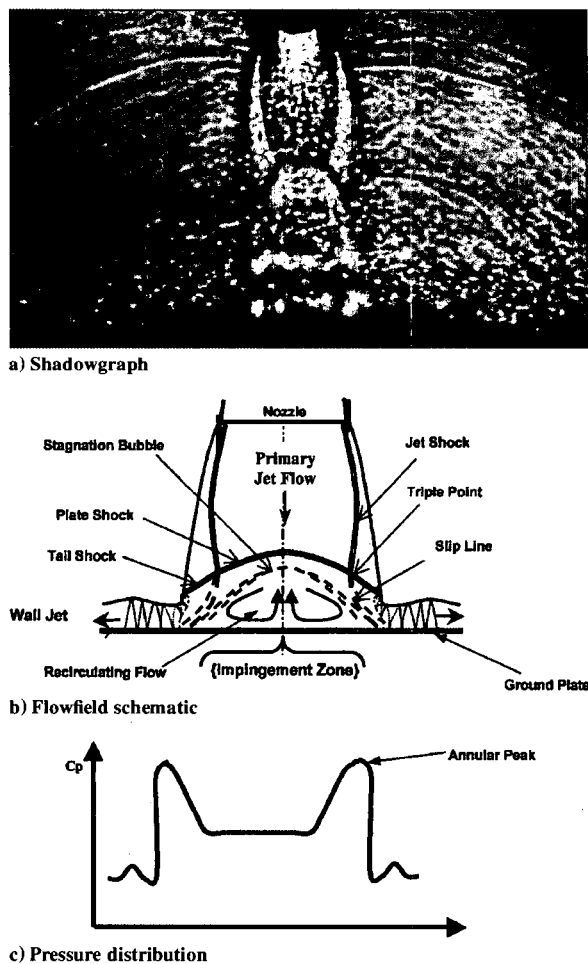


Fig. 1 Stagnation bubble flowfield.

photography, surface flow visualization, mean surface-pressure measurements, and, to a limited extent, surface heat-transfer rates. Carling and Hunt⁹ and Lamont and Hunt¹⁰ have further studied this flow, concentrating on the impingement zone, which lies at the center of the flowfield, and the wall jet region (see Fig. 1). In addition, Gubanova et al.,¹¹ Ginzberg et al.,¹² and Gummer and Hunt¹³ have also examined the flow structure in detail, particularly in the impingement zone. The impingement zone is perhaps the most important and certainly the most complex part of this flow, and although previous studies have provided some insight into this flow region some issues such as the conditions for the formation of a stagnation bubble in the impingement zone^{11,13} are still not well understood. Further discussion of this issue is delayed until the beginning of the Results and Discussion section; a more detailed review of this issue can be found in Alvi and Iyer.¹⁴ In summary, although earlier studies provided valuable insight into the flowfield behavior, they mainly relied on measurements of mean surface-pressure distributions and surface flow visualization. Until recently, very little quantitative data have been available in the flowfield above the surface, especially in the critical near-surface flow in the impingement and wall-jet regions.

To address some of these issues and to gain a better understanding of supersonic impinging jet flows, especially their behavior in the context of STOVL aircraft, a comprehensive experimental investigation of the impinging jet flowfield was initiated at the Fluid Mechanics Research Laboratory (FMRL), Florida A&M University and Florida State University, Tallahassee, Florida, a few years ago. One of the most notable contributions of this ongoing experimental effort has been the velocity field data obtained using the particle image velocimetry (PIV) technique. To the authors' knowledge

these data are the first of their kind to provide detailed velocity and vorticity field information over the entire flow. The PIV measurements combined with acoustic data, flow visualization, and mean and unsteady pressure fields have provided significant insight into the overall behavior of this flow. In addition to the experimental study, a collaborative computational effort was also initiated with The Boeing Company. Boeing is performing computational fluid dynamics (CFD) for selected test cases where the experimental data have been used to benchmark the computational code in order to establish its accuracy. Previous studies of free and impinging compressible jets have been made at Boeing by Wlezien et al.,¹⁵ who computed acoustic fields from a direct Navier-Stokes simulation and the acoustic analogy equation. An assessment of several one- and two-equation turbulence models for twin impinging jets was made by Ladd and Korakianitis,¹⁶ who obtained good predictions of impingement region velocity data and fair predictions of upwash fountain properties when compared to water-tunnel laser doppler velocimetry data. Detailed results of some of these experimental studies addressing the aeroacoustic properties of the single impinging jet flows have been published by Krothapalli et al.¹ and Alvi and Iyer.¹⁴ In the present paper we present a review and comparison of significant experimental and computational results for selected relevant cases. By combining experimental and computational results, one might gain further insight into physics governing this complex flow, thus revealing the value of such collaborative computational and experimental studies. A discussion of the strengths and weaknesses of the computational code and suggestions for future improvement is also presented.

Experimental Methods

Test Models and Facilities

The relatively simple configuration used for the experimental and computational study is shown in Fig. 2. It consists of an axisymmetric nozzle, which produces the high-speed jet impinging on a ground plane. For some cases a circular disk, referred to as a "lift" plate, is placed at the nozzle exit plane. The disk has an annular hole from which the jet issues and is meant to represent a generic outer moldline from which the jet exhausts. The relevant geometric parameters, also indicated in Fig. 2, include d , the nozzle exit diameter; D , the lift plate diameter; and h , the distance between the ground plane and the nozzle exit. Two axisymmetric nozzles, a Mach 1.5 C-D and a converging or sonic nozzle both with identical throat diameters of 25.4 mm, are used to generate the primary flow. The diameter of the lift plate is approximately $10d$ or 25.4 cm. The experimental studies were conducted using both nozzles over a wide range of nozzle pressures and ground plane distances, with and without the lift plate^{1,14}; however, in the present paper discussion will be limited to the sonic nozzle operating at a fixed pressure ratio without the lift plate. The test conditions for the primary case used for comparison in this study are as follows: nozzle pressure ratio (NPR) = 5, where NPR is defined as the ratio of the jet stagnation pressure P_0 to ambient pressure P_∞ at the nozzle exit. The ambient pressure was assumed to be constant at 14.7 psia, hence the jet was operated at $P_0 = 73.5 \pm 0.5$ psia. The nominal jet stagnation temperature for the experimental study was 20°C. The ground plane was a distance of three diameters from the nozzle exit ($h/d = 3$) for the primary test case; results for other ground plane heights are also briefly discussed to examine the influence of nozzle height on the flow behavior.

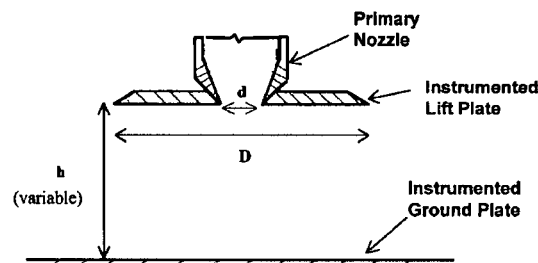


Fig. 2 Supersonic impinging jet test configuration.

The experiments were conducted in the STOVL facility of FMRL. A high-pressure blowdown compressed air facility was used to supply air to the nozzles. The air is stored in a bank of large-capacity storage tanks, which are supplied by a high-displacement reciprocating air compressor. To simulate different aircraft heights above the ground, the ground plane is mounted on a hydraulic lift and can be moved relative to the model. In the experiments described here, the ground plane consisted of an instrumented 1×1 m aluminum plate, which was centered underneath the model. More details of the STOVL hover rig can be found in Wardwell et al.¹⁷

Measurement Techniques

To obtain whole-field velocity data in this flow using PIV, the primary jet was seeded with small ($\sim 1 \mu\text{m}$) oil droplets generated using a modified Laskin nozzle, and the ambient air was seeded with smoke particles approximately $5 \mu\text{m}$ in diameter using a Rosco fog generator. The flow was illuminated with a thin light sheet generated by a dual-head Spectra Physics Nd-Yag laser with a repetition rate of 15 Hz. Each PIV image pair was acquired using a Kodak ES1.0 digital video camera capable of recording 8-bit digital image pairs in separate frames at a rate of 15 image pairs/s. Further details of this PIV technique can be found in Refs. 1 and 14. One of the main advantages of this PIV technique is a novel processing scheme with high spatial resolution that uses image matching to extract the particle displacements, hence the velocities, from particle image pairs.¹⁸ This image-processing technique allows for measurements to be made in regions of high velocity gradients.

Despite the use of the advanced processing scheme, particle lag is inherent in any particle-tracking scheme, and some lag will always occur. This is especially true in regions with very high velocity gradients, such as in the vicinity of shock waves. Consequently, it is expected that the location of strong shocks will be partially "smeared" because of particle lag. Similarly, although to a lesser extent, particle lag will also occur in other regions with high velocity gradients such as the wall jet or in the large-scale vortical structures with highly rotational flow. In addition, in areas very close to the surface, such as the impingement zone and the wall jet, reflections of the laser sheet by the surface can also lead to larger errors in the velocity field and/or yield regions where velocity data cannot be obtained. Ross et al.¹⁹ conducted a detailed investigation of the effect of particle size and shock strength on the accuracy of PIV measurements using an earlier and less accurate processing scheme. Their measurements show that for $\sim 1 \mu\text{m}$ seed particles, particle deceleration caused by a strong oblique shock begins within 1 mm of the actual shock location, where the deceleration rate increases with increasing shock strength. Hence, we expect that the initial location of the normal shock, the strongest possible shock, should be accurately represented within 1–2 mm in the PIV data. A more detailed investigation of the particle lag is outside the scope of this paper, and the reader is referred to Ross et al.¹⁹ and Alvi and Iyer¹⁴ for a more comprehensive discussion. The conclusions regarding the flowfield behavior that are reached in light of the PIV velocity field data will not be materially affected. This is particularly true for the present paper where the PIV data are used only to examine the mean flow features and behavior. It is impossible to determine the absolute uncertainty of the PIV measurements because detailed velocity field data are not available in literature for this flowfield—a motivation for the present study. However, in the absence of shock waves the mean velocity field data obtained using PIV show that the velocity data are in very good agreement, in general within 3%, with the exit velocity calculated using isentropic relations. The mean PIV results presented in this paper were obtained by averaging 80 image pairs. Although a larger number of images were recorded for most cases, using more than 80 image pairs did not change the mean velocity field.

The mean surface-pressure distributions were obtained by sequentially scanning a series of surface-pressure taps along a radial line on the ground plane. The pressures were scanned using a ScanivalveTM unit connected to a Validyne strain-gauge transducer. Several seconds of data were digitized and recorded at each port to obtain an accurate measurement of the mean surface pressures. The surface pressures were measured with an accuracy of ± 0.3 psia,

which translates to an uncertainty in the pressure coefficient C_p (defined later) of ± 0.005 . In addition to the mean pressure ports, the ground plane was also equipped with high-frequency pressure transducers to allow for unsteady surface pressures to be measured; however, the unsteady properties will not be discussed in this paper, and the reader is referred to Refs. 1 and 14. Mean and instantaneous flow visualization images were obtained using a shadowgraph system with a field of view of approximately 30 cm in diameter. The shadowgraph system employed a conventional single pass arrangement with a collimated beam; a variable frequency, white light stroboscopic flash unit was used as the light source.

Computational Methods

The computations were conducted using the WIND computer program. This flow solver is based on a time-marching solution to the Reynolds-averaged Navier–Stokes equations. The code is applicable for flow speeds ranging from approximately Mach 0.05 to hypersonic and supports a variety of flow types including finite rate, chemically frozen, and perfect gas. The full form of the stress tensor is used (no thin-layer approximations). The equations are solved via an approximately factored upwind scheme that has been shown to be second-order accurate in physical space. A more detailed description of the numerical procedure can be found in Bush²⁰ or Cain and Bush.²¹ Ideal gas is assumed in the present work, and Sutherland's law is used to vary the laminar viscosity as a function of temperature. The molecular and turbulent Prandtl numbers are assumed constant at values of 0.72 and 0.9, respectively. To minimize computation times, all solutions presented in this paper were obtained assuming axisymmetric flow.

In the WIND program flow turbulence can be represented using algebraic, one-equation, or two-equation modeling. For the present study three different types of turbulence models were employed. These included the one-equation Spalart–Allmaras model,²² the two-equation shear stress transport (SST) model,²³ and the Spalart–Allmaras model with a correction for streamline curvature and system rotation (SARC).²⁴ As the results will show, both the two-equation SST model and the one-equation SARC model provide very similar results, which are both in very good agreement with the experimental data.

Spalart One-Equation Model with Rotation and Curvature Correction

Various corrections have been introduced in the past by other researchers, such as Launder et al.²⁵ and Park and Chung,²⁶ to account for streamline curvature and rotation. These corrections, however, are applicable only to the specific flows for which they were designed. To account for these phenomena for general flow applications, more complex turbulence models such as Reynolds-stress formulation have been employed. These sophisticated models require fewer assumptions than one- or two-equation models but are too computationally intensive to be practical for routine engineering applications. Recently, the curvature correction modification of Spalart and Shur²⁴ has been added to the baseline Spalart model and applied to several three-dimensional configurations.²⁷ The baseline Spalart model has been shown to produce results similar to the two-equation SST model for many flows but does not perform as well for problems such as the supersonic impinging jet where the shear-layer growth rates and strong rotation effects are significant. Differences between predictions from the baseline Spalart and SARC one-equation models are presented for some cases in this paper and are studied more in depth in Mani et al.²⁷

Shear-Stress Transport Two-Equation Model

The SST two-equation turbulence model from Menter²³ is now used routinely in many aerospace CFD applications at The Boeing Company, St. Louis, Missouri. It is a blended model that exploits the advantages of both the k - ϵ model and the k - ω of Wilcox.²⁸ The k - ϵ models, such as those from Jones and Launder,²⁹ have numerical difficulties when attempting to integrate to the wall. There are assumptions about the boundary values of ϵ , which give rise to a high degree of numerical stiffness in this region. Conversely, the k - ϵ model does quite well for free shear-layer problems, particularly in two dimensions. The main advantage of the k - ω model is

that it behaves well for wall-bounded problems because of the physically sound boundary conditions on both k and ω . The Menter SST model employs the Wilcox $k-\omega$ model near the wall but transitions to the $k-\epsilon$ model via a switching function. This model is sometimes referred to as the SST model because it has the ability to account for the transport of the principal turbulent shear stress in adverse pressure gradient boundary layers. This modeling feature is based on Bradshaw's³⁰ assumption that the principal shear stress is proportional to the turbulent kinetic energy and is expressed through a modification of the eddy viscosity. The interested reader is referred to the original paper by Menter²³ for details of this two-equation turbulence model formulation.

Results and Discussion

Before a detailed discussion and comparison of the experimental and computational results, we provide an overview of the global impinging jet flowfield noting some of its principal features. Figure 1a shows an instantaneous shadowgraph of the principal test case, $\text{NPR} = 5$, $h/d = 3$; shown directly below the shadowgraph image is a schematic of the impinging jet flowfield model (Fig. 1b) and a corresponding pressure distribution sketch (Fig. 1c). The impinging jet flowfield can be divided into three main regions.⁷ The first region is the main jet column, where the flow is primarily inviscid and contains expansion and compression/shock waves for nonideally expanded jets. The impingement zone is the second region and is an area in the vicinity of the jet impingement point characterized by strong gradients leading to significant changes in local flow properties. This area is also referred to as the shock layer. Finally, the radial wall jet, the third distinct region, is the area outside the impingement zone, which contains the jet flow redirected radially outward after impingement. All three zones have been indicated in Fig. 1b. The flow schematic depicts the impingement region with a stagnation bubble, and the sketch of the surface-pressure distribution beneath shows the distinctive pressure profile corresponding to the presence of a stagnation bubble. Surface-pressure distributions with such annular peaks are commonly used as distinct indicators of the presence of a stagnation or separation bubble; for cases where a stagnation bubble is not formed, the surface-pressure distribution shows a central peak. The details of the impinging jet flow features (e.g., shape of the plate and tail shocks) are strongly dependent on the jet Mach number and the ground plane distance and will vary from the sketch in Fig. 1b.

The presence, and the reasons for the formation, of a stagnation bubble have been and remain the subject of some debate. Gubanov et al.,¹¹ Gummer and Hunt,¹³ and Kalghatgi and Hunt³¹ have conducted detailed investigations of the impinging jet flow structure, particularly in the impingement zone, for a range of conditions. These investigators discuss reasons for the formation (or

lack thereof) of a stagnation bubble. The interested reader is referred to these references, especially the study by Kalghatgi and Hunt,³¹ which specifically addresses this issue. Very briefly, as the supersonic flow in the primary jet approaches the ground plane, it decelerates through the formation of a plate shock. If the jet is not ideally expanded, oblique shocks in the jet plume (indicated as "jet shocks" in Fig. 1b) interact with the plate shock resulting in the well-known triple-shock structure, where the third shock is generally referred to as the tail shock. It is the nature of this interaction that appears to determine the flowfield in the impingement zone. When present, the stagnation bubble was hypothesized to enclose a region of recirculating fluid with relatively low velocities. However, until the present study very little direct and detailed evidence of the flow in this stagnation bubble has been available, and the nature of the flow in the stagnation bubble had primarily been understood through interpretation of surface-pressure distributions, surface streakline patterns,^{7,9} and schlieren or shadowgraph flow visualization.

Experimental Velocity Field

As already mentioned, detailed, whole flowfield velocity measurements were obtained using PIV for a range of NPRs and ground plane distances using both sonic and converging-diverging nozzles, with and without the lift plate. However, in this paper the discussion will be limited to the sonic nozzle without the lift plate, operating at $\text{NPR} = 5$ with the ground plane at $h/d = 3$. This was selected as our feature case because, as the shadowgraph image and the flowfield sketch in Fig. 1 reveal, the flow is very complex with shock/shock and shock/shear-layer interactions and areas of flow acceleration and deceleration into locally supersonic and subsonic regions. All PIV measurements are obtained in the central plane of the jet. The mean velocity field for the primary test case is shown in Fig. 3, where the vector plot has been overlaid on the out-of-plane vorticity color contour plot on the left half of the figure. The right half displays the streamline pattern superposed on the vorticity contours, where the units of vorticity for this and other similar vorticity contours are s^{-1} . In the velocity vector plots shown in this paper, the length of the vector is proportional to the velocity magnitude. The streamline patterns were created from the measured velocity vector field using the software package TecPlotTM.

Several features are clearly revealed in Fig. 3. First, the shear layer at the jet boundary is readily apparent as a region of high vorticity in the vorticity contour plots. As the jet shear layer approaches the surface, it turns outward around $r/d \approx 1$ and forms the outer boundary of the wall jet. Also clearly evident in this figure is the presence of the strong Mach disk shock revealed by the dramatic decrease in the flow velocity, apparent from the change in vector lengths. The velocity field data show that the Mach disk occurs around $y/d \approx 1.8$,

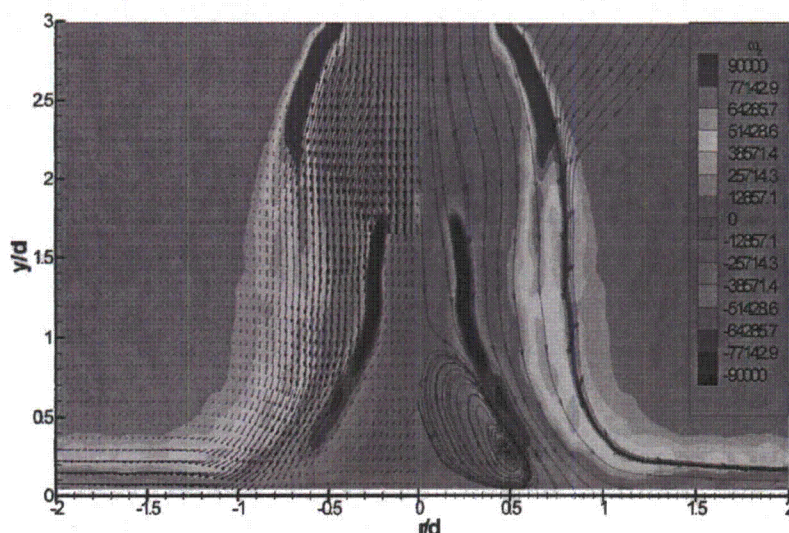
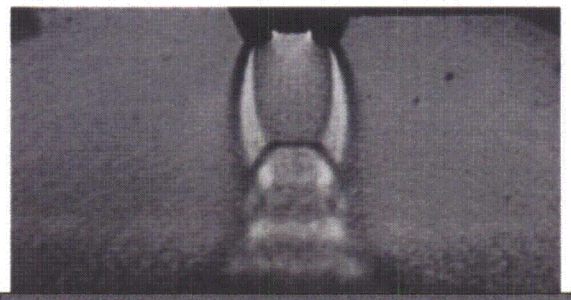
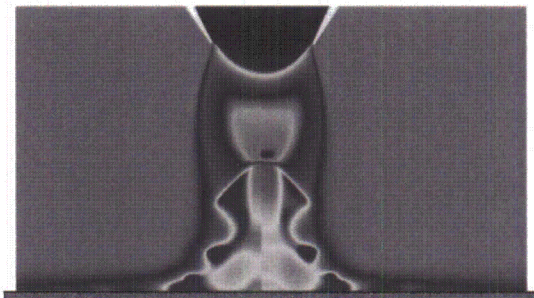


Fig. 3 Experimental vorticity contour plot with velocity vectors and streamlines: sonic nozzle, $\text{NPR} = 5$, $h/d = 3$.

which roughly corresponds to the Mach disk location observed in the instantaneous and mean shadowgraphs shown in Figs. 1a and 4, respectively. One of the most striking features observed in Fig. 3 is the region of recirculating flow, the stagnation bubble, in the center of the impingement zone. The presence and extent of the recirculating flow in the stagnation bubble is best revealed in the streamline plot in the right half of Fig. 3. The streamline plot also shows that the impinging flow is divided into two streams, where the outer one flows into the wall jet while the inner stream is wrapped into the stagnation bubble. In addition to the outer shear layer at the jet periphery, the inner shear layer or slip line is also visible in the vorticity plots as a region of high shear. Because the slip line emanates from the triple-shock intersection, the beginning of the inner shear layer should in principle correspond to the triple-point location on the shadowgraphs. Although the precise location of the triple point is difficult to determine from the shadowgraphs, its relative location on the PIV plots and shadowgraphs is approximately the same. The region where the inner shear layer impinges on the ground plane approximately coincides with the location of the annular pressure peak on the measured surface pressure distribution for this case (shown in Fig. 5). Although not shown here, the slip-line



Experiment: shadowgraph



CFD computed: density contours

Fig. 4 Comparison of mean shadowgraph image and density contours from two turbulence models: sonic nozzle, $NPR = 5$, $h/d = 3$.

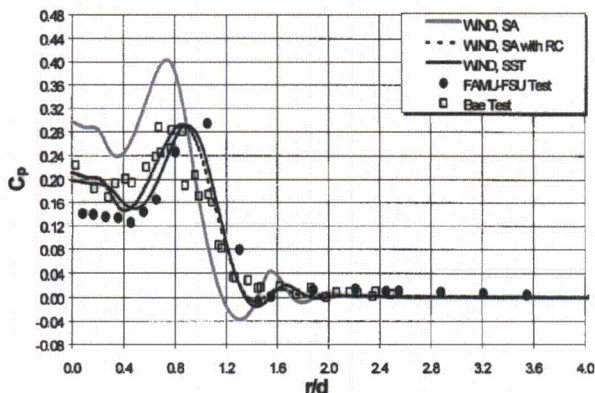


Fig. 5 Computed and measured ground plane pressures for sonic nozzle, $NPR = 5$, $h/d = 3$.

impingement locations in the PIV data and the annular peaks in the mean surface-pressure distributions were found to be in agreement for most of the cases examined.¹⁴ This lends some credence to the hypothesis proposed by earlier investigators,¹¹ who suggested that the impingement of the slip-line flow leads to the formation of the separation bubble.

Comparison of Computational Results from Different Turbulence Models

Initially we will compare computational results for the primary test case using the SARC and SST turbulence models to determine the relative accuracy of each model. This will be followed by a comparison between the experimental and computational results with each of the two models. As mentioned before, the $NPR = 5$, $h/d = 3$ case was selected because of the complexity of the flow revealed by the measurements where a strong shock appears in the jet plume followed by a recirculation bubble near the ground plane. An axisymmetric grid plane containing five zones and nearly 30,000 points was employed for the simulation. Almost two-thirds of this number were concentrated in the nozzle plume and wall-jet formation region.

Initial attempts at using local time stepping to obtain a steady-state solution for this case yielded large oscillations in the shear-layer and wall-jet formation regions. This unsteady behavior, supported by experimental data,^{14,32} then required the computation to be made using the time-accurate mode of the program. The solution from the relaxation method was then used only to provide an initial solution for the unsteady computation. In the time-accurate calculation integration of the dependent variables is obtained using a constant time interval at all spacings. This time interval must be chosen to be sufficiently small so that the numerical scheme remains stable at the smallest grid points having the largest flow gradients. This same time interval must then be used at all grid points to preserve the time accuracy. This approach, although requiring many more iterations, allows an estimate of the time-averaged flowfield to be obtained. The temporal scheme used for the current simulations is first order, but, as shown in the following sections, it still yields fairly accurate estimates of the mean flowfield. The mean flow data are obtained by averaging the data over several hundred time intervals, each interval being around $1.5 \mu s$. These intervals are approximately five times larger than the required $0.3\text{-}\mu s$ time interval used as the integration step in the numerical scheme. Several time averages of different numbers of samples were found to produce the same mean flowfield as long as at least 50 $1.5\text{-}\mu s$ intervals were averaged. This number of samples represents a good compromise between resolving the higher-frequency content of the flow and keeping the required amount of data storage to a manageable level. The computation time for a typical two-dimensional unsteady problem is then roughly 20 CPU hours on a single-processor SG-O₂ workstation.

A comparison of the computed Mach-number contours from the SARC and the two-equation SST model is shown in Fig. 6. There is a strong shock present for this configuration, which occurs after the flow expands to nearly $M = 2.8$. The shock location is seen to be approximately the same for both models. It has been determined that an accurate prediction of the location and strength of this shock is vital in obtaining a good prediction of the recirculation bubble shown in Fig. 6 and the streamline patterns in Fig. 7.

The Mach contours in Fig. 6 indicate that the computed growth of the radial wall-jet thickness is slightly higher from the SARC model. The mean streamline traces are seen to be nearly identical from both methods and are consistent with the experimental observations. The excellent agreement in the computational results using the two models is clearly evident in these and subsequent plots. Both models appear to capture the essential features of this flow; a more detailed comparison between experimental and computational results is presented in the following section. In a numerical study for a limited number of cases, Kitamura and Iwamoto³³ computed the presence of such a stagnation bubble. However, their published results were of limited resolution, and the comparison to experimental results was nominal. To the authors' knowledge, the present work provides the first detailed comparison of experimental and computational results for this flowfield, especially in the

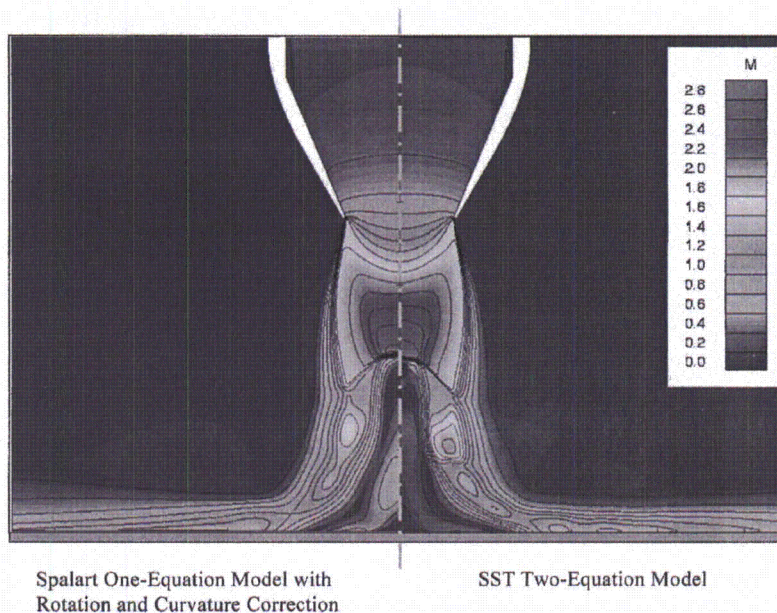


Fig. 6 Comparison of computed Mach-number contours using two turbulence models: sonic nozzle, $NPR = 5$, $h/d = 3$.

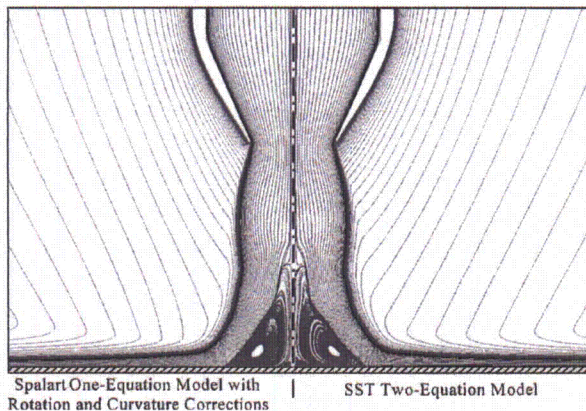


Fig. 7 Computed streamline paths using two turbulence models: sonic nozzle, $NPR = 5$, $h/d = 3$.

impingement and wall-jet regions, at a level of resolution not obtained before.

Although the computed data presented in the current work were obtained using the full 30,000-point computational grid, simulations using half the number of points in the vertical and lateral direction yielded nearly identical results. This is a good indication of grid independence and that adding additional points in the domain will not improve the accuracy. The mesh was constructed so that the height of the first point above the wall is near $y^+ = 3$ at the location of maximum wall-jet velocity near $r/d = 1.25$. Unfortunately, the tight clustering at this location limits the maximum stable time-step size that can be used for the entire simulation.

Comparison of Experimental and Computational Results: Primary Test Case

An example of a time-averaged shadowgraph revealing the flow structure can be seen in Fig. 4. This figure also shows mean density contours from the CFD simulation using both models. A direct comparison among the details observed in the shadowgraphs and density contours is not strictly valid because a shadowgraph is an integrated image, sensitive to the second spatial derivative of density in the flowfield. However, a comparison in the overall flow structure and primary flow features can still be made. Computed

density contours from both turbulence models are almost identical, and there is a striking similarity between the computed flow structures with features observed in the shadowgraph. The triple-shock structure, which includes the jet shock, tail shock, and the Mach disk, is captured by the computations, and their locations approximately coincide with the experimental observations. The computed density contours also reveal the presence of the inner shear layer and the outer boundaries of the stagnation bubble.

To further assess the accuracy of the CFD predictions, comparisons are presented in Fig. 8 of the line contours plots of the mean velocity field obtained from the PIV data and the computation using the SST turbulence model. The computed data have been interpolated to the same locations represented by the PIV data for a direct comparison. Only the velocity contours from the SST model are presented in this figure, although results from the SARC model (not shown) are nearly identical. Once again, the computations predict the measured velocity field very well with some discrepancies. Both computational models predict the location of the Mach disk slightly closer to the ground plane than does the measurement. Consequently, the vertical extent of the separation bubble is also marginally underpredicted. The magnitude and extent of the high velocity region in the jet core, upstream of the Mach disk, is somewhat higher in the PIV measurements than in the CFD predictions, and there is a discrepancy in the velocity magnitudes in the wall jet, very close to the wall. However, it is clearly evident that overall the computations yield very good predictions for the entire flowfield, including the jet core velocities, the recirculation region, and in the wall jet. These characteristics are of critical importance from a practical perspective because of their influence on ground erosion.

The comparison between CFD and PIV results continues in Fig. 9, which shows the mean vorticity contours and the velocity vectors from experimental and computational data. (The numbers in parentheses above the contours indicate the grid size used for the interpolated data.) The similarity of the CFD and PIV data in the recirculation region and the overall flow structure can be easily seen. There appears to be a greater expansion angle at the nozzle exit in the experiment than what is predicted in the CFD results. Also, as in Fig. 8, the Mach disk appears closer to the ground in the computations than the PIV data, resulting in a smaller separation bubble above the surface. However, the radial extent of the stagnation bubble, defined by the impingement location of the inner shear layer/slip line on the surface, is in very close agreement with the experimental results within $r/d \sim 0.1$. This agreement in the radial extent of the stagnation bubble is also supported by the

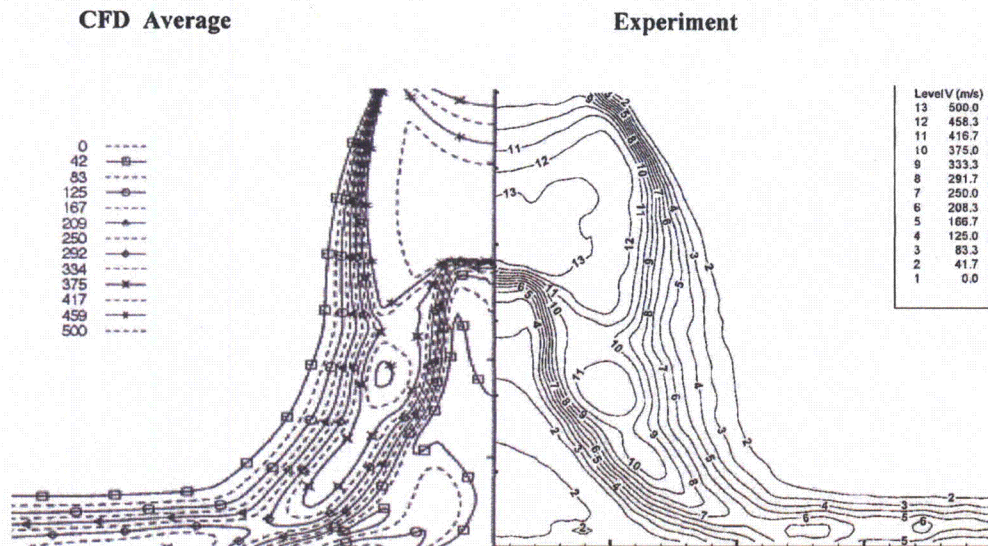


Fig. 8 Comparison of velocity contours from CFD and experimental PIV data: sonic nozzle, NPR = 5, $h/d = 3$.

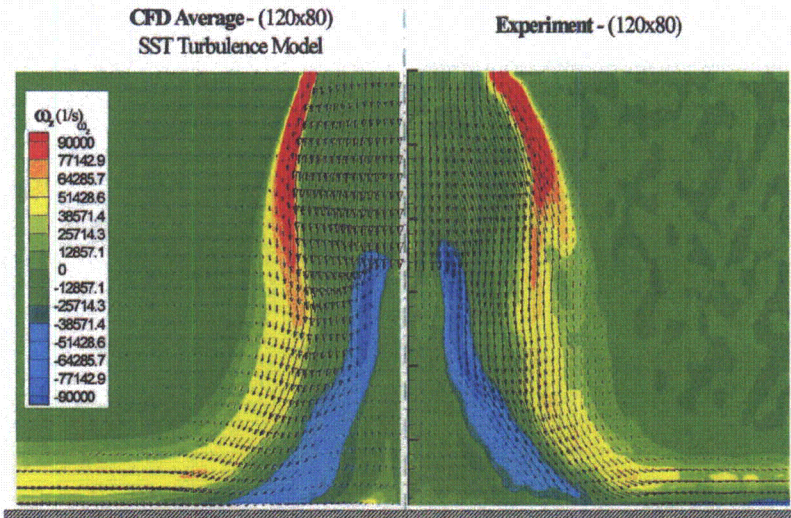


Fig. 9 Measured (PIV) and computed velocity vectors and vorticity contours: sonic nozzle, NPR = 5, $h/d = 3$.

comparison of the surface pressure distributions, presented earlier in Fig. 5. A comparison of the vorticity contours reveals the remarkable similarity in the shape and magnitude of the diffusing vorticity values between the computational and experimental results. It is clear that the vorticity field is well predicted by the computations indicating an accurate simulation of the strength and location of the primary jet shear layer, which is redirected into the wall-jet shear layer. As noted earlier, the inner shear layer that emanates from the triple point (Fig. 1b) is also extremely well predicted in terms of shape and vorticity levels.

A comparison of the predicted and measured ground plane surface-pressure distributions is shown in Fig. 5. Results from numerical solutions employing several turbulence models are included and compared to the experimental data. The dependent variable in this figure C_p represents the nondimensional surface-pressure coefficient, where $C_p = (P_s - P_\infty)/(P_0 - P_\infty)$ and P_s is the surface pressure. The x axis represents the radial location, nondimensionalized by the nozzle throat diameter, in this case same as the exit diameter d .

The overall pressure distribution with a low-pressure plateau and an annular peak is typical of an impingement flow with a recirculation bubble (Fig. 1) as discussed earlier. The pressure near the

impingement point is well below the jet total pressure that is normally recovered for an ideally expanded nozzle without a separation bubble. The recirculating bubble divides the jet core and deflects it radially outward so that the peak pressure is lower than the stagnation pressure and occurs away from center of the interaction. In principle, the pressure peak should correspond to the location of the stagnation streamline in the inner shear layer, which divides the jet flow that is redirected into the wall jet from the fluid that is entrained into the recirculation bubble. This is the behavior observed in the present case where the pressure peak occurs roughly around $r/d = 1$, a location that corresponds to the impingement of the inner shear layer as seen in Fig. 9. The baseline Spalart model is seen to significantly overpredict the pressure throughout the impingement region, whereas the inclusion of the curvature formulation (SARC) produces a distribution in agreement with the SST model prediction and in much better agreement with the experimental results. A closer comparison of the SST or SARC results with the experimental data reveals that the greatest discrepancy between computational and the experimental data occurs in the central portion of the impingement zone. In this region (r/d roughly less than 0.4) both models overpredict the plateau pressure by as much as 30%. The overprediction of the pressure in this region is expected if one realizes that $r/d \leq 0.4$

roughly defines the radial extent of the Mach disk formed above the impingement zone (see Fig. 3). As noted earlier, the computations underpredict the strength of the Mach disk (see Fig. 8), which in turn would overpredict the pressures recovered downstream of the Mach disk on the impingement surface. Notwithstanding some differences in pressures in certain regions, the overall agreement between the predicted and measured distributions is very good.

In addition to the primary experimental data, surface pressures obtained for a similar configuration at British Aerospace³⁴ are also shown in Fig. 5. The BAe axisymmetric nozzle had an exit diameter of 120 mm and a jet total temperature of $T_t = 1800^\circ\text{F}$ and operated at the same NPR as the cold jet in the present study. The plot shows that the normalized pressure distributions from this experiment are in good agreement with the present (FAMU-FSU) cold jet data and the computations. The agreement of these three data sets provides further confidence in the ability of the CFD code to capture the features of interest in this complex flowfield.

The ground erosion problem is a result of the unusually high mean and unsteady loads imparted on the impingement surface by the hot, high-speed impinging jet(s). An examination of the velocity contour plot shown in Fig. 8 illustrates that the radial wall-jet region contains fluid with very high velocities, in close proximity to the wall. As an example, Fig. 8 shows that wall-jet velocities in the range of 250–350 m/s are found within a few millimeters from the surface, resulting in very high velocity gradients and wall shear stresses. The radial distribution of the computed nondimensionalized wall shear stress, shown in Fig. 10, provides the magnitudes of the computed shear stresses for the primary test case. In this plot the ordinate depicts the skin friction C_f , defined as $C_f = \tau_w / (P_0 - P_\infty)$, where

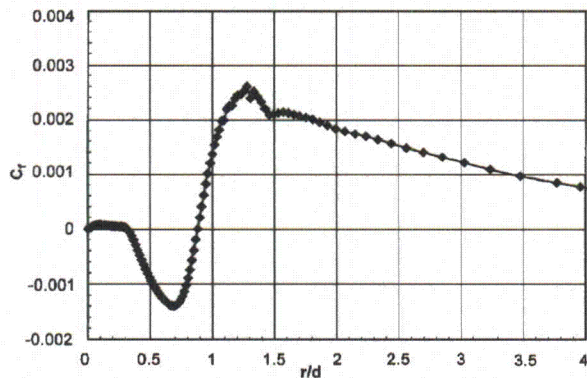


Fig. 10 Computed skin-friction distribution: sonic nozzle, NPR = 5, $h/d = 3$.

τ_w is the wall shear stress and $(P_0 - P_\infty)$ is the difference between the jet stagnation and the freestream ambient pressure.

Several points are of interest in this distribution. First, we see that the skin friction is very low, almost zero, in the central portion of the flowfield. A look at the velocity contour plot (Fig. 8) and the vorticity contour plots (Fig. 9) confirms that this area of the surface lies under the separation bubble and is a region of very low velocities and negligible vorticities, hence minimal shear stresses. Moving radially outward, there is a rapid increase in the skin friction starting at $r/d \approx 0.3$ and ending at $r/d \approx 0.7$, where a (negative) peak in the wall shear stress is present. The negative values of the shear stress are caused by the fact that fluid in the stagnation bubble is moving radially inward in this region, as illustrated in the vorticity/vector plots in Fig. 3 and Fig. 9. Figure 3 also shows that the negative peak at $r/d \approx 0.7$ roughly corresponds to the inner extent of the slip line impingement on the surface, an area where high shear stresses are expected. A more dramatic rise in the skin friction occurs between $r/d \approx 0.7$ and 1.2 with a skin friction peak at the latter location. Figure 3 clearly shows that this region corresponds to the slip-line impingement and the inception of a new boundary layer in the wall jet, which is bounded by a high-speed outer flow, hence the significantly higher shear stresses. The skin friction goes through a sign change in this area with a zero occurring at $r/d \approx 0.9$, which by definition is the location of the attachment line in the computed flow. The agreement between the zero skin-friction location and slip-line impingement point in the experimental results indicates that $r/d \approx 0.9$ is close to the actual location of the attachment line. This attachment line divides the stagnation bubble flow from the wall-jet flow, an observation supported by the surface-pressure distribution of Fig. 9, where the pressure peak occurs at the same radial location. In summary, it is clear that the jet impingement and wall-jet regions are areas of not only very high shear stresses but also large gradients in shear stresses where the flow goes through rapid changes in direction. Given the analogy between skin-friction and heat-transfer coefficients, it is reasonable to expect that this high skin friction be accompanied by high wall heating.³⁵ This behavior, combined with the fact that this region is dominated by very high fluctuating pressure loads,¹⁴ can result in severe ground erosion.³⁴

Comparison of Secondary Cases

Finally, we briefly compare experimental and computational results for two other cases at the same pressure, NPR = 5, and two heights, $h/d = 2$ and 1.6. Similar to Fig. 9, experimental and computational velocity vector/velocity contour plots for these two cases are shown in Figs. 11 and 12. This is followed by a comparison of the experimental and computational surface-pressure distributions for both heights shown in Fig. 13.

The comparison between CFD and PIV results for $h/d = 2$ in Fig. 11 shows an overall agreement in the computed and measured

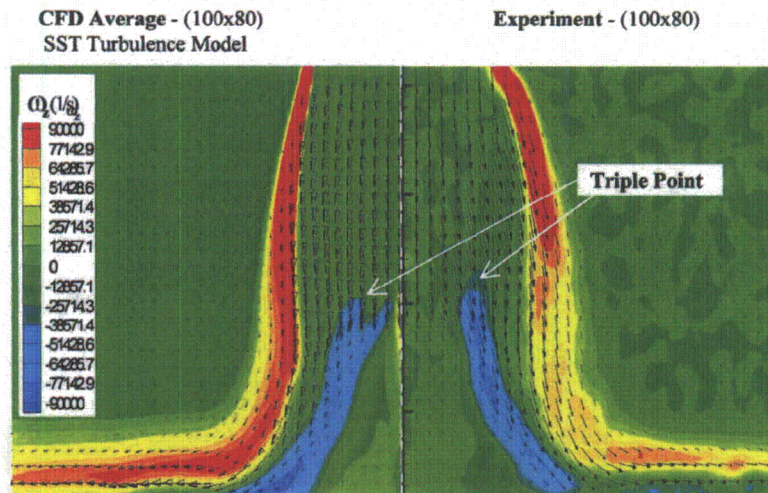


Fig. 11 Comparison of velocity vectors and vorticity contours from CFD and PIV: sonic nozzle, NPR = 5, $h/d = 2$.

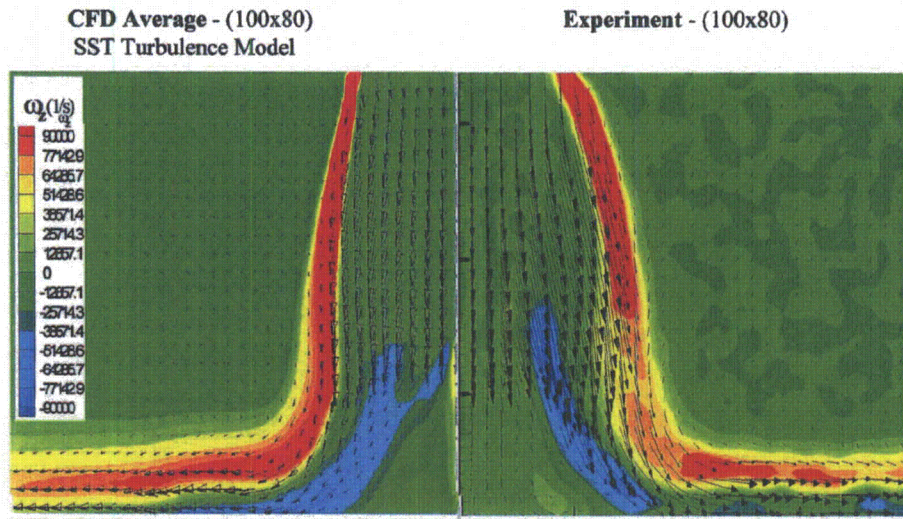


Fig. 12 Comparison of velocity vectors and vorticity contours from CFD and PIV: sonic nozzle, NPR = 5, $h/d = 1.6$.

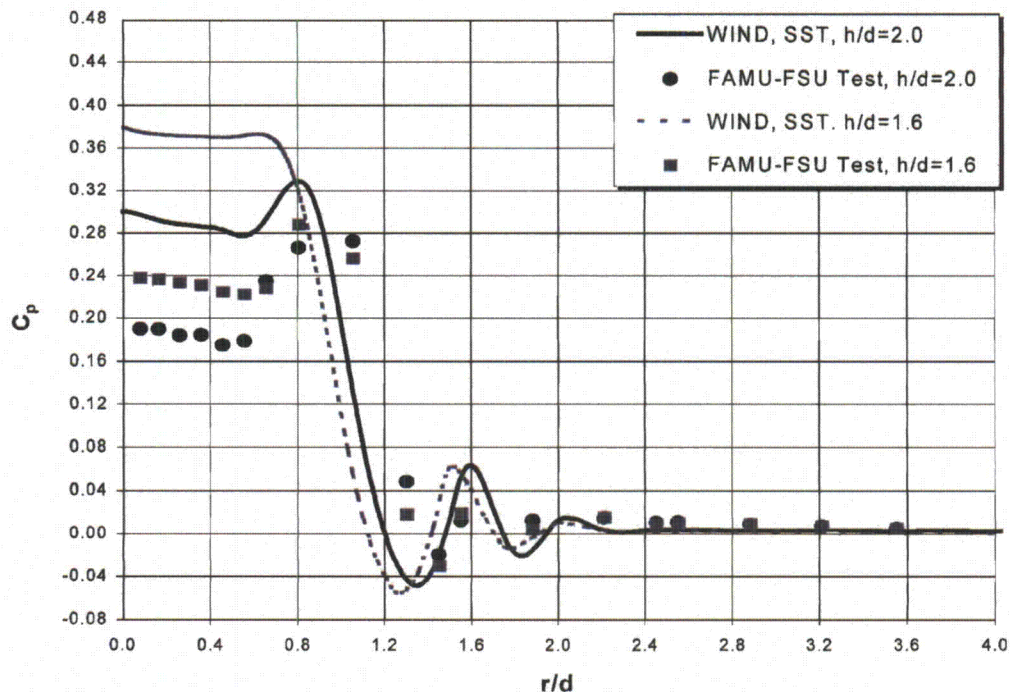


Fig. 13 Comparison of measured and computed surface-pressure distributions: sonic nozzle, NPR = 5, $h/d = 1.6$ and 2.

flow structure and the velocity field. As in the primary test case ($h/d = 3$), the Mach disk, triple point, and the inner shear layer are all captured by the computations. However, a closer look reveals that there is less diffusion of vorticity in the primary jet and wall-jet shear layer in the computed flow, where these shear layers appear more compact with higher vorticity values relative to the measured flowfield. Additionally, the triple point and the origin of the slip line (marked for clarity in Fig. 13) in the computed flowfield appears diffused, almost bifurcated, and the impingement location of the slip line is closer to the centerline than indicated by the PIV data.

As expected, these differences in the computed and measured velocity field translate into a discrepancy in the pressure distribution in Fig. 13. Although the computations reveal the presence of the stagnation bubble, indicated by the annular pressure peaks, the magnitude of the pressure in the impingement region downstream of the Mach disk is significantly overpredicted. This is presumably caused by an underprediction of the strength of the Mach disk for

reasons similar to those outlined in our discussion of Figs. 5, 8, and 9 for the primary test case.

The comparison between CFD and PIV results for $h/d = 1.6$ shown in Fig. 12 follows the same trend as Fig. 11. Although overall there is good agreement between the computed and measured results, there are differences especially in the impingement region in the vicinity of the Mach disk. The triple point is much more diffused relative to the measured flow, even more so than that observed in Fig. 11. Similarly, there is a more significant difference between the experimental and computed pressure distributions (Fig. 13) in the impingement region. The computed flow for this case fails to capture the annular peak clearly present in the measured distribution.

In general, there is very good agreement between the computational results and the measured data, where the computations captured the essential features of the flow. However, it appears that, as the interaction strength increases, that is, as the nozzle to ground plane distance decreases, the differences between the two

data increase systematically. This discrepancy is generally confined to the impingement zone, a region close to the interaction centerline. It appears that the disparity might be caused by the inability of the computational scheme to accurately predict the behavior of the flow in the vicinity of the Mach disk. Differences between the experimental and computational data become more pronounced as the strength of the Mach disk increases. One reason for this behavior could be attributed to lack of adequate axial grid resolution in the region of the Mach disk. Adapting the grid distribution to the flow gradients, either manually or with true grid adaptation, would most likely increase the accuracy of the resulting numerical data. Another important consideration is the time accuracy of the numerical scheme. It is possible that the first-order scheme used in the current work suppresses some of the unsteadiness of the jet and wall shear layers, which in general become more unsteady for lower heights. This behavior would then lead to the apparent "underdiffusion" of the time-averaged vorticity contours already discussed.

Conclusions

In this paper experimental and computational results for a moderately underexpanded supersonic jet impinging on a surface were examined and compared. The ultimate goal of this work was to develop a better understanding of the impinging jet flowfield, which is of significant practical interest because of its presence in STOVL aircraft during hover. The detailed experimental results, especially the velocity field data, were used to verify the accuracy of, and served as benchmark for, the computational methods, which can be used to predict the behavior of these flows. Computational results from the SARC one-equation and SST two-equation turbulence models were nearly identical. Both models were able to capture the significant features of this complex flow and were in remarkably good agreement with the experimental data obtained for the present test case. The SST turbulence model has proven to be robust, efficient, and produce good results for a wide variety of CFD applications in the aerospace industry. The experiments and computations both revealed the presence of the stagnation bubble, at a level of resolution not seen before, which contains low-velocity recirculating flow. The complex shock structure and the high-speed radial wall jet were found to be similar in the experimental and computational data.

Although there are some discrepancies between the experimental and computational results for some cases, which become more significant with increasing interaction strength, the overall agreement is very good. It is expected that more accurate numerical simulations could be obtained through the use of a dynamic adaptive grid technique. This technique clusters the computational grid to where flow gradients are the strongest, such as shear layers and shock and expansion waves. Better resolution of these waves and other flow gradients should lead to more accurate estimations of the mean flowfield when compared to data. Also, the computed results presented here were obtained using only a first-order temporal scheme. It is believed that higher-order methods would better capture unsteady flow features and yield a more accurate prediction of the mean flowfield for a given configuration. Finally, the turbulence model plays a significant role in the accurate prediction of the impinging jet flowfield. A large source of error, in both one- and two-equation models, is the Boussinesq approximation, which must be made to obtain closure for the system of equations. This assumption allows the Reynolds-stress tensor, which arises during the averaging of the momentum equations, to be computed as the product of an eddy viscosity and the mean strain-rate tensor. Although this approximation provides accurate predictions for many flows of interest, there are some applications in which it produces large errors in flow properties when compared with measured data. The impingement of the jet flow on the ground plane gives rise to unequal normal Reynolds stresses, which will cause the Boussinesq approximation to fail. Corrections for streamline curvature, such as that of Spalart and Shur,²⁴ have been shown to enhance the one-equation Spalart turbulence model to yield results equal in accuracy to the more sophisticated two-equation SST model. Without the corrections the baseline Spalart model results significantly differed from the PIV velocity data including the strength and location of the Mach disk. The two-equation SST model, however, still suf-

fers from deficiencies, which cannot be addressed until computer speeds enable large scale, cost-effective solutions to the Reynolds-stress equations or direct-numerical-simulation methods to be utilized.

The ability to measure and predict accurately the impinging jet behavior, especially near the ground plane, is critical because these are regions with very high mean shear, thermal loads, and unsteady pressure forces. An understanding of these flow characteristics is essential because they contribute directly to the study of ground erosion. We believe that this collaborative experimental and computational effort has been very fruitful and has provided unique data and insight into this complex flow behavior.

Acknowledgments

We gratefully acknowledge the continued support of NASA Ames Research Center and NASA Headquarters for sponsoring the experimental portion for this work. We appreciate the advice and help of A. Krothapalli and L. Lourenco during this study. The assistance of R. Elavarasan and K. Iyer in conducting some of the tests is also appreciated. Finally, we thank Charney Davy for her help in processing some of the data.

References

- Krothapalli, A., Rajakuperan, E., Alvi, F. S., and Lourenco, L., "Flow Field and Noise Characteristics of a Supersonic Impinging Jet," *Journal of Fluid Mechanics*, Vol. 392, Aug. 1999, pp. 155-181.
- Neuwerth, G., "Acoustic Feedback of a Subsonic and Supersonic Free Jet Which Impinges on an Obstacle," NASA TT F-15719, July 1974.
- Powell, A., "The Sound-Producing Oscillations of Round Underexpanded Jets Impinging on Normal Plates," *Journal of Acoustical Society of America*, Vol. 83, No. 2, 1988, pp. 515-533.
- Tam, C. K. W., and Ahuja, K. K., "Theoretical Model of Discrete Tone Generation by Impinging Jets," *Journal of Fluid Mechanics*, Vol. 214, May 1990, pp. 67-87.
- Henderson, B., and Powell, A., "Experiments Concerning Tones Produced by an Axisymmetric Choked Jet Impinging on Flat Plates," *Journal of Sound and Vibration*, Vol. 168, No. 2, 1993, pp. 307-326.
- Powell, A., "On Edge Tones and Associated Phenomena," *Acoustica*, Vol. 3, 1953, pp. 233-243.
- Donaldson, C. DuP., and Snedeker, R. S., "A Study of Free Jet Impingement. Part 1. Mean Properties of Free and Impinging Jets," *Journal of Fluid Mechanics*, Vol. 45, Pt. 2, Jan. 1971, pp. 281-319.
- Donaldson, C. DuP., and Snedeker, R. S., "A Study of Free Jet Impingement. Part 2. Free Jet Turbulent Structure and Impingement Heat Transfer," *Journal of Fluid Mechanics*, Vol. 45, Pt. 3, Feb. 1971, pp. 477-512.
- Carling, J. C., and Hunt, B. L., "The Near Wall Jet of a Normally Impinging, Uniform, Axisymmetric, Supersonic," *Journal of Fluid Mechanics*, Vol. 66, Pt. 1, Oct. 1974, pp. 159-176.
- Lamont, P. J., and Hunt, B. L., "The Impingement of Underexpanded Axisymmetric Jets on Perpendicular and Inclined Flat Plates," *Journal of Fluid Mechanics*, Vol. 100, Pt. 3, Oct. 1980, pp. 471-511.
- Gubanova, O. I., Lunev, V. V., and Platinina, L. N., "The Central Breakaway Zone with Interaction Between a Supersonic Underexpanded Jet and a Barrier," *Fluid Dynamics*, Vol. 6, July 1973, pp. 298-301.
- Ginzberg, I. P., Semilentenko, B. G., Terpigorev, V. S., and Uskov, V. N., "Some Singularities of Supersonic Underexpanded Jet Interaction with a Plane Obstacle," *Journal of Engineering Physics*, Vol. 19, 1973, pp. 1081-1084.
- Gummer, J. H., and Hunt, B. L., "The Impingement of a Non-Uniform, Axisymmetric, Supersonic Jet on a Perpendicular Flat Plate," *Israel Journal of Technology*, Vol. 12, No. 3-4, 1974, pp. 221-235.
- Alvi, F. S., and Iyer, K. G., "Mean and Unsteady Flowfield Properties of Supersonic Impinging Jets with Lift Plates," AIAA Paper 99-1829, May 1999.
- Wleziem, R. W., Bower, W. W., Childs, M. S., Howe, M. S., and Kibens, V., "Experimental and Computational Investigation of Supersonic STOVL Jet Flow and Acoustic Fields," NASA CR 189547, Jan. 1992.
- Ladd, J. A., and Korakianitis, T., "On the Assessment of One- and Two-Equation Turbulence Models for the Computation of Impinging Jet Flowfields," AIAA Paper 96-2545, July 1996.
- Wardwell, D. A., Hange, C., Kuhn, R. E., and Stewart, V. R., "Jet-Induced Ground Effects on a Parametric Flat-Plate Model in Hover," NASA TM 104001, 1993.
- Lourenco, L. M., and Krothapalli, A., "Mesh-Free Second Order Accurate Algorithm for PIV Processing," *Proceedings of the International Conference on Optical Technology and Image Processing in Fluid, Thermal and Combustion Flows*, Visualization Society of Japan, Yokohama, Japan, 1998, p. 224.

- ¹⁹Ross, C., Lourenco, L., and Krothapalli, A., "PIV Measurements in a Shock-Containing Supersonic Flow," AIAA Paper 94-0047, Jan. 1994.
- ²⁰Bush, R. H., "A Three Dimensional Zonal Navier Stokes Code for Subsonic Through Hypersonic Propulsion Flowfields," AIAA Paper 88-2830, July 1988.
- ²¹Cain, A. B., and Bush, R. H., "Numerical Wave Propagation Analysis for Stretched Grids," AIAA Paper 94-0172, Jan. 1994.
- ²²Spalart, P. R., and Allmaras, S. R., "A One-Equation Turbulence Model for Aerodynamic Flows," AIAA Paper 92-0439, Jan. 1992.
- ²³Menter, F. R., "Zonal Two Equation $k-\omega$ Turbulence Models for Aerodynamic Flows," AIAA Paper 93-2906, July 1993.
- ²⁴Spalart, R. R., and Shur, M. L., "On the Sensitization of Turbulence Models to Rotation and Curvature," *Aerospace Science and Technology*, Vol. 1, No. 5, 1997, pp. 297-302.
- ²⁵Lauder, B. E., Priddin, C. H., and Sharma, B. I., "The Calculation of Turbulent Boundary Layers on Spinning and Curved Surfaces," *Journal of Fluids Engineering*, Vol. 99, No. 1, 1977, pp. 231-239.
- ²⁶Park, S. V., and Chung, M. K., "Curvature-Dependent Two-Equation Model for Prediction of Turbulent Recirculating Flows," *AIAA Journal*, Vol. 27, No. 3, 1989, pp. 340-344.
- ²⁷Mani, M., Ladd, J. A., and Bower, W. W., "An Assessment of Rotation and Curvature Correction to One- and Two-Equation Turbulence Models for Compressible Impinging Jet Flows," AIAA Paper 2000-2406, June 2000.
- ²⁸Wilcox, D. C., "Reassessment of the Scale Determining Equation for Advanced Turbulence Models," *AIAA Journal*, Vol. 26, No. 11, 1988, pp. 1299-1310.
- ²⁹Jones, W. P., and Launder, B. E., "The Calculation of Low-Reynolds-Number Phenomena with a Two-Equation Model of Turbulence," *International Journal of Heat and Mass Transfer*, Vol. 16, No. 6, 1973, pp. 1119-1130.
- ³⁰Bradshaw, P., "Compressible Turbulent Shear Layers," *Annual Review of Fluid Mechanics*, Vol. 9, 1977, pp. 33-54.
- ³¹Kalghatgi, G. T., and Hunt, B. L., "The Occurrence of Stagnation Bubbles in Supersonic Jet Impingement Flows," *Aeronautical Quarterly*, Vol. 27, Aug. 1976, pp. 169-185.
- ³²Alvi, F. S., Elavarasan, R., Shih, C., Garg, G., and Krothapalli, A., "Active Control of Supersonic Impinging Jets Using Microjets," AIAA Paper 2000-2236, June 2000.
- ³³Kitamura, S., and Iwamoto, J., "Numerical Analysis of Supersonic Impinging Jet," *Transactions of the Japan Society for Aeronautical and Space Sciences*, Vol. 41, No. 132, 1998, pp. 57-64.
- ³⁴"JSF Surface Erosion Materials Characterization Program Test Results," R.G.A. Angel, British Aerospace PLC, FAE-R-RES-4620, Issue 1, April 1999.
- ³⁵Messersmith, N. L., and Murthy, S. N. B., "Thermal and Mechanical Loading on a Fire Protection Shield Due to a Combustor Burn-Through," *Propulsion and Energetics Panel (PEP) 88th Symposium*, CP-587, AGARD, 1996, pp. 22-1-22-13.

M. Sichel
Associate Editor

RAREFIED GAS DYNAMICS

PROCEEDINGS OF THE FOURTH INTERNATIONAL SYMPOSIUM
ON RAREFIED GAS DYNAMICS, HELD AT THE INSTITUTE
FOR AEROSPACE STUDIES, UNIVERSITY OF TORONTO, 1964

Edited by

J. H. de Leeuw

INSTITUTE FOR AEROSPACE STUDIES, UNIVERSITY OF TORONTO, TORONTO, CANADA

Volume II

1966



NEW YORK

LONDON

ACADEMIC PRESS

EXPERIMENTAL METHODS IN RAREFIED GAS DYNAMICS

The Structure and Utilization of Supersonic Free Jets in Low Density Wind Tunnels¹

HARRY ASHKENAS
Jet Propulsion Laboratory, Pasadena, California

and

FREDERICK S. SHERMAN
University of California, Berkeley, California

The aim of this paper is to give a concise and easily employed guide to the results of the theory of inviscid and slightly viscous flow in the central core of a supersonic free jet; to give a résumé and confirmation of experimental results concerning the location of shock waves at high Reynolds number; to apply this information to the prediction of jet sizes and the Mach and Reynolds number ranges corresponding to various pumping systems; and to give a preliminary experimental description of the manner in which the jet flow itself undergoes transition from an inviscid-continuum flow to a free-molecular flow as the orifice Reynolds number decreases.

I. Introduction

At the Rarefied Gas Dynamics Symposium of 1962, considerable attention was drawn to the process of unconfined expansion from a sonic orifice into a low-pressure chamber as an effective means of obtaining high Mach number flows of very low-density gases. These "free jet" flows were discussed in the context of aerodynamically-intensified molecular beam sources (Bier and Hagen, 1963; Scott and Drewry, 1963; Fenn and Deckers, 1963), and were suggested as a useful supplement to conventional nozzle-confined expansions

¹This paper presents the results of one phase of research carried out at the Jet Propulsion Laboratory, California Institute of Technology, under Contract No. NAS7-100, sponsored by the National Aeronautics and Space Administration and at the University of California under Contract Nonr-222(45), sponsored by the Office of Naval Research and the Office of Scientific Research.

for some class
extensively at
separation (Zi

In the last o
progress has b
the pressure r
orifice Reyno
Berkeley and
actively and i
proximity of t

Another pap
ful application
drag in the ne

II. Resu

The transonic
a rapidly con
potential flow
evidently hav
downstream,
based on the
is uniform an
be applied, yi

Owen and
and for many
for experimen
have been in c
applied to an
Love *et al.* (1
1962 by W. S
Alto, using a
barrel shock
assumed a per
and uniform c

A. Centerline

1. The High
relatively sim
region of high
Fig. 1. There

for some classes of wind tunnel tests (Sherman, 1963a). They had also been extensively studied in connection with aerodynamic schemes of isotope separation (Zigan, 1962).

In the last two years interest in these flows has intensified, and considerable progress has been made toward their accurate description, as a function of the pressure ratio across the orifice, the specific-heats-ratio of the gas, and the orifice Reynolds number. Groups at both the University of California at Berkeley and the Jet Propulsion Laboratory in Pasadena have been working actively and in a complementary fashion on this problem, and because of the proximity of the two groups, a joint report of our results was deemed feasible.

Another paper at the symposium (Maslach *et al.*, 1964) will report a successful application of the free jet flow in a determination of cylinder and strip drag in the near-free-molecule regime.

II. Results of Inviscid Flow Theory

The transonic inviscid flow through a circular hole in a thin wall or through a rapidly converging axisymmetric nozzle presents an unsolved problem in potential flow theory. However, the details of flow in the transonic region evidently have little influence in the region more than a nozzle diameter downstream, and successful treatments of the supersonic region have been based on the assumption that flow in the plane of the orifice or nozzle exit is uniform and slightly supersonic. The method of characteristics may then be applied, yielding accurate flow data at a number of discrete mesh points.

Owen and Thornhill (1948) were the first to carry out such a computation, and for many years their solution has been the only standard of comparison for experimentalists. Computer programs more than adequate for the task have been in existence in many organizations for several years, but have been applied to much more complicated problems, exemplified by the work of Love *et al.* (1959). The computations used in this paper were performed in 1962 by W. S. Wolff of the Lockheed Missiles and Space Company in Palo Alto, using a program which is capable of finding the jet boundary and the barrel shock location, almost up to the point of Mach intersection. They assumed a perfect gas with constant specific heats ($\gamma = 1.67, 1.40, \text{ or } 1.2857$), and uniform exit flow at a Mach number of 1.10.

A. Centerline Property Distributions

1. The High Supersonic Region. The computed free jet flows exhibit a relatively simple and self-similar development in the inertia-dominated region of high Mach number isentropic flow, inside the barrel shock (see Fig. 1). There the streamlines appear to radiate from a "source" at a distance

attention
into a
number
d in the
ier and
nd were
pansions

the Jet Pro-
NAS7-100,
University
al Research

x_0 downstream of the orifice, the flow speed has very nearly attained its adiabatic-flow limit, and density decreases along each streamline in proportion to the inverse square of distance from this source. The variation of density from streamline to streamline (i.e., with polar angle θ , at constant distance, R , from the "source") is approximately independent of R . These facts are

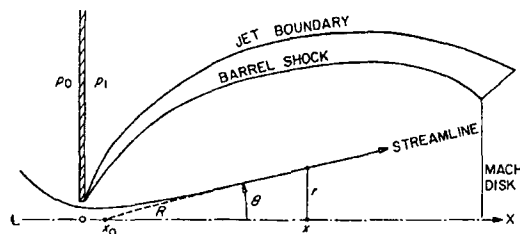


FIG. 1. Inviscid flow geometry:
 $R = [r^2 + (x - x_0)^2]^{1/2} = \tan^{-1} r / (x - x_0)$.

commented on in a preliminary way in an earlier unpublished report (Sherman, 1963b).

a. Mach Number. The analogy to a "simple" (purely radial) source flow is strong and suggested the following extremely accurate fitting formula for the centerline Mach number of a free jet.

$$M = A \left(\frac{x - x_0}{D} \right)^{\gamma-1} - \frac{1}{2} \left(\frac{\gamma + 1}{\gamma - 1} \right) / A \left(\frac{x - x_0}{D} \right)^{\gamma-1}. \quad (1)$$

The constants A and x_0 depend upon γ . A preliminary value of x_0 was found by projecting streamlines back to the axis. The final values were found as follows.

For a chosen value of x_0 , Eq. (1) is solved for

$$A = \frac{M + \left[M^2 + 2 \left(\frac{\gamma + 1}{\gamma - 1} \right) \right]^{1/2}}{2 \left(\frac{x - x_0}{D} \right)^{\gamma-1}}.$$

Values of M and x/D are inserted from the characteristics solution, and if the value of x_0 is good, the same value of A (except only for a small random scatter due to mesh-size errors in the characteristics computation) results for all values of $M > 5.5$, a value which indicates the threshold of the inertia-dominated region. If this does not happen at first, x_0 is adjusted until it does.

The final values in this region with $\gamma = 1.4$ of M .

It is tempting

and indeed value upstream to surp Table I, but will

γ	x_0/D
1.67	0.07
1.40	0.40
1.285	0.85

For values of x_0 within the random scatter, the third term

precludes any de this last term. It formula in this v

b. Impact Pres experimentally, v

$$\frac{P_0}{P_1}$$

While in principi can improve the i large x) by readj Eq. (1) or better pre

2. The Tranzo above about the the details of th Berkeley. The ce tube on the axis in the stagnation

The final values in Table I cause Eq. (1) to reproduce the computer data in this region within this random scatter, the maximum deviations being about 1/2% of M .

It is tempting to continue Eq. (1) with a third term of the form

$$C \left(\frac{x - x_0}{D} \right)^{-3(\gamma-1)}$$

and indeed values of C can be found which give an accurate data fit, extending upstream to surprisingly small values of x/D . These values are included in Table I, but with the explicit warning that the scatter in the computer data

TABLE I

γ	x_0/D	x_0'/D	A	C	x_{min2T}^a	x_{min3T}^a	ϕ
1.67	0.075	0.04	3.26	0.31	2.5D	1.0D	1.365
1.40	0.40	0.13	3.65	0.20	6D	1.0D	1.662
1.2857	0.85	—	3.96	^b	4D	^b	1.888

^a For values of $x > x_{min}$, the two-term or three-term fitting formulas give accuracy within the random scatter of the computer data.

^b No third term of form $C(x - x_0/D)^{-3(\gamma-1)}$ seems to fit.

precludes any definite conclusion as to the correctness of the analytic form of this last term. In fact, we have not even been able to extend our 2-term formula in this way, for the case of $\gamma = 9/7$.

b. Impact Pressure. Since impact pressure is the easiest quantity to obtain experimentally, we give explicit fitting formulas for it in the form

$$\frac{p_i}{p_0} = \left(\frac{\gamma + 1}{\gamma - 1} \right)^{\gamma/\gamma-1} \left(\frac{\gamma + 1}{2\gamma} \right)^{1/\gamma-1} A^{-2/\gamma-1} \left(\frac{x - x_0'}{D} \right)^{-2} \quad (2)$$

While in principle the constant x_0' should be the same as x_0 of Eq. (1), we can improve the impact pressure prediction at small x (without harming it at large x) by readjusting x_0' as shown in Table I. The resulting formula gives 1% or better prediction of the characteristics data for $x/D \geq 2.5$ for all γ .

2. The Transonic Region. Effects of Entry Shape. The assertion made above about the weak reliance of the flow in the high supersonic region upon the details of the transonic exit conditions was verified experimentally at Berkeley. The centerline static pressure was measured with a 0.300-in.-diam tube on the axis of a 3.00-in.-diam nozzle. The nose of the tube was always in the stagnation chamber and the static pressure taps were 13 in. aft of the

the
com
sults
rtia-
loes

nose and 14 in. upstream of the support. The tests compared the flow through a thin-plate ($\frac{1}{16}$ in. thick) orifice with that through a gradually converging nozzle with a 0.9-in.-long constant-diameter throat section. They covered the region in which $0.05 \leq M \leq 4$, for nozzle Reynolds numbers of 7960; 2660; and 690. Mach numbers deduced with an isentropic flow assumption at these Reynolds numbers agreed internally within $1\frac{1}{2}\%$ for a given geometry, there being a very slight systematic trend toward higher Mach number with decreasing Reynolds number.

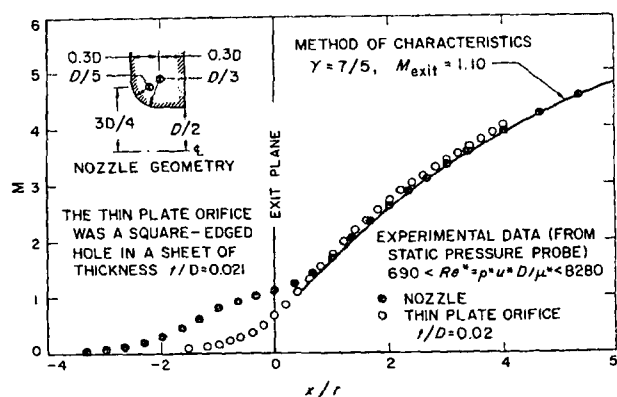


FIG. 2. Effect of entry geometry on centerline Mach number.

Results for the two geometries are compared in Fig. 2. They come together very quickly as x/D exceeds about $\frac{1}{2}$. The small residual difference for $x/D > \frac{1}{2}$, between the results for the two entry shapes and the theoretical result for uniform exit flow at $M = 1.10$, can be effectively removed by assigning to the nozzle or orifice an "effective diameter," D^* , which is slightly smaller than the diameter of the uniform flow section assumed for the theory, and by moving the effective source slightly upstream. For the nozzle $D^*/D = 0.975$; for the orifice $D^*/D = 0.943$ and $x_0/D = 0.6$. As will be discussed later, D^* may decrease further with decreasing Reynolds number, but the values cited here are thought to be characteristic of essentially inviscid flow.

B. Angular Variation of Flow Properties in the Inertia-Dominated Region

The approximately self-similar behavior of the density field, and hence the impact pressure field, in the inertia-dominated region consists in ρR^2 being only a function of θ . When ρR^2 was computed for a large number of

SUP

points selected they exhibited e

with an accurate heats ratio as s
This formula

are sufficiently drag data for r
(the speed u is suggested anal
particular, it g centerline Mac

C. Experiment

Some of the by interferome (1948) cited a data of Hartm; pressure and n body of data; Samples of im sections norm

In general, t which are in a probe not too too small (they highly yawed.

III. Sho

For a given s Mach disk an A computation

points selected from the data of the method-of-characteristics calculation, they exhibited considerable scatter, but could be fitted by the simple formula

$$\frac{\rho(R, \theta)}{\rho(R, 0)} = \cos^2 \left(\frac{\pi\theta}{2\phi} \right) \quad (3)$$

with an accuracy of about 3% of $\rho(R, 0)$. The constant ϕ depends on specific heats ratio as shown in Table I.

This formula, and its counterpart

$$\frac{\rho(r, x)}{\rho(0, x)} = \cos^2 \theta \cos^2 \left(\frac{\pi\theta}{2\phi} \right), \quad (4)$$

are sufficiently accurate for such purposes as the correction of aerodynamic drag data for radial variation of dynamic pressure (Tang, 1964; Ko, 1964) (the speed u is essentially constant in the inertia dominated region) but the suggested analytic form is almost certainly not theoretically significant. In particular, it gives a value of $\partial^2 \rho / \partial \theta^2$ at $\theta = 0$ which is inconsistent with the centerline Mach number distribution given by Eq. (1).

C. Experimental Verification of the Inviscid Theory

Some of the earliest quantitative data on free jet structure were obtained by interferometric techniques by Ladenburg *et al.* (1949). Owen and Thornhill (1948) cited a successful comparison of their theory with impact pressure data of Hartmann and Lazarus (1941). A recent extensive study using impact pressure and mass flow probes was made by Reis (1962) and a considerable body of data has been accumulated by the present authors and their co-workers. Samples of impact pressure data on the jet centerline and in various cross sections normal to the axis are shown in Figs. 3 and 4.

In general, there seems to be no difficulty in obtaining impact pressure data which are in excellent accord with theory if due care is taken to have the probe not too large (thereby incurring probe "displacement" effects) nor too small (necessitating a probe calibration for probe viscous effects), nor too highly yawed.

III. Shock Wave Configurations in Nearly Inviscid Flow

For a given specific heats ratio the shape and size of the barrel shock and Mach disk are determined by the pressure ratio across the orifice or nozzle. A comprehensive photographic study was made by Bier and Schmidt (1961)

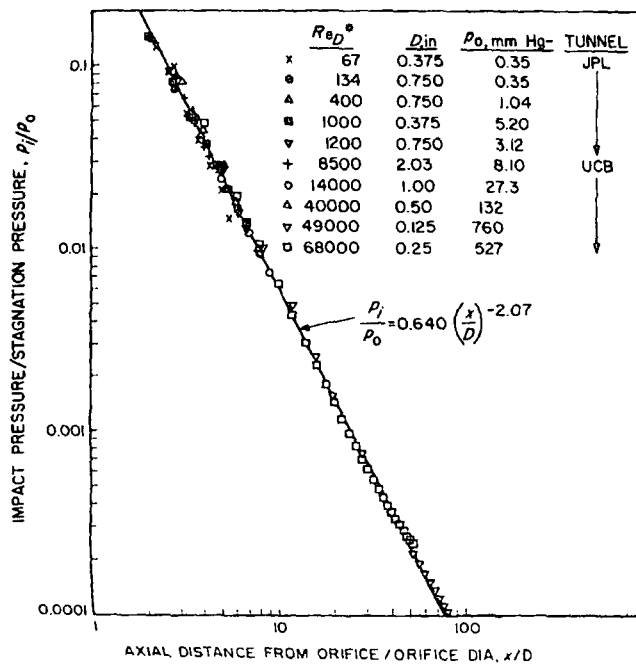


FIG. 3. Axial impact pressure distribution, $\gamma = 7/5$.

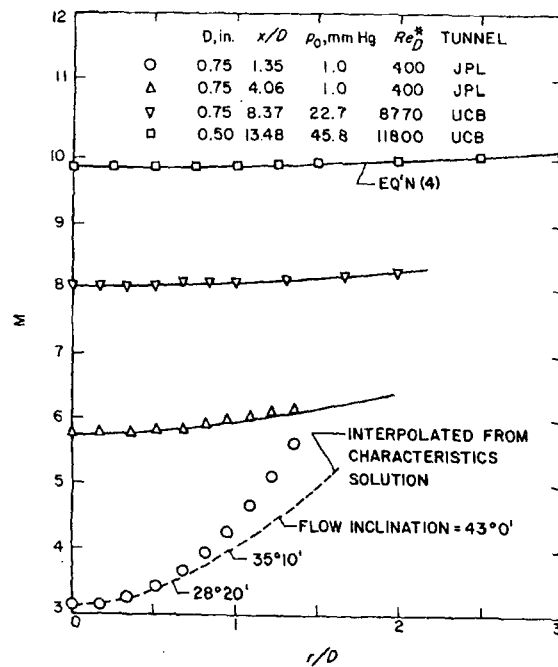


FIG. 4. Radial Mach number distribution, $\gamma = 7/5$.

A relation of the (1978), who argue about equal to it advised for the P_i/P_0 to be very relating of exper spectrum of the M Her and Schmit barrel shock and it

By

Corresponding author
E-mail: [unreadable]

independent of the
Fig. 5. The source
of rather thick sh
impact pressure a

covering a wide r
and tritonic ga
Mach disk by in
that

SI

covering a wide range of pressure ratios and a variety of monatomic, diatomic, and triatomic gases. We have checked their results for axial distance to the Mach disk by impact pressure and free-molecule wire techniques and find that

$$x_M/D = 0.67(p_0/p_1)^{1/2}, \tag{5}$$

independent of the value of γ , for $15 \leq p_0/p_1 \leq 17,000$. Our data are shown in Fig. 5. The scatter which is evident arises in determinations of the "location" of rather thick shocks. For these shocks x_M represents the point of minimum impact pressure as sketched in Fig. 5.

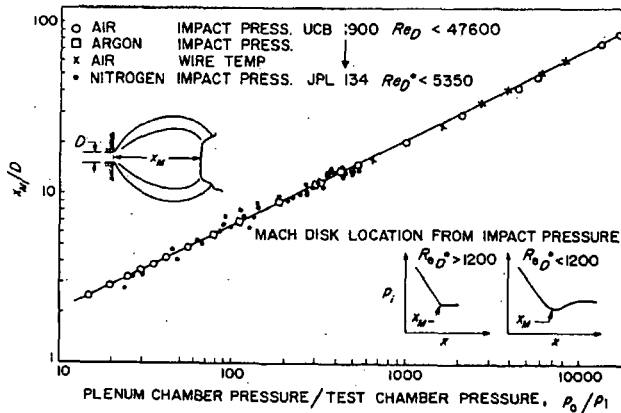


FIG. 5. Mach disk location.

A relation of the form of Eq. (4) was predicted by Adamson and Nicholls (1959), who argued that the static pressure behind the Mach disk would be about equal to the test chamber pressure. A similar argument might be advanced for the impact pressure behind the shock, and we indeed find p_{1M}/p_1 to be very nearly independent of p_0/p_1 , a fact which is useful in the planning of experiments in the free jet, and in estimating conditions just upstream of the Mach disk. Our data are shown in Fig. 6.

Bier and Schmidt (1961) also measured the maximum diameter of the barrel shock and the Mach disk diameter as a function of p_0/p_1 . They found, for air,

$$D_M/x_M = 0.42 \text{ and } 0.48 \text{ at } p_0/p_1 = 20 \text{ and } 1000.$$

Corresponding ratios are about 25% larger for CO_2 ($\gamma \approx 9/7$) and about 20% smaller for argon ($\gamma \approx 5/3$).

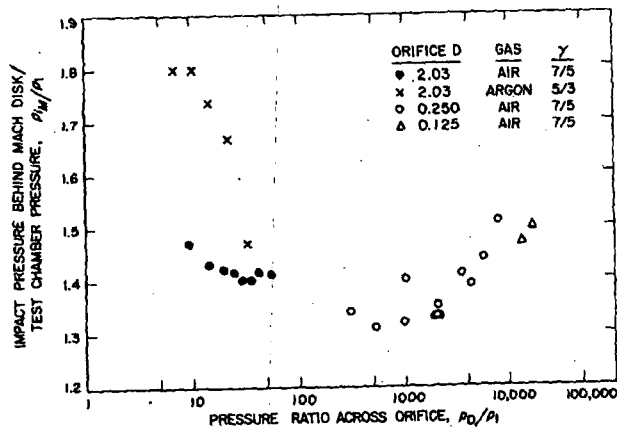


FIG. 6. Impact pressure behind Mach disk.

IV. Viscous Effects in Free Jets

Viscous effects in the free jet are of four types:

(a) boundary-layer growth on the converging nozzle, which can produce a change in effective orifice size and a distortion of the flow pattern near the orifice. This effect is seen in the variation of nozzle discharge coefficient with Reynolds number and in a shrinking of the scale of the flow downstream, and is generally very small if the nozzle Reynolds number is more than a few hundred.

(b) mixing-layer growth at the free jet boundary. This has no effect on the flow inside the shock barrel until, under circumstances of low Reynolds number and high pressure ratio, the mixing layer begins to overlap with the Mach disk and eventually to eradicate the downstream portions of the shock barrel and the Mach disk.

(c) thickening of the shock waves that form the sides and bottom of the barrel. This, in combination with the growth of the mixing layer, is the most prominent qualitative feature of the observed transition from the typical nearly-inviscid flow pattern to free-molecular effusion, but it presumably does not influence the flow upstream of these shocks, as long as any such flow exists.

(d) viscous dissipation, etc., in the "core" of the flow, arising from the slight but nonvanishing velocity and temperature gradients in that region. These effects may be of experimental significance at points on or near the jet axis and far downstream from the orifice, at Reynolds numbers so large that the first three classes of effects are insignificant.

A. Dissipation Effects

This last class of flow, where the flow is investigated on a disk, were investigated on a model. A result was obtained on sonic flow properties using an inviscid theory with a certain small error. The dissipation is due almost entirely to the fact that it depletes the directed energy significantly—

The analysis made use of an asymptotic series in $1/\sqrt{Re}$ as an initial condition which is slightly larger than the actual radius. With the perfect gas assumption, the structure,

can be combined with

to show that

where subscript zero denotes the first viscous perturbation. With a viscosity-temperature law, the asymptotic result

$$m_1 \sim \frac{-2\gamma(\gamma - 1)}{\dots}$$

where μ and λ are the

This asymptotic result is valid for $\gamma = 5/3$, at which point the asymptotic series diverges. Under these conditions

A. Dissipation Effects in the Core

This last class of viscous effects, along with the thickening of the Mach disk, were investigated by Sherman (1964) by use of a simple source-flow model. A result was a prediction of the minimum Reynolds number (based on sonic flow properties and the sonic sphere radius) which would permit the use of inviscid theory to specify the Mach number at a given radius within a certain small error. In particular, it was found that the Mach number perturbation is due almost entirely to a small amount of viscous dissipation, which depletes the directed kinetic energy only negligibly, but raises the internal energy significantly—a characteristic hypersonic effect.

The analysis made use of an "outer" expansion of all flow properties in asymptotic series in inverse integral powers of the Reynolds number, and an initial condition which assigned an inviscid value to the velocity at a fixed radius, slightly larger than the sonic radius.

With the perfect gas assumption, the expansion for velocity and temperature,

$$\begin{aligned} u &= u_0 + (1/\text{Re})u_1 + \dots, \\ T &= T_0 + (1/\text{Re})T_1 + \dots, \end{aligned} \tag{6}$$

can be combined with one for the Mach number

$$M = M_0[1 + (m_1/\text{Re}) + \dots], \tag{7}$$

to show that

$$M_1 = (u_1/u_0) - \frac{1}{2}(T_1/T_0), \tag{8}$$

where subscript zero denotes the inviscid approximation and subscript one the first viscous perturbation.

With a viscosity-temperature law, $\mu \propto T^\omega$, with constant ω , there followed the asymptotic result for large radius,

$$m_1 \sim \frac{-2\gamma(\gamma-1)\left(\frac{\gamma+1}{\gamma-1}\right)^{2\gamma+1-\omega(\gamma-1)}\left(\frac{\lambda}{\mu}+1\right)}{1+2(\gamma-1)(1-\omega)}\left(\frac{r}{r_*}\right)^{1+2(\gamma-1)(1-\omega)}, \tag{9}$$

where μ and λ are the viscosity coefficients in the Navier-Stokes relation

$$\tau_{ij} = \mu(\partial u_i/\partial x_j + \partial u_j/\partial x_i) + \lambda \text{div } \mathbf{u} \delta_{ij}.$$

This asymptotic result is accurate for $M_0 \gtrsim 7$ for $\gamma = 7/5$ and $M_0 \gtrsim 10$ for $\gamma = 5/3$, at which values the contribution of u_1/u_0 to m_1 is quite negligible. Under these conditions we can readily show that $-m_1$ is simply proportional

to the entropy increase of the gas. This follows from the perfect gas relation,

$$\frac{dT}{T} = \frac{dS}{C_v} + (\gamma - 1) \frac{d\rho}{\rho}, \quad (10)$$

and the continuity equation for the simple source flow,

$$\rho u r^2 = \text{const.} \quad (11)$$

Combining these equations and integrating to r from a radius r_1 at which the entropy is called zero, we get

$$\ln T = \frac{S}{C_v} - (\gamma - 1) \ln u - 2(\gamma - 1) \ln r + \text{const.}$$

Expanding this in inverse powers of Re , and combining with the definition of m_1 , we find

$$m_1 = -\frac{1}{2} \frac{S_1}{C_v} + \frac{\gamma + 1}{2} \frac{u_1}{u_0}, \quad (12)$$

in which the second term on the right is negligible for large r .

This same approach can be carried over to the free jet itself, by use of the general continuity equation in place of $\rho u r^2 = \text{constant}$. Then we can combine (9) and (10) into

$$\frac{D(\ln T)}{Dt} = \frac{D(S/C_v)}{Dt} - (\gamma - 1) \text{div } \mathbf{u},$$

which may be integrated along the jet axis from a point in the plenum chamber to the point of observation. When the result is expanded in inverse powers of Re , we find

$$m_1 = -\frac{1}{2} \frac{S_1}{C_v} + \int_{-\infty}^x \left[\frac{d}{dx} \left(\frac{u_1}{u_0} \right) + \frac{\gamma - 1}{2} \frac{\text{div } \mathbf{u}_1}{u_0} - \frac{\gamma - 1}{2} \frac{\text{div } \mathbf{u}_0}{u_0} \frac{u_1}{u_0} \right] dx, \quad (13)$$

where u is the scalar speed along the axis. We shall now assume that for the large values of x (and high Mach numbers) of interest, the contribution of the integral on the right, which will be of order u_1/u_0 , is negligible, and thus we use only

$$m_1 = \frac{1}{2} S_1/C_v. \quad (14)$$

The entropy perturbation S_1 , is readily calculated along the jet axis, if we are given the inviscid flow field. In fact, all that is needed is the distribution of M_0 versus x .

The basic equation employed is

$$S - S_0 = \int_{-\infty}^x (\Phi - \text{div } \mathbf{q}) \frac{dx}{\rho u T}, \quad (15)$$

where Φ is the viscous correction. To expand this in inverse powers of Re , the flow field in the plenum chamber can be represented by a simple source flow. Such results, on the axis,

and

$$\partial v_0 / \partial r = (M_0^2 - 1) v_0 / r$$

Treating the Prandtl number as a function of r and integrating to a final form,

$$\frac{S - S_0}{C_v} = \int_{-\infty}^x \left\{ \frac{4\gamma(\gamma - 1)}{2} \frac{v_0}{r} \right\} dx$$

In this $\omega = d(\ln \mu)/d(\ln r)$ involving T can be expressed in terms of M_0 .

We have integrated Eq. (15) and employing the curve given by the Ames Research Corporation in Fig. 7a are for stagnation conditions at the centerline Mach number M_0 .

It turns out that the dominant term near the plane of the orifice is given in Eq. (16). For large Re and the dominant term is the same as the dominant term in the asymptotic result for m_1 .

$$m_1 \sim \frac{-2\gamma(\gamma - 1)[(\lambda/\mu)]}{1 + 2(\gamma - 1)}$$

which reduces to Eq. (15) for simple source flow. Here we use $\mu \rightarrow \infty$. For the Sutherland

where Φ is the viscous dissipation function and q the heat flux vector. We expand this in inverse powers of Re and assume that the inviscid flow near the axis can be represented by power series in distance from the axis. This gives such results, on the axis, as

$$\text{div } \mathbf{u}_0 = M_0^2 \partial u_0 / \partial x,$$

and

$$\partial v_0 / \partial r = (M_0^2 - 1) \partial u_0 / \partial x \quad (v \text{ and } r \text{ are velocity and position components normal to the axis}).$$

Treating the Prandtl number, $Pr = \mu c_p / k$, as constant, we reduce Eq. (15) to a final form,

$$\frac{S - S_0}{C_v} = \int_{-\infty}^x \left(\frac{4\gamma(\gamma - 1)[(\lambda/\mu) + 1]M^4 - 2M^2 + 3}{[2 + (\gamma - 1)M^2]^2} \left(\frac{dM}{dx} \right)^2 + \frac{\gamma}{Pr} \left[\frac{\nabla^2 T}{T} + \frac{\omega}{T^2} \left(\frac{dT}{dx} \right)^2 \right] \right) \frac{\mu dx}{\rho u}. \quad (16)$$

In this $\omega = d(\ln \mu) / d(\ln T)$ may be treated as a function of T . The terms involving T can be expressed in terms of M .

We have integrated Eq. (16) for air, assuming $\lambda = 0$, $\gamma = 7/5$, $Pr = 3/4$, and employing the curves for unit Reynolds number versus Mach number, given by the Ames Research Staff (1953), to determine $\rho u / \mu$. The cases shown in Fig. 7a are for stagnation temperatures of 50°, 500° and 1400°F, and use the centerline Mach number distribution for the thin-plate orifice.

It turns out that the heat condition terms are relatively most important near the plane of the orifice, where they actually produce a negative net integrand in Eq. (16). For large x , these terms become negligible rather rapidly, and the dominant term in the integrand is the very first one, which is just the same as the dominant term in the simple source flow. Physically, this term represents viscous dissipation arising from the "hoop stresses" due to the lateral stretching of the expanding fluid particles. The corresponding asymptotic result for m_1 is

$$m_1 \sim \frac{-2\gamma(\gamma - 1)[(\lambda/\mu) + 1]A^{[2\gamma/(\gamma - 1)] - 2\omega}}{1 + 2(\gamma - 1)(1 - \omega)} \left(\frac{\gamma + 1}{\gamma - 1} \right)^{\omega - [(\gamma + 1)/2(\gamma - 1)]} \times \left(\frac{x - x_0}{D} \right)^{1 + 2(\gamma - 1)(1 - \omega)}, \quad (17)$$

which reduces to Eq. (15) when $A = [(\gamma + 1)/(\gamma - 1)]^{(\gamma + 1)/4}$, the value for a simple source flow. Here we have assumed that ω approaches a constant limit as $x \rightarrow \infty$. For the Sutherland viscosity law, which is used in NACA TR 1135,

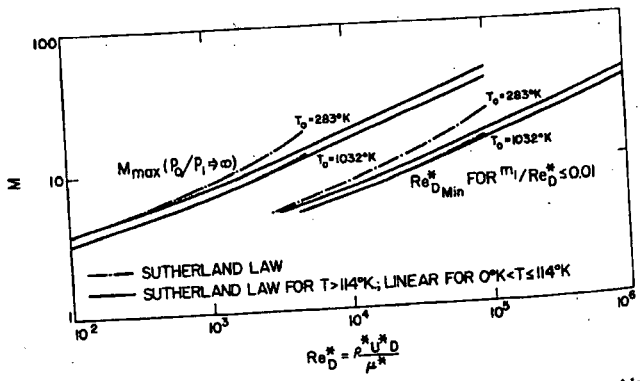
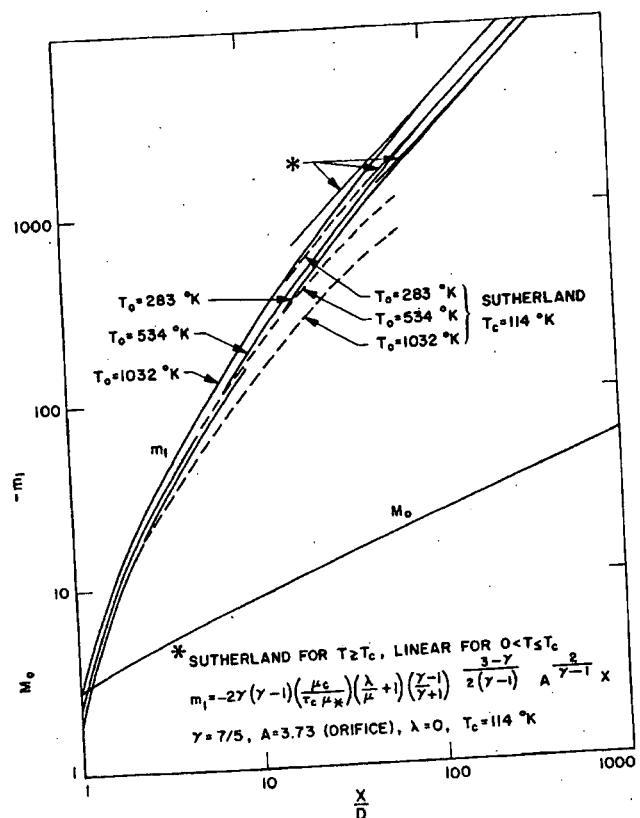


FIG. 7.(a) Mach number perturbation in air. (b) Mach number-Reynolds number relations in air, p_0/p_1 .

the limiting value of $(x - x_0/D)^{-7}$. In practice expanded to very low x in this region, and they diverge from the origin to the Sutherland law (i.e., a curve that is different at large x to an eventual linear reduction of model test well-based method is needed.²

The curve for $m_1(x)$ (a) of the minimum Mach number for given accuracy in a given orifice Re . The theory, but is included when m_1/Re is only shown in Fig. 7b.

B. Boundary Layer Effects

The variation of m_1 investigated experimentally < 2500, with a square orifice that the experimental probe viscous effects are significant in flow, and for shock waves with the predictions dependent upon Re . The effects of larger magnitudes seen in the flows from other authors, this constitutes a problem, since this is due to the lowest Re effects to the lowest p .

C. Thickening of Shock

Little can be said about mixing-layer thickening.

² Results reported in the literature for low temperature $w = \frac{1}{2}$

the limiting value of ω is $3/2$, and m_1 eventually grows in proportion to $(x - x_0/D)^{2-\gamma}$. In practice, wind tunnel workers having to deal with flows expanded to very low temperatures often disregard the Sutherland law in this region, and they extrapolate viscosity data along a line $\mu \propto T$ ($\omega = 1$), from the origin to the point of tangency with a linear $\mu - T$ plot of the Sutherland law (i.e., at about $T = 114^\circ\text{K}$ for air). This procedure would lead to an eventual linear growth of m_1 with x , and results which are quantitatively very different at large x , as seen in Fig. 7a. In this calculation, as in the reduction of model test data obtained in high Mach number free jets, some well-based method of viscosity prediction for low temperatures is sorely needed.²

The curve for $m_1(x)$ can be employed for two types of useful predictions, (a) of the minimum orifice Re required if the inviscid theory is to be trusted for given accuracy in M , and (b) the maximum M which can be obtained at a given orifice Re . The latter prediction strains one's faith in a small perturbation theory, but is included because the calculations show that M_{max} is attained when m_1/Re is only about 0.2 to 0.3. Some results are shown for air in Fig. 7b.

B. Boundary Layer Effects in the Entry Section

The variation of effective orifice diameter with Reynolds number was investigated experimentally at the Jet Propulsion Laboratory for $13 < \text{Re} < 2500$, with a square-edged orifice of thickness $t = 0.0266D$. It was found that the experimental axial impact-pressure distribution, when corrected for probe viscous effects by calibration factors determined in a uniform nozzle flow, and for shock displacement effect, could be brought into agreement with the predictions of inviscid flow theory by the assumption of a D^*/D dependent upon Re . The results are presented graphically in Fig. 8. Similar effects of larger magnitude and qualitatively different Re -dependence are seen in the flows from gradually converging nozzles. In the opinion of the authors, this constitutes an advantage of the thin-plate orifice for free jet formation, since this geometry postpones the onset of one class of viscous effects to the lowest possible Reynolds number.

C. Thickening of Shock Waves and Mixing Layer

Little can be said theoretically about the dramatic process of shock and mixing-layer thickening, and the interaction between them as Reynolds

² Results reported in this volume by Anderson, Andres, Fenn, and Maise indicate a value $\omega = \frac{1}{2}$ for low temperature argon.

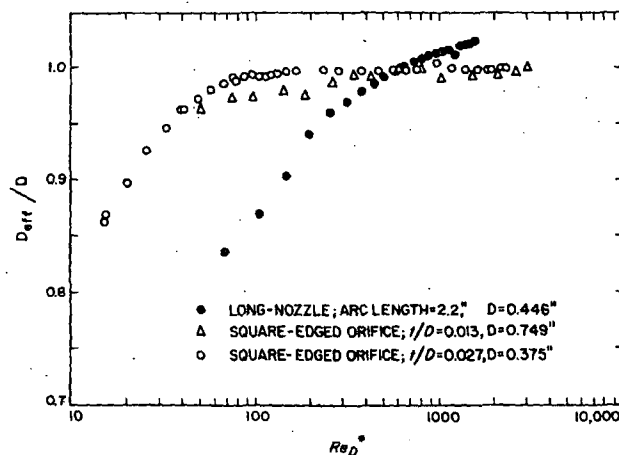


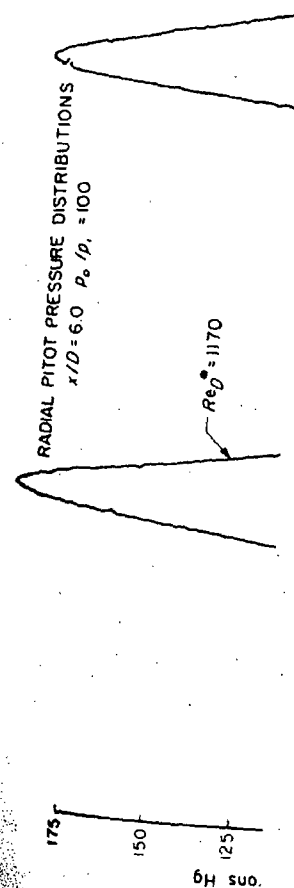
FIG. 8. Effective orifice diameter.

number decreases. Experimental evidence to date is limited to impact pressure surveys and flow visualization studies.

Axial impact pressure surveys exhibit a broadening of the "dip" which we associate with the Mach disk. Since the upstream entry into this dip is very smooth it is very hard to detect the upstream beginnings of the Mach disk from impact pressure data.

Radial impact pressure surveys taken at JPL for air at $x/D = 6$ and $p_0/p_1 = 100$ are shown for a wide range of Re in Fig. 9. The ordinate is direct pressure transducer output, uncorrected for probe, viscous, or yaw effects. The peak impact pressure associated with the recompressed flow outside the shock barrel falls relative to the centerline pressure as Re decreases, and the residual peaks move slightly toward the axis as they are consumed by the mixing layer. Visual observations of this process, using the sodium vapor resonant-scattering technique suggested for rarefied gas flows by Vali and Thomas (1962), have also been made at Berkeley.

As suggested by Bier and Hagen (1963), an appropriate dimensionless criterion for the disappearance of the Mach disk and its neighboring barrel shock as recognizable entities is the approach toward unity of a Knudsen number based on Mach disk diameter and mean free path behind the Mach disk. The latter mean free path is very nearly equal to that of the gas in the test chamber, with pressure p_1 and temperature T_0 . When we take the inviscid flow value for Mach disk diameter corresponding to the measured p_0/p_1 and form a Knudsen number, K_M , with it and the "test chamber mean free



re
ve
sk
nd
ect
:s.
he
the
the
por
and
less
irrel
isen
lach
the
iscid
o/P₁

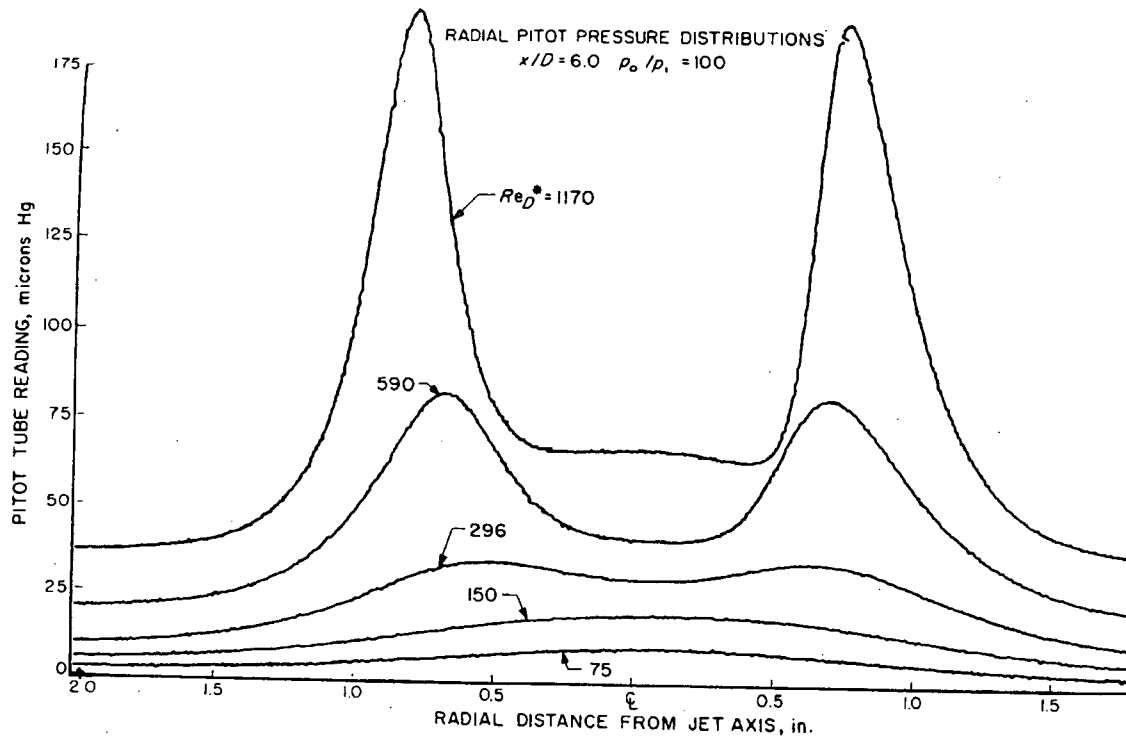


FIG. 9. Radial pitot pressure distributions.

path," we find that the impact pressure peaks of the radial survey just ahead of the Mach disk vanish at $K_M = 0.1$, and the last recompression by the Mach disk, visible by the sodium-scattering technique, vanishes at $K_M = 0.3$.

V. Application of Free Jets as Wind Tunnel Streams

A. Attainable Jet Size

The distance x_M turns out, under reasonable assumptions, to be a simple measure of the volumetric capacity of the wind tunnel pumping plant. Suppose the pumps will handle a mass flow rate \dot{m} at a suction pressure equal to the test chamber pressure p_1 . The stagnation temperature is T_0 . Then

$$x_M = 0.75 \frac{(RT_0)^{1/4}}{\gamma} \left(\frac{\gamma + 1}{2} \right)^{4[(\gamma+1)/(\gamma-1)]} \left(\frac{\dot{m}}{p_1} \right)^{1/2}$$

For the No. 4 Wind Tunnel at the University of California, x_M turns out to be 11 to 14 in., the variation being due to the nonlinearity of the (\dot{m} vs. p_1) pump curve. For the Jet Propulsion Laboratory low density wind tunnel x_M is about 6 in. The relationship above is quite accurate if $p_0/p_1 \geq 15$ and if the boundary layer thickness in the nozzle throat is only a small fraction of the nozzle radius.

B. Available Mach and Reynolds Number Ranges

The roughest outline of available Mach and Reynolds number range is obtained by fixing T_0 and then determining the boundaries corresponding (a) to a minimum test chamber pressure, $p_{1,\min}$ and (b) to a maximum plenum chamber pressure, $p_{0,\max}$. Then we fix attention on conditions just upstream of the Mach disk, which is the most desirable test region. Simple arguments, assuming isentropic flow in the core, lead to

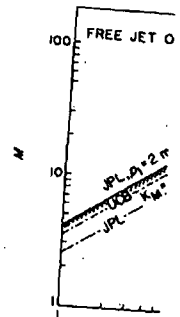
$$(a) \quad \frac{Re_M}{L} \approx \frac{1.35 p_1 \left(\frac{\gamma - 1}{2} \right)^\omega}{\left(\frac{2}{\gamma - 1} RT_0 \right)^{1/2} \mu(T_0)} M_M^{2\omega}$$

for which we have assumed $\mu(T)/\mu(T_0) = (T/T_0)^\omega$

$$(b) \quad \frac{Re_M}{L} \approx \frac{1.10 p_0 \left(\frac{\gamma - 1}{2} \right)^\omega}{\left(\frac{2}{\gamma - 1} RT_0 \right)^{1/2} \mu(T_0)} \left(\frac{\gamma + 1}{\gamma - 1} \right)^{\gamma/\gamma - 1} \left(\frac{\gamma + 1}{2\gamma} \right)^{1/\gamma - 1} M_M^{2[\omega - (1/\gamma - 1)]}$$

These boundaries are sketched in Fig. 10 for the University of California

SUPERSONIC



FIG

Berkeley No. 4 wind tu
atmosphere, $T_0 = 300^\circ$

Propulsion Laboratory

Actually, this view of
of if \dot{m}/p_1 is small. An
desire to have negligible

The viscous flow an:

Fig. 10 curves for m_1/L

is used, a curve results

nearly inviscid flow at L

The criterion $K_M = C$

picture in the vicinity of

of the relation of jet d

to a fixed value of p_1

≈ 5.3 in., $p_1 = 0.0038$ to

able with the steam ejec

within the available ran

The high pressure limi

because of the possibili

currently investigating t

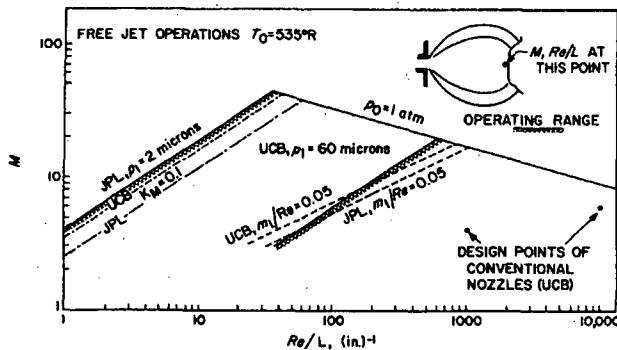
any condensation effects

the STP conditions to a

in this volume makes a

C. Effect of Stagnation t

It may be desirable t
local static temperature:


 FIG. 10. Free jet operations; $T_0 = 535^\circ\text{R}$.

Berkeley No. 4 wind tunnel, for which we take $p_{1,\min} = 0.060$ torr, $p_{0,\max} = 1$ atmosphere, $T_0 = 300^\circ\text{K}$, and consider air to have $\omega = 3/4$, and for the Jet Propulsion Laboratory Leg 1 tunnel, $p_{1,\min} = 0.002$ torr.

Actually, this view of things may be quite oversimplified if p_1 is very low, or if m/p_1 is small. Another low-pressure boundary criterion is set by the desire to have negligible viscous effects in the core of the jet.

The viscous flow analysis of Section III has been applied to draw into Fig. 10 curves for $m_1/Re_* = 0.05$, again with $\omega = 3/4$. If the Sutherland law is used, a curve results for this boundary, which improves the prospects for nearly inviscid flow at high M .

The criterion $K_M = 0.1$, indicating the total collapse of the inviscid flow picture in the vicinity of the Mach disk, is also indicated in Fig. 10. By virtue of the relation of jet dimensions to pumping speed, this criterion reduces to a fixed value of p_1 for a given pumping plant. For Berkeley, with $D_M \approx 5.3$ in., $p_1 = 0.0038$ torr, an order of magnitude lower than the p_1 attainable with the steam ejectors. For JPL, $D_M = 2.9$ in., $p_1 = 0.0069$ torr, well within the available range.

The high pressure limit ($p_{0,\max} = 1$ atmosphere) may also be too approximate, because of the possibility of condensation of the air components. We are currently investigating this experimentally, and have been unable to isolate any condensation effects on impact pressure data, even when expanding from the STP conditions to a Mach number of 22! (The paper of Bier and Hagena in this volume makes a major contribution on this point.)

C. Effect of Stagnation Heating

It may be desirable to increase T_0 to avoid condensation, and to bring local static temperatures up to values at which the viscosity may be reliably

estimated. This has a number of collateral consequences, which may be estimated if we assume that \dot{m}/p_1 is independent of T_0 , and take $\omega = \frac{1}{4}$. The latter assumption leads to a considerable oversimplification.

- (a) D increases as $T_0^{1/4}$ for fixed p_0/p_1 or M_M .
- (b) M_M increases as $T_0(\gamma - 1)/4$ for fixed D .
- (c) M/Re_* decreases as $T_0^{-1/4}$ for fixed M_M , Re_M/L .
- (d) Re_M/L decreases as $T_0^{-(1/2)-\omega}$ for fixed p_0 and M_M .
- (e) Re_M/L decreases as $T_0^{-(1/2)-\omega}$ for fixed p_1 and M_M .

VI. Techniques of Experimental Evaluation in Viscous and More Rarefied Regimes

At the present date even the experimental picture of free jet structure in the highly viscous regime is not clear, because the viscous effects are at first rather subtle, influencing only those flow properties, such as static temperature and pressure, which are hardest to measure.

A. Impact Pressure Measurements

The key point to recognize in use of the impact tube in hypersonic flow is that $p_i \approx \rho u^2$ quite accurately independent of M and T . Hence a viscous effect which greatly increases T but hardly affects ρ or u will not be easily seen in impact pressure data, except through the influence of M and T on the viscous or molecular flow effects on probe readings.

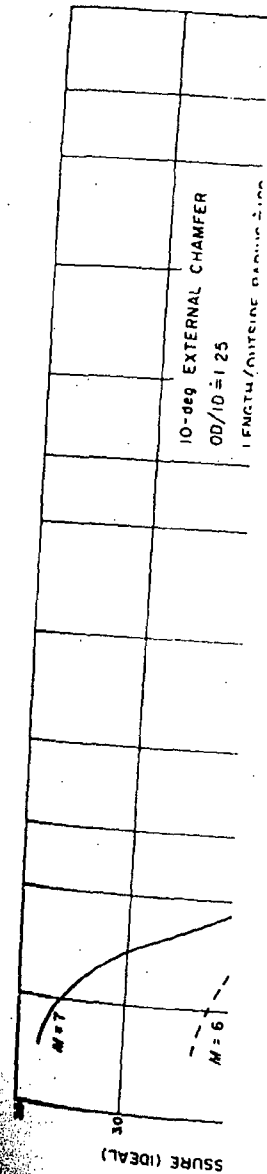
The evaluation of the latter effects in the extended range of M and Re made available by the free jet is a major task in itself, which has been extensively undertaken at the Jet Propulsion Laboratory. Measurements were made using externally chamfered pitot tubes in conjunction with an unbonded-strain-gage-diaphragm pressure transducer. The geometry of the tubes used was similar, viz.

- (a) 10° external chamfer
- (b) Ratio of O.D. to I.D. = 1.25
- (c) Ratio of length to outside radius = 100.

Pitot tube corrections applicable to the low density, high Mach number flow in the jet were deduced as follows:

The pitot tube data of Ashkenas (1962) (obtained in a conventional low density nozzle flow at $M = 4$) were used as a starting point for a boot-strap procedure using three geometrically similar pitot tubes; the small region in the free jet between $3.5 \leq M \leq 4.5$ was systematically covered with these three pitot tubes at stagnation pressures ranging from 0.1 to 7.0 mm Hg. The

SUPER.



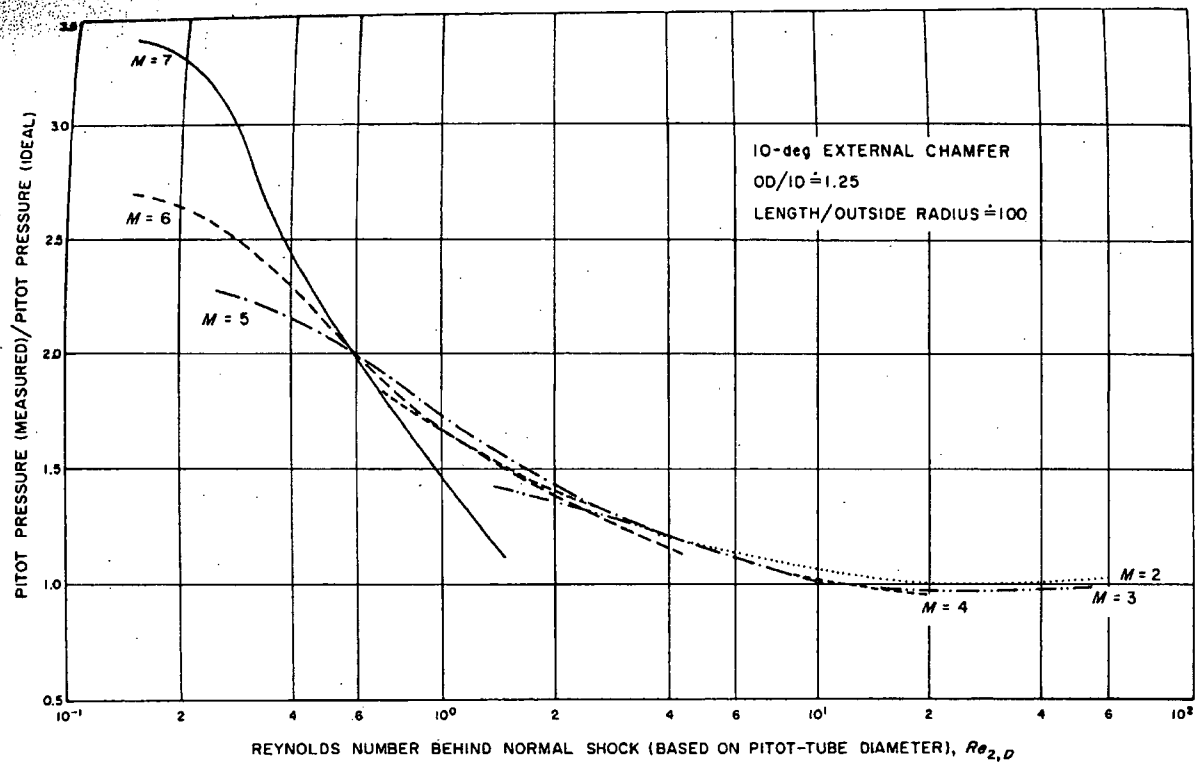


FIG. 11. Pitot tube corrections.

impact pressure determined from the corrected pitot tube data was found to be within 2% of the Owen and Thornhill values, over the entire pressure range, and thus the characteristics solution for the axial impact pressure distribution is assumed valid for the flow conditions studied. The pitot tube may then be calibrated over the entire range of Mach numbers available in the jet. Pitot tube correction curves obtained in this manner are shown in Fig. 11. Note that these curves were obtained for integer Mach numbers; linear interpolation between curves was used in reducing data for noninteger Mach numbers. It will be noted in Fig. 11 that the pressures sensed by the pitot tube can range as high as 300% of the ideal value calculated from the Rayleigh pitot tube formula.

B. Molecular Beam Methods

A powerful, but subtle, approach to the free-jet diagnostic problem involves the skimming of molecular beams from the jet flow and the determination of the velocity distribution of the beam, as has been done by Bier and Hagena (1963). It is imperative, however, that the "skimming" process be perfect, in the sense of causing no perturbation of the distribution function, and it is hard to prove that a perfect skim has been obtained except in a flow of known properties. A careful boot-strap procedure, involving iterative improvements in knowledge of the flow properties and the skimmer operation, seems indicated.³

C. Electron Beam Methods

Another attractive possibility, to obtain the local static temperature by the excitation of rotational band spectra of N_2 by an electron beam (Muntz, 1961) is being explored at Berkeley by F. Robben. His preliminary results seem to indicate the necessity of an elaboration of Muntz's theory for the excitation and de-excitation processes. Whether this can be successfully achieved remains to be seen.

VII. Conclusions

After two years of further study, the proposal that free jets be seriously considered as an alternative type of low density wind tunnel stream seems to be substantiated. Truly impressive extensions of the Mach and Reynolds number ranges of a tunnel such as that at Berkeley can be obtained, while

³ Significant progress in this direction is reported elsewhere in this volume, by Andres, Fenn, and Maisie.

nearly inviscid flow conditions effects arises with pump lower operating pressure but it appears likely that understood.

The inviscid theory or expressed by simple for slightly viscous flow seen

For implementation of experimental data at very low temperature viscosity at very low temperature

Conclusive experimental involve direct measurement quantities as static pressure methods look promising the perfection of the beam

- Adamson, T. C., and Nicholl Ames Research Staff (1953).
 Ashkenas, H. (1962). JPL Cal
 Bier, K., and Hagena, O. (1963). pp. 478-496. Academic Press.
 Bier, K., and Schmidt, B. (1963). Fenn, J. B., and Deckers, J. Vol. 1, pp. 497-515. Academic Press.
 Hartmann, J., and Lazarus, F. Ko, D. (1964). Univ. Calif. Berkeley.
 Ladenburg, R., Van Voorhis, Love, E. S., Grigsby, C. E., L. Maslach, G. J., Willis, D. R., Muntz, E. P. (1961). UTIA Report.
 Owen, P. L., and Thornhill, C. Reis, V. H. (1962). Princeton University.
 Scott, J. E., Jr., and Drewry, ed.), Vol. 1, pp. 516-538. Academic Press.
 Sherman, F. S. (1963a). In "Supersonic Flow," pp. 228-260. Academic Press, New York.
 Sherman, F. S. (1963b). Lockheed Research Report.
 Sherman, F. S. (1964). Arch. Mech.
 Tang, S. (1964). Univ. Calif. Berkeley.
 Valli, W., and Thomas, G. M. (1962). Z. Naturforsch.

nearly inviscid flow conditions are maintained. A greater concern with viscous effects arises with pumping systems with lower mass flow capacities and lower operating pressure levels, such as that at the Jet Propulsion Laboratory, but it appears likely that the resulting flows will be very useful when fully understood.

The inviscid theory of free jets is in good shape and can be conveniently expressed by simple formulas in the region where $M \gtrsim 5.5$. The theory of slightly viscous flow seems reasonable, but is experimentally unconfirmed.

For implementation of the viscous flow theory and for the reduction of experimental data at very high Mach numbers, better means for estimating viscosity at very low temperatures are urgently required.

Conclusive experimental evidence concerning viscous effects in the jet must involve direct measurement of the Mach number or of such inaccessible quantities as static pressure or temperature. Molecular beam sampling methods look promising, but must be accompanied by conclusive proof of the perfection of the beam-skimming process.

REFERENCES

- Adamson, T. C., and Nicholls, J. A. (1959). *J. Aerospace Sci.* 26, 16.
Ames Research Staff (1953). NACA Tech. Rept. 1135.
Ashkenas, H. (1962). JPL CalTech Space Programs Summary 37-15, Vol. 4.
Bier, K., and Hagen, O. (1963). In "Rarefied Gas Dynamics" (J. Laurmann, ed.), Vol. 1, pp. 478-496. Academic Press, New York.
Bier, K., and Schmidt, B. (1961). *Z. Angew. Phys.* 13, 493.
Fenn, J. B., and Deckers, J. (1963). In "Rarefied Gas Dynamics" (J. Laurmann, ed.), Vol. 1, pp. 497-515. Academic Press, New York.
Hartmann, J., and Lazarus, F. (1941). *Phil. Mag.* 31, 35.
Ko, D. (1964). Univ. Calif. Aero. Sci. Proj. Rept. AS-64-4.
Ladenburg, R., Van Voorhis, C. C., and Winckler, J. (1949). *Phys. Rev.* 76, 662.
Love, E. S., Grigsby, C. E., Lee, L. P., and Woodling, M. J. (1959). NASA TR-R-6.
Maslach, G. J., Willis, D. R., Tang, S., and Ko, D. (1964). These Proceedings.
Muntz, E. P. (1961). UTIA Rept. 71.
Owen, P. L., and Thornhill, C. K. (1948). Aero. Res. Council R & M 2616, Great Britain.
Reis, V. H. (1962). Princeton Univ. Mech. Eng. Dept. Rept. FLD-7.
Scott, J. E., Jr., and Drewry, J. E. (1963). In "Rarefied Gas Dynamics" (J. Laurmann, ed.), Vol. 1, pp. 516-538. Academic Press, New York.
Sherman, F. S. (1963a). In "Rarefied Gas Dynamics" (J. Laurmann, ed.), Vol. 2, pp. 228-260. Academic Press, New York.
Sherman, F. S. (1963b). Lockheed Missiles and Space Co. Rept. 6-90-63-61.
Sherman, F. S. (1964). *Arch. Mech. Stos.* 16, 471.
Tang, S. (1964). Univ. Calif. Aero. Sci. Proj. Rept. AS-64-3.
Vali, W., and Thomas, G. M. (1962). *ARS (Am. Rocket Soc.) J.* 32, 1114.
Zigan, F. (1962). *Z. Naturforsch.* 17a, 772.

S. I. Kim · S. O. Park

Oscillatory behavior of supersonic impinging jet flows

Received: 20 July 2004 / Accepted: 17 June 2005 / Published online: 18 October 2005
© Springer-Verlag 2005

Abstract Oscillatory flows of a choked underexpanded supersonic impinging jet issuing from a convergent nozzle have been computed using the axisymmetric unsteady Navier–Stokes system. This paper focuses on the oscillatory flow features associated with the variation of the nozzle-to-plate distance and nozzle pressure ratio. Frequencies of the surface pressure oscillation and flow structural changes from computational results have been analyzed. Staging behavior of the oscillation frequency has been observed for both cases of nozzle-to-plate distance variation and pressure ratio variation. However, the staging behavior for each case exhibits different features. These two distinct staging behaviors of the oscillation frequency are found to correlate well if the frequency and the distance are normalized by the length of the shock cell. It is further found that the staging behavior is strongly correlated with the change of the pressure wave pattern in the jet shear layer, but not with the shock cell structure.

Keywords Self-sustained oscillation · Supersonic impinging jet · Staging behavior · Underexpanded jet · Plate shock

PACS 02.60.Cb; 47.40.–x; 47.40.Nm; 47.35.+I; 47.15.–x

1 Introduction

A supersonic jet impinging onto a flat plate is a fundamental flow often encountered in space or missile launch vehicle systems and supersonic STOVL aircraft. The flow is of practical significance, since it may undermine safe operations. In spite of the simple geometry, the flowfield is rather complex;

it contains both supersonic and subsonic flow regions, and involves interaction of shock and expansion waves with jet shear layers. An important problem in a supersonic impinging jet flowfield is that the jet of very high temperature and speed leads to a severe thermal and mechanical loading on the impinging plate. The supersonic impinging jet becomes oscillatory under certain operating conditions after the initial transient impinging behavior. The unsteady oscillation can make thermal and mechanical loading more severe. An oscillatory supersonic impinging jet produces severe noise at discrete frequencies, which may cause sonic fatigue of the structures and also may damage various instruments and equipment in the vehicle.

Earlier researchers [1–5] have investigated the flow structure and the mean flow characteristics of the supersonic impinging jet flow by using Schlieren photography and mean surface pressure and temperature measurements. These earlier studies disclosed many significant features of the flow including surface pressure and temperature distributions. However, the data available in the earlier reports are mostly limited to mean flow properties. A more detailed review of these studies can be found in Alvi and Iyer [6].

Subsequent works have focused on unsteady flow oscillations and acoustic properties. One of the primary outcomes of these studies is that the highly unsteady oscillatory nature of impinging jet, which is accompanied by discrete, high-amplitude acoustic tones referred to as impingement tones, is caused by a feedback loop. Krothapalli [7], Powell [8], and Tam and Ahuja [9] identified a feedback mechanism for self-sustained oscillations of the impinging jet flows. The energy of the feedback loop is provided by the instability waves in the shear layer of the jet. Flow visualization studies show that the shear layer contains large-scale vortical structures. Upon interacting with the impinging surface, the downstream traveling coherent structures of the jet generate strong pressure fluctuations near the impingement region that lead to acoustic waves (intense acoustic disturbances) in the near sound field. These acoustic waves propagate upstream through the ambient medium and, upon reaching the nozzle exit, excite the flow instability waves

Communicated by K. Takayama

S. I. Kim · S. O. Park (✉)
Department of Aerospace Engineering
Korea Advanced Institute of Science and Technology
373-1 Guseong-dong, Yuseong-gu, Daejeon 305-701, Korea
E-mail: sopark@kaist.ac.kr

(or periodic structures) of the shear layer of the jet. This instability usually generates large-scale vortical structures in the shear layer. These coherent structures grow as they propagate downstream. The downstream traveling vortical structures and the upstream propagating acoustic waves form the feedback loop.

It has been reported that the frequency of the impinging tone exhibits staging behavior as the nozzle-to-plate distance varies [7, 8]. Krothapalli [7] obtained the near sound field microphone signal and surface pressure signal at several moderate pressure ratios for a choked underexpanded impinging jet issuing from a rectangular nozzle. It was found that the frequencies of the dominant peak in both the sound and pressure signals coincide. Sakakibara and Iwamoto [10] carried out laminar Navier–Stokes computations of convergent nozzle impinging jet flows for various nozzle-to-plate distances. They found that the flow oscillates when the nozzle-to-plate distance was greater than 2.3 times the exit diameter of the convergent nozzle, and also showed that the frequency of the surface pressure oscillation exhibited staging behavior. Discrepancies between the frequencies of the impinging tone from measurement and of the surface pressure from their computation were identified, these being attributed to the grid problem.

The present study is concerned with the surface pressure oscillation and the oscillatory flow structural changes of axisymmetric supersonic jets from a converging choked nozzle at moderate nozzle pressure ratios. More specifically, we will focus on the staging behavior of pressure oscillations for various conditions. For a given pressure ratio, we change the nozzle-to-plate distance and the pressure ratio for a given nozzle-to-plate distance. We then show how the staging behavior for these two different cases can be correlated.

2 Numerical approaches

2.1 Numerical scheme

We consider a laminar compressible flowfield governed by the following equations written in a cylindrical coordinate (x, r) system:

$$\frac{\partial Q}{\partial t} + \frac{\partial E}{\partial x} + \frac{\partial F}{\partial r} + G = \frac{\partial E_v}{\partial x} + \frac{\partial F_v}{\partial r} + G_v, \quad (1)$$

$$Q = \begin{bmatrix} \rho \\ \rho u \\ \rho v \\ \rho e_t \end{bmatrix}, \quad E = \begin{bmatrix} \rho u \\ \rho u^2 + p \\ \rho uv \\ (\rho e_t + p)u \end{bmatrix},$$

$$F = \begin{bmatrix} \rho v \\ \rho uv \\ \rho v^2 + p \\ (\rho e_t + p)v \end{bmatrix}, \quad G = \frac{1}{r} \begin{bmatrix} \rho v \\ \rho uv \\ \rho v^2 \\ (\rho e_t + p)v \end{bmatrix},$$

$$E_v = \begin{bmatrix} 0 \\ \tau_{xx} \\ \tau_{xr} \\ u\tau_{xx} + v\tau_{xr} - q_x \end{bmatrix}, \quad F_v = \begin{bmatrix} 0 \\ \tau_{rx} \\ \tau_{rr} \\ u\tau_{rx} + v\tau_{rr} - q_r \end{bmatrix},$$

$$G_v = \frac{1}{r} \begin{bmatrix} 0 \\ \tau_{xr} - \frac{2}{3}r \frac{M_\infty}{Re_\infty} \frac{\partial}{\partial x} \left(\mu \frac{v}{r} \right) \\ \tau_{rr} - \tau_{\theta\theta} - \frac{2}{3} \frac{M_\infty}{Re_\infty} \left(\mu \frac{v}{r} \right) - \frac{2}{3}r \frac{M_\infty}{Re_\infty} \frac{\partial}{\partial r} \left(\mu \frac{v}{r} \right) \\ u\tau_{xr} + v\tau_{rr} - q_r - \bar{\tau} \end{bmatrix}.$$

The variables are normalized by the nozzle exit properties. Length is normalized by the nozzle exit diameter, D , density by ρ_e , velocity by the speed of sound, C_e , temperature by T_e , pressure by $\rho_e C_e^2$, time by D/C_e , and viscosity by μ_e . We assume that the gas is perfect so that

$$p = \rho T / \gamma. \quad (2)$$

The stress terms are

$$\tau_{xx} = \frac{M_\infty}{Re_\infty} \frac{2}{3} \mu \left(2 \frac{\partial u}{\partial x} - \frac{\partial v}{\partial r} \right),$$

$$\tau_{rr} = \frac{M_\infty}{Re_\infty} \frac{2}{3} \mu \left(-\frac{\partial u}{\partial x} + 2 \frac{\partial v}{\partial r} \right),$$

$$\tau_{\theta\theta} = \frac{M_\infty}{Re_\infty} \frac{2}{3} \mu \left(-\frac{\partial u}{\partial x} - \frac{\partial v}{\partial r} + 2 \frac{v}{r} \right),$$

$$\tau_{xr} = \tau_{rx} = \frac{M_\infty}{Re_\infty} \mu \left(\frac{\partial u}{\partial r} + \frac{\partial v}{\partial x} \right),$$

$$\bar{\tau} = \frac{2}{3} \frac{M_\infty}{Re_\infty} \mu \frac{v^2}{r} + \frac{2}{3} r \frac{M_\infty}{Re_\infty} \frac{\partial}{\partial r} \left(\mu \frac{v^2}{r} \right) + \frac{2}{3} r \frac{M_\infty}{Re_\infty} \frac{\partial}{\partial x} \left(\mu \frac{uv}{r} \right), \quad (3)$$

and the heat flux terms are

$$q_x = -\frac{M_\infty}{Re_\infty} \frac{\mu}{Pr(\gamma-1)} \frac{\partial T}{\partial x},$$

$$q_r = -\frac{M_\infty}{Re_\infty} \frac{\mu}{Pr(\gamma-1)} \frac{\partial T}{\partial r}. \quad (4)$$

The molecular viscosity is calculated using Sutherland's law:

$$\mu = T^{3/2} \left(\frac{1 + 110.4/T_e}{T + 110.4/T_e} \right). \quad (5)$$

The Modified Low-Diffusion Flux-Splitting Scheme (MLDFSS), adopted in Lee and Park [11], is used to evaluate the inviscid fluxes on the cell surfaces. Central difference is used to calculate viscous terms. For time accurate calculations, we adopt the subiteration time advance scheme of Pulliam [12], which is formulated as

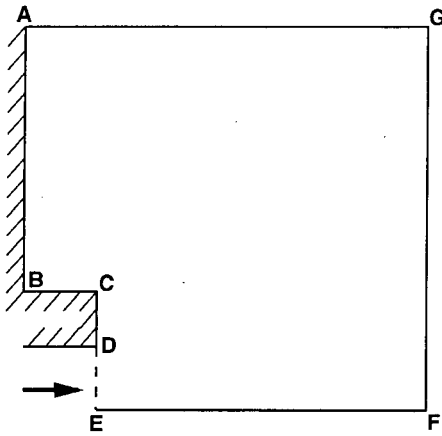


Fig. 3 The computational domain of circular pulse jets

steps: $\Delta t_1 = 0.003D/V_e$ and $\Delta t_2 = 0.0005D/V_e$. These two time steps correspond approximately to 0.0017 and 0.0003 times the pressure oscillation period. By scrutinizing the pressure oscillation patterns including the amplitude and the time period of the oscillation, we have found that Δt_1 is sufficient for unsteady analysis.

2.3 Validation

The use of the present code in predicting unsteady flowfield is validated against the unsteady circular pulse jet of Ishii et al. [13]. In this circular pulse jet, air is accelerated by a shock in a shock tube with a constant circular cross-section and exhausted from the open end into a test chamber. The jet strength was controlled by one parameter P_4/P_1 , where P_1 and P_4 were initial gas pressures in the low-pressure and high-pressure chambers, respectively. The computational domain is shown in Fig. 3. We employ a 600×400 grid system in axial and radial directions with the uniform mesh size of $\Delta x = \Delta y = 0.025$. On the outer boundary AG and the downstream boundary FG, the ambient gas condition is applied: $(P, \rho, u, v) = (P_1, \rho_1, 0, 0)$, where the subscript 1 denotes the ambient value. On the solid walls AB, BC, CD, we apply no slip condition and on the jet axis EF, the symmetric condition. On the upstream boundary DE, the shock condition $(P, \rho, u, v) = (P_E, \rho_E, u_E, 0)$ is applied, where the quantities denoted by the subscript E are obtained through the Rankine–Hugoniot relations for a specified shock Mach number. In accordance with the experiment, the length BC and CD were set to be equal to the duct radius DE ($=1$ cm). In the present validation experiment, we calculate two cases: $P_4/P_1 = 25$ ($P_E/P_1 = 3.61$) and $P_4/P_1 = 50$ ($P_E/P_1 = 5.00$). We compare the time change of the diameter D_M and the axial distance X_M of the Mach disks from the duct exit as shown in Fig. 4a and b. The present results are found to be in good agreement with those of Ishii et al.

Sakakibara and Iwamoto [10] compared the frequencies of the surface pressure from their computation of the

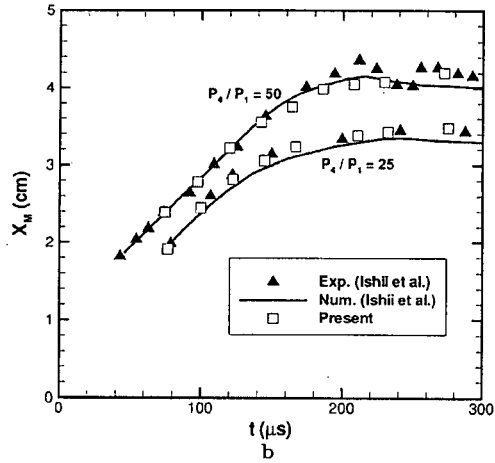
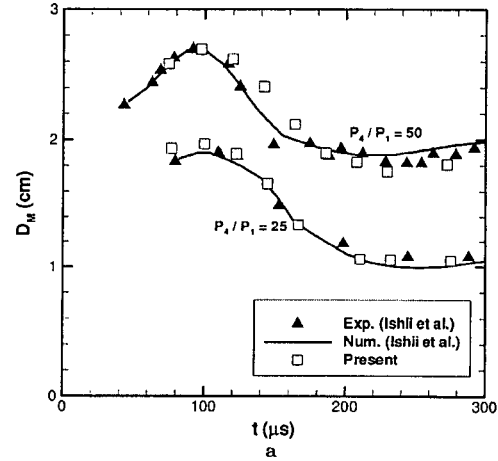


Fig. 4 Comparison with experimental data. (a) The diameter, D_M and (b) the axial distance, X_M of the unsteady Mach disk

supersonic impinging jet flow with those of the impinging tone from the measurement. For the purpose of comparison, the present calculation is done using the same operating condition of Sakakibara and Iwamoto, where the diameter of the convergent nozzle is 10 mm, and the nozzle pressure ratio is $P_0/P_a = 3.0$. The first task of the present analysis is to make sure that a self-sustained oscillation is indeed achieved. This is done by extending the computation time to over $300D/V_e$. Figure 5a gives a time history of pressure variation on the surface of the impinging plate. The flow is seen to have reached a self-sustained oscillatory state after a transient period of about $100D/V_e$. The frequencies of the surface pressure oscillations from the present computation are shown in Fig. 6. Figure 6 shows that the frequencies of the surface pressure oscillation of the present computation are in good accord with the impinging tones of the experimental measurements.

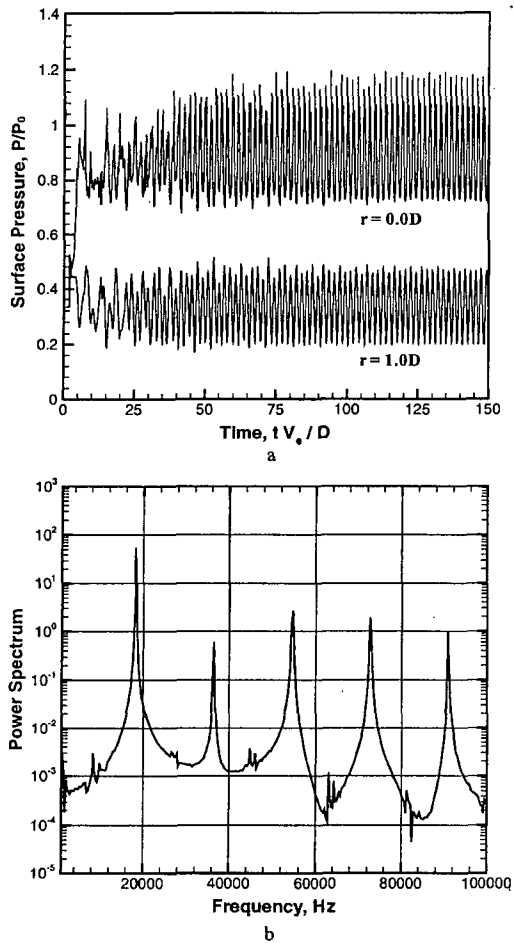


Fig. 5 (a) Surface pressure histories at $r/D = 0.0$ and 1.0 ; (b) power spectrum of pressure signal at $r/D = 0.0$, $H/D = 2.5$, and $P_0/P_a = 3.0$

3 Results and discussion

For impinging supersonic jet flows, important operating parameters that affect the flow characteristic are the nozzle pressure ratio ($NPR = P_0/P_a$) and the distance from the nozzle exit to the impinging plate (H). Therefore, the oscillatory features of surface pressure and the flow structural changes of the impinging jet flows are investigated by varying these two operating conditions.

3.1 Impinging jet flow oscillation: effect of nozzle-to-plate distance

First, we examine the oscillatory behavior of the flow by varying the distance from the nozzle to the plate (H) for a given pressure ratio. The nozzle-to-plate distance is varied from 2.0 to 4.0 times the nozzle exit diameter

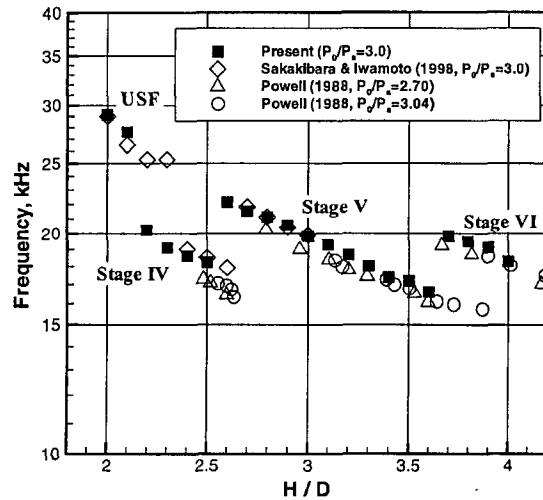


Fig. 6 Frequencies of the pressure oscillation and the impinging tones versus distance (USF stands for upper secondary frequency)

($H/D = 2.0-4.0$) with the nozzle pressure ratio fixed at $P_0/P_a = 3.0$. In this case, the nozzle chamber pressure and the nozzle exit pressure are 3.0 and 1.585 times larger than the ambient pressure, respectively. Thus, the jet is in an underexpanded condition. The jet issuing from the nozzle exit undergoes expansion and compression cycles repeatedly. The shock cell structures of the expansion fan and compression shock are disturbed by the impingement and hence exhibit periodic structural changes accompanying pressure oscillation.

To characterize the oscillatory behavior of the flow, power spectra of the surface pressures have been calculated (Fig. 5b). The frequency of the pressure oscillation was

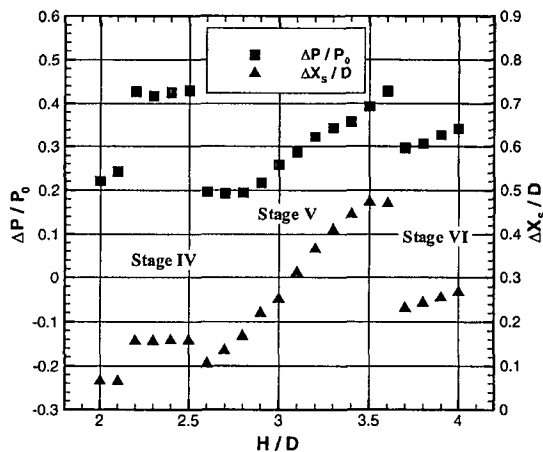


Fig. 7 The amplitudes of the surface pressure and the plate shock oscillations, $P_0/P_a = 3.0$ (ΔP is the amplitude of the pressure oscillation at $r/D = 0.0$, ΔX_s is the amplitude of the plate shock oscillation along the jet axis)

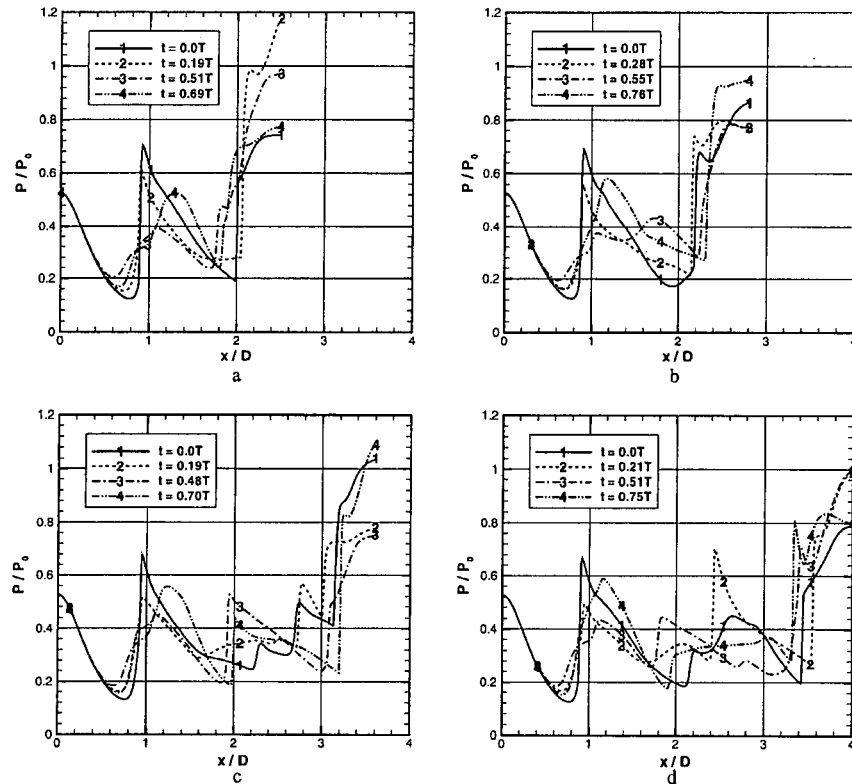


Fig. 8 Variation of pressure distribution along the jet axis, $P_0/P_a = 3.0$. (a) $H/D = 2.5$ in Stage IV; (b) $H/D = 2.8$ in Stage V; (c) $H/D = 3.6$ in Stage V; (d) $H/D = 4.0$ in Stage VI (T is the pressure oscillation period)

obtained through the FFT analysis of the time series of the surface pressure (using 4096 data, the sampling rate is about $0.03D/V_e \cong 0.84 \mu s$). The frequencies of the pressure oscillations at the center ($r/D = 0.0$) of the plate for various nozzle-to-plate distance ratios (H/D) are shown in Fig. 6. Powell [8] found that the impinging tones, referred to as the principal tones, formed a sawtooth pattern with at least, and probably more than, seven possible stages (labeled II through VIII) for the range of $H/D = 0.5-7.0$. Some separate tones were found to occur; these had the same general slope as the principal tones. These were called upper secondary tones in that they are not an integral part of the dominant sawtooth pattern. We see that Powell's findings are essentially demonstrated in Fig. 6. Figure 6 indicates that the frequency changes with a jump at a certain H/D at which the oscillation enters into a different stage. It is not yet clearly understood why this staging behavior occurs. This will be touched upon later in the present discussion. As shown in Fig. 6, the pressure oscillation frequency decreases smoothly as the distance from the nozzle to the plate increases within a specific range of H/D . The traveling time of a disturbance increases as the geometrical length of the feedback loop lengthens due to the increase of

the nozzle-to-plate distance. Thus, within a specific range of each stage the frequency of oscillation decreases as the distance increases. In the present computation, three stages labeled IV-VI and the upper secondary frequencies (the cases of $H/D = 2.0$ and 2.1) have been observed.

Figure 7 depicts how the amplitudes of the surface pressure and the plate shock excursions vary with H/D . The amplitude, ΔP in Fig. 7, denotes the difference between the maximum and the minimum pressure during the oscillation cycle. When a supersonic jet flow impinges perpendicularly on a flat plate, a strong normal shock, known as 'plate shock' or 'standoff shock', appears over the plate. In the oscillatory case, the plate shock moves up and down along the jet axis like a plane wave oscillation. The frequencies of the plate shock oscillations are identical with those of the surface pressure oscillations. The plate shock position, X_s , is measured from the impinging plate to the plate shock. The extent of plate shock position, ΔX_s , is also contained in Fig. 7. When $H/D = 2.5$, the flow oscillation is in Stage IV with relatively large amplitude and lower frequency. When $H/D = 2.6$, the oscillation jumps to Stage V. The frequency of oscillation increases abruptly to a much higher frequency while the amplitude of pressure

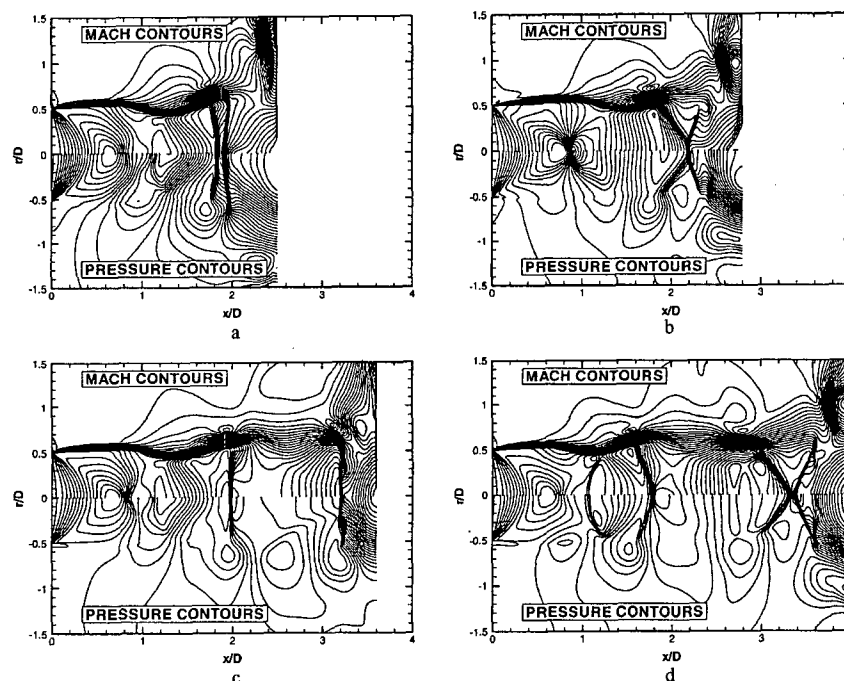


Fig. 9 Instantaneous flowfields for various H/D , $P_0/P_a = 3.0$. (a) corresponds to instant 4 of Fig. 8a; (b) to instant 1 of Fig. 8b; (c) to instant 4 of Fig. 8c; (d) to instant 3 of Fig. 8d

oscillation suddenly drops to about half of the amplitude of the case of $H/D = 2.5$. The amplitude of oscillation, however, increases again together with the frequency decrease as H/D increases. Beyond $H/D = 3.6$, the flow goes into Stage VI accompanying again the abrupt increase of frequency and the decrease of amplitude. We further find from Fig. 7 that the amplitude of pressure oscillation is in direct proportion of the plate shock motion, ΔX_s .

Not only does the plate shock oscillate, but also the jet flow structure changes periodically. We present instantaneous static pressure variations along the jet centerline in Fig. 8 for various cases. From Fig. 8, we find that the pressure distribution of the expansion region in the first cell from the nozzle, characterized by a monotonic decrease, does not vary with time for all the cases. However, the pressure distribution over the compression region in the first cell and the region beyond are seen to undergo significant changes with time. In Fig. 8, $t = 0.0T$ (marked by '1') refers to the instant when the pressure behind the first compression shock (near $x/D = 1.0$) becomes the largest, and the pressure distribution marked by '3' is the distribution at the instant when the pressure behind the first compression region becomes the smallest. Pressure distributions exhibited in all the figures suggest that the shock cell structures are continuously changing during the cycle of oscillation. As can be anticipated, we see that more cell structures are added as H/D increases. Figure 9 illustrates instantaneous flowfields corresponding to some of the pressure distribu-

tions given in Fig. 8. When H/D is small, the plate shock is located behind the second expansion region. During the oscillation, a 'double shock' structure is seen to appear as exemplified in the pressure distribution 4 of Figs. 8a and 9a. As H/D increases up to about 2.8, the second compression region following the second expansion region starts to appear during the oscillation (instant 1 of Figs. 8b and 9b). No 'double shock' structure is found in this case. When H/D increases further, the third and sometimes fourth expansion regions appear. The compression in this case may involve two normal shocks as seen in Fig. 9c. When H/D increases further beyond 3.6, a curved plate shock following the third or fourth expansion region is seen to appear (Fig. 9d). A scrutinization of Figs. 8 and 9 reveals that the 'staging' behavior is not precisely differentiated by the shock cell structure. In two consecutive stages (i.e., Stages IV and V, and Stages V and VI), we can always find very similar flow structures as viewed from the pressure distributions of Fig. 8. Further, we may find distinctly different structural patterns in the same stage as demonstrated in Fig. 8b and c.

It is reported by Powell [8] that the frequency ratio for each successive stage bears the ratio of successive pairs of integers; herein lies the rationale for the assignment of the stage number IV, V, VI, etc. In the present results, the frequency of $H/D = 2.5$ (18.2 kHz) in Stage IV almost bears the ratio 4:5 with that of $H/D = 2.6$ (22.2 kHz) in Stage V, and the frequencies of the cases of $H/D = 3.6$ in Stage V and 3.7 in Stage VI (16.6 and 19.8 kHz) give the

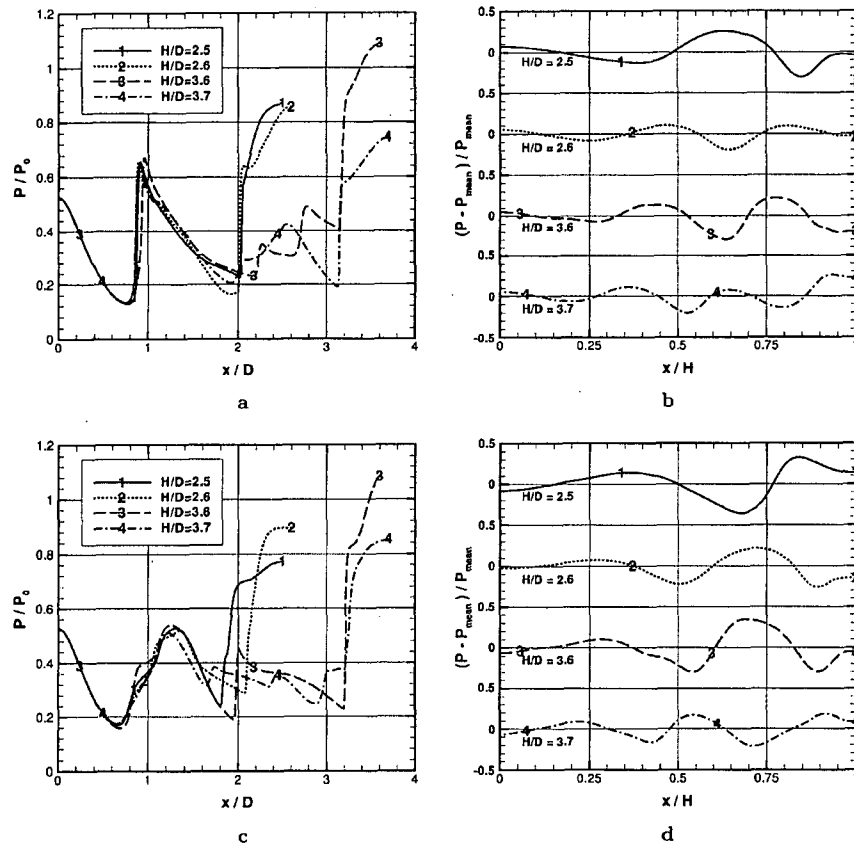


Fig. 10 Instantaneous pressure distributions for various H/D , $P_0/P_a = 3.0$. (a,c) along the jet center line; (b,d) along the $r = 0.75D$ line; (a), (b) correspond to instant 1 of Fig. 8; (c,d) to instant 4 of Fig. 8

ratio of integers 5:6. This reminds us of the behavior of the standing wave in an open-ended pipe. We thus examine the pressure distribution around the jet edge region where the jet interacts strongly with the ambient air. Figure 10 displays the pressure distribution along the $r = 0.75D$ line ($0.25D$ apart from the nozzle lip line) in juxtaposition with the pressure distributions along the jet centerline. Note that the pressure along $r = 0.75D$ line is normalized by the mean pressure of the corresponding pressure distribution. We find that the pressure distribution along $r = 0.75D$ line exhibits a similar pattern with a standing wave in an open-ended pipe. From Fig. 6, we have seen that the 'staging' occurs at around $H/D = 2.5$ and 3.6 : $H/D = 2.5$ belongs to Stage IV and $H/D = 2.6$ to Stage V; $H/D = 3.6$ to Stage V and $H/D = 3.7$ to Stage VI. Figure 10 indicates that the pressure distribution along $r = 0.75D$ line changes its pattern as H/D changes from 2.5 to 2.6, and 3.6 to 3.7, while the pressure distribution along the centerline shows no significant variations as H/D crosses these demarcation points. Further, the pressure distributions along $r = 0.75D$ line for $H/D = 2.6$ and 3.6 are of the same pattern signifying that these two cases belong to the same stage, while

the corresponding pressure distributions along the jet axis are entirely different each other as H/D values are widely apart. These observations lead us to conclude that the 'staging behavior' for H/D variation is directly correlated with the interaction of the jet with the ambient air occurring in the shear layer rather than with the jet shock cell structure.

3.2 Impinging jet flow oscillation: effect of nozzle pressure ratio

The nozzle pressure ratio, which is another important operating parameter, affects the flow characteristics: the shock cell structure in an underexpanded jet is also altered with the variation of the nozzle pressure ratio. Therefore, it is expected that the oscillatory features of the impinging jet are also affected by the nozzle pressure ratio at a given nozzle-to-plate distance. As the nozzle pressure ratio increases, the length of the first shock cell increases. Prandtl [14] derived the following formula for the length, Δ , of the first cell in an underexpanded jet issuing from a convergent nozzle.

$$\Delta/D = 1.2\sqrt{(P_0/P_a - 1.9)} \quad (7)$$

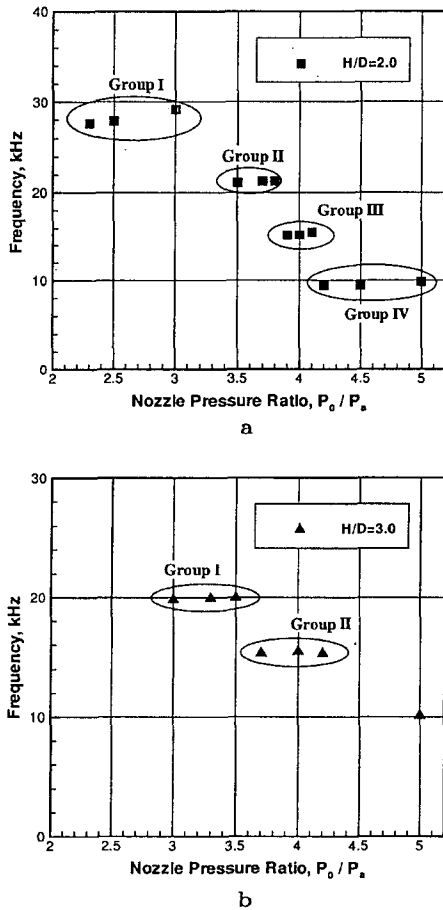


Fig. 11 Frequencies of the pressure oscillation with the nozzle pressure ratio variation. (a) $H/D = 2.0$; (b) $H/D = 3.0$

To investigate the effect of pressure ratio, we carry out computations for various nozzle pressure ratios. The nozzle pressure ratio (NPR = P_0/P_a) is varied from 2.0 to 5.0 with the nozzle-to-plate distance fixed either at $H/D = 2.0$ or 3.0. Frequency variation of the pressure oscillations in these cases is shown in Fig. 11. We see that the oscillation frequencies do not change with pressure ratio within a specific range of P_0/P_a in contrast to the case of the nozzle-to-plate distance variation shown in Fig. 6. However, the frequency goes through a step change at a certain pressure ratio exhibiting again 'staging' behavior. Krothapalli [7] investigated a choked underexpanded impinging jet issuing from a rectangular nozzle. The impinging tone frequency variation corresponding to the pressure ratio (P_0/P_a) from 2 to 5.8 at several fixed distances $H/W = 14, 21, 28$ (W is the width of the rectangular nozzle) also exhibited staging behavior similar to the one shown in Fig. 11.

Figure 12 displays the amplitudes of the surface pressure and the plate shock (or the shock closest to the plate) os-

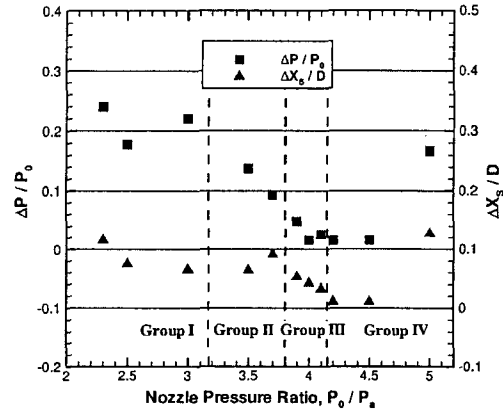


Fig. 12 Amplitudes of the surface pressure and the plate shock oscillations for $H/D = 2.0$ (ΔP is the amplitude of the pressure oscillation at $r/D = 0.0$, ΔX_s is the amplitude of the plate shock oscillation along the jet axis)

cillations for $H/D = 2.0$. In contrast to the corresponding patterns for the case of nozzle-to-plate distance variation (Fig. 7), ΔP and ΔX_s are found to be very irregular. We have also examined these variations for the case of $H/D = 3.0$ to find that they are likewise very irregular. This suggests that the flow structure may vary in a disorderly manner as the chamber pressure increases for a given H/D than that for the case of H/D variation for a given pressure ratio. To illustrate this point, we present typical flow structures for various pressure ratios in Fig. 13. At the pressure ratio of 2.5 the jet has two cells as seen in Fig. 13a. For the cases of Group II, only one cell appears and the plate shock is located at the end of the first cell (Fig. 13b). As the pressure ratio increases further, a strong normal shock (Mach disk) develops in the first cell. All of the cases in Groups III and IV have the Mach disk appearing in the first cell, as seen in Fig. 13c and d. The flow downstream of the Mach disk becomes subsonic, and therefore, no further shock (plate shock) appears. In these flows, the Mach disk oscillates and a large separation bubble is found to be present in the impinging region (Fig. 13c and d). Although Groups III and IV flows have quite different oscillation frequencies (Fig. 11a), they have rather similar flow structures. This rather drastic variation of flow structures including a large separation bubble explains why the amplitudes of pressure and shock oscillations (ΔP and ΔX_s) are so irregular as given in Fig. 12.

When $H/D = 3.0$, the flow structures become more versatile as there is more space available for adjustment when compared to the case of $H/D = 2.0$. For the pressure range of $P_0/P_a = 3.7-4.2$ (Group II in Fig. 11b), flow structures seen in Fig. 14 alternate during the oscillation cycle. Figure 14a illustrates an oblique shock with Mach disk at the center, and in Fig. 14b, we see no strong oblique shock and no Mach disk in the first cell. In this range, the plate shock is always present as demonstrated in Fig. 14. When the pressure ratio is increased further to $P_0/P_a = 4.4-4.6$, the change of the jet flow structure becomes even more drastic

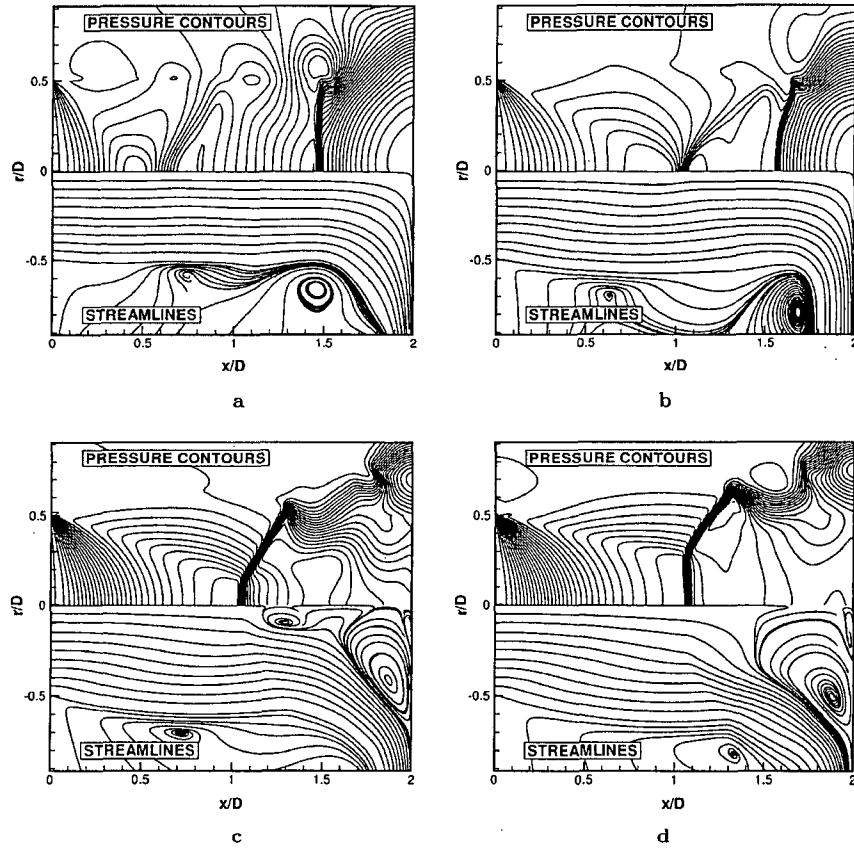


Fig. 13 Typical instantaneous flow structures and streamlines of the supersonic impinging jet for various nozzle pressure ratio, $H/D = 2.0$. (a) $P_0/P_a = 2.5$ in Group I; (b) $P_0/P_a = 3.5$ in Group II; (c) $P_0/P_a = 4.0$ in Group III; (d) $P_0/P_a = 5.0$ in Group IV

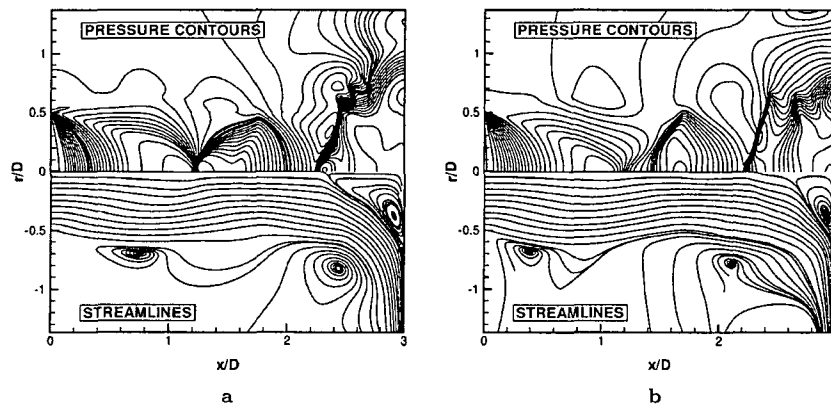


Fig. 14 Typical two instantaneous jet flow structures, $P_0/P_a = 4.0$, and $H/D = 3.0$

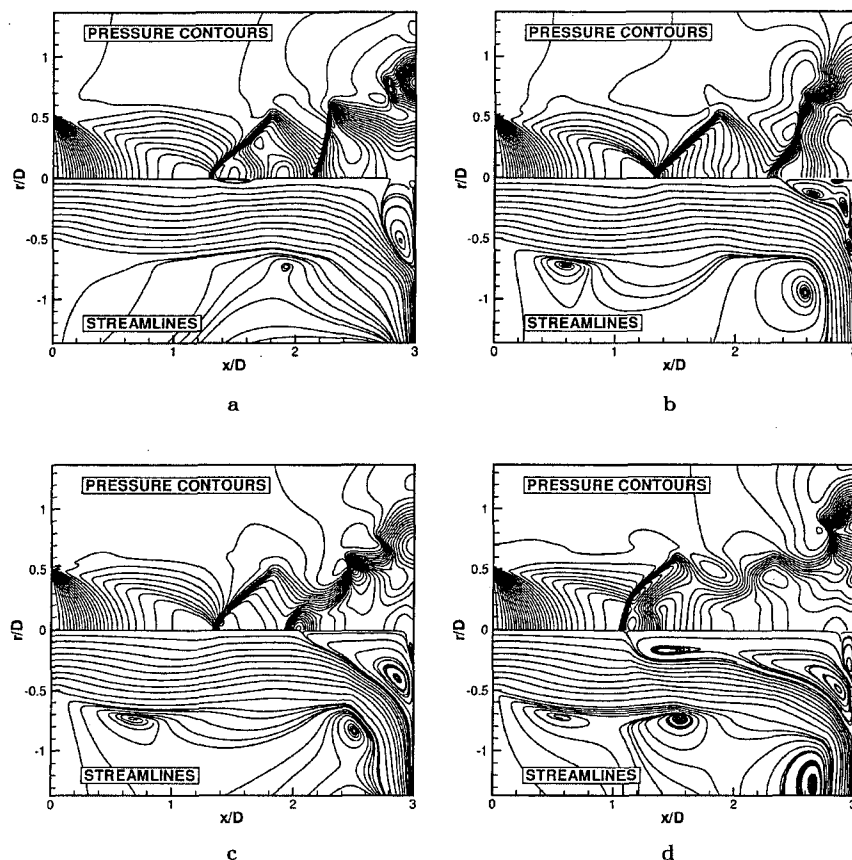


Fig. 15 Various instantaneous jet flow structures at various instants, $P_0/P_a = 4.5$, and $H/D = 3.0$

as seen in Fig. 15. In this case, no discernible oscillation frequency could be found (see Fig. 11b). A typical surface pressure oscillation and its power spectrum are given in Fig. 16c and d where no distinct characteristic frequency can be identified. It is interesting to note that characteristic oscillation frequencies were identified for these pressure ratios when $H/D = 2.0$ (see Fig. 11a). When the pressure ratio is increased to $P_0/P_a = 5.0$, a characteristic oscillation frequency reappeared as plotted in Fig. 11b. In this case, the compression shock with Mach disk was very strong so that no plate shock was observed.

3.3 Connection between the two staging behaviors of 3.1 and 3.2

We now seek for a relation between the staging behaviors for the case of distance variation at a fixed pressure ratio and for the case of pressure variation at a fixed distance. These two distinct staging behaviors are presented in Figs. 6

and 11. At a given pressure ratio, the number of shock cells may increase if the nozzle-to-plate distance increases. At a given nozzle-to-plate distance, if the pressure ratio decreases then the length of the first shock cell will decrease as given by (7). Accordingly, the number of shock cells may increase. This qualitative argument suggests that the length of the first shock cell may serve well as the characteristic length. Henderson [15] also used the first shock cell length, Δ , as the reference length in her study of acoustics of the supersonic impinging jet. Figure 17 displays mean pressure distributions for various cases with the axial distance normalized by the length of the first shock cell, Δ , defined by (7). We see that the mean pressure distributions for pressure variation and those for distance variation exhibit somewhat similar features. The frequency of the surface pressure oscillation is re-plotted in Fig. 18. The frequency is non-dimensionalized by Δ/C_a , C_a being the speed of sound at the ambient condition. The circle and triangle symbols represent the data for the case of pressure variations at a fixed distance, and the rectangle symbols correspond to the

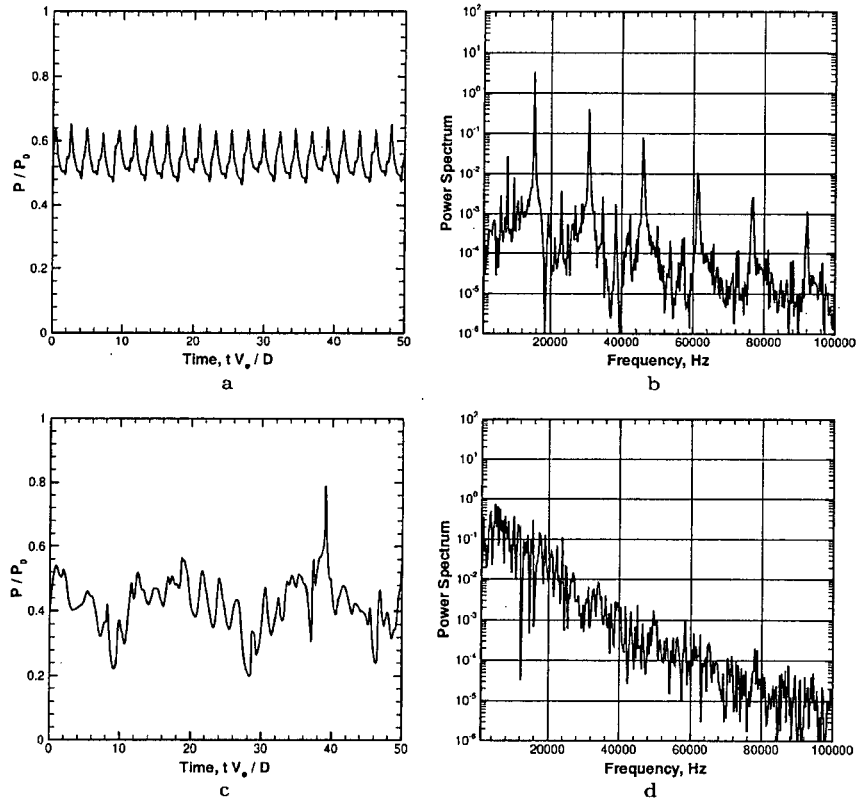


Fig. 16 (a,c) Surface pressure histories and (b,d) power spectrum of the pressure signal at $r/D = 0.0$ and $H/D = 3.0$. (a,b) $P_0/P_a = 4.2$ in Group II; (c,d) $P_0/P_a = 4.5$

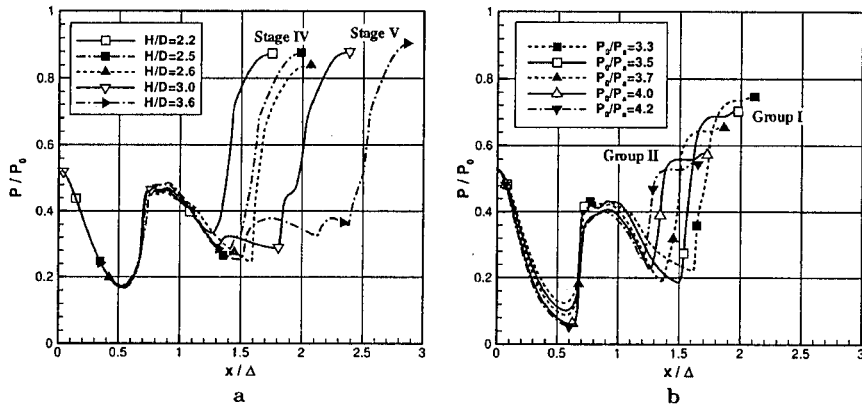


Fig. 17 Mean pressure distributions along the jet axis. (a) case of distance variation and fixed pressure, $P_0/P_a = 3.0$; (b) case of pressure variation and fixed distance, $H/D = 3.0$

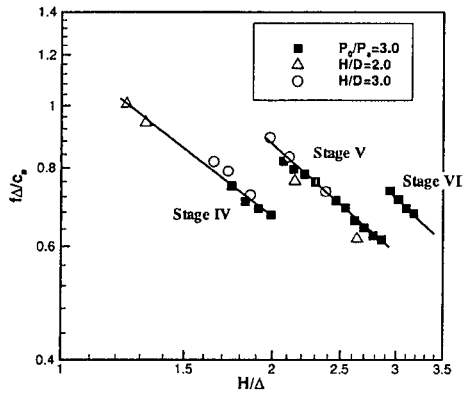


Fig. 18 Normalized frequency–distance characteristics (square, distance variation; triangle and circle, pressure variation)

case of distance variation at a fixed pressure ratio. We find from Fig. 18 that the frequency characteristics for the two cases match very well each other. In Sect. 3.1, we have discussed the staging behavior in terms of the pressure wave pattern in the jet shear layer. To confirm this further, we plot the pressure distributions along the $r = 0.75D$ line for the cases of the pressure variation and the distance variation in Fig. 19. Note that the dotted-line pressure curves have a different scale to effectively present the pressure wave pattern. Figure 19 evidently elucidates that the pressure wave pattern in the jet shear layer characterizes the staging behavior for both cases. This leads us to confirm again that the staging behavior is not due to the jet shock cell structure.

4 Conclusion

By using the axisymmetric unsteady Navier–Stokes system, the oscillatory features of the surface pressure and the flow structural change of supersonic impinging jet are investigated by varying the nozzle-to-plate distance ratio (H/D) and the nozzle pressure ratio (P_0/P_a). For both cases, the frequency of the surface pressure oscillation is found to exhibit ‘staging’ behavior; the frequency does not vary smoothly with either the distance or the pressure ratio. The frequency jumps discontinuously at a specific value of H/D or P_0/P_a . The staging behavior with the distance variation is in good agreement with the previous studies. The staging behavior with the pressure variation in which the oscillation frequency undergoes a step change when the pressure ratio crosses a specific value is different from that of the distance variation in the sense that the frequency of the surface pressure oscillation remains constant in a given stage. These two seemingly very different staging behaviors of the frequency can be correlated well if the frequency and the nozzle-to-plate distance are normalized by the length of the first shock cell and the speed of sound at the ambient condition. The staging behavior for both cases are found to

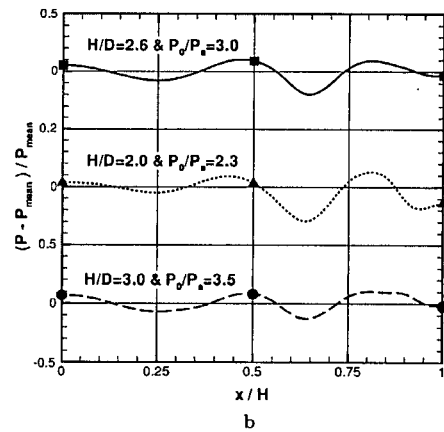
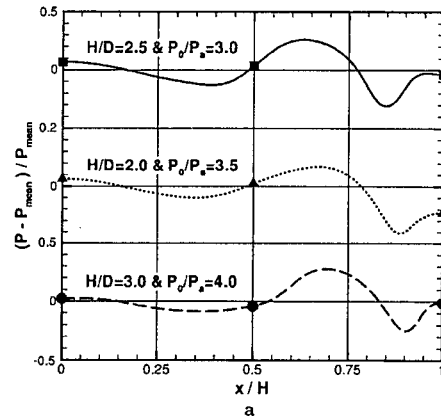


Fig. 19 Patterns of the instantaneous pressure distribution along the $r = 0.75D$ line. (a) pattern of Stage IV; (b) pattern of Stage V (square, the case of distance variation; triangle and circle, the case of pressure variation)

be caused by the interaction of the jet shear layer with the ambient air as evidenced by the pressure wave pattern in the jet edge region but not by the jet shock cell structure.

Acknowledgements This work was financially supported in part by the Agency for Defense Development and by the Brain Korea 21 project from the Ministry of Education, Korea. Constructive criticism and suggestions from the reviewers are also acknowledged.

Nomenclature

C	speed of sound
D	nozzle exit diameter ($= 2R$)
e_t	total energy
f	frequency
H	distance from nozzle exit to impinging plate
P	pressure
r	radial coordinate
t	time

T	temperature, oscillation period
u	velocity in x direction
v	velocity in r direction
V	velocity, $\sqrt{u^2 + v^2}$
x	axial coordinate
X_s	distance from the plate to the plate shock
μ	viscosity
γ	specific heat coefficient
Δ	length of the first shock cell

Subscripts

0	chamber condition, total properties
a	ambient condition
e	properties at the nozzle exit
v	viscous term

References

1. Donaldson, C.D., Snedeker, R.S.: A study of free jet impingement. Part 1. Mean properties of free and impinging jets. *J. Fluid Mech.* **45**, 281–319 (1971)
2. Ginzberg, I.P., Semilentenko, B.G., Terpigorev, V.S., Uskov, V.N.: Some singularities of supersonic underexpanded jet interaction with a plane obstacle. *J. Eng. Phys.* **19**, 1081–1084 (1973)
3. Carling, J.C., Hunt, B.L.: The near wall jet of a normally impinging, uniform, axisymmetric, supersonic jet. *J. Fluid Mech.* **66**, 159–176 (1974)
4. Kalghatgi, G.T., Hunt, B.L.: The occurrence of stagnation bubbles in supersonic jet impingement flows. *Aero. Quart.* **27**, 169–185 (1976)
5. Lamont, P.J., Hunt, B.L.: The impingement of underexpanded axisymmetric jets on perpendicular and inclined flat plates. *J. Fluid Mech.* **100**, 471–511 (1980)
6. Alvi, F.S., Iyer, K.G.: Mean and unsteady flowfield properties of supersonic impinging jets with lift plates. AIAA Paper 99-1829 (1999)
7. Krothapalli, A.: Discrete tones generated by an impinging underexpanded rectangular jet. *AIAA J.* **23**, 1910–1915 (1985)
8. Powell, A.: The sound-producing oscillations of round underexpanded jets impinging on normal plates. *J. Acoust. Soc. Am.* **83**, 515–533 (1988)
9. Tam, C.K.W., Ahuja, K.K.: Theoretical model of discrete tone generation by impinging jets. *J. Fluid Mech.* **214**, 67–87 (1990)
10. Sakakibara, Y., Iwamoto, J.: Numerical study of oscillation mechanism in underexpanded jet impinging on plate. *J. Fluids Eng.* **120**, 477–481 (1998)
11. Lee, C.H., Park, S.O.: Computations of hypersonic flows over blunt body using a modified low-diffusion flux-splitting scheme. *CFD J.* **10**, 490–500 (2002)
12. Pulliam, T.H.: Time accuracy and the use of implicit methods. AIAA Paper 93-3360 (1993)
13. Ishii, R., Fujimoto, H., Hatta, N., Umeda, Y.: Experimental and numerical analysis of circular pulse jets. *J. Fluid Mech.* **392**, 129–153 (1999)
14. Prandtl, L.: Über die stationären Wellen in Einem Gasstrahle. *Phys. Z.* **5**, 599–601 (1904)
15. Henderson, B.: The connection between sound production and jet structure of the supersonic impinging jet. *J. Acoust. Soc. Am.* **111**, 735–747 (2002)



Computation of Tone Noise From Supersonic Jet Impinging on Flat Plates

Ching Y. Loh
Taitech, Inc., Beavercreek, Ohio

The NASA STI Program Office . . . in Profile

Since its founding, NASA has been dedicated to the advancement of aeronautics and space science. The NASA Scientific and Technical Information (STI) Program Office plays a key part in helping NASA maintain this important role.

The NASA STI Program Office is operated by Langley Research Center, the Lead Center for NASA's scientific and technical information. The NASA STI Program Office provides access to the NASA STI Database, the largest collection of aeronautical and space science STI in the world. The Program Office is also NASA's institutional mechanism for disseminating the results of its research and development activities. These results are published by NASA in the NASA STI Report Series, which includes the following report types:

- **TECHNICAL PUBLICATION.** Reports of completed research or a major significant phase of research that present the results of NASA programs and include extensive data or theoretical analysis. Includes compilations of significant scientific and technical data and information deemed to be of continuing reference value. NASA's counterpart of peer-reviewed formal professional papers but has less stringent limitations on manuscript length and extent of graphic presentations.
- **TECHNICAL MEMORANDUM.** Scientific and technical findings that are preliminary or of specialized interest, e.g., quick release reports, working papers, and bibliographies that contain minimal annotation. Does not contain extensive analysis.
- **CONTRACTOR REPORT.** Scientific and technical findings by NASA-sponsored contractors and grantees.
- **CONFERENCE PUBLICATION.** Collected papers from scientific and technical conferences, symposia, seminars, or other meetings sponsored or cosponsored by NASA.
- **SPECIAL PUBLICATION.** Scientific, technical, or historical information from NASA programs, projects, and missions, often concerned with subjects having substantial public interest.
- **TECHNICAL TRANSLATION.** English-language translations of foreign scientific and technical material pertinent to NASA's mission.

Specialized services that complement the STI Program Office's diverse offerings include creating custom thesauri, building customized databases, organizing and publishing research results . . . even providing videos.

For more information about the NASA STI Program Office, see the following:

- Access the NASA STI Program Home Page at <http://www.sti.nasa.gov>
- E-mail your question via the Internet to help@sti.nasa.gov
- Fax your question to the NASA Access Help Desk at 301-621-0134
- Telephone the NASA Access Help Desk at 301-621-0390
- Write to:
NASA Access Help Desk
NASA Center for Aerospace Information
7121 Standard Drive
Hanover, MD 21076



Computation of Tone Noise From Supersonic Jet Impinging on Flat Plates

Ching Y. Loh
Taitech, Inc., Beavercreek, Ohio

Prepared for the
43rd Aerospace Sciences Meeting and Exhibit
sponsored by the American Institute of Aeronautics and Astronautics
Reno, Nevada, January 10-13, 2005

Prepared under Contract NAS3-03072

National Aeronautics and
Space Administration

Glenn Research Center

Acknowledgments

This work received support from the Quiet Aircraft Technology Project Office of NASA Glenn Research Center. Fruitful discussion with Dr. Lennart S. Hultgren and the careful reviewing of the paper by Drs. R.A. Blech and J. Bridges are cordially acknowledged.

This report contains preliminary findings, subject to revision as analysis proceeds.

Available from

NASA Center for Aerospace Information
7121 Standard Drive
Hanover, MD 21076

National Technical Information Service
5285 Port Royal Road
Springfield, VA 22100

Available electronically at <http://gltrs.grc.nasa.gov>

COMPUTATION OF TONE NOISE FROM SUPERSONIC JET IMPINGING ON FLAT PLATES

Ching Y. Loh
Taitech, Inc.
Beavercreek, Ohio 45430

Abstract

A supersonic jet impinging normally on a flat plate has both practical importance and theoretical interests. The physical phenomenon is not fully understood yet. Research concentrates either on the hydrodynamics (e.g. lift loss for STOVL) or on the aeroacoustic loading.

In this paper, a finite volume scheme—the space-time conservation element and solution element (CE/SE) method—is employed to numerically study the near-field noise of an underexpanded supersonic jet from a converging nozzle impinging normally on a flat plate. The numerical approach is of the MILES type (monotonically integrated large eddy simulation). The computed results compare favorably with the experimental findings.

1 Introduction

High speed impinging jets are important to aircraft industry. For vertical landing and short take-off (STOVL) airborne vehicles propelled by jet engines, there are undesirable and adverse effects from the impinging jets. These include up to 60% lift loss and the acoustic loading and noises generated by a feedback loop between the jet and the ground.

Research on jet impinging normally on a flat plate has unfolded in a broad way. Some researchers concentrate on the hydrodynamics and investigate the lift loss, other researchers focus on the sound produced and the aeroacoustic loading of the impinging jets. There are a vast number of papers published on these topics. For example, after careful observations over the experimental data, Powell [1] pointed out that the small instability waves (vortices) around the jet shear layers and the consequent radial wall jet are responsible for the noise as they interact with the flat plate and produce sound waves. Ho and Nosseir [2] explained the feedback loop in the impinging jets; while Tam and Ahuja [3] put forward another

theoretical model for the acoustic feedback loop. In the meantime, experimentalists are conducting various physical experiments in search for the feedback mechanism in different impinging jet situations. Alvi and Iyer [9] studied the impinging jet with lift plate, Krothapalli *et al* [8] investigate both the jets with convergent nozzle and convergent-divergent (C-D) nozzles. Henderson *et al* [4-7] performed experiments of sound producing impinging jets on small and large plates.

Numerical simulations of unsteady impinging jets have also been carried out. Kim and Park [10] used the popular TVD upwind scheme. Sakakibara and Iwamoto [11] also used TVD scheme to study oscillations in impinging jets and the generation of acoustic waves.

In the present paper, a MILES (monotonically integrated large eddy simulation) type scheme is used to investigate the problem of a jet impinging on a flat plate. The MILES approach appears somewhat similar to LES, but there is no explicit filtering since the cell-averaging process is already equivalent to spatial filtering. Due to certain built-in numerical dissipation in a MILES finite volume scheme, the SGS (subgrid scale) model is not needed. The recent space-time conservation element and solution element method (CE/SE) [12-13] is a MILES type finite volume method with generally less numerical dissipation and is adopted for the computation. As demonstrated in previous papers, the CE/SE scheme is well suited for aeroacoustics computation [15,16]. Because of the CE/SE non-reflecting boundary conditions (NRBC), which are based on the physics of plane wave propagation [14], a smaller near field computational domain can be used in the present numerical simulation and helps to save both memory and CPU time.

The governing equations and the 2-D axisymmetric unstructured Navier-Stokes (N-S) CE/SE scheme used here is briefly reviewed in Section 2. Section 3 illustrates the noise problems of an impinging jet on normal flat plates, both large and small, with the initial and boundary conditions. The numerical results are presented and

compared to available experimental findings [4 - 7] in Section 4. Concluding remarks are drawn in Section 5.

2 The Governing Equations and the Unstructured Axisymmetric CE/SE Navier-Stokes Solver

As our main concern lies in the aeroacoustical behaviors of the impinging jets which remain axisymmetric in the problems under investigation according to the experimental results [4 - 7], it is appropriate to adopt and solve the axisymmetric Navier-Stokes equation system.

2.1 Conservation Form of the Unsteady Axisymmetric Navier-Stokes Equations

Consider a dimensionless conservation form of the unsteady axisymmetric Navier-Stokes equations of a perfect gas. Let ρ , u , v , p , and γ be the density, streamwise velocity component, radial velocity component, static pressure, and constant specific heat ratio, respectively. The axisymmetric Navier-Stokes equations then can be written in the following vector form:

$$U_t + F_x + G_y = Q, \quad (1)$$

where x , $y \geq 0$, and t are the streamwise and radial coordinates and time, respectively. The conservative flow variable vector U and the flux vectors in the streamwise and radial directions, F and G , are given by:

$$U = \begin{pmatrix} U_1 \\ U_2 \\ U_3 \\ U_4 \end{pmatrix}, \quad F = \begin{pmatrix} F_1 \\ F_2 \\ F_3 \\ F_4 \end{pmatrix}, \quad G = \begin{pmatrix} G_1 \\ G_2 \\ G_3 \\ G_4 \end{pmatrix},$$

with

$$U_1 = \rho, \quad U_2 = \rho u, \quad U_3 = \rho v, \\ U_4 = p/(\gamma - 1) + \rho(u^2 + v^2)/2.$$

The flux vectors are further split into inviscid and viscous fluxes:

$$F = F_i - F_v, \quad G = G_i - G_v,$$

where the subscripts i and v denote 'inviscid' and 'viscous' respectively. Details of these terms can be found in e.g. [17, 16].

The right hand source term Q is the same as in the axisymmetric Euler equations [17, 16]:

$$Q = \begin{pmatrix} Q_1 \\ Q_2 \\ Q_3 \\ Q_4 \end{pmatrix},$$

where

$$Q_1 = -U_3/y, \quad Q_2 = -U_2U_3/U_1y,$$

$$Q_3 = -U_3^2/U_1y, \quad Q_4 = -G_4/y.$$

By considering (x, y, t) as coordinates of a three-dimensional Euclidean space, E_3 , and using Gauss' divergence theorem, it follows that Eq. (1) is equivalent to the following integral conservation law:

$$\oint_{S(V)} H_m \cdot dS = \int_V Q_m dV, \quad m = 1, 2, 3, 4, \quad (2)$$

where $S(V)$ denotes the surface around a volume V in E_3 and $H_m = (F_m, G_m, U_m)$.

2.2 Treatment of the Source Term

The treatment is identical to the one used in [17] and is briefly reiterated here. Since the source term Q itself is a function of the unknown U , a local iterative procedure is needed to determine U . The discretized integral equation (2) reduces to the form

$$U - Q(U)\Delta t = U_H, \quad (3)$$

where U_H is the local homogeneous solution ($Q = 0$ locally). Note that U_H only depends on the solution at the previous time step, i.e., U_H is obtained using explicit formulas. A Newton iterative procedure to determine U is then

$$U^{(i+1)} = U^{(i)} - \left(\frac{\partial \Phi}{\partial U}\right)^{-1}[\Phi(U^{(i)}) - U_H],$$

where i is the iteration number and

$$\Phi(U) = U - Q(U)\Delta t.$$

Normally, U at the previous time step is a good initial guess $U^{(0)}$ and the procedure takes about 2-3 iterations to converge. The Jacobian matrix is given by

$$\frac{\partial \Phi}{\partial U} = \begin{pmatrix} 1 & 0 & \frac{\Delta t}{y} & 0 \\ -\frac{U_2U_3\Delta t}{U_1^2y} & 1 + \frac{U_3\Delta t}{U_1y} & \frac{U_2\Delta t}{U_1y} & 0 \\ -\frac{U_3^2\Delta t}{U_1^2y} & 0 & 1 + \frac{U_3\Delta t}{U_1y} & 0 \\ A_1 & A_2 & A_3 & 1 + \frac{\gamma U_3\Delta t}{2U_1y} \end{pmatrix}$$

where

$$A_1 = -\frac{U_3\Delta t}{U_1y} \left[\gamma U_4 - \frac{(\gamma - 1)(U_2^2 + U_3^2)}{U_1} \right],$$

$$A_2 = -(\gamma - 1) \frac{U_2U_3\Delta t}{U_1^2y},$$

$$A_3 = \frac{\Delta t}{y} \left[-\frac{\gamma - 1}{2} \frac{U_2^2 + 3U_3^2}{U_1^2} + \frac{\gamma U_4}{U_1} \right].$$

The inverse of the Jacobian, i.e., $\left(\frac{\partial \Phi}{\partial U}\right)^{-1}$ can easily be derived analytically for this particular case, thus, leading to a savings in CPU time.

2.3 Review of the CE/SE Numerical Scheme

The space-time conservation element and solution element (CE/SE) method is a recently developed finite volume method, with second order accuracy in both space and time. Here, CE (conservation element) stands for a control volume or cell, while SE (solution element) stands for the cell interfaces. Despite its nominal second order accuracy, the scheme may offer high resolution, lower dissipation and dispersion errors [12, 13]. As a result of the following advantageous features, the CE/SE scheme is chosen as the numerical tool for computation:

1. conservation in both space and time, the integral equations of conservation laws are literally solved;
2. only a compact cell stencil is needed, (hence both the conservative variables U and their gradients U_x, U_y are unknowns);
3. careful and accurate surface flux calculation;
4. truly multi-dimensional, simple but effective non-reflecting boundary conditions (NRBC);
5. effortless implementation of computation, no numerical fix or parameter choice is needed;
6. the scheme is of MILES type (monotonically integrated large eddy simulation), the finite volume cell-averaging plays a role of filter, while the van Albada limiter plays a role similar to a SGS model.
7. naturally adapted to unstructured grid, robust enough to cover a wide spectrum of compressible flow: from weak linear acoustic waves to strong, discontinuous waves (shocks), appropriate for both CFD (computational fluid dynamics) and CAA (computational aeroacoustics).

With an unstructured grid, the CE/SE scheme is easily adapted to complicated geometries. More details about the unstructured CE/SE method can be found in [13]. The weighted $a - \epsilon$ CE/SE scheme is used here.

3 The Impinging Jet Problem

When a supersonic underexpanded jet impinges normally on a flat plate, some shock cell structure is formed, and near the flat plate a stand-off or plate shock appears. As the jet flow approaches the plate, it is turned into a radial wall jet (Fig. 1). Then it is believed that the instability waves or vorticities generated in the jet shear layer interact with the plate and produce acoustic waves. As these acoustic waves propagate upstream to the nozzle exit where the shear layer receptivity is the highest, they trigger a new cycle of instability waves and thus complete the feedback loop.

The impinging jet problems are set up following the configuration in Henderson's experiment [4 - 7]. The

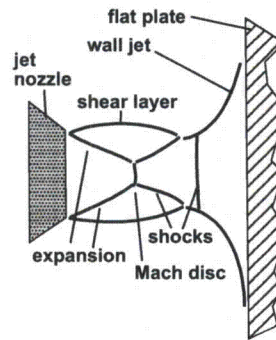


Figure 1: A sketch of the impinging jet problem.

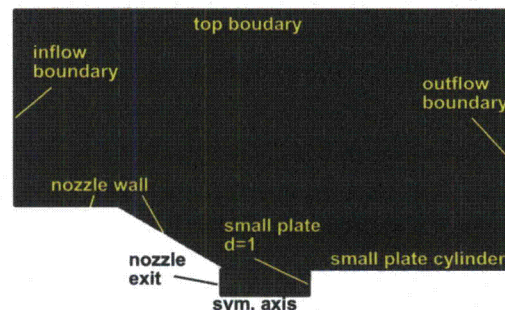


Figure 2: Typical computational domain for impinging jet nozzle exit.

ambient density ρ_0 , the ambient speed of sound and the diameter of the nozzle exit are chosen as the scales for density, velocity and length. The computational domain includes a near field of the flow. Figure 2 and 3 show typical computational domains for the current impinging jet problems. As the flow is considered as axisymmetric, the two-dimensional computational domains are half of the axial section of the corresponding 3-D domains. In the case of a small plate with diameter d , equal to D , the domain ranges from $x = -3$ to $x = 7$ (sponge/buffer zone not included) in the stream direction; while in the case of a large plate, the domain ranges from $x = -2$ to $x = 3.4$ or $x = 4.5$ with the nozzle exit always located at $x = 2$. The axial location of the end flat plate depends on the ratio of h/D . Here $h/D=1.4$ and 2.5 . Typically, there about 35,000 to 40,000 triangulated cells in the domain. They are formed by dividing a rectangle cell diagonally into four pieces, as shown in Fig. 2 and 3. In the area critical to aeroacoustic feedback loop around the jet core, the grid sizes are $\Delta x = 0.05$ and $\Delta r = 0.025$ to ensure enough resolution.

3.1 Initial Conditions

Initially, the flow of the entire domain is set at the ambient flow conditions, *i.e.*, (using nondimensional variables)

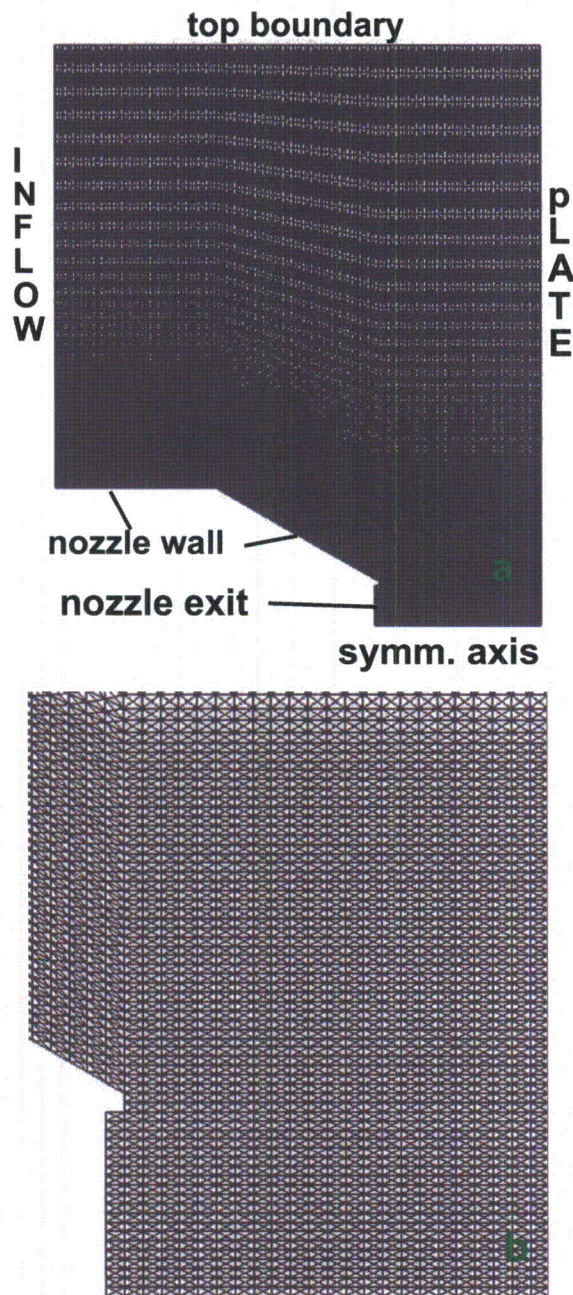


Figure 3: a: Typical computational domain and grid (with buffer/sponge zone at the top) for a large end plate; b: an enlargement of the grid around the nozzle exit.

$$\rho_a = 1, \quad p_a = \frac{1}{\gamma}, \quad u_a = 0, \quad v_a = 0.$$

here, the subscript a stands for 'ambient'.

3.2 Boundary Conditions

At the inlet boundary, the conservative flow variables and their spatial derivatives are specified to be those of the ambient flow, except at the nozzle exit, where an elevated pressure is imposed, *i.e.*, the jet is underexpanded, as in the experiments. As the jet flow at the nozzle exit is choked ($M_e = 1$), and the ratio of stagnation (plenum) pressure p_0 to the ambient pressure p_a , $NPR = p_0/p_a = 4.03$, by using the ideal gas isentropic relations, it follows that

$$\frac{p_0}{p_e} = \left[\frac{\gamma + 1}{2} \right]^{\frac{\gamma}{\gamma-1}} = 1.893, \quad \text{or} \quad p_e = 2.1289p_a$$

Other nondimensional flow variables at the nozzle exit, with $M_e = 1$ (choked flow with convergent nozzle), are given by

$$\rho_e = \frac{\gamma(\gamma + 1)p_e}{2T_r},$$

$$u_e = \left(\frac{2T_r}{\gamma + 1} \right)^{1/2}, \quad v_e = 0,$$

where T_r is the reservoir (plenum) temperature. We will also follow the experimental cold-flow condition where the reservoir temperature equals the ambient one, *i.e.*, $T_r = 1$.

At the symmetry axis, *i.e.*, $y = 0$, a simple reflective boundary condition is applied. At the top boundary, the Type I CE/SE non-reflecting boundary conditions as described in the next subsection are imposed. The no-slip boundary condition is applied on the nozzle walls and the end plate.

3.3 Non-Reflecting Boundary Conditions

As the spatial derivatives of the conservative flow variables are also considered as unknowns, the CE/SE scheme supports a simple but robust non-reflecting boundary condition (NRBC). Details and proof of the new NRBC can be found in [14]. The following is the Type I NRBC employed in this paper.

For a grid node (j, n) lying at the outer radius of the domain the non-reflective boundary condition (Type I) requires that

$$(U_x)_j^n = (U_y)_j^n = 0,$$

while U_j^n is kept fixed at the initial steady boundary value. At the downstream outflow boundary, the non-reflective boundary condition (Type II) requires that

$$(U_x)_j^n = 0,$$

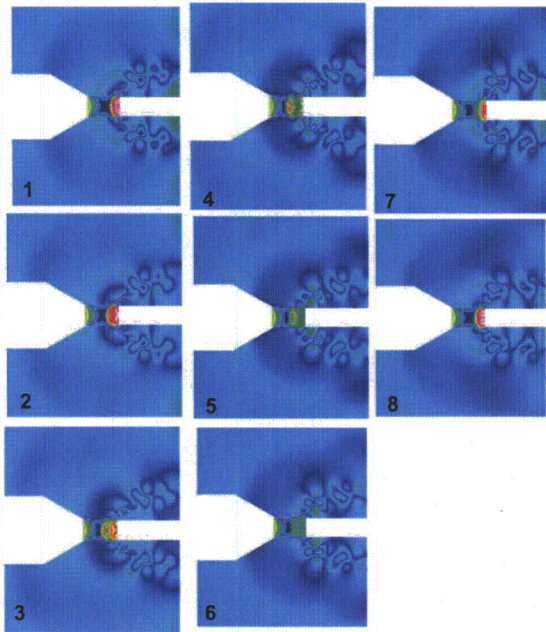


Figure 4: Plots 1-8: isobars at different time steps in a cycle, showing oscillations of the shock cell, the plate shock, the radiating acoustic waves and the vortices in the wakes in the small plate case.

while U_j^n and $(U_y)_j^n$ are now defined by simple extrapolation from the nearest interior node j' , *i.e.*,

$$U_j^n = U_{j'}^{n-1} \quad (U_y)_j^n = (U_y)_{j'}^{n-1}.$$

As will be observed later, these NRBCs, when combined with the buffer zone, are robust enough to allow a clean near field computation without disturbing or distorting the flow and acoustic fields.

4 Numerical Results

As sketched in Fig. 1, when the jet hits the plate, a radial wall jet is formed along with the instability waves. It is believed that when the instability waves interact with the flat plate and generate acoustic waves that propagate upstream via either the jet shear layer or the jet exterior to the nozzle lip and complete the acoustic feedback loop. In this section, the cases of a small plate and a large plate are considered.

4.1 Jet Impinging on a Small Plate

Consider a supersonic underexpanded jet from a convergent nozzle. With a small plate of diameter d placed downstream of the jet nozzle exit, the free jet becomes an impinging jet. The small plate is indeed a solid circular cylinder aligned with the nozzle axis. According to the experiment [5], the small plate has a diameter $d=D$ and the distance between the jet nozzle exit to the plate is

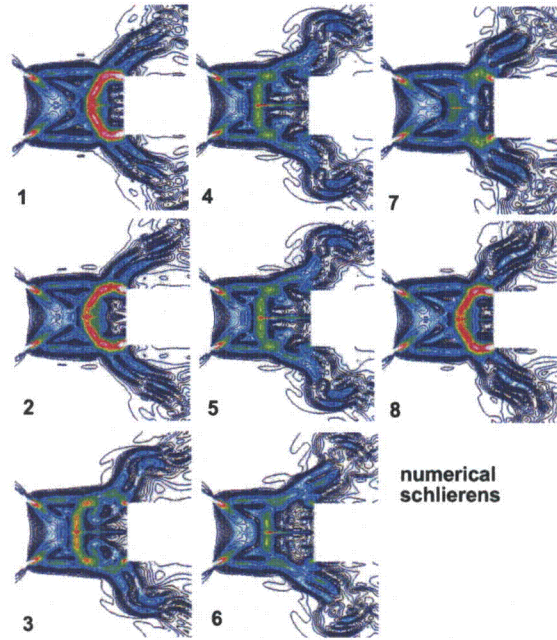


Figure 5: Plots 1-8: numerical schlierens showing the cyclic movements of the shock cell and plate shock.

$h=1.65D$, where $D=2.54$ cm is the jet diameter at nozzle exit. The ratio of stagnation pressure to ambient pressure is set at $NPR = 4.03$.

4.1.1 The unsteady oscillating flow Figure 4 illustrates the isobars at different time steps in about a cycle, after 1.47 million steps were already run. It is clearly displayed that the toroidal instability vortical waves grow along the jet shear layer upstream of the plate cylinder, and then interact with the bow shock (plate shock) and more importantly with the edge of the plate cylinder. The vortices are deflected and convect downstream with the flow, while the interaction generates acoustic waves that propagate in the field. As the waves reach the nozzle exit lip, where the receptivity is the highest, another cycle of vortices is triggered and the feedback loop is thus completed. In our view, the situation is somewhat similar to the feedback loop of a high speed cavity noise problem, although the situation may be different for a larger plate diameter.

Figure 5 is the numerical schlierens showing the cyclic movements of the shock-cell, in particular, the shock cell shocks and the plate shock. The strong oscillation of the shocks indicates strong, nonlinear waves in the near field.

4.1.2 Acoustic waves and frequency Figure 6 shows the same isobar plots as in Fig. 4 but with pressure limited between 0.6–0.8 (non-dimensional val-

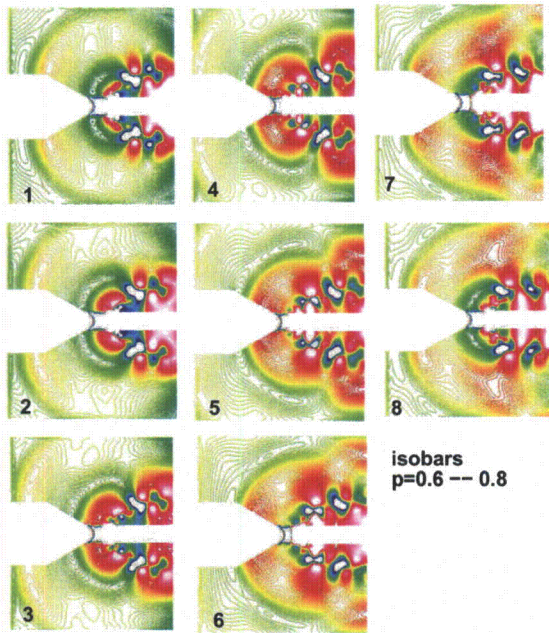


Figure 6: Plots 1-8: isobar contours with pressure limited within 0.6-0.8, showing acoustic waves generation and propagation.

ues). The generation and propagation of acoustic waves are clearly observed. The pressure history is recorded for a location $(-1.5, 2)$ upstream of the nozzle exit. Fourier analysis is then performed to obtain the spectrum. Figure 7 is the computed SPL (sound pressure level) plot at this location. It is observed that the waves are strong (over 150 dB), as expected. The fundamental frequency is about 3,300 Hz with ample harmonics. This compares well with a similar but not *exactly* the same case in [4], where $h=1.65D$ but $NPR=4.40$ instead of 4.03, which has a fundamental frequency of 3,570 Hz.

4.2 Jet Impinging on a Large Plate ($h/D = 1.4$)

For the case of a jet impinging on a large normal flat plate, the plate diameter is $d=10D$ (note that there is a buffer zone beyond $d=10D$ in the computational domain), and $NPR=4.03$. Two spacings between the nozzle exit and the plate, namely, $h=1.4D$ and $h=2.5D$, are considered. Figure 8 is the numerical schlierens at different time steps, the shock cell and the plate shock (stand-off shock) are clearly displayed but their hydrodynamic movements are much weaker than the previous case. Figure 9 illustrates snapshots of a similar experimental schlierens [6] for qualitative comparison.

With the pressure values limited in a narrow range of 0.71 - 0.72, Fig. 10 demonstrates how the acoustic waves are generated and propagate in a series of snapshots. Figure 11 is a snapshot of isobars, giving particular details of

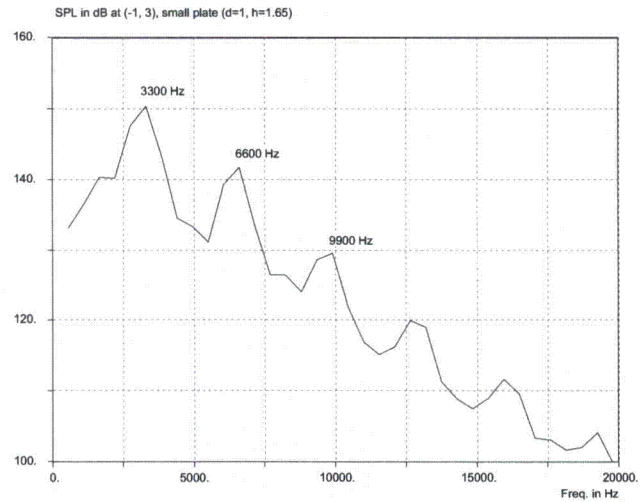


Figure 7: SPL at $(-1, 2)$ (upstream of nozzle exit) for a small plate of $d=D$, binwidth = 80 Hz.

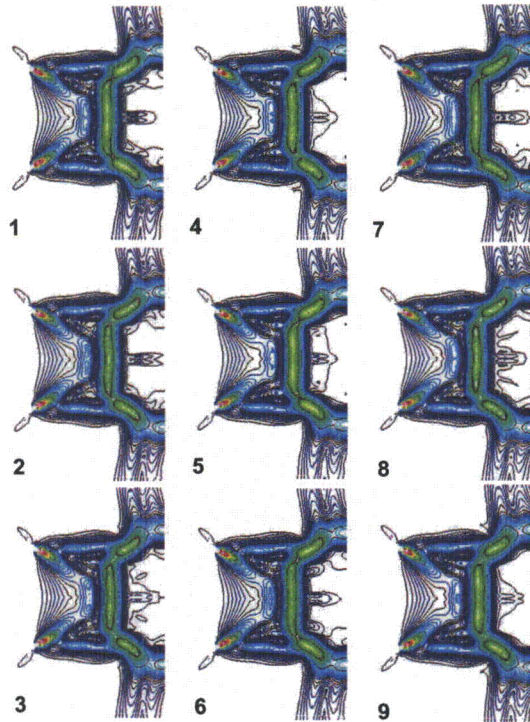


Figure 8: Plots 1-9: numerical schlierens for large flat plate case, the cyclic hydrodynamic movements of the shock cell and plate shock are weaker than the previous case of small plate.

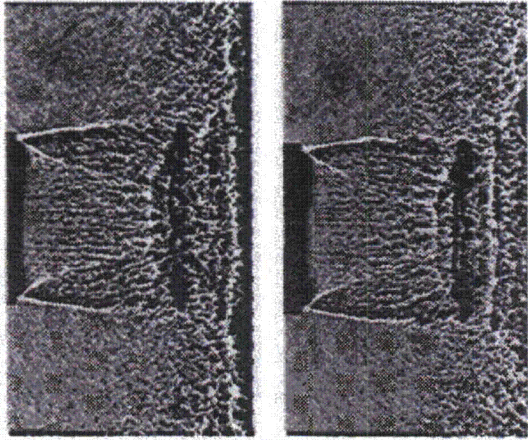


Figure 9: Snapshots of experimental schlierens for a similar case with $h/D = 1.4$, $NPR=4.06$ (from [6 - 7])

the vortices along the jet and wall jet shear layers, which are believed to be responsible for the noise generation. Figure 12 shows the vortices around the jet and wall jet in experiment, for qualitative comparison with Fig. 11.

The computed SPL at a point upstream of the nozzle exit is shown in Fig. 13. The spectrum is calculated after 2.7 million time steps has run. The computed tone SPL is slightly greater than 110 dB, which means the waves are much weaker than in the case with a small plate. Also, there are ample harmonics, as described in Henderson's work [6].

4.3 Jet Impinging on a Large Plate ($h/D = 2.5$)

As the physical behaviors for this large plate case with large spacing between nozzle exit and the plate is similar to the previous case, only the SPL at a point upstream of the nozzle exit is presented in Fig. 14.

4.4 Comparison to Experimental Acoustic Data

In addition to the above qualitative comparison of the structures of shock cell or vortical instability waves around the wall jet, comparisons of the computed frequencies in both small and large plate cases with similar experimental data show that they are similar. The comparisons are still somewhat qualitative, since we can only find similar experimental data under slightly different operating conditions. The experimental data are from Henderson and Powell [4] (figure 11 in their paper) and Alvi and Iyer [9] (Fig. 22 in their paper). Table 1 shows the comparisons. As the data are measured visually from the charts, a small error is inevitable. From Table 1, it is confirmed that the computed frequencies are in the right range.

Although the sound producing mechanism in the im-

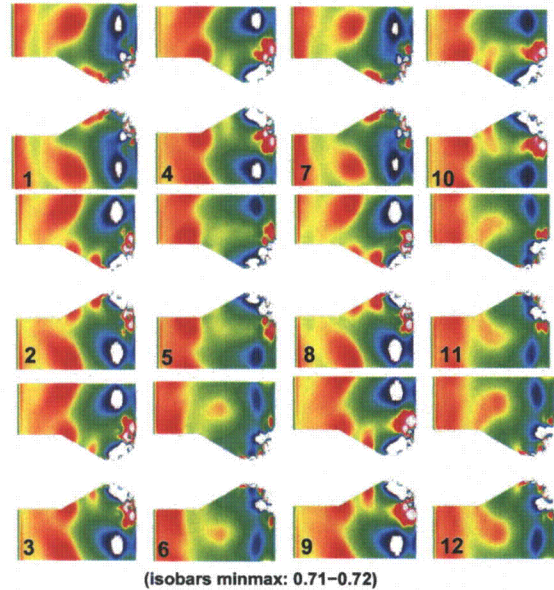


Figure 10: Wave generation in an impinging jet with a large plate, $h/D=1.4$. Isobar values are limited within 0.71-0.72 in order the weaker acoustic waves can be displayed.

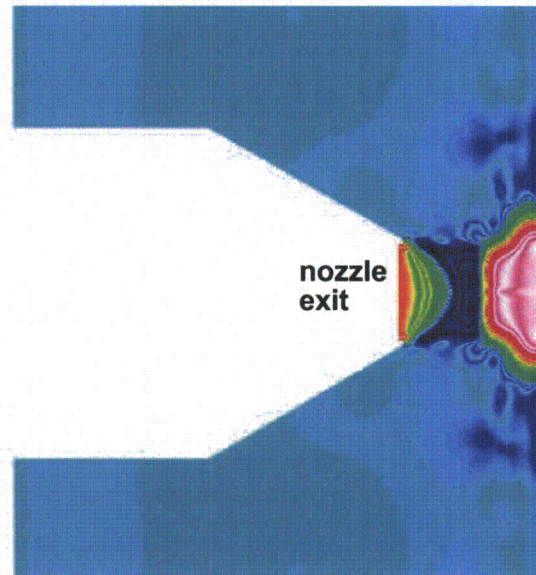


Figure 11: A snapshot of isobars showing presence of various vortical eddies around the jet core and wall jet

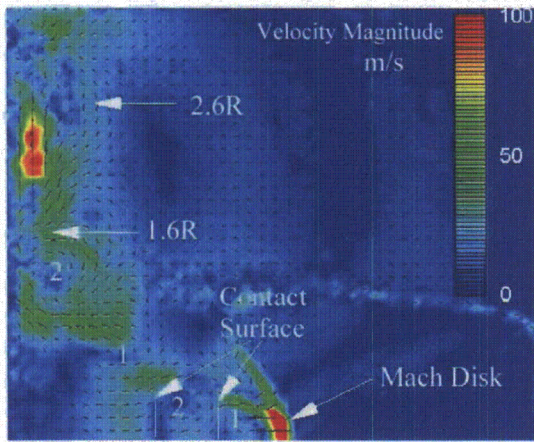


Figure 12: Experimental subtracted velocity vectors around the jet core and wall jet[6], showing the complicated vortical eddies there. (note that the flow is in opposite direction in the experiment)

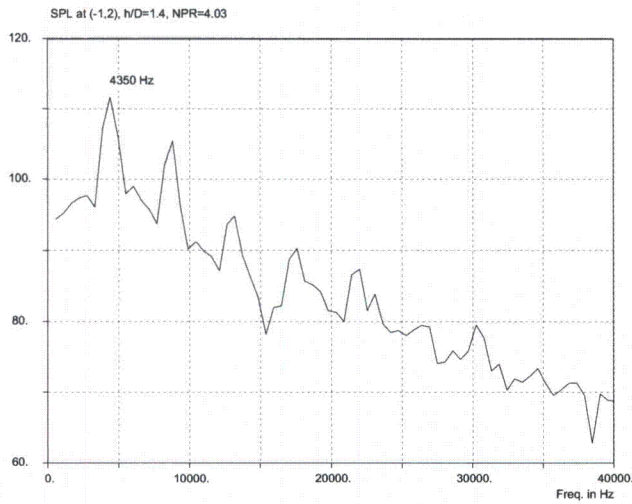


Figure 13: SPL at (-1,2) (upstream of nozzle exit) for a large plate, $h/D=1.4$, $NPR=4.03$, binwidth = 80 Hz.

Table 1: comparison of tone frequencies

	computed	Henderson [4] (exp.)	Alvi [9] (exp.)
small plate $d=D$	3.3 kHz $NPR=4.03$	3.57 kHz $NPR = 4.40$ S4 mode	— —
large plate (case 1)	4.4 kHz $h=1.4D$ $NPR=4.03$	5.1 Hz $h=1.4D$ $NPR=4.40$	4.2 kHz $h=1.6D$ $NPR=3.70$ w. lift plate
large plate (case 2)	5.43 kHz $NPR=4.03$ $h/D=2.5$	5.38 kHz $NPR=4.40$ $h/D=2.5$	—

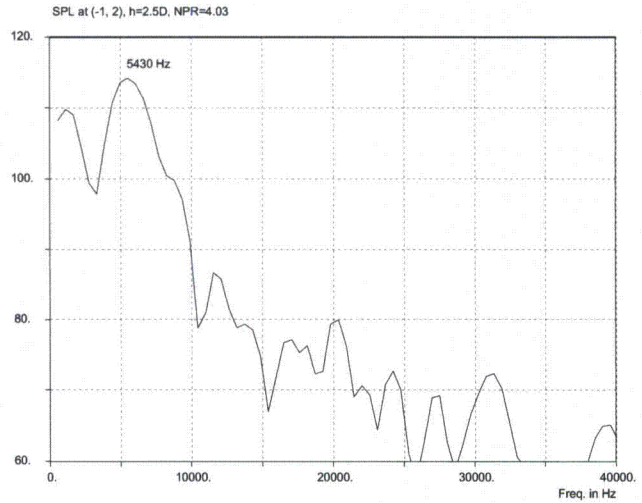


Figure 14: SPL at (-1,2) (upstream of nozzle exit) for a large plate, $h/D=2.5$, $NPR=4.03$, binwidth = 80 Hz.

pinging jet is not fully understood, the numerical work may shed some light on how the acoustic wave is generated near a flat plate. Figure 15 shows a typical instantaneous pressure field plus a velocity vector field on top of it (Here $h=2.5D$ with a large plate). Near the stagnation point of the plate, a high pressure bubble with diameter of about $1-1.5D$ is formed. Outside the bubble, the pressure quickly reduces to the ambient level. In the feedback loop, instability waves (vortices) are shed from the nozzle lip and grow in strength and size along the jet shear layer. When the vortices pass through the tips of the shock in the jet core and the plate shock, and enter the high pressure stagnation bubble (Fig. 15), the entire flow experiences severe changes in terms of all the flow variables u , v , p and ρ . The vortices will be deformed and distorted, and an acoustic wave is thus generated. For example, when a vortex turns 90° inside the high pressure jet stream, it interacts with high gradient compression wave or shock, and generates an acoustic wave. Outside the stagnation bubble, the acoustic wave appears to originate from a location near the plate but right outside of the stagnation bubble as sketched in Fig. 15. This also explains the experimental observation in [6] that the sound waves occur at a location of the plate $1.3D$ from the centerline (Fig. 12), because this location lies just outside the high pressure bubble.

5 Concluding Remarks

In this paper, we attempt to numerically simulate the important phenomena of a supersonic underexpanded jet impinging normally on flat plates, with emphasis on their aeroacoustic behaviors.

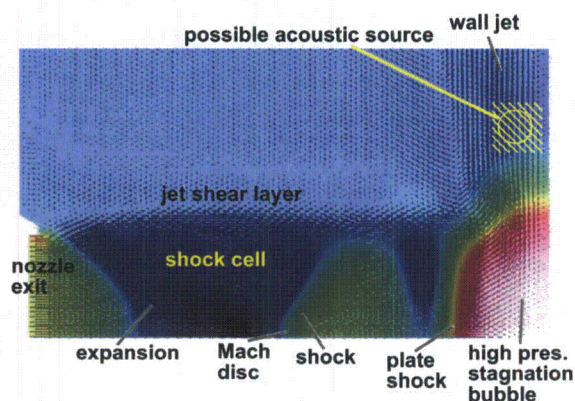


Figure 15: Instantaneous pressure field and velocity vector field, $h=2.5D$.

The numerical method used is based on the recently developed CE/SE scheme solving the axisymmetric Navier-Stokes equations. As the scheme possesses low dissipation while being capable of capturing shocks, the numerical results compare favorably to both hydrodynamic and acoustic experimental findings [4 - 9] even given the two-dimensional axisymmetric approximation. However, for jet impinging on a large plate, the sound generation mechanism is still not fully understood and we have put forward an explanation for the mechanism based on the numerical results. More investigations are needed in the impinging jet problem to further validate the numerical work.

References

- [1] A. Powell, "The sound-producing oscillations of round underexpanded jets impinging on normal plates", *J. Acoust. Soc. Am.* vol. 83 (2), pp. 515-533, 1988.
- [2] C-M. Ho and N. Nosseir, "Dynamics of an impinging jet. Part I. The feedback phenomenon", *J. Fluid Mech.* vol. 105, pp. 119-142, 1981.
- [3] C.K.W. Tam and K.K. Ahuja, "Theoretical model of discrete tone generation by impinging jets", *J. Fluid Mech.* vol. 214, pp. 67-87, 1990.
- [4] B. Henderson and A. Powell, "Experiments Concerning Tones Produced by an Axisymmetric Choked Jet Impinging on Flat Plates", *J. Sound Vib.* vol. 169(2), pp. 307-326, 1993.
- [5] B. Henderson and A. Powell, "Sound Production Mechanisms of the Axisymmetric Choke Jet Impinging on Small Plates: the Production of Primary Tones", *J. Acoust. Soc. Am.* vol. 99 (1), pp. 1996.
- [6] B. Henderson, J. Bridges and M. Wernet, "An Investigation of the Flow Structure of Tone Producing Supersonic Impinging Jets", *AIAA Paper 2002-2529*, 2002.
- [7] B. Henderson, "An Experimental Investigation into the Sound Producing Characteristics of Supersonic Impinging Jets", *AIAA Paper 2001-2145*, 2001.
- [8] A. Krothapalli, E. Rajkuperan, F. Alvi and L. Lourenco, "Flow field and noise characteristics of a supersonic impinging jet", *J. Fluid Mech.* vol. 392, pp. 155-181, 1999.
- [9] F.S. Alvi and K.G. Iyer, "Mean and Unsteady Flow Field Properties of Supersonic Impinging Jets with Lift Plates", *AIAA Paper 99-1829*.
- [10] S.I. Kim and S.O. Park, "Unsteady Simulation of Supersonic Impinging Jet", *AIAA Paper 2003-621*, 2003.
- [11] Y. Sakakibara and J. Iwamoto, "Oscillation of Impinging jet with generation of acoustic waves", *Aeroacoustics*, vol. 1(4), pp. 385-402, 2002.
- [12] Chang, S.-C., Wang, X.-Y. and Chow, C.-Y., "The Space-Time Conservation Element and Solution Element Method—A New High Resolution and Genuinely Multidimensional Paradigm for Solving Conservation Laws," *J. Comp. Phys.* vol. 159, pp. 89-136 (1999).
- [13] Wang, X.-Y. and Chang S.-C., "A 2-D Non-splitting Unstructured Triangular Mesh Euler Solver Based on the Space-Time Conservation Element and Solution Element Method" *C.F.D. J.* vol. 8, pp. 309-325 (1999).
- [14] Loh, C. Y., "On a Nonreflecting Boundary Condition for Hyperbolic Conservation Laws" *AIAA Paper 2003-3975* (2003).
- [15] Loh, C. Y., Hultgren, L. S. and Chang S.-C., "Computing Waves in Compressible Flow Using the Space-Time Conservation Element Solution Element Method," *AIAA J.*, vol. 39, pp. 794-801 (2001).

- [16] Loh, C. Y. and Zaman, K.B.M.Q., “ Numerical Investigation of Transonic Resonance with a Convergent-Divergent Nozzle”, AIAA J., vol. 40, no. 12, pp. 2393-2401 (2002).
- [17] Loh, C. Y., Hultgren, L. S., and Jorgenson, P. C. E., “Near Field Screech Noise Computation for an Underexpanded Supersonic Jet by the CE/SE Method”, AIAA Paper 2001-2252, (2001).

REPORT DOCUMENTATION PAGE

Form Approved
OMB No. 0704-0188

Public reporting burden for this collection of information is estimated to average 1 hour per response, including the time for reviewing instructions, searching existing data sources, gathering and maintaining the data needed, and completing and reviewing the collection of information. Send comments regarding this burden estimate or any other aspect of this collection of information, including suggestions for reducing this burden, to Washington Headquarters Services, Directorate for Information Operations and Reports, 1215 Jefferson Davis Highway, Suite 1204, Arlington, VA 22202-4302, and to the Office of Management and Budget, Paperwork Reduction Project (0704-0188), Washington, DC 20503.

1. AGENCY USE ONLY (Leave blank)		2. REPORT DATE March 2005	3. REPORT TYPE AND DATES COVERED Final Contractor Report	
4. TITLE AND SUBTITLE Computation of Tone Noise From Supersonic Jet Impinging on Flat Plates			5. FUNDING NUMBERS WBS-22-781-30-69 NAS3-03072	
6. AUTHOR(S) Ching Y. Loh			8. PERFORMING ORGANIZATION REPORT NUMBER E-14959	
7. PERFORMING ORGANIZATION NAME(S) AND ADDRESS(ES) Taitech, Inc. 1430 Oak Court, Suite 301 Beavercreek, Ohio 45430			10. SPONSORING/MONITORING AGENCY REPORT NUMBER NASA CR-2005-213426 AIAA-2005-0418	
9. SPONSORING/MONITORING AGENCY NAME(S) AND ADDRESS(ES) National Aeronautics and Space Administration Washington, DC 20546-0001			11. SUPPLEMENTARY NOTES Prepared for the 43rd Aerospace Sciences Meeting and Exhibit sponsored by the American Institute of Aeronautics and Astronautics, Reno, Nevada, January 10-13, 2005. Project Manager, Richard A. Blech, Engine Systems Technology Branch, NASA Glenn Research Center, organization code RTS, 216-433-3981.	
12a. DISTRIBUTION/AVAILABILITY STATEMENT Unclassified - Unlimited Subject Categories: 02 and 71 Available electronically at http://gltrs.grc.nasa.gov This publication is available from the NASA Center for AeroSpace Information, 301-621-0390.			12b. DISTRIBUTION CODE	
13. ABSTRACT (Maximum 200 words) A supersonic jet impinging normally on a flat plate has both practical importance and theoretical interests. The physical phenomenon is not fully understood yet. Research concentrates either on the hydrodynamics (e.g., lift loss for STOVL) or on the aeroacoustic loading. In this paper, a finite volume scheme—the space-time conservation element and solution element (CE/SE) method—is employed to numerically study the near-field noise of an underexpanded supersonic jet from a converging nozzle impinging normally on a flat plate. The numerical approach is of the MILES type (monotonically integrated large eddy simulation). The computed results compare favorably with the experimental findings.				
14. SUBJECT TERMS Aeroacoustics; Impinging jet; CE/SE method			15. NUMBER OF PAGES 16	
17. SECURITY CLASSIFICATION OF REPORT Unclassified			16. PRICE CODE	
18. SECURITY CLASSIFICATION OF THIS PAGE Unclassified		19. SECURITY CLASSIFICATION OF ABSTRACT Unclassified		20. LIMITATION OF ABSTRACT

Flow field and noise characteristics of a supersonic impinging jet

By A. KROTHAPALLI, E. RAJKUPERAN, F. ALVI
AND L. LOURENCO

Department of Mechanical Engineering, Florida A & M University and
Florida State University, 2525 Pottsdamer Street, Tallahassee, FL 32310, USA
e-mail: kroth@fmrl.fsu.edu

(Received 24 June 1998 and in revised form 13 March 1999)

This paper describes the results of a study examining the flow and acoustic characteristics of an axisymmetric supersonic jet issuing from a sonic and a Mach 1.5 converging–diverging (C–D) nozzle and impinging on a ground plane. Emphasis is placed on the Mach 1.5 nozzle with the sonic nozzle used mainly for comparison. A large-diameter circular plate was attached at the nozzle exit to measure the forces generated on the plate owing to jet impingement. The experimental results described in this paper include lift loss, particle image velocimetry (PIV) and acoustic measurements. Suckdown forces as high as 60% of the primary jet thrust were measured when the ground plane was very close to the jet exit. The PIV measurements were used to explain the increase in suckdown forces due to high entrainment velocities. The self-sustained oscillatory frequencies of the impinging jet were predicted using a feedback loop that uses the measured convection velocities of the large-scale coherent vortical structures in the jet shear layer. Nearfield acoustic measurements indicate that the presence of the ground plane increases the overall sound pressure levels (OASPL) by approximately 8 dB relative to a corresponding free jet. For moderately underexpanded jets, the influence of the shock cells on the important flow features was found to be negligible except for close proximity of the ground plane.

1. Introduction

While hovering in close proximity to the ground, short take-off and vertical landing (STOVL) aircraft experience a suckdown force, commonly known as ‘lift loss’. This lift loss is due to the entrainment flow associated with the lifting jets which induce low surface pressures on the airframe resulting in a force opposite to lift. The lift loss in hover increases in magnitude as the aircraft approaches the ground. When the aircraft is in vertical landing mode and is near touch down, in addition to lift loss, the impingement of the high-speed lifting jets on the ground plane lead to significant ground erosion (Margason *et al.* 1997). Increased overall sound pressure levels (OASPL) associated with the supersonic jets are also of concern with respect to sonic fatigue of structural elements in the vicinity of the nozzle exhaust. These problems become more severe when the jets operate at supersonic speeds, which is the case in the future generation STOVL aircraft (e.g. the Joint Strike Fighter). Very limited data are currently available in the literature to characterize accurately the supersonic jet induced effects in hover. Using the simple configuration shown in figure 1, a series of experiments is conducted aimed at providing some understanding of the flow physics and identifying the main effects contributing to the hover lift loss.

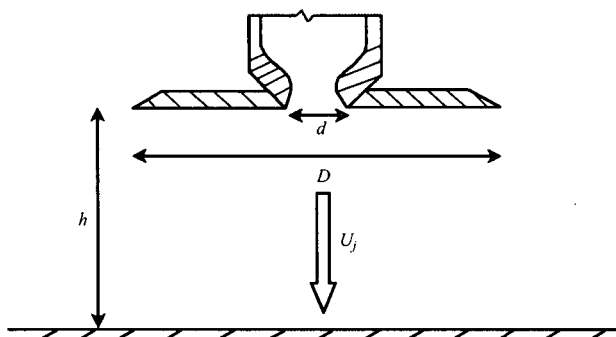


FIGURE 1. Schematic of the experimental set-up.

With the exception of the lift plate, the configuration chosen for this investigation closely resembles that used by a number of other investigators (Marsh 1961; Neuwerth 1974; Ho & Noisseir 1981; Powell 1988; Tam & Ahuja 1990; Henderson & Powell 1993; Messersmith 1995; Kuo & Dowling 1996) for the study of discrete sound generation of normally impinging jets. One of the key findings of these investigations is that the oscillation of the jet becomes a dominant feature of the flow when the ground plane is in close proximity to the jet exit. These oscillations are accompanied by high intensity sound (~ 160 dB, when the ground plane is at a distance of approximately 10 diameters) whose spectrum is dominated by discrete tones. In the past, the focus has been upon characterizing these tones and their generation mechanisms, especially in subsonic jets.

1.1. The feedback mechanism

The resonance-like behaviour of sound-producing oscillations is generally explained using a feedback loop that has its origins as far back as 1912. However, most of the current understanding of the feedback mechanism comes from the work of Powell (1953*a, b*). In his seminal paper (1953*a*), Powell not only discusses the physical mechanism governing feedback but also provides a simple feedback formula for predicting the frequencies of discrete tones so generated.

Although the formula proposed by Powell was mainly in the context of edge tones from high-speed jets, it applies equally well to impinging tones which, as pointed out by many investigators, including Powell himself (Neuwerth 1974; Ho & Noisseir 1981; Powell 1988; Tam & Ahuja 1990; Henderson & Powell 1993), are also generated by a feedback loop. Tam & Ahuja noted that the energy for the feedback loop is provided by the instability waves in the shear layers of the jet. These waves are generated by acoustic excitation in the region near the nozzle exit. The waves grow as they propagate downstream and manifest themselves as large-scale vortical structures that are commonly seen in flow-visualization pictures (cf. §3). Upon impingement on the wall, these large structures generate coherent pressure fluctuations, which result in acoustic waves with significant intensity, sufficient to render them visible in shadowgraph pictures. The acoustic waves travel through the ambient medium and upon reaching the nozzle exit, excite the shear layer of the jet, leading to the generation of instability waves thus closing the feedback loop. Krothapalli (1985) used the feedback-loop mechanism to predict the frequencies generated by an impinging supersonic rectangular jet, thus verifying its validity. When the impinging plate size is

small (a few jet diameters), additional tones are observed (Powell 1988; Henderson & Powell 1993) that relate to flow features associated with the oscillations of the normal standoff shock (cf. §3). Such standoff shocks are observed in experiments using underexpanded jets. When the jets are 'highly underexpanded' the oscillations of the Mach disk also appear to play a role in the feedback mechanism (Glaznev 1977).

The present study is concerned with the sound produced by axisymmetric supersonic jets exiting either from a converging-diverging (C-D) nozzle or a converging choked nozzle at moderate nozzle pressure ratios (NPR), where NPR is defined as the ratio of the stagnation pressure to the ambient pressure. In the present experiments NPR is less than 6. The plate representing the ground plane upon which the jet impinges is very large compared to the jet diameter ($4000d$, where d is the nozzle throat diameter). More details of the experimental hardware are discussed in §2.

In the present context, it is believed that the phenomenon associated with discrete sound generation is governed by the simple acoustic feedback loop as discussed earlier. The impingement tone frequency f_N is determined from the following formula proposed by Powell (1953a):

$$\frac{N+p}{f_N} = \int_0^h \frac{dh}{C_i} + \frac{h}{C_a} \quad (N = 1, 2, 3, \dots) \quad (1)$$

Here h is the distance between the wall and the nozzle exit and C_i and C_a are the convection velocities of the downstream-travelling large structures and the speed of upstream-travelling acoustic waves, respectively. N is an arbitrary integer and p represents a phase lag due to the fact that the phases of the acoustic wave and of the convected disturbance are not always exactly equal at both the nozzle exit and the source of the sound.

In order to predict the impinging tone frequencies using the above formula, accurate values of the large-scale structure velocities are needed. Owing to the difficulty of measuring these velocities experimentally, especially in supersonic jets, most previous investigators assumed a constant value for C_i — usually in the range of 60% to 70% of the primary jet velocity. The results presented later will show that this is not always the case; rather, the propagation speeds of the large structures exhibit significant variation with plate height. For example, the measured convection velocity of identifiable vortical structures in the shear layer of the free jet was found to be about $0.6 U_j$, where U_j is the fully expanded jet velocity, whereas, for an impinging jet, it was found to be about $0.5 U_j$ at $h/D = 4$. Karamcheti *et al.* (1969) also found such variation in the convection velocity in earlier low-speed edge tone experiments.

In this paper, we will verify the validity of the simple feedback formula using the present experimental data. The uniqueness of this comparison lies in the fact that the convection velocities of the downstream-travelling large-scale structures (C_i) used in the formula were obtained directly from velocity measurements using the PIV technique. Recent theoretical attempts by Tam & Ahuja (1990) and Kuo & Dowling (1996), using linear stability analysis, provided better models for the frequency determination. The amplitude prediction of the tones, which are of primary interest in practical applications, still remains elusive. However, using computational tools, progress is being made by How & Tam (1998) to predict the amplitude of screech tones.

1.2. Broadband noise

In addition to the discrete sound generated due to a feedback loop as described above, the broadband noise also becomes important as it contributes to an increase

in the OASPL for an impinging jet by approximately 10 dB, relative to a free jet. The full-scale noise investigations of Harrier aircraft by Soderman (1990) suggest that the strong jet oscillations discussed above may be an artifact of small-scale laboratory cold jets. However, when two jets are in close proximity, as is the case in the proposed Boeing Joint Strike Fighter (JSF) configuration, a strong flow-acoustic coupling occurs between the two jets resulting in violent oscillations. These oscillations may lead to sonic fatigue of the nearby structures.

When the jet approaches the ground, the OASPL levels increase significantly as will be shown in §3. In addition to the commonly known sources of sound from free supersonic jets, such as mixing noise and shock associated noise, the increased levels may also be attributed to the acoustic reflection from the ground, and the generation of additional noise sources in the jet impingement and wall-jet region of the flow field. The reflection of jet noise by the ground was modelled by Sutherland & Brown (1972) using an array of image sources placed symmetrically with respect to the ground plane where both sources (due to the jet) and their images radiate into unbounded space. Acoustic amplifications of up to 14 dB were predicted using this simple model. However, experimental observations by Soderman (1990) indicate much lower amplification levels.

To the authors' knowledge, measurements regarding the aeroacoustic behaviour of full-scale supersonic impinging jets (heated or cold) are not currently available in open literature. However, investigations of small-scale supersonic heated free jets show the presence of screech tones governed by a feedback mechanism similar to the impingement tones of the present study (see Krothapalli *et al.* 1997 for more details and references). Typically, in high-temperature supersonic jets, the broadband mixing noise levels are high enough to disguise the discrete tones (Krothapalli *et al.* 1997) and, as a result, their contribution to the OASPL is minimal. In light of the presence of screech tones in hot model jets we believe that impingement tones may persist in full-scale STOVL aircraft, i.e. in full-scale, hot, supersonic impinging jets.

There is clearly a lack of high-quality data information in the literature necessary to accurately model the noise generated by a supersonic jet impinging on the ground. In particular, the prediction of OASPL still remains elusive. The present study is an attempt to provide quality baseline data that can provide some insight into the flow physics as well as guidance for modelling efforts and their validation.

1.3. Hover lift loss

The loss of lift in STOVL aircraft while in hover mode has been extensively studied for subsonic aircraft where the impinging jets are also subsonic or subcritical. A good discussion of this issue, especially for subsonic jets, may be found in Margason *et al.* (1997). Briefly, the entrainment of the ambient fluid by the primary lifting jet(s) induces low pressures on the lower surface of the airframe, which in the present configuration is represented by a circular lift plate. Additional entrainment by the radial wall jet formed because of the impingement of the lifting jet can further reduce the surface pressures on the lift plate. It is expected that the entrainment due to the wall jet will become more significant when the ground plane is in close proximity to the nozzle exit and the ambient region from which the fluid is entrained becomes increasingly confined. As a result of the low surface pressures, a force in a direction opposite to the jet thrust is created, leading to a lift loss. The magnitude of this suckdown force and lift loss increases as the ground plate approaches the nozzle exit. As a consequence of the above mechanism responsible for lift loss, it is expected that increasing the jet entrainment would result in a higher lift loss. Based on extensive

data, this fact has been established for subsonic jets which show that jets which decay rapidly in terms of the centreline velocity (presumably due to higher entrainment rates), induce increased flow along the lower surface of the lift plate, resulting in reduced surface pressures and an increased lift loss (Margason *et al.* 1997).

In contrast to subsonic flows, very few data are at present available for supersonic impinging jets in STOVL configurations. In a recent study, researchers observed a nonmonotonic lift loss as a function of jet NPR for a supersonic impinging jet (Levin & Wardwell 1997). From the flow-visualization data, they speculated that this nonlinear lift loss behaviour may be related to the jet shock cell structure; however, a more rigorous explanation remains elusive. One of the objectives of this study is to investigate the lift loss phenomenon for supersonic impinging jets and to examine the physical mechanism responsible for this behaviour. Among other parameters, the role of shock cells on lift loss will also be examined. It is also well-known that jets with self-excited oscillations at discrete frequencies decay more rapidly than their counterparts without the oscillations. Hence, it is of interest to establish whether there is a correlation between the oscillatory behaviour of the jet column and the hover lift loss. It should be noted that other ground effects associated with single and multiple impinging jets, such as: ground erosion; fountain flow; and pitching moment due to the roll-up of a wall jet into a horseshoe-shaped ground vortex in transition to forward flight, can also significantly affect aircraft performance (Kuhn 1997). However, these issues will not be addressed in the present paper.

Keeping the above observations in mind, a basic research program has been initiated to investigate the aeroacoustics of supersonic single and multiple impinging jets. In this paper, the results of an investigation of the near sound field and the lift loss characteristics generated by an axisymmetric supersonic jet issuing from a convergent and a C-D nozzle are presented.

2. Experimental apparatus and procedures

The details of the hover test facility used for the experiments discussed in this paper are given by Wardwell *et al.* (1993). The facility was designed to obtain the jet-induced forces on STOVL model aircraft hovering in and out of ground effect. In order to simulate different heights above the ground, the ground plane is mounted on a hydraulic lift and can be moved relative to the model (figure 2). For the experiments described here, the ground plane was 2.44 m × 2.44 m and was centred underneath the model. To obtain measurements in the ground plane for ground erosion studies, a secondary instrumented 2.54 cm thick, 1 m × 1 m Plexiglas plate was mounted on the larger ground plane.

Two different nozzles were used in this study. A converging axisymmetric nozzle with an exit diameter of 2.54 cm was used to simulate an underexpanded choked jet. A shock-free nearly ideally expanded jet was obtained using a C-D axisymmetric nozzle with a throat diameter of 2.54 cm designed for an exit Mach number of 1.5. The exit diameter of the C-D nozzle was 2.75 cm. The divergent portion of the nozzle was a straight conic section with a 3° divergence angle to mimic the realistic nozzle geometry used in practice. Several nozzles were made with different diverging angles to study its influence on the lift loss. However, the data in this paper is restricted to the 3° nozzle. The nozzle upstream of the throat was designed using a third-order polynomial with a contraction ratio of approximately 5.

A high-pressure blow-down compressed air facility was used to supply air to the nozzles. A high-displacement reciprocating air compressor drives the facility, which

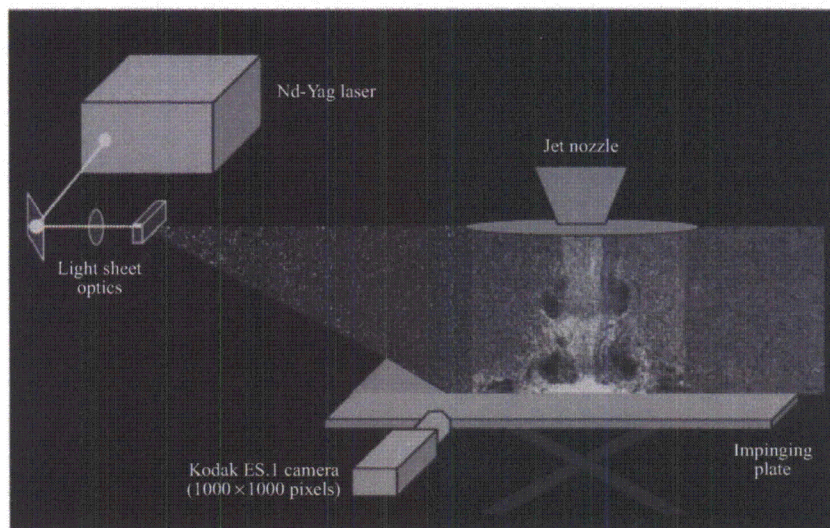


FIGURE 2. Schematic of the PIV set-up.

is capable of supplying air at a maximum storage pressure of 160 bars. Large storage tanks provide a total capacity of 10 m^3 and are capable of driving the Mach 1.5 jet continuously up to 40 min.

The nozzle was flush mounted with a circular lift plate of diameter D , as shown in figure 1. The lift plate diameter is 25.4 cm (approximately ten times the nozzle exit diameter) and is instrumented with 17 surface pressure taps along a radial line. The pressure taps are used to obtain detailed surface pressure distribution on the lift plate. The taps are more closely spaced near the nozzle exit where the mean pressure variations are expected to be more significant. The pressures were measured with a Validyne strain-gauge transducer mounted in a Scanivalve unit. At each port, several seconds of digitized data was recorded to obtain the mean surface pressure. The jet-induced mean surface pressure distributions were subsequently used to calculate the lift force on the plate.

A shadowgraph system with a field of view of 30 cm was used to visualize the flow field. It employed a conventional single-pass arrangement with a stroboscopic flash unit having a flash duration adjustable from 1.3 to $7 \mu\text{s}$ at five discrete settings. The frequency of the pulsed light source can be varied up to a maximum of 1 kHz.

In the particle image velocimetry experiments, the jet was seeded with small ($\sim 1 \mu\text{m}$) oil droplets generated using a modified Laskin nozzle. The ambient air was seeded with smoke particles ($\sim 5 \mu\text{m}$ in diameter) produced by a Rosco fog generator. A schematic of the experimental arrangement of the PIV system is shown in figure 2. Because of the unique nature of the PIV measurements used in this study, a brief description of this technique is provided in the following section.

Near-field acoustic measurements were obtained using a 0.635 cm diameter B & K microphone oriented 90° to the jet axis and placed approximately 25 cm away from the nozzle exit. The conditioned signals from the microphone and the surface pressures on the lift plate were acquired using a National Instruments data acquisition system with associated 'LabView' software. For acoustic measurements, the nearby exposed metal surfaces were covered with 10 cm thick acoustic foam to minimize sound reflections.

The main controlling parameters in the experiment were as follows: nozzle pressure ratio (NPR), which was varied from 1.5 to 5.5; the ground plate height h with respect to the nozzle exit, varied from $2.5d$ to $60d$ (d , diameter of the nozzle throat = 2.54 cm). The jet stagnation temperature was nominally maintained at 20°C. A top-hat velocity profile with laminar boundary layers was maintained at the nozzle exit. The nominal exit Reynolds number was 7×10^5 .

2.1. Particle image velocimetry

The main feature of the particle image velocimeter used in this experiment is its ability to record two images in quick succession, from which the velocity field is derived using a cross-correlation algorithm. This is possible by integrating the PIV system's two main hardware components: the Kodak ES1.0 digital video camera and the dual Spectra Physics Nd-Yag laser illumination system, with a repetition rate of 15 Hz. At the heart of the camera is the CCD interline transfer sensor, KA1-1001 with a resolution of 1008(H) \times 1018(V) pixels. Each square pixel measures 9 μm on the side with 60% fill ratio with a microlens, and a centre to centre spacing of 9 μm . The camera is also equipped with a fast electronic shutter and outputs eight-bit digital images, via a progressive scan readout system, at a rate of 30 frames per second.

The arrangement described above makes it possible to acquire up to 15 image pairs per second. The fact that the image pairs are recorded in separate frames and that the image pair separation can be reduced to a few microseconds makes this instrument appropriate for high-speed flows. In the present experiments, a 2 μs pulse separation was used. The image is acquired from the camera using an Imaging Technologies ICPCI board, which resides on a single slot of the PCI bus of a personal computer. The computer CPU is an Intel 300 MHz Pentium with 256 Mbytes of RAM, running under the Windows NT operating system.

An image-matching approach is used for the digital processing of the image pairs to produce the displacement field. One of the shortcomings of the conventional processing scheme is the spatial resolution. This limitation is due to the averaging caused by the typical correlation window size, of the order of 16^2 – 32^2 pixels. Since the measurement represents an average over the correlation window, it can be weighted towards the areas of the window with higher seeding density and/or reduced velocity. This weakness especially limits the use of this technique in flows with large velocity and/or seeding density gradients, e.g. reacting flows.

To achieve velocity data with high spatial resolution a novel processing algorithm was developed (Lourenco & Krothapalli 1998). With the new processing approach, the particle images themselves comprise the interrogation region, which have sizes ranging from 3 to 4 pixel square. Such a high-resolution scheme not only allows for accurate measurements of the gradient fields but also permit measurements in very close proximity of solid surfaces.

The displacement between image pairs was found in the usual manner by means of cross-correlation, and a velocity (displacement) vector is assigned at the mid-distance between image pairs. Therefore, each particle pair contributes to a second-order approximation of the velocity. However, in contrast to the traditional approach which uses structured grids, these velocities are evaluated in an unstructured grid. The flow field at any point is described by an analytical function using a least-squares-fitting algorithm. The function that is used is a second-order polynomial:

$$\mathbf{u} = ax^2 + bx + cy^2 + dy + exy + f. \quad (2)$$

The marked advantage of this approach is that the field is described at any point with

second-order accuracy, including the derivatives that are found by differentiating the previous equation, given as

$$\left. \begin{aligned} \frac{\partial}{\partial x} \mathbf{u} &= 2ax + \mathbf{b} + ey, \\ \frac{\partial}{\partial y} \mathbf{u} &= 2cy + \mathbf{d} + ex. \end{aligned} \right\} \quad (3)$$

Although an unstructured grid is used for calculating the velocity, for ease of visualization, the velocity field is usually presented at regular intervals. This new scheme is very efficient and incorporates a vector validation procedure, making it independent of operator intervention. The time it takes to compute a vector field depends on the computer hardware and it ranges from 1400 mesh points s^{-1} on a 200 MHz dual Pro Pentium PC up to several thousand on a 500 MHz Alpha based PC.

Despite the use of the novel processing scheme described above, some particle lag always occurs, especially in regions with very high velocity gradients, such as in the vicinity of shock waves. A careful study examining the behaviour of particles in supersonic flows with shocks was conducted by Ross, Lourenco & Krothapalli (1994) using a similar PIV system. As expected, the particle relaxation time was found to be a strong function of the particle diameter and shock strength. Consequently, it is expected that the location of strong shocks will be somewhat 'smeared' owing to particle lag, a fact noted in a subsequent discussion of velocity profiles obtained from PIV measurements (cf. §3.2, figure 13*b*). Similar particle lag will also occur in other regions with high velocity gradients such as the wall jet although this effect will be of a lesser degree than that across a shock. A more detailed investigation, which is outside the scope of this study, is required to assess the particle behaviour accurately in regions with large velocity gradients and highly rotational flows such as the large-scale vortical structures and the near-wall region of the wall. However, in the absence of shock cells the mean velocity field data obtained using PIV shows that the velocity of the particles is in very good agreement ($\pm 1\%$) with the exit velocity calculated using isentropic relations. Furthermore, instantaneous velocity field data, such as that shown in figure 8, clearly reveals that the PIV technique is capable of capturing the presence of large-scale structures in the primary jet and the wall jet. Despite the uncertainty introduced because of particle lag, it is expected that the effects of shocks and large-scale vortical structures do not significantly alter the conclusions reached in this investigation and are of ancillary importance in this study.

3. Results and discussion

3.1. Flow visualization

A conventional shadowgraph technique was used to visualize the jet flow. The images were captured using an SVHS video camera. Selected images displaying important flow and acoustic features are shown in figures 3–5 and will be discussed in this section.

It is well known that the axisymmetric free-jet instability manifests itself in symmetric as well as helical and/or flapping modes depending upon the exit Mach number, NPR (i.e. over/under-expansion condition), and the exit boundary-layer characteristics. The mode type also depends upon the height of the ground plane with respect to the nozzle exit. The flow-visualization images of an ideally expanded free jet at

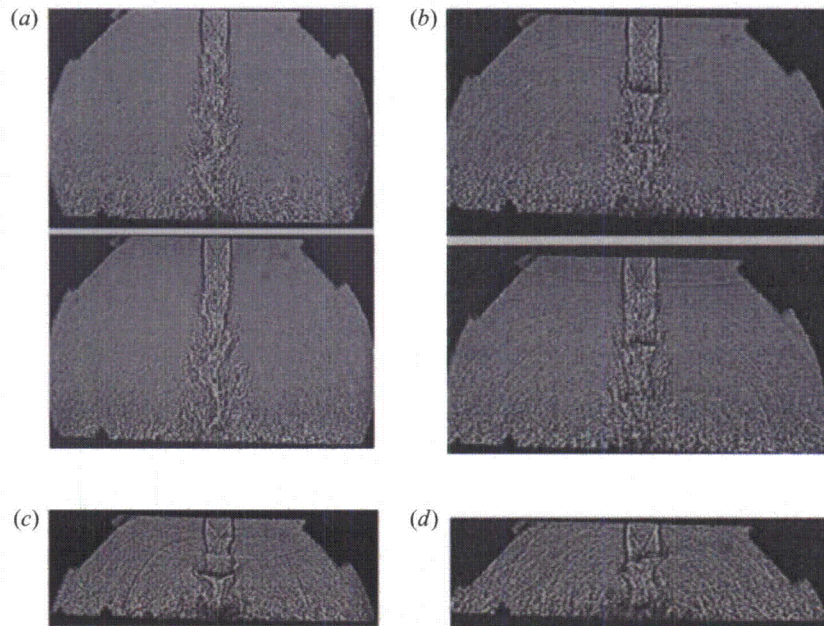


FIGURE 3. Instantaneous shadowgraphs depicting helical and symmetric modes of an ideally expanded supersonic impinging jet at $M = 1.5$. (a) $h/d \sim 8$; (b) $h/d \sim 6$; (c) $h/d \sim 4$; (d) $h/d \sim 3$.

$M = 1.5$ (not shown here) suggest that this jet is dominated by the helical mode instability. When the impinging plate is present, the helical mode continues to dominate up to $h/d \sim 8$, as shown in figure 3(a). Note that, in these and subsequent images, the lift plate and the ground plane appear as dark horizontal lines on the top and bottom of the pictures, respectively. The two pictures included in figure 3(a) represent the jet at two different phases of the resonance condition. An examination of the continuous video record suggests that the acoustic modes allowed at these conditions are also asymmetric in nature. When the ground plane is moved closer to the jet exit to $h/d \sim 6$, the axisymmetric mode begins to dominate, as shown in figure 3(b). The axisymmetric nature of the flow is also evident by the presence of the symmetric large-scale turbulent structures in the jet. The axisymmetric instability and acoustic modes persist until $h/d \sim 4$ (figure 3c). A further decrease in ground plate distance results in the re-emergence of the helical mode, as shown in figure 3(d). Also evident from figures 3(b) and 3(c) are the incident and reflected acoustic waves in the jet near field. The incident waves are concave upwards and travel upstream (relative to the primary jet flow) while the waves reflected by the lift plate are of opposite curvature and travel downstream in the ambient medium. Owing to the straight divergent section and finite nozzle lip thickness, a weak shock cell structure is present in the jet. The presence of only a weak shock cell structure precludes the generation of screech, a fact verified by the acoustic measurements.

A better illustration of the incident and reflected acoustic waves is seen in figure 4(a) where the ground plane is at $h/d \sim 4$. Also seen clearly in the image are the downstream-propagating axisymmetric structures in the jet column. The source of the upstream-propagating acoustic wave system be identified in the picture by locating

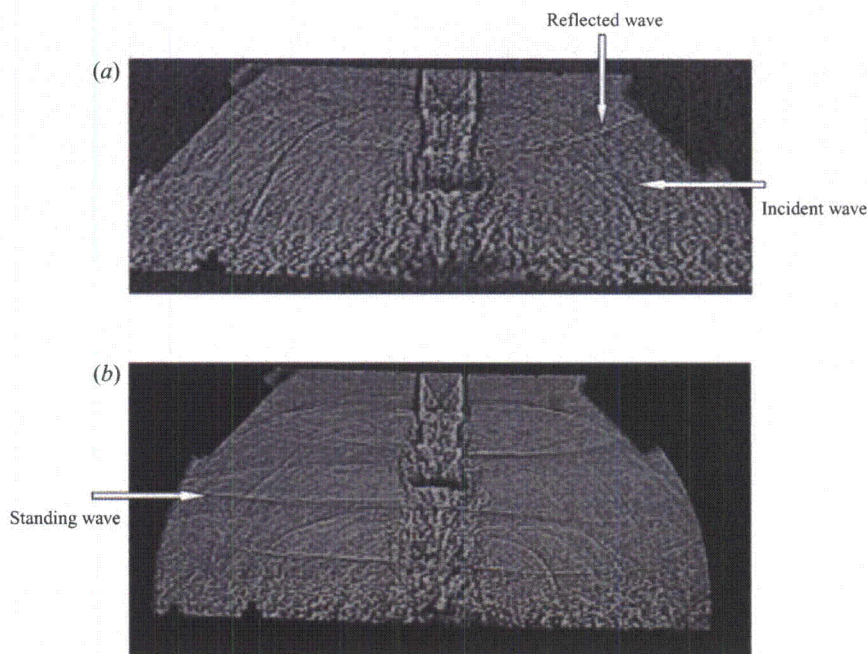


FIGURE 4. Instantaneous shadowgraphs depicting helical and symmetric modes of an ideally expanded supersonic impinging jet at $M = 1.5$. (a) $h/d \sim 4$; (d) $h/d \sim 5.5$.

the centre of the arcs. This source location is found to be in the stagnation region on the ground plane. Additionally, under certain conditions, a standing wave pattern is also produced between the lift plate and the ground plane, as shown in figure 4(b). The wavelength between the successive upstream-propagating acoustic waves roughly corresponds to a frequency calculated from the feedback loop (cf. § 3.4). The standing wave pattern represented by the horizontal lines corresponds to another resonance frequency that depends upon the distance between the lift plate and the ground plane (Krothapalli & Hsia 1996).

When the jet is moderately underexpanded, at $\text{NPR} = 5$, a series of shock cells appears as shown in figure 5(a). To accentuate the features of the shock cell structure, time-averaged (average of 17 instantaneous images) shadowgraph images are presented here. In the presence of a shock cell structure, when the ground plane is close to the jet exit, the most notable feature is the generation of a stand-off or plate shock which in some cases is accompanied by a local stagnation bubble in the impingement region. The stand-off shock can be seen in figures 5(b)–5(d) while the bubble can be observed in figure 5(c) and is indicated on the image for clarity. Although the stand-off shock was not observed for $h/d > 8$, it was not always present for all conditions corresponding to $h/d < 8$; in fact its size, shape and presence is a strong function of NPR and h/d . The appearance and disappearance of the shock and the associated separation or stagnation bubble may play an important role in determining the local aerodynamic and acoustic field, thereby affecting the lift loss and acoustic loading (cf. § 3.3 and 3.4). The oscillations of the underexpanded jet were quite similar to those observed in figure 4 and both axisymmetric and helical modes

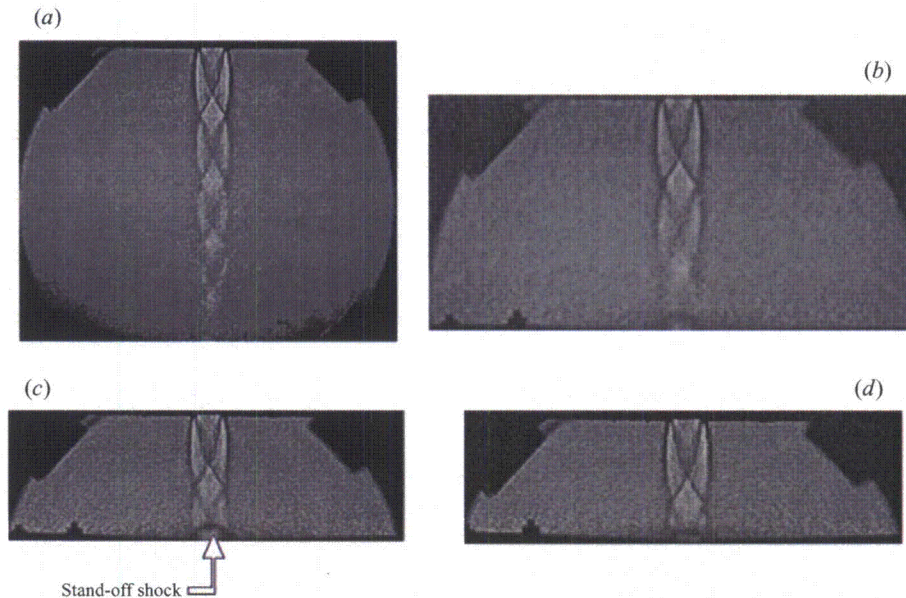


FIGURE 5. Mean shadowgraphs of an underexpanded supersonic jet at $NPR = 5.0$ for $M = 1.5$ C-D nozzle. (a) $h/d \sim 60$; (b) $h/d \sim 6$; (c) $h/d \sim 4$; (d) $h/d \sim 3.4$.

of oscillation were observed. Henderson & Powell (1993) considered the stand-off shock distance from the ground plane and different disturbance convection velocities upstream and downstream of the stand-off shock region to calculate the self-excited oscillation frequency (cf. §§ 3.4). The flow associated with the stand-off shock has been the focus of several investigations (Lamont & Hunt 1980). The detailed discussion of this aspect is outside the scope of the present paper, since it is more pertinent to the ground erosion problem.

3.2. PIV flow-field measurements

A detailed investigation of the jet characteristics was carried out using the PIV technique. All the measurements are confined to the central plane of the jet. Typical double exposure images of the free jet and the impinging jet are shown in figure 6. The main jet is seeded with the oil droplets while the ambient medium is seeded with smoke particles. The flow field produced by the jet impingement consists of three flow regimes: the free jet upstream of the ground plane, the impingement region and the wall jet. Donaldson & Snedeker (1971) provide a very good discussion of the basic flow characteristics of these regions, especially, the mean flow. The focus of the PIV measurements is the unsteady characteristics of the flow field and their effect on lift loss. Hence, little attention is paid here to the radial wall-jet flow field on the ground plane. However, a companion investigation is currently underway to investigate the impingement and the accompanying wall-jet regions (Alvi & Iyer 1999).

For the case of a free, nearly ideally expanded jet, shown in figure 6(a), there are no discernible large-scale organized structures such as those found in figure 6(b) which corresponds to an impinging jet at $h/d = 4$. The large structures appear to be nearly symmetrical, corresponding to the axisymmetric nature of this flow, also observed

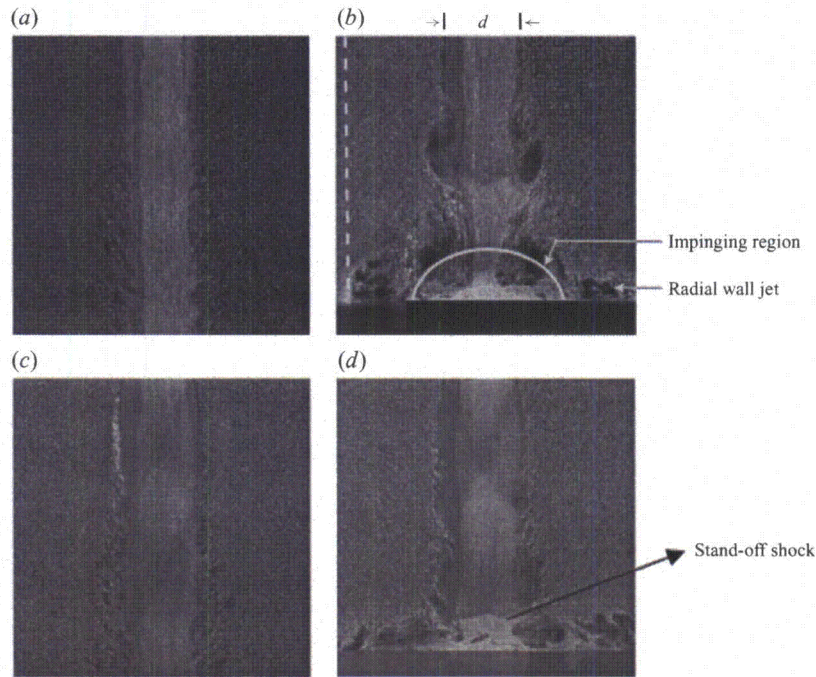


FIGURE 6. Instantaneous PIV images for $M = 1.5$ C-D nozzle. (a) Ideally expanded free jet, $NPR = 3.7$; (b) ideally expanded impinging jet, $NPR = 3.7$, $h/d = 4$, vertical dotted line is measurement location for entrainment velocity, q ; (c) underexpanded free jet, $NPR = 5.0$; (d) underexpanded impinging jet, $NPR = 5.0$, $h/d = 4$.

earlier in figure 3. Upon impingement on the ground plane, the structures move laterally in the radial wall jet without losing much of their coherence. In the case of an underexpanded jet at $NPR = 5$ (figure 6c), the vortical structures appear to be smaller and much less organized relative to those shown in figure 6(b). The stand-off shock, a prominent feature of this flow, is indicated by an arrow in figure 6(d).

The instantaneous velocity field was obtained by the method described in §2.1, with interrogation regions of 8×8 pixels corresponding to a physical dimension of 0.8×0.8 mm. The data was obtained using a $120 \times 80(x, r)$ Cartesian grid. Typical instantaneous velocity fields corresponding to the images in figure 6 are shown in figure 7. The magnitude of the out-of-plane component of the vorticity shown in colour contours is superimposed on the velocity field. In this fashion, the identity of large-scale vortical structures in the shear layer of the jet can be accentuated. Forty such instantaneous velocity fields were obtained for each of the condition tested.

One of the key parameters in the frequency prediction formula given in §1.1 is the convection velocity of the large-scale structures, C_i . In the absence of any direct measurements of the convection velocity, many of the previous investigators estimated its value to be between 0.6 and 0.7 U_j (U_j : mean jet exit velocity). From the velocity field data, it is possible to identify the regions of concentrated vorticity. For example, a typical region of high vorticity corresponding to a coherent vortical structure is shown in figure 8. Once a structure is identified, its convection velocity can be obtained easily

from the velocity data. Free-jet convection velocities of $0.6 U_j$ were measured in this fashion. However, in the case of an impinging jet, the convection velocity varies as a function of the plate height and the NPR. Figure 9 shows the convection velocities measured from individual PIV images, each represented by a single data point on the plot. Obviously, the location of the large-scale vortical structures (given on the x -axis) varies from one PIV image to another. The solid line in the plot represents the average value of the convection velocity, which in this case is equal to $0.52 U_j$. Because of the non-uniform variation of the centreline velocity owing to the presence of the shock cell structure, U_j is substituted here by a mean velocity, U_{clm} , obtained from averaging the centreline velocity of the free jet within the first five diameters.

As the plot in figure 9 shows, measurement of the convection velocities, C_i of large-scale structures were obtained only for $x \leq 75 \sim 80$ mm. This is typical for all the cases presented in this paper, where the convection velocity measurements could not be obtained in regions close to the wall. This is due to the presence of the impingement zone and the wall jet in the near-wall region which makes it very difficult, if not impossible, to identify large-scale structures and obtain reliable data for C_i . We suspect that the lack of this data may somewhat bias the average convection velocities towards higher values since one would expect the structures to slow down as they approach the ground plane. However, since the region where this occurs is relatively small, we expect the bias to be small and the convective velocities presented here to be fairly accurate. The variation of the average convection velocity with the plate height is shown in figure 10 for three different NPR. For example, for an ideally expanded jet (NPR = 3.7), the convection velocity increases linearly with h/d from $0.52 U_j$ at $h/d = 4$ towards the free-jet value. Figure 10 also shows that for a fixed h/d , the presence of shock cells increases the convection velocities of the vortical structures. From the flow visualization pictures (see figure 6) and PIV data, it appears that these vortical structures are much smaller in the presence of shock cells and are located mostly towards the high-speed side of the shear layer. The convective Mach number of the large structures, M_c , ($M_c = (U_{clm} - C_i)/a_j$; a_j is speed of sound in the jet) at NPR = 5 was found to vary from 0.73 at $h/d = 10$ to 0.66 at $h/d = 4$. These values are consistent with the measurements of Powell (1988) who derived them from the flow-visualization pictures.

The magnitude of the surface pressures on the lift plate is closely linked to the jet entrainment velocities in the near hydrodynamic field, especially when the jet is confined by two solid boundaries (lift plate and the ground plane). These velocities can be obtained easily from the PIV data. Typical instantaneous velocity variation with downstream distance at a radial location of $1.5d$ is shown in figure 11. Included in the figure are the data for a free jet and the impinging jet at two different pressure ratios. The magnitude of the near-field instantaneous entrainment velocity, q ($q = (u^2 + v^2)^{1/2}$) for a free jet is about 8 ms^{-1} , while for the impinging jet, it can be as high as 50 ms^{-1} , as indicated by the peaks in the velocity plot. Such large velocities in the near hydrodynamic field correspond to the presence of large vortical structures which can be clearly seen in figure 7. These high entrainment velocities will result in suction pressures on the bottom surface of the lift plate resulting in a downward force (lift loss), details of which are discussed in the next section. The entrainment field is quite unsteady as seen from three different instantaneous velocity profiles at the same radial location, shown in figure 12. The large velocities seen in the region $x > 75$ mm correspond to the radial wall jet. The thickness of the radial wall jet changes with time as suggested by the location of the peak velocity magnitude close to the ground plane $x > 75$ mm (figure 12). From the examination of a number of instantaneous

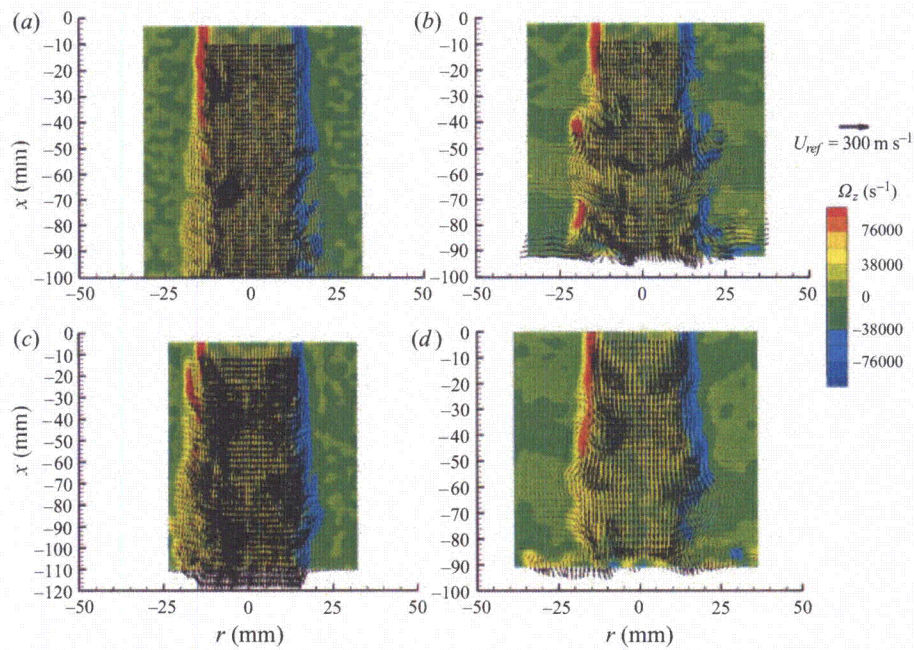
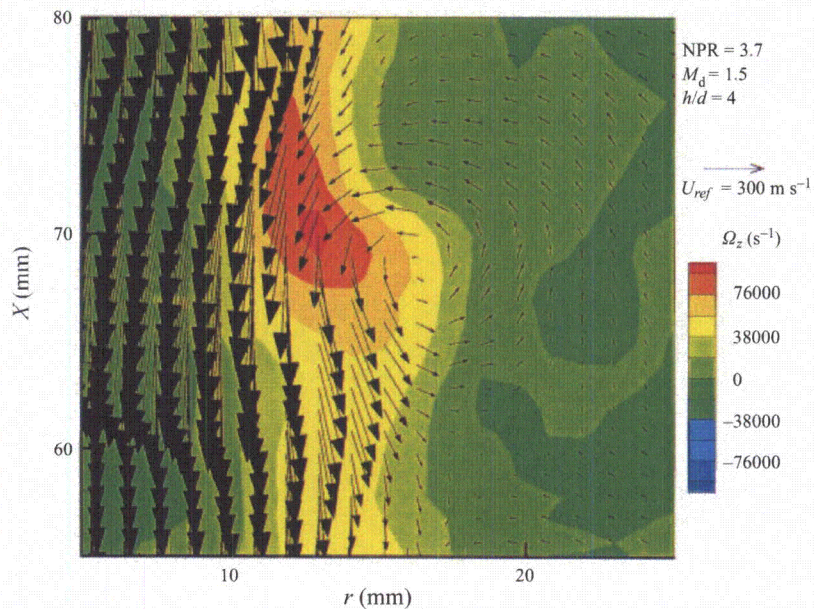


FIGURE 7. Instantaneous velocity fields corresponding to images shown in figure 6.

FIGURE 8. Details of the large-scale vortical structure. Underexpanded impinging jet, $M = 1.5$ C-D nozzle, $NPR = 3.7$, $h/d = 4$.

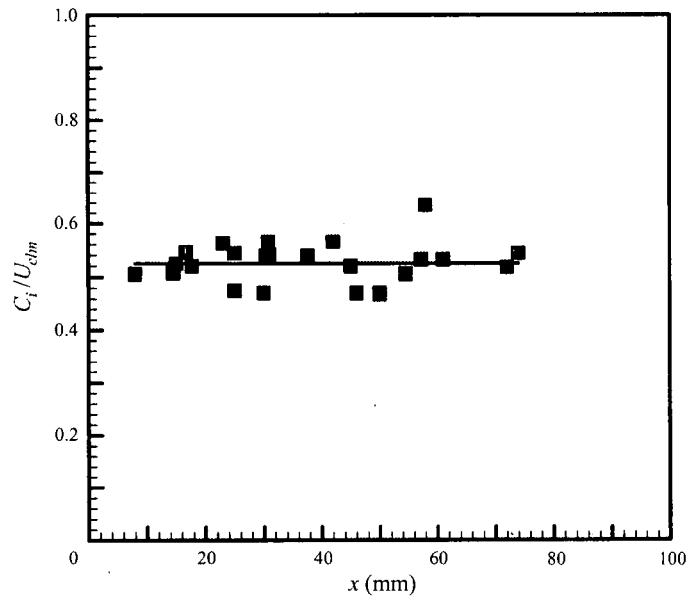


FIGURE 9. Instantaneous convection velocities of large-scale vortical structures obtained from PIV data. Ideally expanded impinging jet, NPR = 3.7, $h/d = 4$.

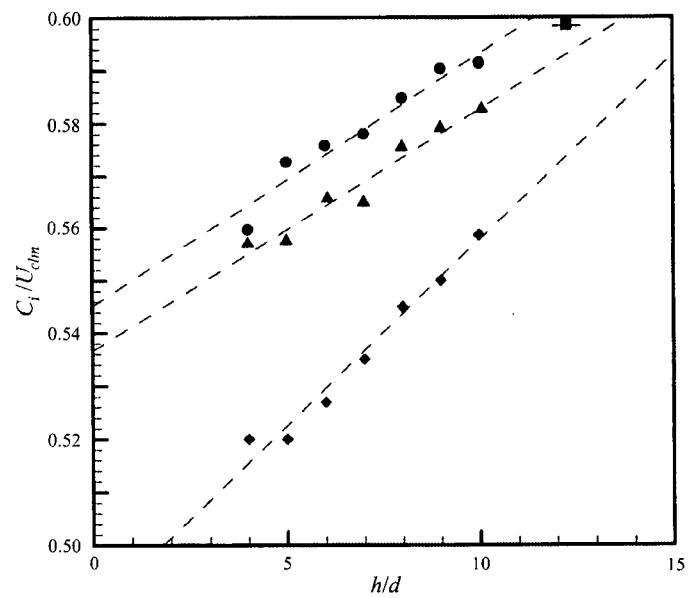


FIGURE 10. Variation of the normalized convection velocity of the large vortical structures with ground plane distance. ●, NPR=5.0; ◆, 3.7; ▲, 2.5; ■, Free jet $h/d = 60$.

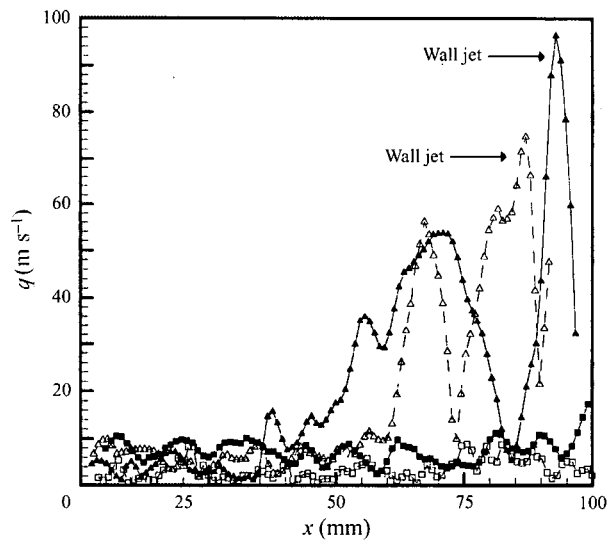


FIGURE 11. Instantaneous entrainment velocity for free and impinging jets at $r/d = 1.5$ (see figure 6). NPR=5.0: ■, freejet; ▲, $h/d = 4$; NPR=3.7: □, free jet; △, $h/d = 4$.

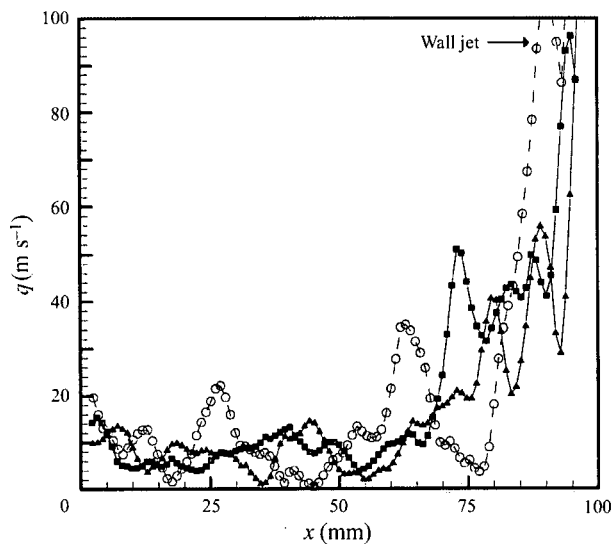


FIGURE 12. Instantaneous entrainment velocities at three different instances at $r/d = 1.5$. Underexpanded impinging jet, NPR = 5.0, $h/d = 4$.

velocity fields, it is observed that the wall jet is primarily characterized by the large vortical structures that originate in the jet shear layer.

The mean velocity field was obtained by averaging 40 instantaneous velocity fields. The number of samples used here is not sufficient to obtain a true mean velocity field. However, the trends provided by the averaged data are adequate to observe the

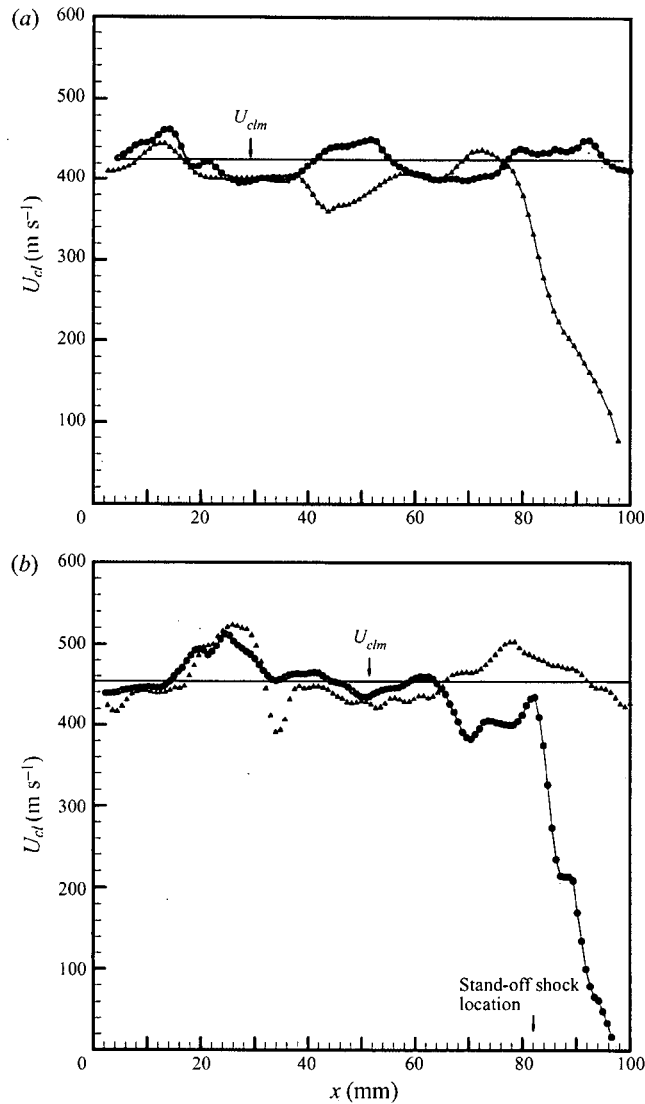


FIGURE 13. Mean centreline velocity variation for free and impinging jets. (a) $\text{NPR} = 3.7$; \blacktriangle , $h/d = 4$; \bullet , free jet; (b) $\text{NPR} = 5.0$; \blacktriangle , free jet; \bullet , $h/d = 4$.

significant changes due to the impingement process. Figure 13 shows the centreline velocity variation with downstream distance for free and impinging jets. For the impinging jet, the ground plane was located at $x = 101.6$ mm ($x/d = 4$). The variation in the averaged centreline velocity in the free jet is primarily due to the shock cell structure. The spatial mean centreline velocity U_{clm} , calculated using the data from $x/d = 0.2$ to $x/d = 5$ for a free jet, is depicted by the solid line. For an impinging jet at $\text{NPR} = 3.7$, the mean centreline velocity remains nominally constant up to $x/d \sim 3$.

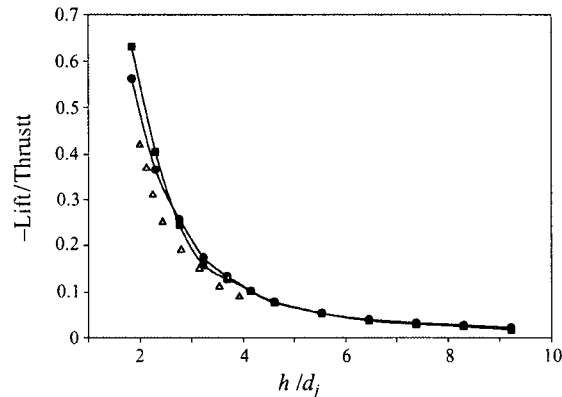


FIGURE 14. Lift loss variation with ground plane distance. ●, Mach 1.5, NPR=3.7; ■, Mach 1.0, NPR=3.7; ▲, Levin & Wardwell (1997), NPR=2.75.

Further downstream, the flow gradually decelerates, presumably through a system of compression waves, until it reaches sonic velocity. An examination of figure 13(a) reveals that the sonic condition occurs at $x = 86$ mm ($x/d \sim 3.4$) which corresponds to a change in axial velocity gradient. In contrast, the centreline mean velocity profile of the underexpanded jet (NPR = 5), shown in figure 13(b), displays a more drastic deceleration downstream of $x \sim 84$ mm ($x/d \sim 3.3$), indicating the presence of a much stronger shock than the ideally expanded case. Indeed, as pointed out earlier, the flow visualization clearly indicates the presence of this normal shock, commonly referred to as stand-off shock. Ideally, the velocity gradient across a normal shock will be extremely high. However, owing to particle lag inherent in PIV measurement, the velocity gradient across strong shock will be somewhat smeared, as evident in figure 13(b).

From the examination of all the instantaneous velocity fields, it is observed that critical changes in the jet flow field primarily occur in the vicinity of the jet impingement region (figure 6). This region extends as much as one jet diameter upstream of the ground plane. The behaviour of the flow field in this region is essential for understanding the ground erosion problem, a topic that is outside the scope of this paper but is the subject of an ongoing study (Alvi & Iyer 1999).

3.3. Hover lift loss

The negative jet-induced lift force that acts on the lift plate in the vicinity of the ground plane was obtained from the measurements of mean surface pressure. The estimation of the magnitude of this force becomes important as the ground plane approaches the nozzle exit. Typical variation of the negative lift force with h/d_j (d_j is the fully expanded jet diameter) is shown in figure 14. The lift force is normalized with the jet thrust calculated using one-dimensional isentropic equations. Included in the plot are the data of an underexpanded jet issuing from a conical nozzle. As the ground planes approach the lift plate, a large downward force is generated. For example, at $x/d = 2$, the magnitude of the lift loss is about 60% of the primary jet thrust. This force decreases rapidly in magnitude with increasing h/d and approaches an asymptotic value of the free jet, as shown in the figure. A comparison of the lift loss behaviour between the ideally expanded and underexpanded jet indicates that

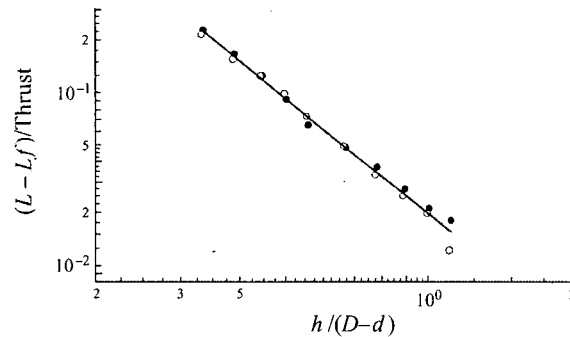


FIGURE 15. Lift loss correlation at NPR = 3.7. ●, Mach 1.5 nozzle; ○, Mach 1.0 nozzle; —, $0.02 x^{-2.24}$.

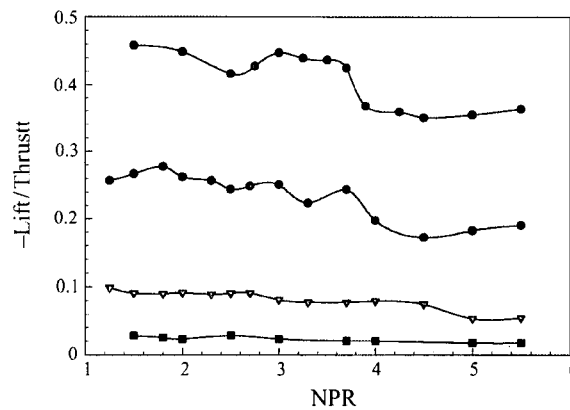


FIGURE 16. Lift loss variation with NPR for a sonic nozzle. ●, $h/d = 2.5$; ○, 3; ▽, 5; ■, 10.

the shock cells appear to play an insignificant role, except when the ground plane is in close proximity to the jet exit. This issue will be further explored later. Also included in the figure is the data for an underexpanded jet ($NPR = 2.75$) taken from Levin & Wardwell (1997). Their measurements were obtained directly using a thrust balance and a sonic nozzle. The agreement between the two sets of data provides confidence in the present data which were obtained from integrated surface pressure profiles on the lift plate.

Figure 15 shows the same data plotted in coordinates that are commonly used in the literature related to this subject. The data shows a linear variation which can be described by the following simple relation:

$$(L - L_f)/T = 0.02 (h/(D - d))^{-2.24}.$$

Here, L is the downward force on the plate; L_f is the downward force on the plate for a free jet; T is the jet thrust, D is the diameter of the lift plate and d is the nozzle throat diameter. This relationship is very similar to that obtained by Levin & Wardwell (1997).

The dependence of lift loss on NPR was further explored to investigate the role of

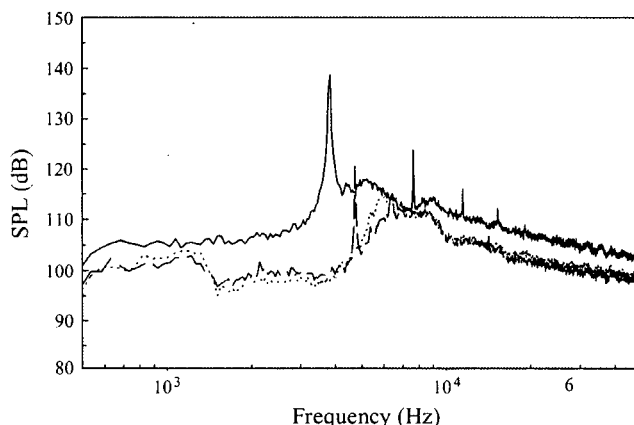


FIGURE 17. Near-field narrowband frequency spectra for $M = 1.5$ nozzle with and without the lift plate. ..., NPR=3.7, free jet, no lift plate; —, 3.7, free jet, with lift plate; —, 5.0, free jet, with lift plate.

the shock cell structure at small values of h/d . A summary of these measurements for the sonic nozzle is provided in figure 16. This plot confirms the earlier assertion that the shock cells are only relevant for small h/d . Measurable variations in lift loss with NPR are only observed for $h/d \leq 3$. As alluded to in §1 this nonlinear loss in lift was also observed by previous investigators (Levin & Wardwell 1997). It is speculated that the NPR range over which these variations are observed are, in part, related to the appearance of the stand-off shock and associated bubble. For small h/d , the scale and the unsteady characteristics of this stand-off shock are likely to influence the local entrainment velocities, thereby affecting the surface pressure and the resulting lift loss. Furthermore, at such small lift-to-ground plane separations, the entrainment properties of the high-speed (transonic to supersonic) wall jet are likely to play an important role in determining the local pressure field and lift loss.

3.4. Acoustic characteristics

3.4.1. Screech tone characteristics

It is well known that the noise from a supersonic jet existing from a C-D nozzle, operating away from the design condition, exhibits discrete tones commonly known as screech tones. The characteristics of these tones have been the subject of intense investigations; a summary of these studies can be found in review articles by Tam (1991, 1995). The mechanism for screech-tone generation is a feedback loop that is well understood. The presence of sound-reflecting surfaces in the immediate neighbourhood of the jet will alter the screech characteristics (Poldervaart, Wijnands & Bronkhorst 1973). In addition, a thick nozzle lip increases the screech intensity by about 10 dB (Norum 1983). Hence, the lift plate at the nozzle exit is expected to influence the screech tones. The near-field noise spectrum was measured for the free jet, with and without the lift plate, to examine its influence on the screech frequency and amplitude.

Figure 17 shows a typical narrowband spectrum of a near-field microphone signal, for a free jet at NPR = 3.7 (nominally ideally expanded). As expected, the spectrum shows no discernible discrete tones corresponding to screech. A broad peak corre-

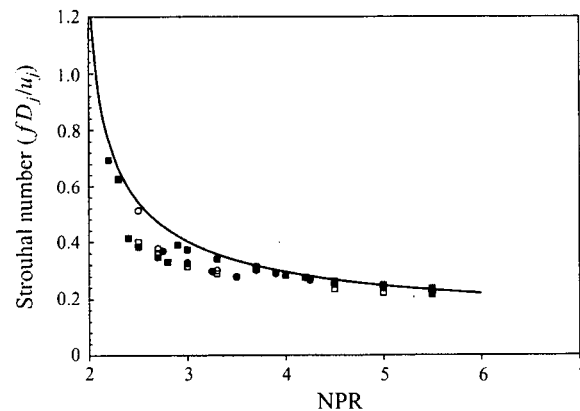


FIGURE 18. Free-jet screech tone variation with NPR. \circ , Mach 1.5 nozzle, no lift plate; \bullet , Mach 1.5 nozzle, with lift plate; \square , Mach 1 nozzle, no lift plate; \blacksquare , Mach 1 nozzle, with lift plate; $-$, Tam's prediction.

sponding to the broadband shock-associated noise (generated because of the presence of the weak shock cell structure) is present at this condition. However, in the presence of the lift plate, a distinct tone appears in the spectrum, as shown in the figure. Consistent with previous observations, the presence of the lift plate increased the amplitude of the screech tone. When the jet is underexpanded, the tones will become much stronger, resulting in several harmonics, as shown in the figure for $\text{NPR} = 5.0$. The tones measured in the present study are compared with the prediction formula given by Tam (1991), which has been thoroughly validated against a number of earlier measurements. Figure 18 shows a comparison of the data with Tam's prediction. Tam's formula only accounts for the helical mode, hence, in jets where symmetric or toroidal modes are present, primarily at NPR below 3, the data deviate from the curve. The good agreement of the data with the theoretical prediction for higher NPR s suggests that, although its magnitude is enhanced, the screech Strouhal number is not measurably altered by the presence of the lift plate. The effect of impingement on the screech frequency will be discussed in the following section.

3.4.2. Impinging tones

In addition to the screech tone, another dominant discrete tone appears when the jet impinges on the ground plate. These tones are commonly referred to as impinging tones (Krothapalli 1985; Powell 1988). Several different prediction formulae exist in the literature for the frequency prediction of these tones. Using the present experimental data, and in light of the measurements of the convection velocity of the large-scale vortices in the shear layer of the jet, the feedback loop will be further examined in this section.

Typical near-field narrowband spectra of an impinging jet at $\text{NPR} = 3.7$ for three different h/d are shown in figure 19. For the sake of clarity, the $h/d = 4$ and 4.25 spectra are displaced relative to the $h/d = 3.75$ spectra as follows: $h/d = 4$ by 10 dB and $h/d = 4.25$ by 20 dB. The shock cell structures are very weak at this NPR , as indicated by the PIV measurements. The spectra show the presence of several distinct tones, and a slight change in h/d can result in a significant change in the magnitude and frequency of these tones. In order to identify the origins of these tones,

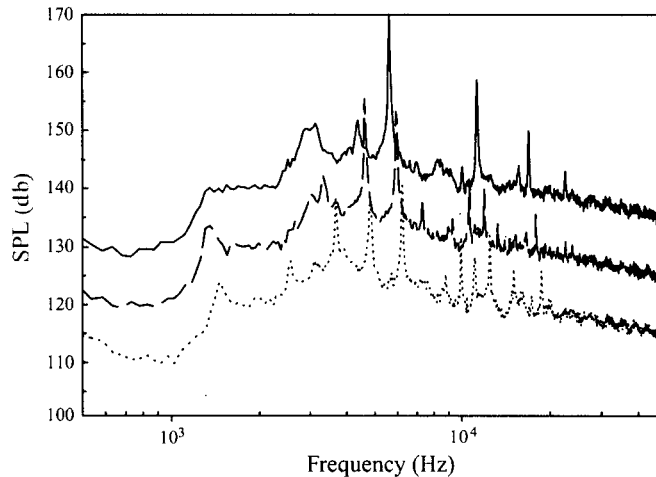


FIGURE 19. Near-field narrowband spectra for $M = 1.5$ impinging jet. \dots , $\text{NPR} = 3.7$, $h/d = 3.75$; $---$, $\text{NPR} = 3.7$, $h/d = 4$; $---$, $\text{NPR} = 3.7$, $h/d = 4.25$.

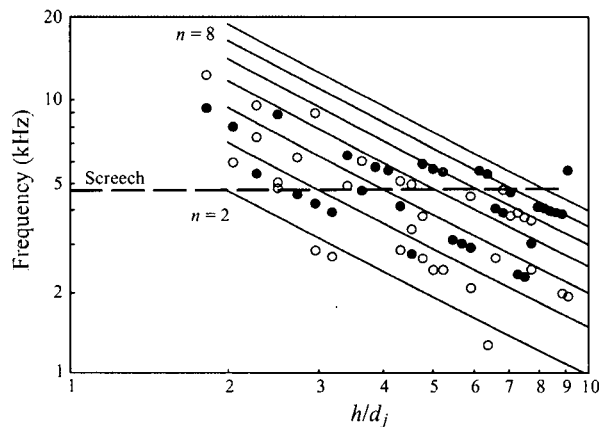


FIGURE 20. Impinging tone variation with ground plane distance for an ideally expanded jet, $\text{NPR} = 3.7$, $M_d = 1.5$. Comparison with $---$, the feedback formula assuming phase lag, $p = 0$. \bullet , amplitude dominant tones.

a summary plot of their variation as a function of h/d is shown in figure 20 where the solid symbols represent the amplitude-dominant tones. The data fall roughly along parallel lines, in accordance with the well-known staging behaviour. Such a variation of frequency with the impinging plate height suggests that a feedback mechanism is governing the flow. Also shown in the figure, is the free-jet screech frequency, indicated by the dotted line. From the data, it appears that, in most cases, the dominant tones do not lie on the free-jet screech line. This suggests that the majority of the tones are generated because of jet impingement.

In order to predict the frequency variation with h/d shown in figure 20, the feedback-loop formula (equation (1)) was used. The convection velocities used in the

formula are obtained from the PIV measurements and a phase lag of zero, i.e. $p = 0$ was assumed. The solid lines shown in figure 20 represent the predicted frequencies using the feedback formula. They clearly do not agree with the measured tones. This is in contrast to the observations made for subsonic jets where, assuming a zero phase lag, the feedback formula predicts the tones reasonably well. To account for this discrepancy in the measured and predicted frequencies, one must re-examine the use of the feedback formula and ask whether any significant physical mechanisms responsible for generating impinging tones have been neglected. One such candidate was suggested by Henderson & Powell (1993) for underexpanded jets where they propose that oscillations of the stand-off shock play an important role in the generation of tones. Accordingly, Henderson & Powell (1993) proposed a modified feedback formula which accounts for stand-off shock oscillations. However, in the present case, the flow-visualization pictures and the PIV data indicate that the sound emanates from the jet impingement region and there is no appearance of a stand-off shock. This is because only weak shock cells are present in the jet, and the flow approaching the plate transitions through a series of compression waves, as indicated by the smooth variation of the centreline velocity in the impingement region (figure 13a). Hence, it is suggested that the feedback model of Powell (1988) which includes stand-off shock oscillations as a dominant source of sound may not be valid here. Consequently, a different source for this discrepancy had to be accounted for in the feedback mechanism.

The mechanism by which instability waves are produced by the incident sound wave at the nozzle exit is assumed to be quite simple in arriving at the feedback formula given earlier. A strong coupling between the sound wave and the instability waves takes place over the distance of a few instability wavelengths immediately downstream of the nozzle exit. A comprehensive discussion of this aspect can be found in Tam (1978) and Ahuja & Tam (1982). In the present case, the presence of the lift plate generates reflected waves (figure 4). These reflected waves, along with the upstream propagating waves, are expected to interact with the shear layer near the nozzle exit to generate instability waves. Consequently, this interaction between these acoustic waves and the shear layer near the nozzle exit may be much more complex and requires further investigation. As mentioned earlier, Powell argued that the phases of the acoustic wave and of the convected large-scale disturbances do not necessarily exactly correspond to each other at the nozzle exit and the source. This may be accentuated in this particular case by the reflective surface at the nozzle exit. It is suggested that the complex interaction between the instability waves and the acoustic waves will lead to a phase lag. Therefore the assumption of a zero phase lag, $p = 0$, is probably incorrect and the likely source of discrepancy between predicted and measured frequencies in figure 20. Good agreement with the prediction formula is obtained when the phase delay is accounted for using $p = -0.4$. The agreement can be clearly seen in figure 21 in which data from figure 20 is replotted using this value of p .

To examine the effect of shock cells on the tones, a limited number of data for an underexpanded jet at NPR = 5 ($M = 1.5$ nozzle) were also obtained. Similar to behaviour observed for the ideally expanded case (NPR = 3.7), there is a significant discrepancy between the predicted and measured impingement tones when a zero phase lag is assumed. As before, assuming the same value of $p = -0.4$ resulted in good agreement between the predicted and measured frequencies. This suggests that either the stand-off shock oscillations play a minor role or their effect is accounted for in the phase lag, p . Another reason for this difference may be due to the under-

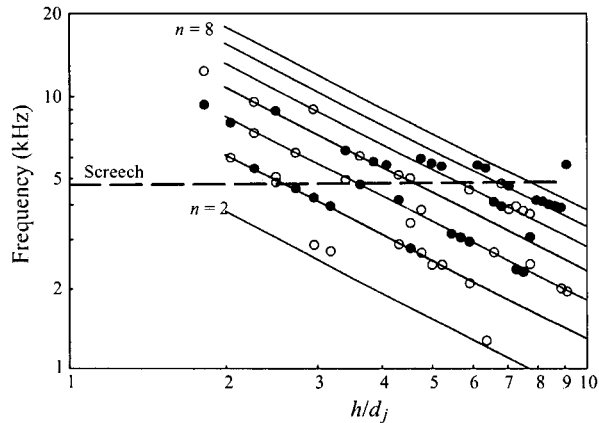


FIGURE 21. Impinging tone variation with ground plane distance for an ideally expanded jet, $\text{NPR} = 3.7$, $M_d = 1.5$ (same as figure 20). Comparison with —, the feedback formula assuming phase lag, $p = -0.4$. •, measured tones.

prediction of the convection velocities of the large-scale structures, as pointed out in the discussion of figure 9 (§3.2). Note that the particular value of the phase lag used here was not obtained from a rigorous analysis, rather this value of p simply provided the best agreement with the predicted frequencies over a wide range of conditions. Unfortunately, the relative contributions of the stand-off shock oscillation, under-prediction of convective velocities and the actual phase lag, to the total value of p used here cannot be determined. It should also be noted that for highly underexpanded jets, the stand-off shock oscillations are likely to play more significant role in determining the feedback loop.

Because of the confined nature of the geometry formed by the lift plate and the ground plane, some of the oscillatory modes can be strengthened. In cases where the screech or the impinging tone frequency matches the 'duct' mode, standing waves can be produced (Krothapalli & Hsia 1996). Such waves can be seen clearly in figure 4(b). Messersmith (1995) also made similar observations.

3.4.3. Overall noise

From the near-field narrowband spectra, overall sound pressure levels were calculated and plotted as a function of NPR in figure 22. A comparison of the $M = 1.5$ free jet, with and without the lift plate, shows that the plate has negligible influence on OASPL. However, in the presence of the ground plate, a significant increase in the OASPL was observed. For example, at the nearly ideally expanded condition at $\text{NPR} = 3.7$, an increase of about 8 dB is observed. The magnitude of the increase in OASPL owing to the impingement is consistent with the full-scale measurements obtained by Soderman (1990). A comparison of $h/d = 3$ and 5 shows that the location of the ground plate height for small h/d does not produce significant variations in OASPL.

4. Conclusions

The understanding of the oscillatory nature of impinging supersonic jets and their associated noise is of paramount importance for predicting the mean and

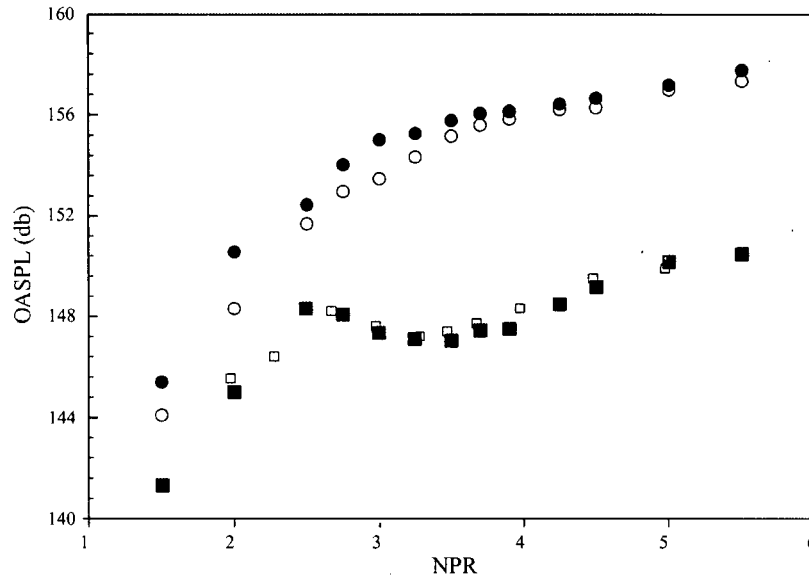


FIGURE 22. Near-field over all sound pressure level variation with NPR for $M = 1.5$ nozzle.
 ●, $h/d = 3$; ○, $h/d = 5$; □, free jet, no plate; ■, free jet, with plate.

unsteady loads on the airframe from which the jets are issuing. The experimental results described in this paper include lift loss, whole field velocity and acoustic measurements. Considered as a whole, these complementary measurements provide a coherent picture of the flow field associated with the oscillatory impinging supersonic jets and their near-field acoustic characteristics.

The self-sustained oscillatory behaviour of the impinging supersonic jet generates large-scale coherent vortical structures in the flow. These structures play a primary role in determining the entrainment properties of the jet and the acoustic field. From a practical perspective, knowledge of the entrainment flow is essential towards an understanding of the lift loss mechanism. Similarly, an understanding of the acoustic properties is important for predicting the unsteady acoustic loads on the airframe. A unique contribution of this study is the use of a novel high-resolution PIV technique to obtain the velocity field information with a high degree of accuracy. The velocity data clearly show that, as the ground plane approaches the nozzle exit, large-scale vortical structures of the increasing strength are generated. As a result, the jet entrainment velocities in the vicinity of the lift plate are significantly increased. This leads to lower pressures on the lift plate, followed by a suckdown force or lift loss. In the present study, suckdown forces as high as 60% of the primary jet thrust were measured. A significant reduction in thrust loss can be accomplished by eliminating the self-sustained oscillations of the jet. For example, the impinging tone could be suppressed and stopped by placing a small plate normal to the centreline of the jet in the outside ambient flow region (Karamcheti *et al.* 1969; Elavarasan, Venkatakrishnan & Krothapalli 1998).

The self-sustaining oscillation frequencies of the jet are frequently predicted using a feedback mechanism. Models describing this mechanism require a knowledge of the convection velocity of large-scale vortices in the shear layer. Using the vorticity

as a tracer quantity, the convection velocities of the large structures in the impinging jets were accurately measured. It was found that when the jet is operating in close proximity to the ground plane, the convection velocity of the structures is smaller than that of free jets ($0.52 U_j$; U_j is the jet exit velocity). Using the measured convection velocities in a feedback formula, an accurate prediction of the measured frequencies was obtained. However, the amplitude determination remains elusive.

Near-field acoustic measurements indicate that the presence of the ground plane increases the OASPL by approximately 8 dB over a corresponding free jet. This increase was relatively insensitive to variations in the nozzle pressure ratio (NPR) for $\text{NPR} > 3$.

This study briefly addressed the role of shock cells on the features discussed above. The convection velocities of the vortical structures was found to increase in the presence of shock cells. Except for very close ground plane proximity, the shock cells have a negligible influence on the suckdown force. For moderately underexpanded jets, the feedback mechanism appeared to be unaffected by the shock cells. When the jets are operating at highly underexpanded conditions, a strong highly unsteady shock cell structure is present. A detailed study is currently underway to examine its effects on the features discussed in this paper.

We would like to thank the continued support of NASA Ames Research Centre through a grant monitored by Mr Douglas Wardwell. Dr R. Elavarason and Dr L. Venkatakrisnan, helped us immensely in acquiring and processing the PIV data.

REFERENCES

- AHUJA, K. K. & TAM, C. K. W. 1982 A Note on the coupling between flow instabilities and incident sound. *J. Sound Vib.* **83**, 433–439.
- ALVI, F. S. & IYER, K. G. 1999 Mean and unsteady flowfield properties of supersonic impinging jets with lift plates. *AIAA Paper* 99-1829.
- DONALDSON, C. DUP. & SNEDEKER, R. S. 1971 A study of free jet impingement. Part 1. Mean properties of free and impinging jets. *J. Fluid Mech.* **45**, 281–319.
- ELAVARASAN, R., VENKATAKRISHNAN, L., KROTHAPALLI, A. & LOURENCO, L. 1998 A PIV study of a supersonic impinging jet. *Proc. Intl Conf. On Optical Technology and Image Processing in Fluid, Thermal and Combustion Flow, Yokohama, Japan, December 1998*.
- GLAZNEV, V. N. 1977 Sound field of an underexpanded supersonic jet impinging on a barrier. *Sov. Phys. Acoust.* **23**, 142–145.
- HENDERSON, B. & POWELL, A. 1993 Experiments concerning tones produced by an axisymmetric choked jet impinging on flat plates. *J. Sound Vib.* **168**, 307–326.
- HO, C. M. & NOSSEIR, N. S. 1981 Dynamics of an impinging jet. Part 1. The feedback phenomenon. *J. Fluid Mech.* **105**, 119–142.
- HOW, S. & TAM, C. K. W. 1998 Numerical simulation of generation of axisymmetric mode jet screech tones. *AIAA Paper* 98-0283.
- KARAMCHETI, K., BAUER A. B., SHIELDS, W. L., STEGEN, G. R. & WOOLLEY, J. P. 1969 Some features of an edge tone flow field. *NASA SP* **207**, 275–304.
- KROTHAPALLI, A. 1985 Discrete tones generated by an impinging underexpanded rectangular jet. *AIAA J.* **23**, 1910–1915.
- KROTHAPALLI, A. & HSIA, Y. C. 1996 Discrete tones generated by a supersonic jet ejector. *J. Acoust. Soc. Am.* **99**, 777–784.
- KROTHAPALLI, A., SODERMAN, P. T., ALLEN, C. S., HAYES, J. A. & JAEGER, S. M. 1997 Flight effects on the far-field noise of a heated supersonic jet. *AIAA J.* **35**, 952–957.
- KUHN, R. E. 1977 Pressures and forces induced by the ground vortex. *Proc. Intl Powered Lift Conf. SAE P-306, March 1997*, pp. 35–44.
- KUO, C. Y. & DOWLING, A. P. 1996 Oscillations of a moderately underexpanded choked jet impinging upon a flat plate. *J. Fluid Mech.* **315**, 267–291.

- LAMONT, P. J. & HUNT, B. L. 1980 The impingement of underexpanded axisymmetric jets on perpendicular and inclined flat plates. *J. Fluid Mech.* **100**, 471–511.
- LEVIN, D. B. & WARDWELL, D. A., 1997 Single jet-induced effects on small scale hover data in ground effect. *J. Aircraft* **34**, 400–407.
- LOURENCO, L. M. & KROTHAPALLI, A. 1998 Mesh-free second order accurate algorithm for PIV processing. *Proc. Intl Conf. On Optical Technology and Image Processing in Fluid, Thermal and Combustion Flows, Yokohama, Japan, December 1998*, p. 224.
- MARGASON, R., ARLEDGE, T. K., WARDWELL, D. A., HANGE, C. & NAUMOWICZ, T. 1997 Jet efflux characteristics and their influence of STOVL aircraft propulsion-induced effects. *Proc. Intl Powered Lift Conf. SAE P-306, March 1997*, pp. 3–10.
- MARSH, A. H. 1961 Noise measurements around a subsonic air jet impinging on a plane rigid surface. *J. Acoust. Soc. Am.* **33**, 1065–1066.
- MESSERSMITH, N. L. 1995 Aeroacoustics of supersonic and impinging jets. *AIAA Paper* 95-0509.
- NEUWERTH, G. 1974 Acoustic feedback of subsonic and supersonic free jet which impinges on an obstacle. *NASA TT F-15719*.
- NORUM, T. D. 1983 Screech suppression in supersonic jets. *AIAA J.* **21**, 235–240.
- POLDERVAART, L. J., WIJNANDS, A. P. J. & BRONKHORST, L. 1973 Aeroacoustic games with the aid of control elements and externally generated pulses. *AGARD Conf. Proc.* 131, Noise Mechanisms, pp. 20.1–20.4.
- POWELL, A. 1953a On edge tones and associated phenomena. *Acoustica* **3**, 233–243.
- POWELL, A. 1953b On the mechanism of choked jet noise. *Proc. Phys. Soc. Lond. B* **66**, 1039–1057.
- POWELL, A. 1988 The sound-producing oscillations of round underexpanded jets impinging on normal plates. *J. Acoust. Soc. Am.* **83**, 515–533.
- ROSS, C., LOURENCO, L. & KROTHAPALLI, A. 1994 PIV measurements in a shock-containing supersonic flow. 32nd Aerospace Sciences Meeting, *AIAA Paper* 94-0047.
- SODERMAN, P. T. 1990 The prediction of STOVL noise-current semi-empirical methods and comparisons with jet noise data. *NASA Tech. Mem.* 102833.
- SUTHERLAND, L. C. & BROWN, D. 1972 Prediction method for near field noise environments of VTOL aircraft. *AFDL-TR* 71-180, AD 900405.
- TAM, C. K. W. 1978 Excitation of instability waves in a two-dimensional shear layer by sound. *J. Fluid Mech.* **89**, 357–371.
- TAM, C. K. W. 1991 Jet noise generated by large-scale coherent motion. *Aeroacoustics of Flight Vehicles: Theory and Practice*, *NASA RP* 1258, vol. 1, pp. 311–390.
- TAM, C. K. W. 1995 Supersonic jet noise. *Ann. Rev. Fluid Mech.* **27**, 17–43.
- TAM, C. K. W. & AHUJA, K. K. 1990 Theoretical model of discrete tone generation by impinging jets. *J. Fluid Mech.* **214**, 67–87.
- WARDWELL, D. A., HANGE, C., KUHN, R. E. & STEWART, V. R. 1993 Jet-induced ground effects on parametric flat-plate model in hover. *NASA Tech. Mem.* 104001.

AN EXPERIMENTAL INVESTIGATION INTO THE SOUND PRODUCING CHARACTERISTICS OF SUPERSONIC IMPINGING JETS

Brenda Henderson*

Kettering University, Mechanical Engineering Department, 1700 W. Third Ave., Flint, MI 48504

Abstract

The results of an experimental investigation into the jet structure associated with the production of sound by a supersonic impinging jet are presented. A convergent nozzle operated at nozzle-pressure ratios (NPR) between 3.38 and 4.47, where NPR is the ratio of the stagnation pressure to the pressure at the nozzle lip, exhausted onto a square plate with side dimensions equal to 12 nozzle exit diameters. Results from random and phase-locked shadowgraph photographs indicate that tonal production ceases when the first or second shock waves develop a conical shape. When tones are produced, the standoff shock wave oscillates and periodic changes in the impingement and near wall flows occur. Sound is produced in the near wall region and is associated with changes in the flow caused by the standoff shock wave motion. Unstable flow usually occurs when the central portion of the flow is subsonic upstream of the standoff (annular) shock wave.

1. Introduction

The impingement of a jet on a flat plate produces ground effects including surface erosion, non-uniform surface heat transfer, lift loss, and acoustic loading. Intense discrete frequency sound is often produced with sound pressure levels exceeding the local broadband levels by more than 10 dB. Although a number of studies have documented the oscillatory nature of the flow, the connection between the oscillating flow structures and the production of intense acoustic radiation is not well understood for impingement on large plates.

The production of discrete frequency sound by a supersonic impinging jet depends highly on plate size and moderately on nozzle-to-plate spacing and nozzle-pressure ratio (NPR)^{1,2,3,4}, where NPR is the ratio of the stagnation pressure to the pressure at the nozzle lip. Tones produced by impingement on small plates have significantly different tonal characteristics than those produced by impingement on large plates.

For NPR less than, or equal to 2.7³, large plate tones occur for plate diameters greater than or equal to ½ the nozzle exit diameter. Multiple discrete frequency tones are often produced simultaneously and are associated with multiple jet oscillation modes. Staging behavior about the choked jet screech frequency is also common for larger plate spacings. At higher pressures, large plate tones occur for plate diameters greater than, or equal to, 2 nozzle exit diameters. Single discrete frequency tones usually occur and are associated with symmetrical jet disturbances.

Small plate tones are produced at pressure ratios greater than, or equal to, 3.04 and for plate diameters less than, or equal to, 2 nozzle exit diameters. Two classes of small plate tones have been identified. Primary small plate tones are associated with large shock wave oscillations⁵ and secondary small plate tones are produced by the interaction of jet disturbances with the standoff shock wave and shock waves in the deflected flow along the plate⁶.

The production of large plate impinging tones by underexpanded jets is not well understood due to the complicated flow structure of these jets. A number of flow phenomena have been associated with large plate impingement such as a recirculation zone in front of the plate^{7,8,9}, oscillating shock waves^{4,7,8,10,11,12}, and vortex acceleration in the impingement region. However, the operating conditions vary significantly in the reported experiments and the connection between these flow features and the production of sound has not been systematically studied.

Discrete frequency sound has been reported for ideally expanded supersonic impinging jets despite the lack of a strong shock cell structure¹³. Although there has been no direct comparison between the tonal characteristics of the ideally expanded and underexpanded supersonic impinging jets, studies indicate that the radiation from twin jets issuing from ideally expanded jets is more intense than that issuing from underexpanded jets¹⁴.

* Associate Professor, Mechanical Engineering Department, member AIAA

Copyright © 2001 by Brenda Henderson. Published by the American Institute of Aeronautics and Astronautics, Inc. with permission.

The present study investigates the structure of tone-producing moderately and highly underexpanded supersonic impinging jets. Far-field acoustic measurements are coupled with random and phase-locked shadowgraph photographs. The oscillation cycle associated with the production of tones is documented and a sound production model is presented.

2. Experimental Apparatus

The experiments were conducted in the Acoustic Jet Flow facility at NASA Glenn Research Center. A schematic of the facility is shown in Fig. 1. Compressed air passed through a 200 mm pipe equipped with acoustic treatment and flow straightening devices. A round convergent nozzle with a 25.4 mm exit diameter was operated at NPR between 3.38 and 4.74. The jet impinged on a 305 mm x 305 mm aluminum plate placed perpendicular to the jet axis and located between 2.54 cm and 12.7 cm from the nozzle exit.

Acoustic measurements were taken in the far field with a calibrated B & K type 4135 microphone and analyzed with an Ono Sokki type CF-5200 spectrum analyzer.

The shadowgraph system consisted of a Photonics Analysis Pal Flash with a 1-2 μ sec spark duration, two 152 mm diameter spherical mirrors with 152.4 cm focal lengths, two collecting lenses, one focussing lens, and a 35 mm camera body. Phase-locked photographs were triggered by the far field microphone signal. The microphone signal was filtered then displayed on a digital oscilloscope. A trigger delay signal was generated by the oscilloscope and sent to a programmable waveform generator used to send a single pulse to the light source. The signal from a photodiode was recorded on the oscilloscope to determine the exact location in the cycle where the photographs were obtained. The photographs were taken in different oscillation cycles.

3. Results

3. (a) Acoustic Measurements

Discrete impingement tones are typically greater than 10 dB above the local broadband noise. In this section, acoustic data were plotted for the fundamental frequency tones with amplitudes exceeding the local broadband noise by 5 dB.

The acoustic data from the present study and the data from the study of Krothapalli et al.¹³ are shown in Fig. 2. In the experiments of Krothapalli et al., acoustic data were only presented for the ideally expanded jet. The acoustic wavelength, λ , and the nozzle-to-plate spacing, h , have been normalized by the nozzle exit diameter, d .

The tones falling along the L1 line are associated with symmetrical jet disturbances².

Despite the differences in the flow structure of the ideally expanded and underexpanded jets, there are some similarities in the two sets of data. Both types of jets produce impinging tones that display staging behavior. However, staging behavior is much more common for the ideally expanded jet. The frequencies produced by both jets often fall along the L1 line for $1.5 < h/d < 3.5$, although multiple tones appear to be more common for the ideally expanded jet.

The most notable difference in the data from Krothapalli et al.¹³ and the present study is the occurrence of 'zones of silence' for underexpanded flow that are not present for shock free flows. 'Zones of silence' where no tones are produced are indicated in Fig. 3. Data for h/d greater than 5 were taken by Henderson and Powell² and it was found that regions of tonal activity occurred at larger nozzle-to-plate spacings for NPR equal to, or greater than, 3.72 but these tones displayed staging behavior around the choked jet screech frequency. The tones produced at larger spacings are assumed to be related to the choked jet screech phenomenon and will not be addressed in this study. Since the shock wave structure is significantly different for ideally and underexpanded jets, it appears that the production of tones is affected by the shock wave structure.

An instability plot indicating the regions where tones are produced is shown in Fig. 4. The nozzle-to-plate spacing has been normalized by the first cell length in the free jet, Δ . The limiting nozzle-to-plate spacing beyond which impinging tones are not produced is slightly greater than two cell lengths of the free jet. This is close to the plate position where the second shock wave forms in the free jet location. For NPR less than 3.8, the first unstable zone ends when the first shock wave develops a conical shape. The formation of a Mach disk appears to be important to the sound production process for underexpanded impinging jets.

3. (b) Random shadowgraph photographs

Figure 5 shows a series of random shadowgraph photographs taken at NPR = 4.06 for a range of nozzle-to-plate spacings. Two shadowgraph photographs were taken at random points in the oscillation cycle for operating conditions where tones were produced and a single photograph was taken when no tones were produced. Discrete frequency tones falling along the L1 line in Fig. 2 are produced by the operating conditions associated with Figs. 5 (a) - (c), and 5 (e).

A low frequency sound wave centered on the near wall region and high frequency sound waves centered on the

first shock wave and the standoff shock wave are observed in the photographs of Fig. 5 (b) and (c). Although the high frequency sound waves appear to be intense, their frequencies are beyond the detection range of the microphones used in the experiments. These tones are not the focus of the present paper.

The photographs in Fig. 5 (a) show that when the plate is located near the end of the first free jet cell length, the first shock wave forms close to the nozzle and the diameter of the first Mach disk is larger than it would be in the free jet. During portions of the cycle, a second shock wave forms in front of the plate and the shape and diameter of the first Mach disk change. As the plate is moved downstream into the second free jet shock cell (see Fig. 5 (b)), the diameter of the Mach disk decreases and the first shock wave moves downstream. During the oscillation cycle, the first shock wave changes shape, the standoff shock wave moves along the jet axis, and a wave is observed in the central region of the jet between the first shock wave and the standoff shock wave. When the plate is located near the end of the first unstable region as shown in Fig. 5 (c), the axial distance between the nozzle and the end of the first shock wave is approximately 88 % of the distance to the first cell ending in the free jet. The second shock wave develops a nearly conical shape for a portion of the oscillation cycle as it does in the free jet. A third shock wave also appears in front of the plate for portions of the oscillation cycle.

The photograph in Fig. 5 (d) was taken for a nozzle-to-plate spacing falling between the first and second unstable zones in Fig. 4. No discrete tones are produced at this operating condition. The first shock is located in the free jet position and, because of the small diameter of the Mach disk, the flow rapidly accelerates to supersonic speeds downstream due to the expansion fan developed at the end of the first shock wave. A second dome shaped shock wave forms close to the plate. A third (annular) shock wave appears in the supersonic flow behind the second shock wave.

When the plate is located just in front of the second free jet cell ending, the second unstable region is reached and the photographs in Fig. 5 (e) are obtained. The second shock wave changes shape throughout the oscillation cycle and develops a slightly conical shape at some positions in the cycle. At times, a third (annular) shock wave appears in front of the plate.

Photographs taken for plate spacings greater than the second free jet cell length Figs. 5 (f) and (g). No tones are produced beyond approximately $h/\Delta = 2.1$. The stable second shock wave has a conical shape as occurs

in the free jet and is located close to its axial position in the free jet. A third stable shock wave is also present.

The results obtained from Fig. 5 indicate that tonal production is associated with unsteady motion of the standoff shock wave. During the oscillation cycle, the standoff shock wave moves axially, changes shape, and, for some operating conditions, periodically disappears. The end of the first unstable region occurs when the plate position is such that the first shock wave is located near its position in the free jet and a second dome shaped shock wave appears near the plate. As the plate spacing is increased, the second shock wave begins to oscillate and develops a slight conical shape for portions of the oscillation cycle. A further increase in the nozzle-to-plate spacing causes the second shock wave to be positioned near the free jet location and tonal production ceases. This occurs for plate spacings approximately equal to 2.1 - 2.2 free jet cell lengths. For all greater spacings, the second shock wave is nearly conical.

A plot of the shock wave locations in the impinging jet for a range of nozzle-to-plate spacings and NPR is shown in Fig. 6. The results from this figure indicate that the shock locations depend highly on the location of the plate in the free jet cell structure and only slightly on NPR. In general, the first shock wave forms in the free jet location for nozzle-to-plate spacings greater than, or equal to, approximately 1.8 cell lengths. The second shock wave forms in the free jet location for nozzle-to-plate spacings greater than, or equal to, approximately 2.1 - 2.2 cell lengths which is close to the plate position where discrete tones are no longer produced (see Fig. 4).

3. (c) Phase-locked shadowgraph studies

Phase-locked shadowgraph photographs were taken for nozzle-to-plate spacings ranging from 0.9 to 1.6 free jet cell lengths and for NPR equal to 3.72 and 4.06

Phase-locked shadowgraph photographs for a nozzle-pressure ratio of 3.72 and $h/\Delta = 1.35$ are shown in Fig. 7. Figure 7 (a) has been arbitrarily selected as the beginning of the oscillation cycle. Although the photographs were taken in different cycles, the time delay, t , between Fig. 7 (a) and subsequent photographs is measured as a fraction of the period, T , in one cycle.

Near the beginning of the oscillation cycle as shown in Fig. 7 (a), the standoff annular shock wave is in its most upstream location and a weak moving shock wave is located along the central regions of the jet behind the first Mach disk. Relative to the moving shock wave, the flow behind the first Mach disk must be supersonic. As shown in Figs. 7 (b) and (c), the wave in the central

region of the jet moves upstream and the standoff annular shock moves slightly downstream as time progresses. In Fig. 7 (c), the moving shock wave in the central region of the jet is replaced by a series of sound waves. Jet disturbances are observed near the first shock wave and the radius of the first shock wave decreases. The standoff shock wave begins to move downstream in Fig. 7 (d). The photographs in Fig. 7 (e) and (f) indicate that, near the end of the cycle, the standoff shock wave moves toward the plate, disappears, and is replaced by a series of compression and expansion waves. The angle of the first shock wave decreases dramatically when the standoff shock wave disappears.

An intense sound wave radiates from the near wall region and is observed near the nozzle exit in Fig. 7 (d). High frequency sound waves visible in Figs. 7 (b), (c), and (e) appear to originate from the standoff shock wave the first shock wave and are most likely produced by jet disturbances, visible in Fig. 7 (c), interacting with the first and standoff shock waves.

A plot of the shock wave motion over one cycle for the operating conditions used in Fig. 7 is shown in Fig. 8. The axial position of the first shock wave changes only slightly while the axial position of the standoff shock wave increases throughout the cycle until a position is reached where the standoff shock wave briefly disappears. The standoff shock wave reforms upstream at the beginning of the next cycle.

The point in the oscillation cycle where sound is produced is indicated in Fig. 8. This point was calculated by measuring the distance from the near wall region to the sound wave in Fig. 7(d), then calculating the propagation time from the near wall region. The sound appears to be emitted near the point in the oscillation cycle where the standoff shock wave disappears.

3. (d) Plate pressure measurements

Unsteady plate pressure measurements were conducted by Henderson¹⁵ for NPR 4.06 and $h/\Delta = 1.05$. A PCB type 105A transducer was mounted on a sliding arm so that the transducer could be moved incrementally across the diameter of the plate. For these operating conditions, a single tone falling along the L1 line in Fig. 2 is produced

The data from the experiments of Henderson¹⁵ are presented in Fig. 9. Only the amplitudes associated with the L1 tone are plotted in the figure. The plate pressures are normalized by the pressure at the plate center. The plot only reflects unsteady pressures in the jet since steady jet pressures occur at 0 frequency. As

indicated in the plot, the pressure is higher in the impingement region and drops off rapidly at approximately 1.2 jet radii. The higher pressure in the impingement region may be associated with plane wave motion in the impingement region, a result consistent with the observed wave motion along the central region of the jet in Fig. 7. The increase in the pressure amplitude near 1.6 jet radii may be associated with motion of the expansion and compression regions in the near wall jet as the standoff shock wave oscillates.

4. Proposed sound source mechanism

The experiments reported here focussed on moderately and highly underexpanded jets impinging on large plates. Although Mach disks do not occur in the free jet below NPR = 3.8, Mach disks occur in the impinging jet for NPR less than, or equal to, 3.38 for h/d less than approximately 1.5 free jet cell lengths. Impinging jets operating in this pressure range predominantly produce tones associated with symmetrical disturbances, display zones of silence, have Mach disks along the central portion of the jet for the first unstable region (based on nozzle-to-plate spacing), and become stable when the first or second shock waves develop a conical shape. Low frequency "impinging" tones are produced in the near wall region and higher frequency tones are sometimes produced in the jet at the first shock wave and standoff shock wave locations.

The instability of these jets appears to be confined predominantly to the impingement and near wall regions. The first shock wave remains relatively stationary, a result in direct contrast to small plate tones where the first shock wave exhibits large axial oscillations. A comparison made between small plate impingement and large plate impingement at the same NPR and nozzle-to-plate spacing indicates that, when a large plate is used, the first shock wave forms downstream of the greatest axial distance to the first shock wave occurring in small plate impingement flow.

Large plate impinging tones are part of a feedback loop to the nozzle. Jet disturbances created at the nozzle exit travel downstream and interact with the first shock wave causing shock wave and expansion fan distortions, changes in the slip stream location, and the production of sound waves in the flow. The sound waves and stream disturbances travel downstream and affect the slip stream and standoff shock wave. The sound waves reflect from the plate with no phase shift and travel upstream in the subsonic flow along the central region of the jet. The creation of a large Mach disk in the first shock wave and a plate location that is reasonably close to the first shock wave causes the flow downstream of the Mach disk to remain at subsonic speeds. As the sound waves move upstream, the slip

stream and intersecting expansion fan change causing changes in the supersonic flow in the peripheral regions of the jet. The motion of the stream disturbances and the sound waves within the jet cause the standoff shock wave to move along the jet axis and sometimes disappear. For NPR less than, or equal to 3.72, sound ceases when the plate distance increases and the first Mach disk disappears causing the entire flow behind the first shock wave to remain at supersonic speeds. Tones also cease for higher pressures when the second shock wave develops a conical shape at approximately $h/\Delta = 2.2$.

A 'zone of silence' occurs at intermediate spacings for $NPR = 4.06$ when the second shock wave forms close to the plate and is dome shaped. For this situation, the flow behind the first shock wave accelerates before reaching the second shock wave. Sound wave motion can only occur in the limited impingement region flow and a strong resonance is not produced. This is presumably due to the fact that the sonic line is close to the jet boundary and wave motion in the impingement region does not significantly effect the location of this line or the supersonic flow in the peripheral regions of the jet. When the distance between the second shock wave and the plate increases slightly, the flow velocity behind the second shock wave increases and the standoff shock wave oscillates.

An expansion fan occurs at the intersection of the jet boundary and the standoff shock wave. The waves from the fan reflect from the sonic line behind the standoff shock wave as compression waves. The reflected compression waves reach the jet boundary and are reflected as expansion waves. A successive pattern of compression and expansion continues in the wall jet for a few jet radii. In steady jets, local separation has also been observed in the near wall region (see Carling and Hunt¹⁶) for some operating conditions. As the standoff shock wave oscillates, changes occur in the downstream expansion fan and in the compression and expansion regions in the wall jet. Oscillations of the wall jet boundary result. Oscillatory separation of the flow along the plate may also enhance the motion of the jet boundary. The oscillatory motion of the flow in the near wall region produces sound that travels back to the nozzle to create stream disturbances, thus closing the feedback loop. Glaznev's¹⁷ sound production model which treats the oscillating jet boundary as an oscillating conical membrane may apply to large plate tones although his experiments were conducted on small plates.

The feedback loop must include jet disturbances created at the nozzle. Strong resonance is not produced by one-dimensional wave motion confined to the impingement

region (see Morch¹⁸). Although wave motion is observed in the central subsonic flow, the process must be forced from upstream most likely when the jet disturbances and first shock wave interact. As the stream disturbances and sound waves travel downstream, the slip stream distorts and causes the standoff shock wave to oscillate.

A better understanding of the flow along the central regions of the jet and in the impingement and near wall regions is necessary to develop a more precise feedback model and a better understanding of the sound production mechanism. The relative importance of the stream disturbances and the sound waves in the subsonic flow to the distortion of the slip stream is not known. Although Carling and Hunt¹⁶ found that, the occurrence of a stagnation bubble did not significantly effect the wall jet in steady flow, an oscillating stagnation bubble may be important in an unstable jet and this aspect of the flow should be investigated further. The nature of the unsteady wall jet also needs further attention. Unsteady plate pressure measurements indicate that an unsteady region of pressure occurs at approximately 1.6 nozzle radii which appears to be close to the location where impinging tones are created in the flow. A better understanding of the flow in this region of the wall jet will enhance the development of a more precise sound production model.

5. Conclusions

Low frequency impingement tones produced by moderately and highly underexpanded supersonic jets are produced in the near wall region of the jet. The tones cease when the second shock wave is located in the free jet position which occurs for a nozzle-to-plate spacing of approximately 2.1 - 2.2 free jet cell lengths. 'Zones of silence' appear to be associated with the formation of conical shock waves in the flow. Discrete frequency sound is produced in the near wall region and is associated with oscillations of the standoff shock wave and motion of the expansion and compression regions in the near wall jet.

Acknowledgements

This work was supported by NASA Glenn Research Center through the Summer Faculty Researcher program. I would like to thank James Brides of NASA Glenn Research Center and J. Panda of Modern Technologies Corporation for their assistance and support of this project.

References

- Powell, A. (1988). "The sound-producing oscillations of round underexpanded jets impinging on normal plates," *J. Acoustic. Soc. Am.* **83**, 515-533.
- Powell, A., and Henderson, B. (1990). "On the tones of round underexpanded jets impinging on normal plates, AIAA-90-3985.
- Henderson, B. and Powell, A. (1993). "Experiments concerning tones produced by an axisymmetric choked jet impinging on a flat plate," *J. Sound Vib.* **168**(2), 307-326.
- Glaznev, V. N., and Popov, V. Y. (1992). "Effects of the face dimensions of a flat barrier on the self-oscillations generated in the interaction with a supersonic underexpanded jet," Translated from *Izvestiya Rossiiskoi Akademii Nauk, Mekhanika Zhidkosti i Gaza* **6**, 164-168.
- Henderson, B. and Powell, A. (1996). "Sound producing mechanisms of the axisymmetric choked jet impinging on small plates: The production of primary tones," *J Acoust. Soc. Am.* **99**, 153-162.
- Henderson, B., and Powell, A. (1997). "The use of an array to explain the sound characteristics of secondary small plate tones produced by the impingement of an axisymmetric choked jet," *J. Acoust. Soc. Am.* **102**, 1454-1462.
- Gubanova, O. I., Lunev, V. V., and Plastinina, L. N. (1973). "The central breakaway zone with interaction between a supersonic underexpanded jet and a barrier," *Fluid Dynamics* **6**, 298-301 (Translated from *Izvestiya Akademii Nauk SSSR, Mekhanika Zhidkosti i Gaza* **2**, 135-138 (1971)).
- Ginzburg, I. P., Semiletenko, V. N., and Uskov, V. N. (1975). "Experimental study of underexpanded jets impinging normally on a plane baffle," *Fluid Mechanics-Soviet Research* **4**(3), 93-105.
- Alvi, Iyer (1999). "Mean and unsteady flowfield properties of supersonic impinging jets with lift plates," AIAA 99-1829.
- Nakatogawa, T., Hirata, M. and Kukita, Y. (1971). "Disintegration of a supersonic jet impinging normally on a flat plate," *J. Spacecraft* **8**(4), 410-411.
- Semiletenko, B. G., Sobkolov, B. N., and Uskov, V. N. (1974). "Features of unstable interaction between a supersonic jet and infinite baffle," *Fluid Mechanics-Soviet Research* **3**(1), 90-95.
- Back and Sarohia (1978). "Pressure pulsations on a flat plate normal to an underexpanded jet," *J. AIAA* **16**(6), 634-636.
- Krothapalli, A., Rajkuperan, E. Alvi, F., and Lourenco, L. (1999). "Flow field noise characteristics of a supersonic impinging jet," *J. Fluid Mech.* **392**, 155-181.
- Wlezien, R. W., and Ferraro, P. J. (1990). "Aeroacoustic environment of an advanced STOVL aircraft in hover," AIAA 90-4016.
- Henderson, B. (1993). *Sound Source Mechanisms of the Axisymmetric Supersonic Impinging Jet*, Ph. D. Dissertation, University of Houston.
- Carling, J. C. and Hunt, B. L. (1974). "The near wall jet of a normally impinging, uniform, axisymmetric, supersonic jet," *J. Fluid Mech.* **66**, 159-176.
- Glaznev, V. N. (1977). "Sound field of an underexpanded supersonic jet impinging on a barrier," *Sov. Phys. Acoust.* **23**, 142-145.
- Morch (1964). "A theory for the mode of operation of the Hartmann air jet generator," *J. Fluid Mech.* **20**, 141-159.

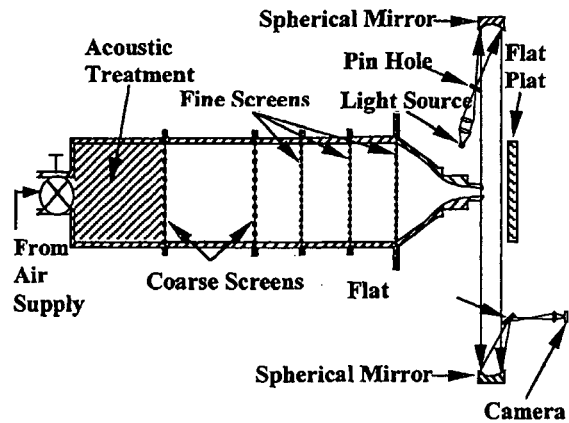


Figure 1. A schematic of the experimental facility at NASA Glenn Research Center.

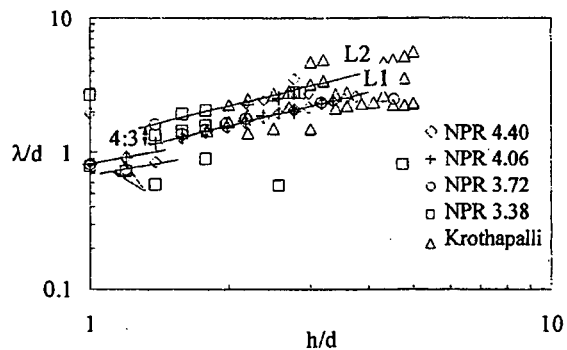


Figure 2. The acoustic data from the present study and from Krothapalli et al.¹³

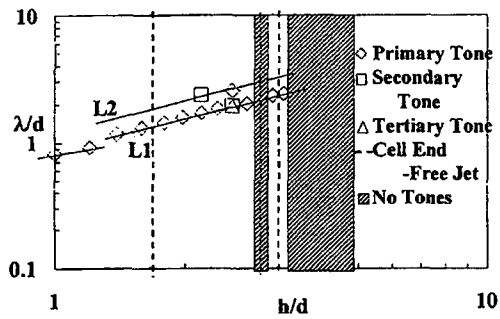


Figure 3. The acoustic data for NPR = 4.06.

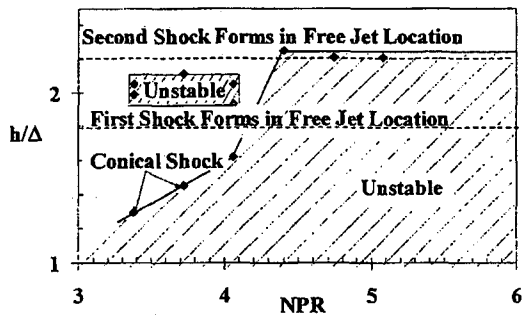
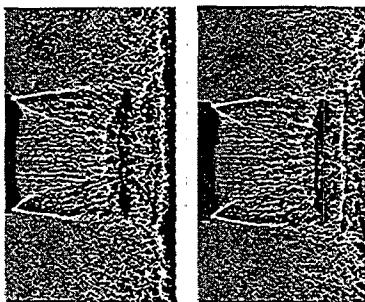
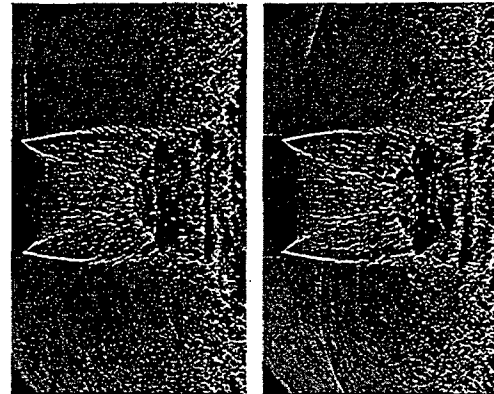


Figure 4. The unstable regions where discrete impinging tones are produced.

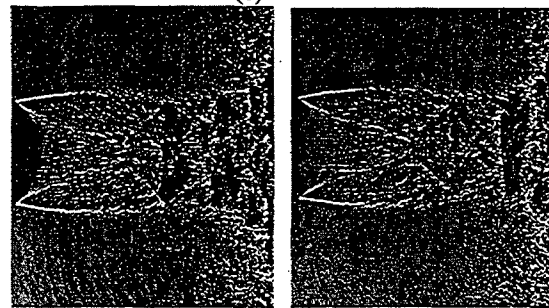


(a)

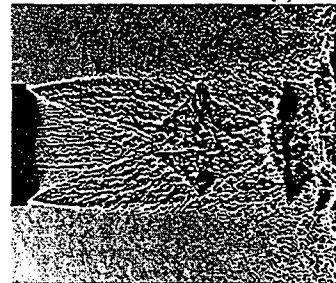
Figure 5 (a). See next page for caption.



(b)

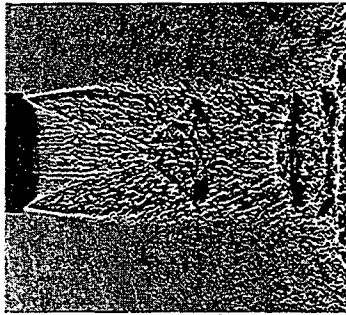


(c)

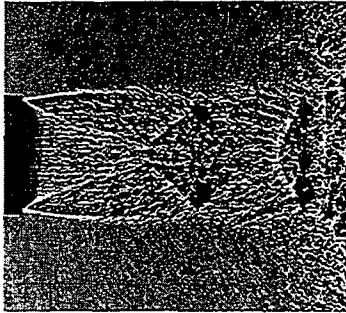


(d)

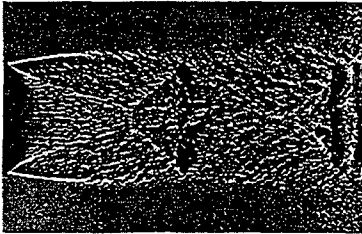
Figures 5 (b), (c), (d). See next page for caption.



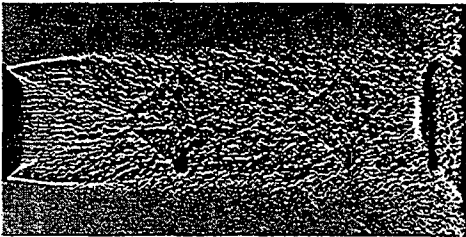
(e)



(e)



(f)



(g)

Figure 5. Shadowgraph photographs taken at NPR = 4.06 and (a) $h/\Delta = 0.95$ ($f = 10$ kHz), (b) $h/\Delta = 1.38$ ($f = 7.9$ Hz), (c) $h/\Delta = 1.61$ ($f = 6.75$ Hz), (d) $h/\Delta = 1.78$ (no tones), (e) $h/\Delta = 1.90$ ($f = 5.75$ Hz), (f) $h/\Delta = 2.13$ (no tone), and (g) $h/\Delta = 2.60$ (no tones).

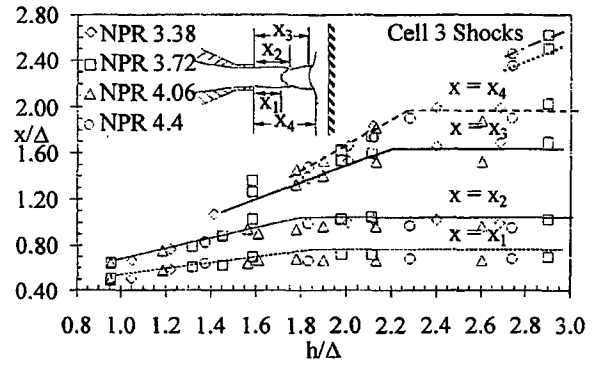


Figure 6. The axial locations of the first, second, and third shock waves.

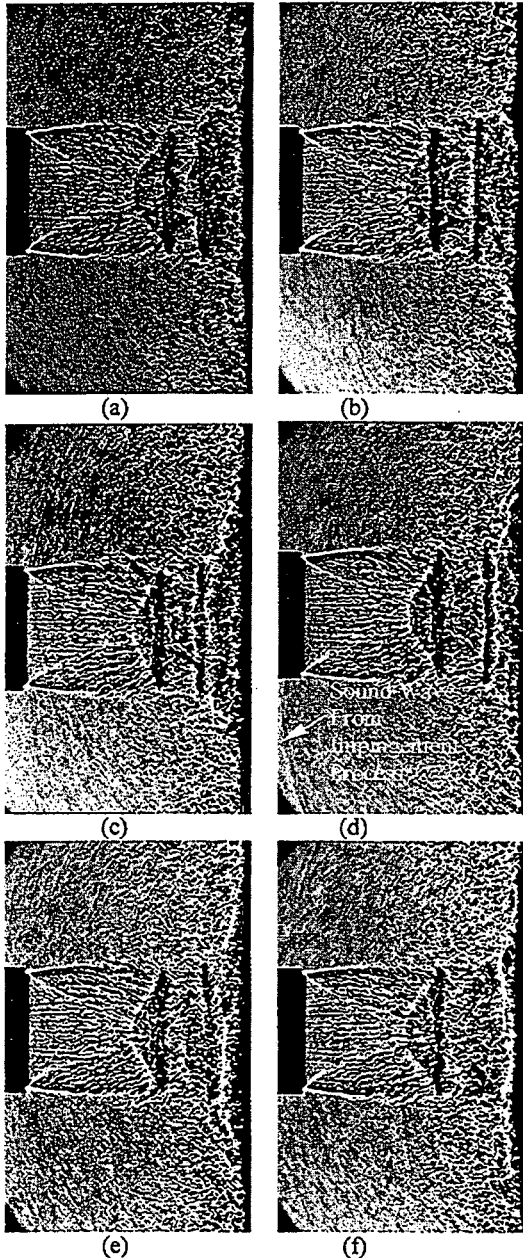


Figure 7. Phase-locked photographs taken at $NPR = 3.72$ and $h/\Delta = 1.35$ for (a) $t/T = 0$, (b) $t/T = 0.12$, (c) $t/T = 0.28$, (d) $t/T = 0.48$ (e) $t/T = 0.60$, and (f) $t/T = 0.78$.

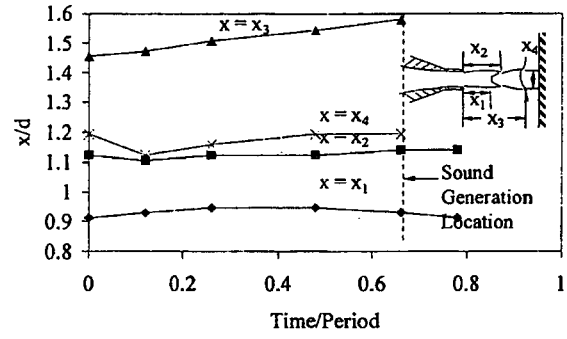


Figure 8. Shock wave motion over one oscillation cycle for $NPR = 3.72$ and $h/\Delta = 1.35$.

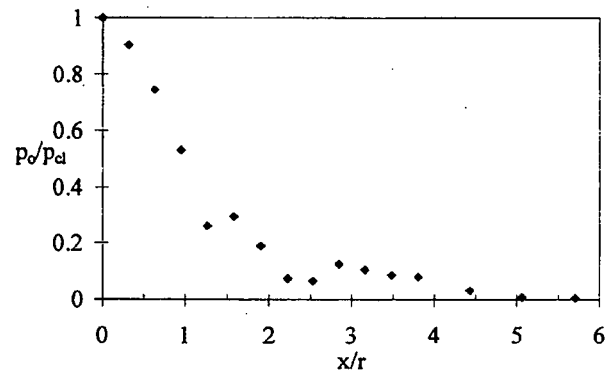


Figure 9. Root-mean-square plate pressures at radial locations along the plate, where x is the distance from the center of the plate to the pressure tap, and r is the nozzle exit radius.

Fluorescence Imaging Study of Impinging Underexpanded Jets

Jennifer A.(Wilkes) Inman^{*}, Paul M. Danchy[†], Robert J. Nowak[‡], and David W. Alderfer[§]
NASA Langley Research Center, Hampton VA, 23681-2199

An experiment was designed to create a simplified simulation of the flow through a hole in the surface of a hypersonic aerospace vehicle and the subsequent impingement of the flow on internal structures. In addition to planar laser-induced fluorescence (PLIF) flow visualization, pressure measurements were recorded on the surface of an impingement target. The PLIF images themselves provide quantitative spatial information about structure of the impinging jets. The images also help in the interpretation of impingement surface pressure profiles by highlighting the flow structures corresponding to distinctive features of these pressure profiles. The shape of the pressure distribution along the impingement surface was found to be double-peaked in cases with a sufficiently high jet-exit-to-ambient pressure ratio so as to have a Mach disk, as well as in cases where a flow feature called a recirculation bubble formed at the impingement surface. The formation of a recirculation bubble was in turn found to depend very sensitively upon the jet-exit-to-ambient pressure ratio. The pressure measured at the surface was typically less than half the nozzle plenum pressure at low jet pressure ratios and decreased with increasing jet pressure ratios. Angled impingement cases showed that impingement at a 60° angle resulted in up to a factor of three increase in maximum pressure at the plate compared to normal incidence.

Nomenclature

D_e	=	nozzle exit diameter
D_{imp}	=	impingement distance, measured from nozzle exit plane to impingement target
JPR	=	jet pressure ratio (ratio of nozzle exit to ambient pressure)
NO	=	nitric oxide
p_0	=	nozzle plenum pressure
p_a	=	test chamber (ambient) pressure
p_e	=	static pressure at nozzle exit
p_{max}	=	maximum (peak) pressure
PLIF	=	planar laser-induced fluorescence
Re_{exit}	=	Reynolds number at nozzle exit
RTF	=	Return to Flight
V_e	=	velocity at nozzle exit
μ_e	=	dynamic viscosity at nozzle exit
θ_{imp}	=	impingement angle
ρ_e	=	density at nozzle exit

I. Introduction

In the wake of the loss of the Columbia orbiter due to a breach in the leading edge of its left wing, a series of tests were conducted in an effort to better understand the flowfields resulting from breaches in the outer structure of reentry vehicles. Penetration of hot gas through breaches could impact internal structures, causing failure of the

^{*} Research Scientist, Advanced Sensing and Optical Measurement Branch, MS 493, AIAA Member

[†] Research Scientist, Advanced Sensing and Optical Measurement Branch, MS 493, AIAA Associate Fellow

[‡] Research Scientist, Aerothermodynamics Branch, MS 408A, AIAA Member

[§] Research Scientist, Advanced Sensing and Optical Measurement Branch, MS 493

vehicle. These tests were conducted in support of the Orbiter Aerothermodynamics Working Group as part of NASA's Shuttle Return to Flight (RTF) effort. A subset of these tests used planar laser-induced fluorescence (PLIF) of nitric oxide (NO) to visualize the flow issuing from a nozzle into a low-pressure chamber. The flow environments encountered in these tests include regions of low static pressure, turbulent and/or three-dimensional flow structures, and regions of interest with both strong and weak density gradients. Such conditions, though frequently encountered in aerospace simulation facilities, cannot be satisfactorily visualized using traditional path-averaged techniques such as schlieren and shadowgraph, which rely on sufficiently strong density gradients. An alternative approach was therefore required in order to satisfy the objectives of these tests to characterize the features of these nozzle flows. PLIF is a flow visualization technique that provides non-intrusive measurements with sub-millimeter spatial resolution and flow-stopping ($1 \mu\text{s}$) temporal resolution in many of these challenging testing regimes¹. PLIF images reveal the size and location of flow structures. Additionally, these images can be used to identify the laminar or turbulent state of these flows². We have previously reported the use of PLIF to investigate free (non-impinging) underexpanded sonic jets³ and have compared a subset of these results with computational fluid dynamics (CFD)⁴. This paper will focus on the results of the test cases in which the nozzle flow was directed onto the surface of a flat plate (hereafter referred to as the "impingement target") at various distances and angles. A future paper will report the results of these tests in regards to the effect of jet impingement upon the process of transition to turbulence. This paper will mainly focus upon the test cases involving steady, laminar, impinging jet flows.

A major difference between this work and the majority of previous investigations of similar impinging flows by others is that this work focused on relatively low Reynolds numbers, spanning from many fully laminar test cases to transitional and turbulent cases. By contrast, other investigations have generally involved higher Reynolds numbers—up to three orders of magnitude higher than the very highest Reynolds numbers investigated in the present work and well within the turbulent flow regime. Table 1 gives a summary of test conditions for several past investigations.

	M_e	Re_{exit}	JPR (p_j/p_e)	p_a (atm)	D_{imp} $/D_e$	θ_{imp} (deg)	Type(s) of measurements
Alvi & Iyer ⁵ (1999)	1	1.9E6	2.6	1	1.8-2	90	PIV, shadowgraph, acoustic, surface pressure
Donaldson & Snedeker ^{6,7} (1971)	0.57,1	1.8E5- 1.3E6	1-3.57	1	1.96- 39.1	15-90	Pitot & surface pressure, grease streak, heat transfer
Kim et al. ⁸ (2003)	1	9.7E5- 2.7E6	1.1-3.7	1	1.8-2	90	Computational (3D unsteady NS)
Lamont & Hunt ⁹ (1980)	2.2	4.0E6- 6.7E6	1.2,2	1	0.75-15	30-90	Shadowgraph, surface pressure
Love & Lee ¹⁰ (1958)	1-3	1.7E5- 5.7E7	0.25-19, 60- 41,820	1, 5e-5	NA	NA	Schlieren, method of characteristics calculations
Stitt ¹¹ (1961)	1-9.85	3.7E4- 2.7E7	545- 1.5E5	4.7E-4	0.4-40	90	Schlieren, surface pressure, surface erosion
Present work	1, 2.6	170- 3.6E4	1-37	1.3E-3 -0.094	10.5- 39.5	90, 60, 45	PLIF, surface pressure

Table 1. Comparison of previous underexpanded jet studies with the present investigation. The quantities compared here are, from left to right: nozzle exit Mach number, exit Reynolds number, jet (nozzle-exit-to-ambient) pressure ratio, ambient pressure of test section, impingement distance in nozzle diameters, impingement angle, and type of study and/or measurements.

atmospheric pressure. Of the studies listed in Table 1, only those of Stitt¹¹ and Love and Lee¹⁰ investigated flows into sub-atmospheric pressure environments. For those studies, the intended application was rocket and thruster operation in the vacuum of space, and so the ambient pressures used were one to two orders of magnitude lower than those of the present study, the conditions of which were designed to be relevant to the reentry conditions experienced by the space shuttle orbiter.

Another distinction is that these previous studies have generally been concerned with near-field impingement, on the order of a few jet diameters. The impinging jet configurations in the present work, with the closest impingement distance being about 10.5 nozzle diameters and the furthest being 39.5 nozzle diameters, are all relatively far-field compared to the studies listed in Table 1 (with the exception of Stitt.¹¹ Note also that, even though the investigations of Donaldson and Snedeker^{6,7} had some limited data at about 40 nozzle diameters, the vast majority of their data were within about 15 nozzle diameters). In rocket plume/ground interaction applications, ground erosion was a primary concern, and the near field was thus of greatest significance. Many of these studies were conducted at

In addition to flow visualization, pressure measurements were recorded on the surface of the impingement target. The observed pressure profiles along the centerline of the target were found to fall into two broad categories: those with the maximum pressure corresponding to the centerline of the jet axis, and those with the maximum pressure occurring in an annular ring, away from this axis. PLIF images helped to elucidate the characteristics of the resulting pressure profiles by highlighting the flow structures corresponding to distinctive features of these pressure profiles.

II. Experimental Description

A. Facility and Hardware

Tests were conducted at the NASA Langley Research Center using the test section of the 15-Inch Mach 6 Air Tunnel as a vacuum chamber. For a detailed description of the facility and hardware, see Ref. 12. A schematic of the layout is shown in Fig. 1. Nitrogen or helium seeded with 0.5% nitric oxide was plumbed into a heated stainless steel plenum, through a nozzle, and into the vacuum chamber.

Two different nozzles were used. The geometry of these nozzles is illustrated in Fig. 2. The first was a converging nozzle with a nominal exit Mach number of 1. This nozzle is hereafter referred to as the *sonic* nozzle. The second was a converging/diverging nozzle with a nominal exit Mach number of 2.6, hereafter called the *supersonic* nozzle. Mass flow controllers controlled the flow rates, which indirectly controlled the plenum pressure upstream of the nozzle.

Optics directed a 100mm wide by ~0.2mm (FWHM) thick laser sheet vertically downward through a window in the top of the test chamber. The laser sheet was oriented in a plane perpendicular to the nozzle exit plane. The sheet forming optics were mounted to a translation stage. A stepper motor attached to the translation stage allowed fine adjustment of the spanwise position of the laser sheet.

A 4-inch diameter stainless steel impingement disk was positioned at various distances and angles downstream of the nozzle exit. Figure 3 shows a diagram of this apparatus. The center of this disk included 32 pressure taps. They were spaced 0.045 inches apart, and had an inside diameter of .021 inches. The taps were oriented in a vertical plane (the plane of the laser sheet), on the jet centerline. From the camera's viewing angle, the jet flow was from left to right.

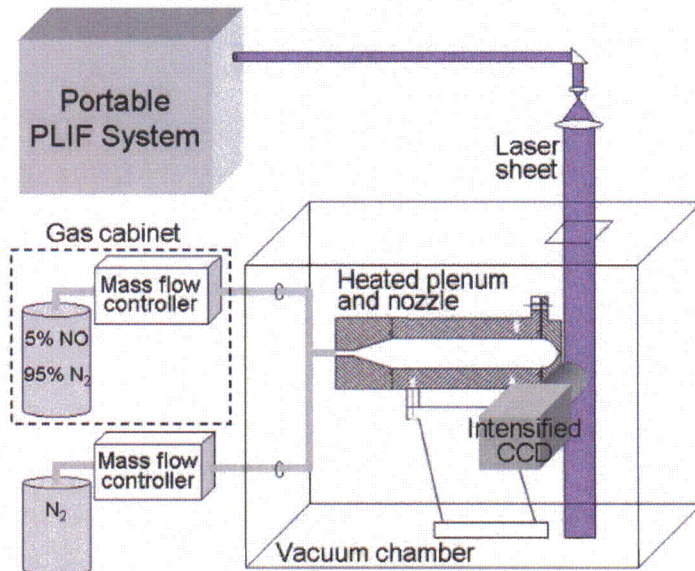


Figure 1. PLIF system and experimental hardware. Gas is plumbed through a heated plenum and nozzle into a vacuum chamber. A laser sheet enters the top of the vacuum chamber and excites nitric oxide molecules in the flow. An intensified CCD camera positioned at right angles to the laser sheet images the fluorescence.

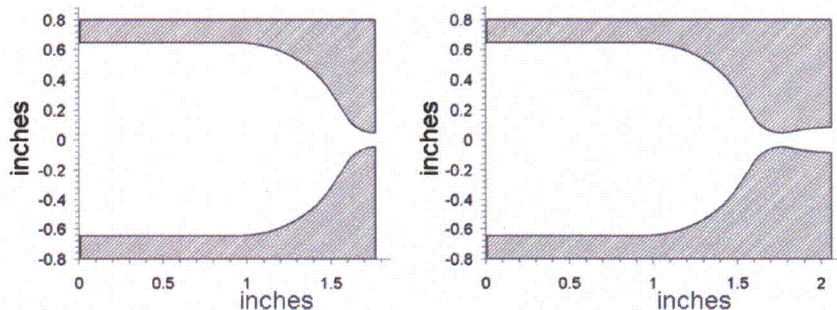


Figure 2. Sonic and supersonic nozzle geometries. The design exit Mach numbers for these two nozzles are 1 and 2.6, respectively.

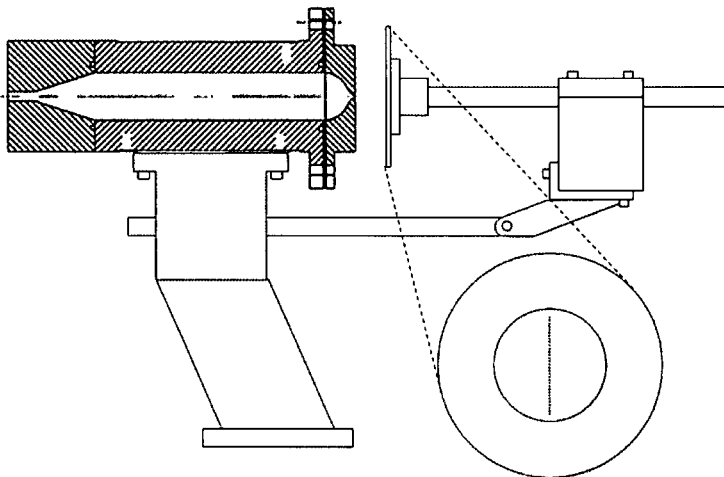


Figure 3. Stainless steel plenum and impingement target hardware. The impingement angle and distance were continuously variable. A close-up view shows the orientation of the 32 pressure taps in the center of the impingement disk.

camera viewing angle, about the horizontal axis perpendicular to the jet axis.

For each hardware configuration, two flow parameters were varied: the exit Reynolds number (Re_{exit}) and the jet pressure ratio (JPR). Re_{exit} was defined in terms of the nozzle exit diameter, D_e , and the density ρ_e , velocity V_e , and dynamic viscosity μ_e at the nozzle exit, as given by (1).

$$Re_{exit} = \frac{\rho_e V_e D_e}{\mu_e} \quad (1)$$

Re_{exit} was varied by changing the mass flow rates and nozzle plenum temperature. JPR was defined as the ratio of the static pressure at the nozzle exit, p_e , to the ambient pressure in the test chamber, p_a , according to (2), and was varied by changing the test section pressure for a given Reynolds number (and therefore, a fixed p_e).

$$JPR = \frac{p_e}{p_a} \quad (2)$$

C. Planar Laser-Induced Fluorescence (PLIF) Flow Visualization Technique

The PLIF laser system includes a tunable Nd:YAG-pumped dye laser followed by doubling and mixing crystals. The resulting output, at 226.256 nm, was tuned to excite the strongly fluorescing spectral lines of NO near the Q_1 branch head (Q denotes a change in rotational quantum number equal to zero). Optics formed the beam into a laser sheet that was 100 mm wide x ~0.2 mm thick (FWHM) in the measurement region. Fluorescence was imaged onto a gated, intensified CCD at a viewing angle normal to the laser sheet. Images were acquired at 10 Hz with a 1 μ s camera gate and a spatial resolution of between 3 and 7 pixels/mm, depending on the required field of view for a given hardware configuration. This system is detailed in Refs. 3, 4, and 12. The PLIF system is also capable of pressure-sensitive and velocity-sensitive flow imaging.

III. Analysis Methods: Flow Visualization Image Processing

Sets of 100 single-shot images were acquired for a range of unit Re_{exit} (177 to 35,700) and JPR (1.8 to 38). So-called *background images* were also acquired on each day of testing for a range of vacuum chamber pressures. During the acquisition of these background images, the laser was fired but no gas was flowing through the nozzle. Any nonzero intensity in these background images is attributed to either camera dark current or the laser scatter and room light not blocked by the filter in front of the camera lens. Averaged background images were created from the average of 100 single-shot images in order to smooth out random shot-to-shot variations in background intensity.

Single-shot images were processed to correct for background scattered light and camera dark current as well as mean spatial variations in laser sheet intensity. Conveniently, jet gas containing nitric oxide diffused relatively uniformly into the test chamber in regions away from the jet, but still imaged by the camera. The fluorescence from

B. Model Configuration Parameters

Impingement distance was continuously variable from 0 to 6 inches and impingement angle was continuously variable from 90° to 0°, though the minimum impingement distance at non-normal impingement angles was limited by the physical size of the target. In practice, changing impingement distance or angle required approximately a half day of down time, and so a limited number of discrete distances and angles were included in the test matrix. For the majority of cases, the impingement disk was oriented normal to the jet axis (which is defined to be a 90° impingement angle). Two configurations included oblique impingement angles of 45° and 60°. For these cases, the target was rotated clockwise, as viewed from the

the diffuse nitric oxide in these regions provided a convenient laser-energy reference, allowing the spatial variation in the laser intensity to be corrected. This was accomplished on a shot-by-shot basis by first selecting an area of the image above the core of the jet flow and then establishing the average pixel intensity along each column in that region.

Raw images were 512 x 512 pixels; images presented in this paper have been cropped top and bottom to show the regions of greatest interest. In some of the earlier runs, the spatial resolution was determined by imaging a ruler in the same plane as the laser sheet. This process was improved midway through this set of tests, after Run 200. A *dotcard* was used in place of a ruler. Dotcards consisted of a rigid metal plates covered with a sheet of paper. The paper was white with black squares printed in a regular grid pattern. Spatial resolution was calculated by capturing images of a dotcard positioned in the same plane as the laser sheet. The optical access in these experiments permitted perpendicular viewing of the measurement plane and no significant perspective or lens distortion was found in the images.

IV. Results

Table 2 shows the range of conditions and hardware configurations for which data were taken during the impinging jet study. Reynolds numbers and jet pressure ratios were calculated based on nozzle exit conditions. The table lists the number of cases that were studied for each combination of hardware configuration and type of PLIF imaging that was investigated in these tests. For each flow visualization case, 100 single-shot images were acquired. The laser sheet was also swept spanwise through the flow, providing slices of the flow field, though these results are not shown here. The velocity-sensitive, pressure-sensitive, and density-sensitive imaging data are not presented in this paper, with the exception of one pressure-sensitive image in Fig. 9.

A. Characteristic Flow Structures

1. Sonic and supersonic free jet structures

Free (non-impinging) laminar jet cases are seen to exhibit flow structures that are similar to those of other cases having the same JPR^{12} . That is, two laminar cases with similar JPR s but different Reynolds numbers will appear more similar than two cases with the same Reynolds numbers but different JPR s. For sonic nozzle cases, flows can be divided into two major groups: those with a repeating diamond shock structure, and those with a barrel shock structure, a Mach disk, and a streamwise high-velocity jet boundary (seen for flows with JPR s greater than about 3).^{2,3} The diamond shock structure is seen for JPR s less than about three, such as in Fig. 4, where several diamond shock cells can be seen in the first several jet diameters downstream of the nozzle exit. Figures 5 and 6 show higher JPR PLIF images resulting in an underexpanded jet issuing from a sonic nozzle. Key flow structures are labeled in these figures. Figure 5 shows the nozzle plenum, nozzle exit, and ambient conditions, as well as the major shock structures and relative Mach numbers in each region of the flow. Additional flow features are labeled in Fig. 6. The arrows within the high-velocity jet boundary qualitatively indicate the velocity profile of the gas in this region. For a good description of the flow features shown in these figures, see Refs. 5 and 12.

Impingement configuration	Supersonic Nozzle				Sonic Nozzle		
	FV/VI	V	P	ρ	FV/VI	V	P
1" @ 90°					25		5
1.75" @ 90°	25	22	22	1	25		
2.5" @ 90°	22	19	21		24		
2.5" @ 60°	18						
3.75" @ 90°	23				23		
3.7" @ 45°	23						
5" @ 90°	22						
∞ (free jet)	88	11		12	53	8	8
Re_{exit}	600-14,000				2,400-35,000		
JPR	1-16				3-27		

Table 2. Matrix of configurations for which data were acquired in the impinging jet cases. FV/VI indicates flow-visualization and volume-imaging runs, V indicates velocity runs, P indicates pressure-sensitive runs, and ρ indicates density-sensitive runs.

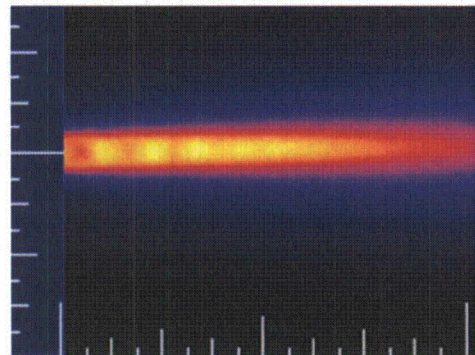


Figure 4. Diamond shock pattern in flow from sonic nozzle. This image is a 100-shot average of a flow with $JPR = 1.9$ and $Re_{exit} = 417$ (Run 5). The scales are in inches, with the smallest hash marks measuring 1/16th in.

For cases with the Mach 2.6 supersonic nozzle, the division between repeating shock patterns and barrel shock/Mach disk patterns happens at a *JPR* of about 4. For smaller *JPR*s, a repeating pattern analogous to the diamond shock pattern is evident, with a chain-like pattern of alternating spatial minima (high-pressure nodes) and maxima (low-pressure antinodes). This oscillating flow pattern can be seen for two cases in Fig. 7. As *JPR* increases, the wavelength of this oscillating pattern decreases. As a result, the number of cell structures within a fixed distance decreases for larger *JPR*s. Above a *JPR* of about 4, high pressure nodes are no longer evident, and as *JPR* continues to increase, the oscillations in the high-velocity jet boundary gradually decrease. Even larger *JPR*s lead to a modified barrel shock structure—elongated into a more egg-like shape than its comparable sonic jet counterpart—with a Mach disk and a streamwise high-velocity jet boundary, as shown in Fig. 8. In the upper image, note how the upper and lower jet boundaries appear parallel to one another. The lower image was acquired with greater magnification, and the shock and expansion reflections in the high-velocity jet boundary (labeled in Fig. 6) are visible in this lower image.

2. Impinging jet structures

Impinging jet flows can be divided roughly into three regions: the jet flow upstream of the impingement region, the impingement region, and the wall jet flow (where the flow has become parallel to the surface of the impingement target). For steady flows, the flow structures that are observed in the upstream region are essentially identical to those in free jet cases. Impingement region flow structures are described below. In the wall jet region, several factors act to decrease the intensity of the fluorescence. First, mixing of the jet fluid with the ambient gas is enhanced by the physical dispersion of the jet gas. This results in a decreasing mole fraction of nitric oxide as the gas moves away from the jet centerline. This, in turn, results in a reduction of fluorescence signal near the plate, and so the details of the flow in the wall jet region are not necessarily well-resolved.

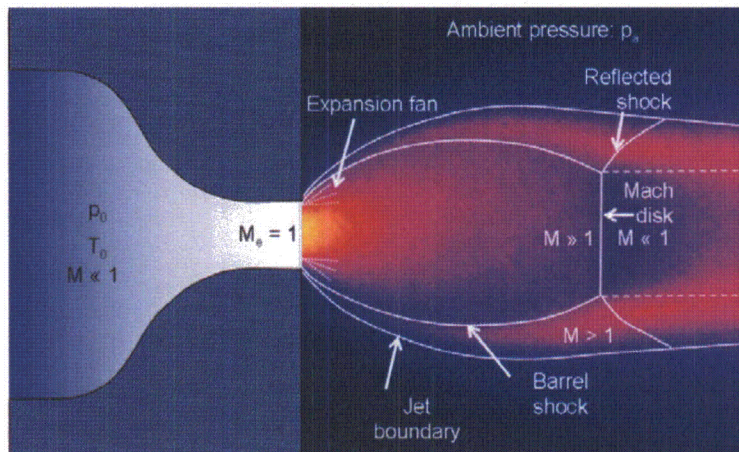


Figure 5. Major flow structures of highly-underexpanded jets. The appearance of a Mach disk is associated with jet pressure ratios greater than about 3 for the sonic nozzle and greater than about 4 for the supersonic nozzle.

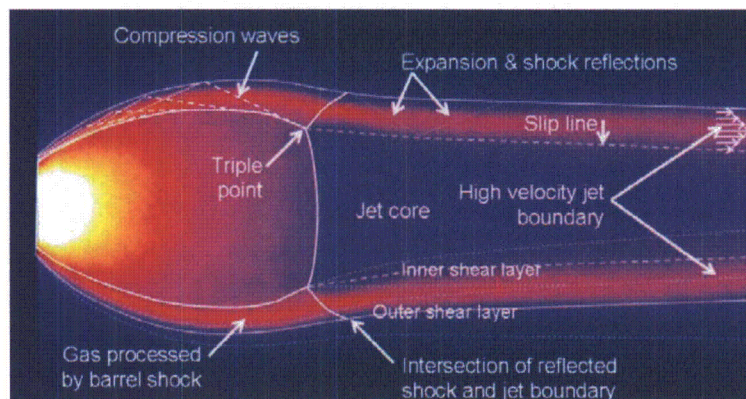


Figure 6: Detailed flow structures of highly-underexpanded sonic jets. PLIF image is from Run 56 with $JPR = 29.1$ and $Re_{exit} = 4,294$.

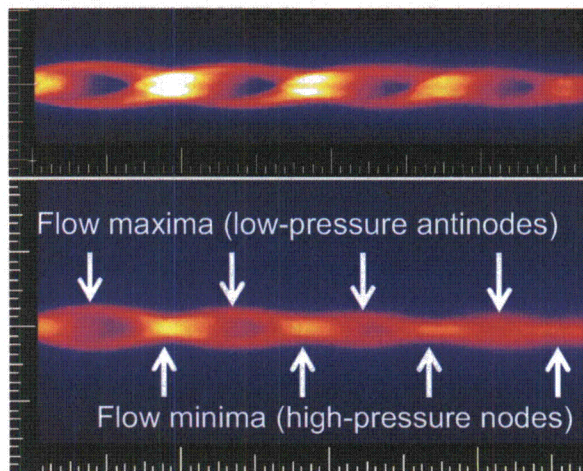


Figure 7. Underexpanded supersonic jets at low pressure ratios. Images are 100-shot averages. Top: Run 354, $JPR = 2.0$, $Re_{exit} = 4,605$; bottom: Run 222, $JPR = 3.0$, $Re_{exit} = 3,370$. Arrows mark examples of flow minima and maxima. Scales are in inches; the smallest hash marks measure 1/16th in.

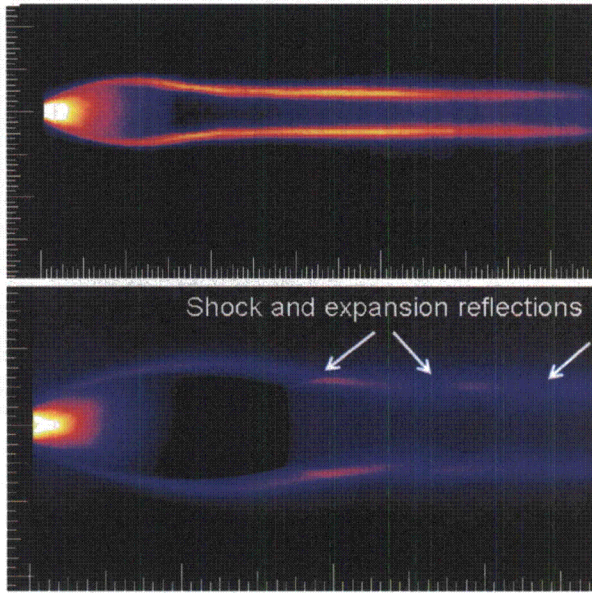


Figure 8. Supersonic free jets with Mach disks and parallel high-velocity jet boundaries. Both images are 100-shot averages. The first image is from Run 236, with $JPR = 16.2$ and $Re_{exit} = 13,104$; the second is from Run 347 with $JPR = 12.6$ and $Re_{exit} = 10,173$. Scales are in inches; the smallest hash marks measure $1/16$ th in. Note the magnified scale of the lower image.

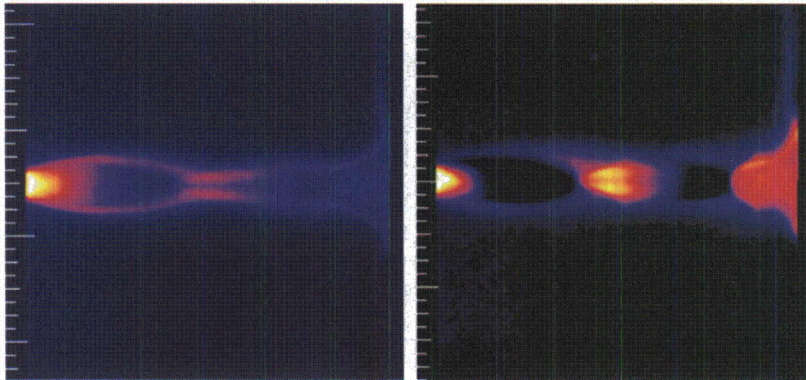


Figure 9. Comparison of flow visualization and pressure-sensitive PLIF. Left: $JPR=3.1$ (Run 363). Right: $JPR=3.0$ (Run 451). $D_{imp}/D_c=10.7$ (1.75 in.) for both. The scales are in inches, with the smallest hash marks measuring $1/16$ th in.

phenomena; that is, two dimensional jets (quasi-two dimensional in experimental studies, or truly two-dimensional in computational studies) never resulted in recirculation bubble formation. This is less surprising in the experimental cases (which can never be truly two-dimensional), since the recirculation bubble is shaped like a bell, and requires the annular pressure “seal” around the ring where it intersects with the impingement plate in order to be a stable feature. The gas inside the recirculation bubble acts as a high-pressure reservoir, contained by the plate shock upstream, the high-velocity jet boundary impingement along the outer edge, and the impingement disk surface.

Flows in the impingement region may exhibit several additional flow structures. When the flow impinging on the flat plate is supersonic, a normal shock parallel to the impingement surface, called a *plate shock*, may be formed.⁵ Under certain flow conditions, a high pressure bubble of gas may build up between this shock and the impingement surface, causing the shock to move further away from the surface.^{13,14} Choosing to excite pressure-sensitive spectral lines¹² at a laser wavelength of 225.693 nm (in which the fluorescence signal is most strongly dependent on pressure, with much weaker dependence on temperature) makes identification of such a *stagnation bubble* (also called a *recirculation bubble*) and/or normal plate shock much easier, as the pressure rise inside the recirculation region results in a large increase in intensity compared to the free jet region. Figure 9 illustrates this, with two images of similar flows, taken with the laser at two different frequencies. Both images are averages of 100 single-shots of supersonic flows, taken at an impingement distance of 1.75 in. (10.7 nozzle diameters). The image on the left was acquired with the laser tuned to flow visualization lines (226.256 nm). The image on the right was taken with the laser tuned to pressure-sensitive lines (225.693 nm). Note the well-defined boundaries of the recirculation bubble in the pressure-sensitive image as compared with the flow-visualization image. By contrast, note the lack of signal in the low pressure region inside the barrel shock in the pressure-sensitive as compared to the flow-visualization image, where there is signal throughout the flow and the jet boundary is more clearly defined.

Several studies in the literature have discussed the formation of recirculation bubbles for some combinations of jet pressure ratio and impingement distance. Alvi et al.^{15,5} give a good description of recirculation bubble formation. Mackie and Taghavi¹⁶ found that recirculation bubble formation was purely a three-dimensional

phenomena; that is, two dimensional jets (quasi-two dimensional in experimental studies, or truly two-dimensional in computational studies) never resulted in recirculation bubble formation. This is less surprising in the experimental cases (which can never be truly two-dimensional), since the recirculation bubble is shaped like a bell, and requires the annular pressure “seal” around the ring where it intersects with the impingement plate in order to be a stable feature. The gas inside the recirculation bubble acts as a high-pressure reservoir, contained by the plate shock upstream, the high-velocity jet boundary impingement along the outer edge, and the impingement disk surface.

B. Flow Structure Comparison with Pressure Profiles

Consider an impinging jet flow with a uniform momentum profile throughout the core of the jet. One would expect the pressure profile of such a jet to resemble a top hat function, with roughly uniform pressure across the intersection of the jet with the impingement target, dropping to near ambient pressure away from the core of the jet. Modifying the situation to include viscous effects, one would expect to see a decrease in momentum—and therefore a decrease in pressure on the impingement surface—along the edges of the jet. This modified pressure profile would be peaked in the center, smoothly dropping off to the ambient pressure toward the edges of the jet flow. In fact, for some cases, this describes the pressure profiles that have been measured. An example is shown in Fig. 10. The PLIF image on the left and the graph of measured impingement pressure on the right are shown aligned and equally scaled, so that the vertical axis on the graph matches the vertical location along the impingement plate in the image. All pressure profiles presented herein are time-averaged.

For some flow conditions, the pressure profiles are quite different than the smooth single-peaked profile predicted by the simple explanation. For example, some profiles typically exhibit a double-peaked structure, with the maximum pressure occurring away from the flow centerline. The peaks in pressure are found to coincide with the location of the impingement of the high-velocity jet boundary or with the intersection of the shock structure surrounding a recirculation bubble. Fluid mechanically, this can be understood because the high-velocity jet boundary carries with it a great deal of the momentum and thus creates a larger pressure rise as it impinges on the flat plate, compared to the slower jet core, which has passed through a normal shock wave at the Mach disk. The pressure between these peaks is often nearly constant, while the pressure outside these peaks drops off toward—and sometimes dips briefly below—the ambient pressure. Figure 11 shows an example of this type of profile. The high-velocity jet boundary impinges on the flat plate, and is partly reflected. That is, the flow does not immediately become tangent with the wall, but rather first appears to reflect off the surface before becoming a pure wall jet. This results in an annular suction region beneath the place where the flow is skipping above the surface, where the pressure is actually *lower* than ambient. Figure 12 shows a close up of the flow in Fig. 11. This is a case with a strong suction ring.

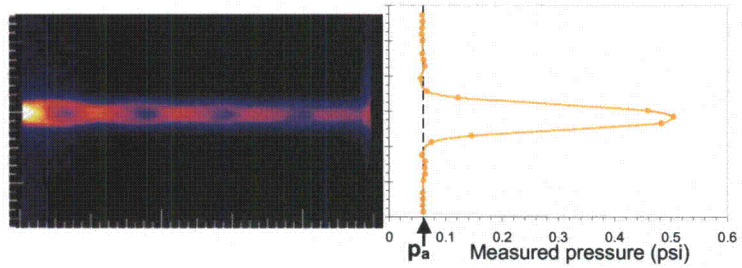


Figure 10. Pressure profile with a single, central peak. This profile is for supersonic nozzle Run 544 with $JPR = 1.5$, $Re_{exit} = 1,317$, $\theta_{imp} = 90^\circ$ and $D_{imp}/D_e = 15.2$, $p_a = 0.062$ psi. A dashed line indicates the ambient pressure. A single-shot PLIF image from this run is shown on the left. The scales on both the image and the graph are in inches, with the smallest hash marks equal to $1/16$ th in.

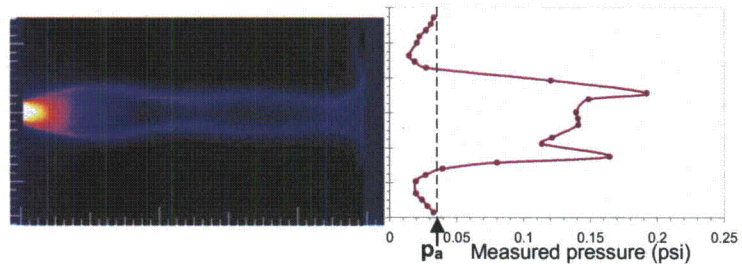


Figure 11. Pressure profile with a double peak. This profile is for supersonic nozzle Run 536 with $JPR = 5.4$, $Re_{exit} = 2,302$, $\theta_{imp} = 90^\circ$ and $D_{imp}/D_e = 15.2$, $p_a = 0.035$ psi. A dashed line indicates the ambient pressure. A single-shot PLIF image from this run is shown on the left. The scale on the image is in inches, with the smallest hash marks equal to $1/16$ th in.

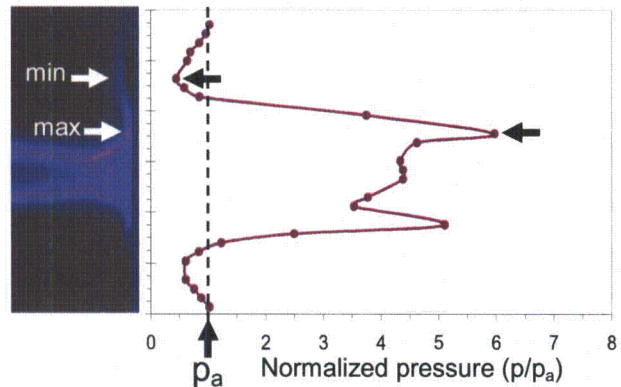


Figure 12. Relation of flow features to the maximum and minimum measured pressures. The PLIF image is a close-up of the impingement region for the flow in Fig. 11 and is show to scale with the graph. The smallest hash marks on the vertical scale of the graph are $1/16$ th in.

clearly illustrating the connection between flow features and surface pressures. A dashed vertical line indicates the ambient pressure (the pressure has been normalized by this pressure). Note that the actual peak pressures may occur between pressure taps, and thus may be greater than the measured peak pressure.

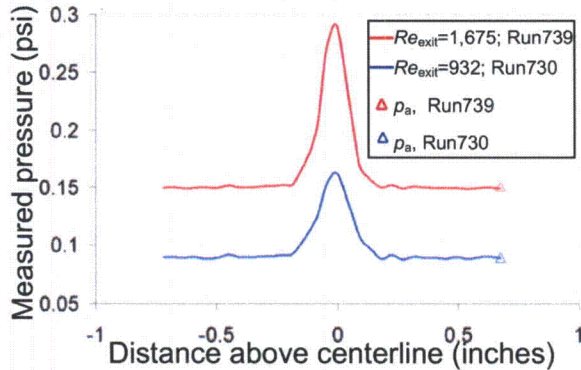


Figure 13. Measured pressure profiles. Two impingement surface pressure profiles from laminar runs with the same jet pressure ratio but different exit Reynolds numbers are shown.

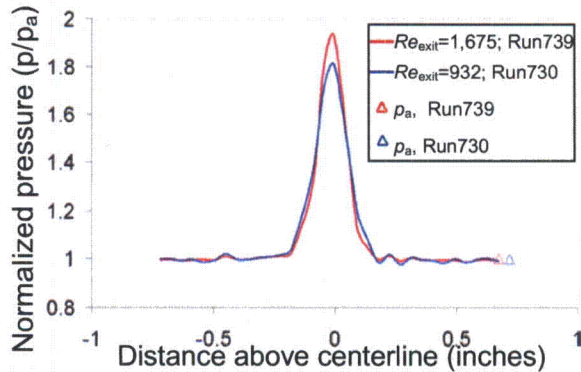


Figure 14. Normalized pressure profiles. This shows the same impingement surface pressure data as Fig. 13, normalized by the ambient (chamber) pressure of each run. This normalization results in nearly self-similar profiles.

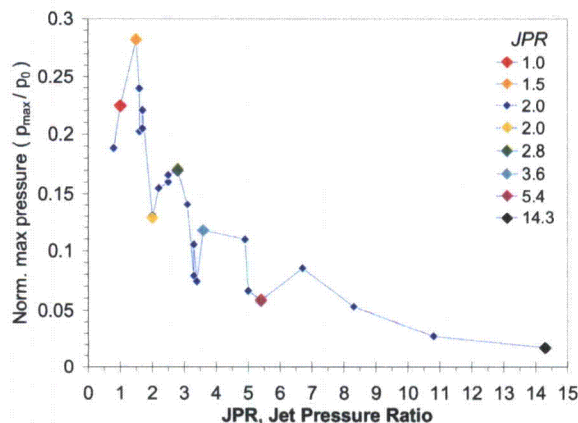


Figure 15. Supersonic nozzle recovery pressure as a function of JPR for one impingement distance, 90° impingement. $D_{\text{imp}}/D_e = 15.2$ (2.5 in.). Data from runs having exit Reynolds numbers ranging from 380 to 12,500 are included in this graph.

C. Reynolds Number Effect on Pressure Profiles

Like their free jet counterparts, the shape of impinging jet flow structures are similar for those runs that have similar JPR s (for a given nozzle type), so long as the runs are all laminar. It is then not surprising that the shapes of the pressure distributions for runs with the same JPR have similar features. However, for runs with matching JPR but different values of Re_{exit} , the magnitude of the measured pressure profiles increases with increasing Re_{exit} . This is expected to be the case because, for constant gas plenum temperatures, Re_{exit} is proportional to plenum pressure (p_0). Self-similar pressure profiles can be obtained for runs with the same JPR by normalizing all the measured impingement disk pressures by either p_0 or p_a .

Figures 13 and 14 graphically depict the effect of normalization by p_a . Figure 13 shows pressure profiles from two runs with essentially the same JPR (2.8), but different values of Re_{exit} (1,675 and 932). Figure 15 shows these same data after they have been normalized by the ambient pressure for either run. The two normalized profiles exhibit a high degree of overlap.

D. Jet Pressure Ratio Effect on Pressure Profiles

The shape of the pressure profile was found to depend heavily on the jet pressure ratio. To illustrate this, consider Figs. 15-17. In Fig. 15, the maximum (peak) pressure (p_{max}) has been graphed versus JPR . Data have been included for both steady and unsteady laminar supersonic runs with an impingement distance (D_{imp}) of 15.2 nozzle diameters (2.5 in.) and impingement angle θ_{imp} of 90° . In this graph, the pressures have been normalized by the nozzle plenum pressure (p_0). Peak pressures are significant in aerothermal applications because they may be associated with regions of peak heating. The maximum pressure, normalized by the plenum pressure, will be called the *recovery pressure* to indicate that this quantity represents the maximum plate pressure as a fraction of the stagnation pressure. Keep in mind that the discrete (as opposed to continuous) nature of the pressure taps results in measured peak pressures that are less than or equal to the actual peak pressure, which may occur between taps.

In Fig. 15, notice that the recovery pressure for this nozzle/plate configuration is always less than 0.3. Next, notice that for JPR s of less than about 5, the values are seen to exhibit relatively large variations around the apparent mean. Above about 5, the value of the recovery pressure is seen to decline smoothly,

without these large fluctuations. The oscillations that are seen for low JPR s are not simply noise in the data, but corresponds to variations in flow structures that are very sensitive to small changes in JPR in this region. The colored data points in Fig. 15 correspond to the PLIF images and their associated pressure profiles shown in Fig. 16. The images are labeled by their JPR . The number of cells (that is, the number of low-pressure antinodes or flow maxima) between the nozzle exit and the impingement target is seen to decrease for increasingly large JPR , from about 4 cells in the second image, to about $2\frac{1}{2}$ cells in the fifth image. In the sixth image, no high-pressure nodes are evident. Instead, this image and the last image both show a flow with a barrel shock and normal Mach disk.

As a further illustration of the dependence of the recovery pressure on JPR , consider Fig. 17. Here, pressure profiles are shown for two runs with very similar jet pressure ratios. The top profile has a double-peaked structure, whereas the bottom profile is single-peaked. This is due to the existence of a recirculation bubble in the top image, and the lack of such a feature in the bottom image. The sudden emergence or disappearance of a recirculation bubble that results for small changes in JPR is an effect known as *staging*.¹² Staging behavior is the exhibition of non-continuous phenomena in a flow, or rather, discrete jumps from one continuous region (or *stage*) to another. This staging behavior causes the oscillations shown in Fig. 15. Subsequent peaks of these oscillations correspond to different numbers of nodes, and also correspond to swapping between single and double peaked pressure profiles.

For supersonic normal impingement cases with JPR s above about 4, a double-peaked pressure profile was always seen, even in cases with no recirculation bubble. In such cases, the peak pressures were found to occur at the intersection of the high-velocity jet boundary with the impingement target.

The behavior of the recovery pressure as a function of JPR is shown in Fig. 18 for four supersonic normal impingement ($\theta_{imp}=90^\circ$) configurations with different impingement distances. All four configurations are similar to that shown in Fig. 15 in that they all show fluctuations in peak pressure for JPR s associated with oscillating flow structures and show a lack of fluctuations for higher JPR s associated with flows having a Mach disk. Interestingly, the behavior appears to be relatively independent of impingement distance, at least for the range of impingement distances (10.7-30.5 nozzle diameters) in this study. A solid black line denotes a

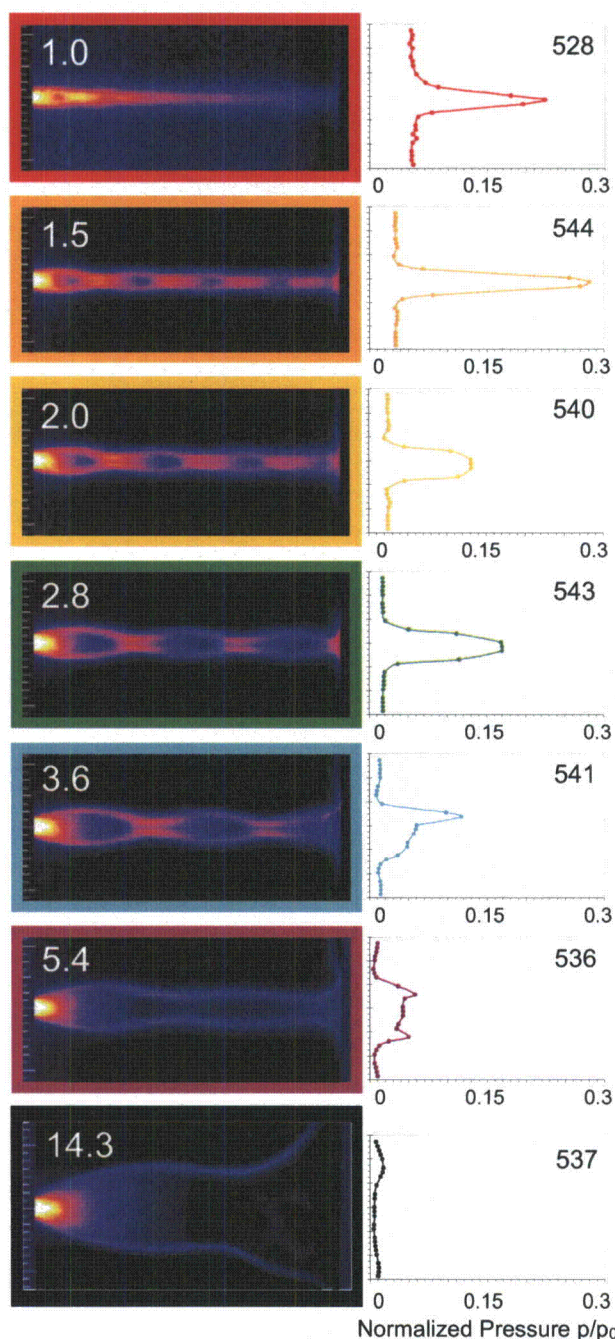


Figure 16. Single-shot PLIF images and the corresponding normalized pressure profiles for the colored data points in Fig. 15. JPR are listed in white on each figure and run numbers are listed in black in the upper right-hand corner on each graph. All runs have $\theta_{imp}=90^\circ$, $D_{imp}/D_e = 15.2$ (2.5 in.). The smallest hash marks on the scales are $1/16^{\text{th}}$ in.

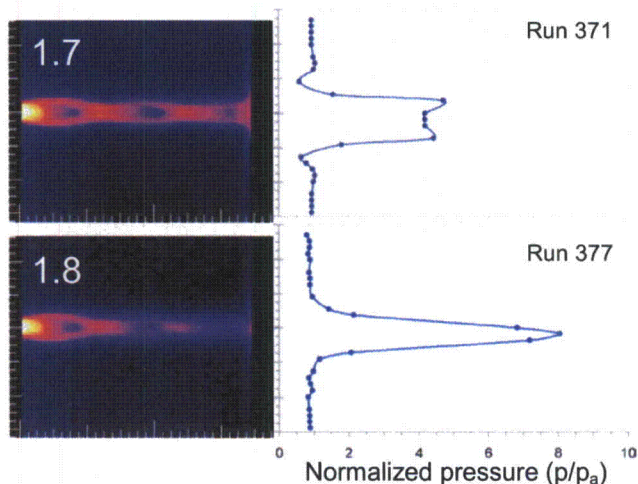


Figure 17. Staging effect in impingement pressure profiles. Graphs show the sensitivity of profile features to small changes in JPR , for two cases with $\theta_{imp} = 90^\circ$ and $D_{imp} / D_e = 10.7$ (1.75 in.). The upper image is for $JPR = 1.7$ (Run 371) and the lower images is for $JPR = 1.8$ (Run 377). Pressures have been normalized by the ambient pressure, p_a . Scales on images and vertical scales on graphs are in inches, with smallest hash marks equal to $1/16^{th}$ in.

increased surface area over which the jet flow impacts the impingement target. An additional effect may result from the pressure losses associated with normal shock waves (the Mach disk) at higher JPR versus the oblique shocks associated with oscillating flow structures at lower JPR .

Although Fig. 18 indicates that the *peak* pressure is found to be somewhat independent of distance for supersonic nozzle cases, the shape of the pressure profile does change with distance. This is illustrated in Fig. 19. Four single-shot PLIF images are shown for four runs with similar JPR but different impingement distances. Pressure profiles (normalized by p_0) are shown on the same graph. Note that the pressure transducer at the -0.135 in. location was faulty and so it appears that the peak pressure was not captured on both sides of the jet for two of the cases. The pressure profiles are all double-peaked (as expected since these flows all have Mach disks and $JPR > 5$) and all have similar peak pressures. However, the pressure deficit near the jet centerline is more or less pronounced, depending

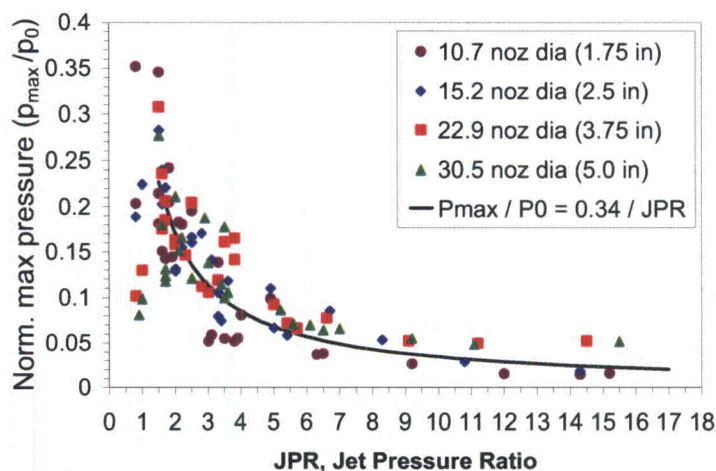


Figure 18. Supersonic nozzle recovery pressures for four impingement distances, 90° impingement. The black line shows a plot of Eq. (3).

proposed empirical model for the mean behavior of the recovery pressure (neglecting the higher order oscillations around the mean). The equation for the empirical model is given by Eq. (3):

$$\frac{p_{max}}{p_0} = \frac{0.34}{JPR} \quad (3)$$

This coefficient in Eq. (3) was found by performing a least squares fit to the data for $JPR > 1.5$. Note particularly that, for impingement distances between about 10 and 30 nozzle diameters, this result does not depend on impingement distance. This relation may not hold for arbitrarily large or small impingement distances, so caution is warranted in its application to flows outside the range of tested configurations. But within this range, one can see that the recovery pressure for supersonic (Mach 2.6) underexpanded ($JPR > 1.5$) jets, the recovery pressure will be less than 0.34 times the plenum pressure. The decrease in recovery pressure at large jet pressure ratios results partially from the

decrease in recovery pressure at large jet pressure ratios results partially from the increased surface area over which the jet flow impacts the impingement target. An additional effect may result from the pressure losses associated with normal shock waves (the Mach disk) at higher JPR versus the oblique shocks associated with oscillating flow structures at lower JPR . Although Fig. 18 indicates that the *peak* pressure is found to be somewhat independent of distance for supersonic nozzle cases, the shape of the pressure profile does change with distance. This is illustrated in Fig. 19. Four single-shot PLIF images are shown for four runs with similar JPR but different impingement distances. Pressure profiles (normalized by p_0) are shown on the same graph. Note that the pressure transducer at the -0.135 in. location was faulty and so it appears that the peak pressure was not captured on both sides of the jet for two of the cases. The pressure profiles are all double-peaked (as expected since these flows all have Mach disks and $JPR > 5$) and all have similar peak pressures. However, the pressure deficit near the jet centerline is more or less pronounced, depending on distance. One explanation for this is that the intersection of the jet with the impingement target sometimes occurs near a high-pressure node (flow minima), but other times occurs at a lower-pressure antinode (flow maxima). When the intersection occurs at a node, the pressure difference between the core and outer high-velocity boundary of the jet is less than when the intersection occurs at an antinode. A secondary effect may result from the loss in total pressure associated with the Mach disk. Immediately downstream of the Mach disk, the centerline gas is subsonic (see Fig. 5). Further downstream, viscous effects exert their influence through the inner shear layer (see Fig. 6), and the centerline velocity begins to recover. Likewise, the impingement pressure is

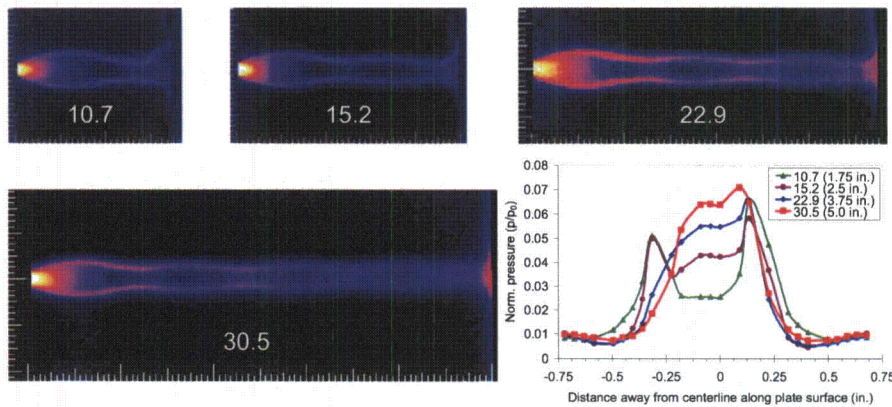


Figure 19. Similar supersonic jet conditions ($JPR \sim 5.7$) at four impingement distances. Single-shot images are labeled according to the corresponding value of D_{imp}/D_e (nozzle diameters). In order of increasing distance, they are 1.75 in. (Run364), 2.5 in. (Run553), 3.75 in. (Run578), and 5.0 in. (Run605). Note that the peak pressure in the 3rd and 4th cases probably occurred near the location of a faulty pressure transducer at -0.135 in.

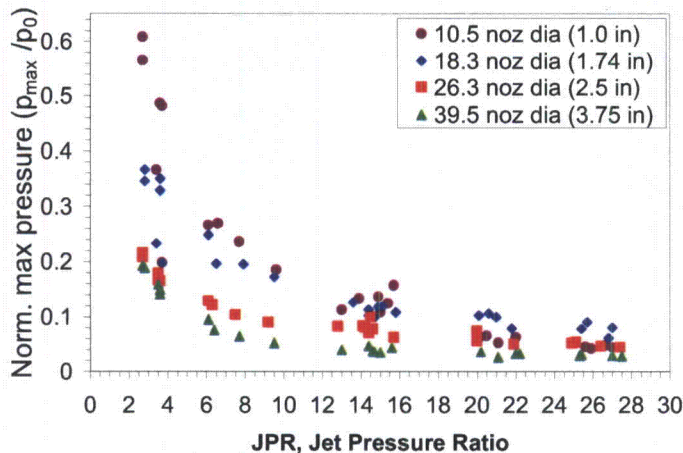


Figure 20. Sonic nozzle recovery pressures, 90° impingement. Smaller impingement distances are seen to result in larger recovery pressures, especially for small JPR . No data were taken at JPR less than about 2.5, so the maximum possible recovery pressure was not determined. For small impingement distances and low JPR , it may approach the plenum pressure.

the sonic cases show a dependence on impingement distance, with larger recovery pressures associated with smaller impingement distances, especially for low JPR s. For these sonic impingement cases, no simple empirical model passes through all the data.

E. Angled Impingement

In the literature, some studies (most notably, the experimental studies of Lamont and Hunt⁹, as well as the computational studies of Wu et al.¹⁷ which simulated flows at conditions identical to those of Lamont and Hunt) found that the maximum impingement pressure on angled impingement targets could be much greater (up to a factor of three greater) than the maximum pressure in the corresponding normal impingement cases. In our experiments, we have observed results consistent with these observations. Figure 21 shows three single shot images from runs at three impingement angles and their associated normalized pressure profiles. Although 45° and 60° configurations were not tested at the same impingement distances, the results shown in Fig. 18 and described above suggest that a rough comparison might still be made among runs at different impingement distances.

reduced along the centerline immediately downstream of the Mach disk, but may gradually recover as the impingement distance is increased.

For sonic nozzle cases, slightly different trends are observed. Figure 20 shows recovery pressure as a function of JPR for four different impingement distances. Like the supersonic nozzle cases, peak pressures are observed to decrease with increasing JPR . Additionally, oscillations

are again observed for the region of low JPR (less than about 3), the same flow regime in which oscillating flow structures are manifest. However, oscillations are not observed for the two larger impingement distances (26.3 and 39.5 nozzle diameters). It has been previously noted that the spatial wavelengths associated with sonic nozzle flows tended to be smaller than their supersonic nozzle counterparts (on the order of 2 nozzle diameters in length, versus 3 to 8 nozzle diameters in length in the case of a supersonic nozzle), and that diamond shock structures in low JPR sonic nozzle flows tended to dampen out after 2 or 3 oscillations¹². So at larger impingement distances, flow oscillations are no longer present (see Fig. 4, for example), and so do not result in staging behavior of impingement pressure. The sonic cases also exhibit an inverse relationship of recovery pressure to JPR . However, unlike the supersonic cases,

As previously stated, measured peak pressures may be less than actual peak pressures, due to the finite nature of the pressure measurements performed, and compounded by several faulty pressure transducers. Nevertheless, of the recorded pressures, the graph in Fig. 21 shows that the normalized peak pressure in the 60° case is roughly twice that of the 45° case and roughly three times that of the 90° case, in agreement with prior experimental⁹ and computational¹⁷ studies. By closely examining the images associated with these runs, it is seen that in the 60° configuration, the high-velocity jet boundary along the bottom of the jet impacts the impingement target at nearly normal incidence, which likely results in a pressure maximum at that point. By contrast, at 45°, this part of the flow strikes the plate at a slightly more glancing angle. In both cases, the upper boundary of the jet impacts the target at a gentler angle, resulting in asymmetric pressure profiles with peak pressures below the jet centerline. Figure 22 shows the recovery pressure plotted as a function of *JPR* for all 45° and 60° supersonic impingement cases. The general trend is for increased recovery pressure for 60° cases relative to 45° cases for low values of *JPR*.

V. Conclusion

PLIF images have been used to visualize free and impinging underexpanded jet flows and have provided detailed information about flow structures. The insights into flow structure characteristics provided by PLIF images have helped to elucidate the results of pressure measurements taken at the surface of a flat impingement target and have shed light on the features of the pressure distributions across the face of the target. Under certain conditions, the shape of these pressure distributions was seen to be a very sensitive function of jet pressure ratio; under other conditions, the dependence was rather insensitive to *JPR*. In all cases, the absolute magnitude of the measured pressures was seen to be a linear function of plenum pressure, and therefore, of Reynolds number. The recovery pressure (that is, the peak pressure relative to the plenum pressure) was found to oscillate for low *JPR* and then decrease as the inverse of the jet pressure ratio for high *JPR*. In supersonic nozzle cases, this trend was found to be relatively independent of impingement distance for the cases studied. In sonic nozzle cases, it was found to depend inversely on impingement distance as well. Finally, it was found that recovery pressure was greater for angled impingement than for normal impingement with 60° impingement angle having three times higher peak pressure than normal incidence. These results, while providing good test cases for computations, demonstrate the significant contribution that flow visualization can provide in the understanding and interpretation of surface measurements.

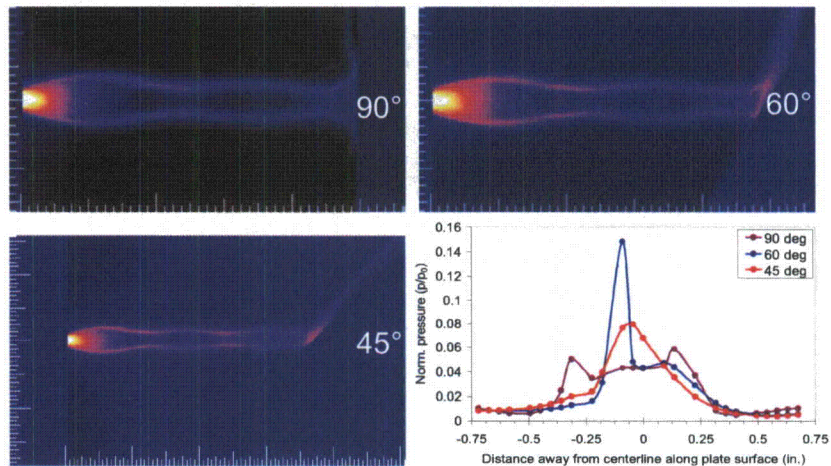


Figure 21. Three impingement angles. Single shot images are shown for similar jet conditions (supersonic nozzle, *JPR* ~5.7, *Re_{exit}* ~2,300), and $\theta_{imp}=90^\circ$ (Run536), 60° (Run553), and 45° (Run630). For the first two, $D_{imp}/D_e=15$ (2.5 in.); for the third, $D_{imp}/D_e=23$ (3.7 in). Note that the peak pressure in the 45° case probably occurred near the location of a faulty pressure transducer at -0.135 in.

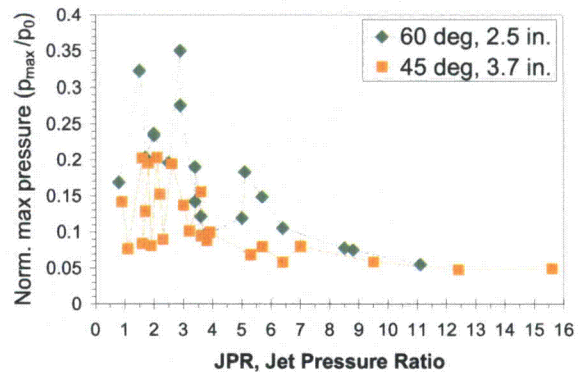


Figure 22. Supersonic nozzle recovery pressures for 45° vs. 60° impingement. Somewhat higher peak pressures are seen in the 60° cases.

Acknowledgments

The authors wish to acknowledge the collaborative input of Scott Halloran of Rocketdyne, Don Picetti of The Boeing Company and Chris Glass of NASA Langley Research Center, as well as the technical assistance of David Alderfer, Stephen Jones, and Paul Tucker, also of NASA Langley Research Center. They also wish to acknowledge the image processing work done by Aiyana Garcia, a graduate physics student from The College of William and Mary and a NASA GSRP (Graduate Student Researchers Program) student. This work was funded as part of the Shuttle Return to Flight effort through Chuck Campbell of Johnson Space Center and Tom Horvath of NASA Langley Research Center. Support was also received from the Aeronautics Research Mission Directorate's Fundamental Aeronautics Hypersonic Project, Experimental Capabilities discipline, under Robert Okojie.

References

- ¹ J. L. Palmer and R. K. Hanson, "Shock tunnel flow visualization using planar laser-induced fluorescence imaging of NO and OH," *Shock Waves*, vol. 4, pp. 313-323, 1995
- ² J. A. Inman, P. M. Danehy, R. J. Nowak, and D.W. Alderfer, "Identification of Instability Modes of Transition in Underexpanded Jets," *38th AIAA Fluid Dynamics Conference, Seattle, WA, 23-26 June 2008* (to be published).
- ³ J. A. Wilkes, P. M. Danehy, and R. J. Nowak "Fluorescence Imaging Study of Transition in Underexpanded Jets," *Proceedings of the 21st International Congress on Instrumentation in Aerospace Simulation Facilities (ICIASF)* [CD-ROM], Sendai, Japan, 29 August – 1 September 2005, pp. 1-8.
- ⁴ J. A. Wilkes, C. E. Glass, P. M. Danehy, and R. J. Nowak, "Fluorescence Imaging of Underexpanded Jets and Comparison with CFD," *44th AIAA Aerospace Sciences Meeting and Exhibit*, AIAA-2006-0910, Reno, NV, 9-12 January 2006.
- ⁵ Alvi, F.S. and K.G. Iyer, "Mean and Unsteady Flowfield Properties of Supersonic Impinging Jets with Lift Plates," *5th AIAA/CEAS Aeroacoustics Conference*, AIAA 99-1829, Bellevue (Greater Seattle), WA, 10-12 May 1999.
- ⁶ Donaldson, C. D., and R. S. Snedeker, "A study of free jet impingement. Part 1. Mean properties of free and impinging jets," *J. Fluid Mech.* **45**, 1971, Part 2: 281-319.
- ⁷ Donaldson, C. D., R. S. Snedeker, and D. P. Margolis, "A study of free jet impingement. Part 2. Free jet turbulent structure and impingement heat transfer," *J. Fluid Mech.* **45**, 1971, Part 3: 477-512.
- ⁸ Kim, Sung In, and Seung O. Park, "Unsteady Flow Simulation of Supersonic Impinging Jet," *41st AIAA Aerospace Sciences Meeting and Exhibit*, AIAA 2003-621, Reno, NV, 6-9 Jan 2003.
- ⁹ Lamont, P.J., and B.L. Hunt, "The Impingement of Underexpanded Axisymmetric Jets on Perpendicular and Inclined Flat Plates," *Journal of Fluid Mechanics* **100**: 471-511, 1980.
- ¹⁰ Love, E. S. and L. P. Lee, "Shape of Initial Portion of Boundary of Supersonic Axisymmetric Free Jets at Large Pressure Ratios," NACA TN 4195, January 1958.
- ¹¹ Stitt, Leonard E., "Interaction of Highly Underexpanded Jets with Simulated Lunar Surfaces," Lewis Research Center, Cleveland, OH. NASA Technical Note D-1095, December 1961.
- ¹² Inman, Jennifer A., "Fluorescence Imaging Study of Free and Impinging Supersonic Jets: Jet Structure and Turbulent Transition," Ph.D. Dissertation, Department of Physics, The College of William and Mary, Williamsburg, VA, 2007.
- ¹³ Henderson, Brenda, "The connection between sound production and jet structure of the supersonic impinging jet," *Journal of the Acoustical Society of America* **111** (2): 735-747, Feb 2002.
- ¹⁴ Henderson, B., J. Bridges, and M. Wernet, "An experimental study of the oscillatory flow structure of tone-producing supersonic impinging jets," *Journal of Fluid Mechanics*, Cambridge University Press, **542**: 115-137, 2005.
- ¹⁵ Alvi, F.S., J.A. Ladd, and W.W. Bower, "Experimental and Computational Investigation of Supersonic Impinging Jets," *AIAA Journal* **40** (4): 599-609, April 2002.
- ¹⁶ Mackie, S. and R. Taghavi, "Supersonic Impinging Jets: A Computational Investigation," *40th AIAA Aerospace Sciences Meeting and Exhibit*, Reno, NV. AIAA 2002-0671, 14-17 Jan. 2002.
- ¹⁷ Wu, J., L. Tang, E.A. Luke, X-L. Tong, and P. Cinnella, "A Comprehensive Numerical Study of Jet Flow Impingement over Flat Plates at Varied Angles," *39th AIAA Aerospace Sciences Meeting and Exhibit*, AIAA-2001-0745, Reno, NV, 8-11 Jan 2001.

Fluorescence Imaging Study of Impinging Underexpanded Jets

Jennifer A. (Wilkes) Inman*[†], Paul M. Danehy[†], Robert J. Nowak[†], and David W. Alderfer[†]

*email address: jennifer.a.inman@nasa.gov

[†]NASA Langley Research Center, Hampton VA, 23681-2199

I. INTRODUCTION

The tests that will be described in this paper were designed to create a simplified simulation of the flow through a hole in the surface of a supersonic aerospace vehicle and the subsequent impingement of the flow on internal structures. They were conducted in support of the Orbiter Aerothermodynamics Working Group as part of NASA's Shuttle Return to Flight (RTF) effort. Planar laser-induced fluorescence (PLIF) of nitric oxide (NO) is used to visualize the flow. PLIF images show the size and location of flow structures, and the laminar or turbulent state of these flows can also be ascertained from these images.

The flow environments encountered in these tests include regions of low static pressure, turbulent and/or three-dimensional flow structures, and regions of interest with both strong and weak density gradients. Such conditions, though frequently encountered in aerospace simulation facilities, cannot be satisfactorily visualized using traditional path-averaged techniques such as schlieren and shadowgraph, which rely on sufficiently high static pressures and strong density gradients. An alternative approach was therefore required. PLIF is a powerful flow visualization technique that provides a means of making non-intrusive measurements with sub-millimeter spatial resolution and flow-stopping temporal resolution in many of these challenging testing regimes [1]. We have previously used PLIF to investigate underexpanded sonic jets [2] and have compared a subset of these results with computational fluid dynamics (CFD) [3].

In addition to flow visualization, pressure measurements were recorded on the surface of an impingement target. PLIF images helped to elucidate the characteristics of the resulting pressure profiles by highlighting the flow structures corresponding to distinctive features of these pressure profiles.

II. EXPERIMENTAL METHODS

A. Facility and Hardware

Tests were conducted at NASA Langley Research Center using the test section of the 15-Inch Mach 6 Wind Tunnel as a vacuum chamber. Nitrogen or helium seeded with 0.5% nitric oxide was plumbed into a heated stainless steel plenum, through a nozzle, and into the vacuum chamber. Two different nozzles were used: the first—a converging nozzle with the exit at the smallest diameter, or throat, and hereafter referred to as the “sonic” nozzle—had a nominal exit Mach number of 1; the second—a converging/diverging nozzle, hereafter called the “supersonic” nozzle—had a nominal exit Mach number of 2.6. Mass flow controllers controlled the flow rates, which indirectly controlled the plenum pressure upstream of the nozzle.

A 4-inch impingement disk was positioned at various distances and angles downstream of the nozzle exit. The center of this disk included 32 pressure taps. They were spaced 0.045 inches apart, and had an inside diameter of .021 inches. The taps were oriented in a vertical plane (the plane of the laser sheet), on the jet centerline. From the camera's viewing angle, the jet flow was from left to right.

B. Model Configuration Parameters

For the majority of cases, the impingement disk was oriented normal to the jet axis (which is defined to be a 90° impingement angle). Two configurations included oblique impingement angles of 45° and 60°. (For these cases, the target was rotated clockwise, as viewed from the camera viewing angle, about the horizontal axis perpendicular to the jet axis.) Impingement distance was continuously variable from 0 to 6 inches. In practice, changing impingement distance or angle required approximately a half day of down time.

For each hardware configuration, two flow parameters were varied: the exit Reynolds number (Re_{exit}) and the jet pressure ratio (JPR). Re_{exit} was defined in terms of the nozzle exit diameter, D_e , and the density ρ_e , velocity V_e , and

dynamic viscosity μ_e at the nozzle exit, as given by (1).

$$\text{Re}_{exit} = \frac{\rho_e V_e D_e}{\mu_e} \quad (1)$$

Re_{exit} was varied by changing the mass flow rates and nozzle plenum temperature. JPR was defined as the ratio of the static pressure at the nozzle exit, p_e , to the ambient pressure in the test section, p_a , according to (2), and was varied by changing the test section pressure for a given Reynolds number (and therefore, a fixed p_e).

$$JPR = \frac{p_e}{p_a} \quad (2)$$

C. PLIF Flow Visualization Technique

The PLIF laser system includes a tunable Nd:YAG-pumped dye laser followed by doubling and mixing crystals. The resulting output, at 226.256 nm, was tuned to excite the strongly fluorescing spectral lines of NO near the Q_1 branch head (Q denotes a change in rotational quantum number equal to zero). Optics formed the beam into a laser sheet that was 100 mm wide x ~0.2 mm thick (FWHM) in the measurement region. Fluorescence was imaged onto a gated, intensified CCD at a viewing angle normal to the laser sheet. Images were acquired at 10 Hz with a 1 μ s camera gate and a spatial resolution of between 3 and 7 pixels/mm, depending on the required field of view for a given hardware configuration. This system is detailed in Ref. 2 and Ref. 3. The PLIF system is also capable of pressure-sensitive and velocity-sensitive flow imaging. Although data

were acquired under these conditions, those results will be reported in a future paper.

III. EXPERIMENTAL RESULTS

Figure 1 shows the range of conditions and hardware configurations for which data were taken during the impinging jet study. Reynolds numbers and jet pressure ratios were calculated based on nozzle exit conditions. The table list the number of cases that were studied for each combination of hardware configuration and type of PLIF imaging that was investigated in these tests. For each flow visualization case, 100 single-shot images were acquired. The laser sheet was also swept spanwise through the flow, providing slices of the flow field, a technique hereafter called "volume imaging." These slices allow us to reconstruct cross-sections of the flow in planes perpendicular to the jet axis, as described in the following section. As previously stated, we plan to report the results of the velocity-sensitive, pressure-sensitive, and density-sensitive imaging data in a future publication, but not in this paper.

A. Characteristic Flow Structures

The data show that free jet cases having the same JPR exhibit the similar flow structures, so long as the cases under consideration are all laminar. For sonic nozzle cases, flows can be divided into two major groups: those with a repeating diamond shock structure (seen for flows with JPRs less than about 3), and those with a barrel shock structure, a Mach disk, and a streamwise high-velocity jet boundary (seen for flows with JPRs greater than about 3)[2]. For cases with the supersonic nozzle, the division happens at a JPR of about 4. For smaller JPRs, a repeating pattern, analogous to the diamond shock pattern, is evident, with a chain-like pattern of alternating spatial minima and maxima. As JPR increases, the repeating pattern becomes less pronounced. Larger JPRs lead to a modified barrel shock structure—elongated into a more egg-like shape than its comparable sonic jet counterpart—with a Mach disk and a streamwise high-velocity jet boundary.

Sometimes these flow structures are more readily understood by using volume imaging data to reconstruct spanwise slices of the flow. The full paper will describe this process in more detail. An example is shown in Figure 2. The top image in the figure shows a single-shot image from the centerline of the flow. The six images in the bottom of the figure are cross-

Impingement configuration	Supersonic Noz.				Sonic Nozzle		
	FV/VI	V	P	ρ	FV/VI	V	P
1" @ 90°					25		5
1.75" @ 90°	25	22	22	1	25		
2.5" @ 90°	22	19	21		24		
2.5" @ 60°	18						
3.75" @ 90°	23				23		
3.7" @ 45°	23						
5" @ 90°	22						
8 (free jet)	88	11		12	53	8	8
Re_{exit}	600-14,000				2,400-35,000		
JPR	1-16				3-27		

Figure 1. Test matrix for impinging jet cases. FV/VI = flow visualization and volume imaging; V = velocity-sensitive imaging; P = pressure-sensitive imaging; ρ = density-sensitive imaging. Because Reynolds numbers and jet pressure ratios were calculated based on nozzle exit conditions, the range of Re and JPR for supersonic nozzle cases is less than for sonic nozzle cases. The controlling limitation was the inability to achieve steady chamber pressures below 1 or 2 Torr (0.2 – 0.4 psi).

sectional slices at various axial locations in the flow.

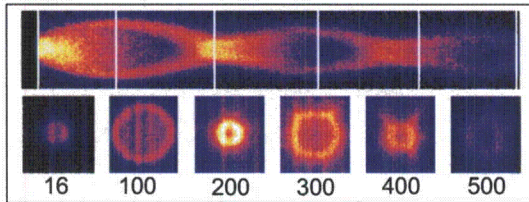


Figure 2. PLIF volume imaging. The white lines on the upper single-shot centerline image show the axial locations for which reconstructed cross-sectional slices are shown. The numbers below the cross-sectional images indicate the column number in the original image, which is 512 columns wide.

B. Flow Structure Relation to Pressure Profiles

Consider an impinging jet flow with a uniform momentum profile throughout the core of the jet. One would expect the pressure profile of such a jet to resemble a top hat function, with roughly uniform pressure across the intersection of the jet with the impingement target, dropping to near ambient pressure away from the core of the jet. Modifying the situation to include viscous effects, one would expect to see a decrease in momentum—and therefore a decrease in pressure on the impingement surface—along the edges of the jet. This modified pressure profile would be peaked in the center, smoothly dropping off to the ambient pressure toward the edges of the jet flow. In fact, for some cases, this describes the pressure profiles that have been measured.

But for other cases, the actual profiles are quite different. Such profiles typically exhibit a double-peaked structure, with the maximum pressure occurring away from the flow centerline. The pressure between these peaks is often nearly constant, while the pressure outside these peaks drops off toward—and sometimes dips briefly below—the ambient pressure. Flow visualization images acquired in the present study have helped to elucidate the origin of these hallmark features by highlighting the flow structures associated with presence of the impingement surface. These images also help to explain the observed sensitivities (and insensitivities) of the pressure profiles to Reynolds number and jet pressure ratio, as explained further in the following two sections.

C. Reynolds Number Effect on Pressure Profiles

Like their free jet counterparts, impinging jet flow structures are similar for those runs that have similar JPRs (for a given nozzle type), so

long as the runs are all laminar. It is then not surprising that the shapes of the pressure distributions for runs with the same JPR have similar features. However, for runs with matching JPR but different values of Re_{exit} , the magnitude of the measured pressure profiles increases with increasing Re_{exit} . This is expected to be the case because, for constant gas plenum temperatures, Re_{exit} is proportional to plenum pressure (p_0). Self-similar pressure profiles can be obtained for runs with the same JPR by normalizing all the measured impingement disk pressures by either p_0 or $p_{chamber}$.

Figure 3 graphically depicts the effect of normalization by $p_{chamber}$. The upper image shows pressure profiles from two runs with essentially the same JPR (2.8), but different values of Re_{exit} (4448 and 2476). The lower image shows these same data after they have been normalized by the plenum pressure for each run. The two normalized profiles show a high degree of overlap.

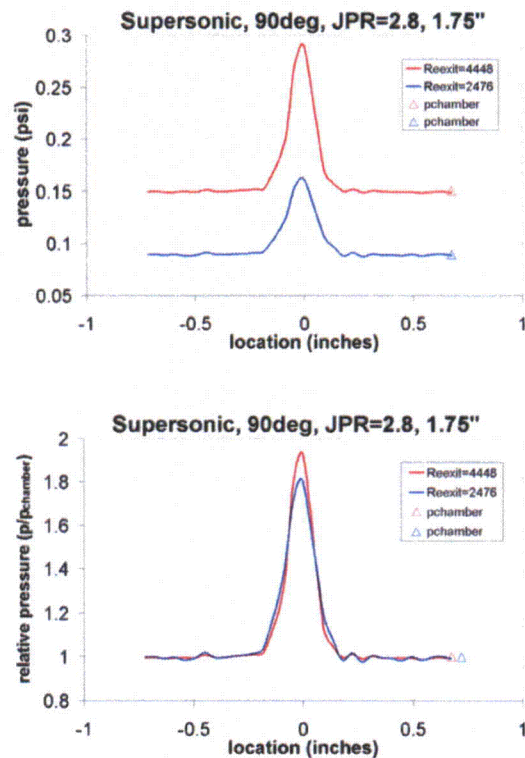


Figure 3. Effect of Reynolds number on pressure profile. Both runs have a jet pressure ratio of 2.8. The red line is for a run with $Re_{exit} = 4448$; the blue line, $Re_{exit} = 2476$.

D. Jet Pressure Ratio Effect on Pressure Profiles

The shape of the pressure profile was found to depend heavily on the jet pressure ratio for laminar runs where the impingement target was located in a region of large local spatial variations. That is, JPR small variations in JPR were seen to cause significant variations in the pressure profile for flows where the spatial cross-section is strongly varying with distance in the streamwise direction. This can be explained by considering that small changes in JPR are roughly equivalent to small changes in impingement distance.

For supersonic cases, this sensitivity to JPR was seen for flows with JPRs less than about 4. This effect is illustrated in Figure 4 and Figure 5. Starting in the upper left of Figure 4, PLIF images show the flow structures associated with impinging supersonic axisymmetric jets for increasing JPRs, from about 1.7 to 2.9. In the first image, the jet impinges on the disk just upstream of what would have been the third spatial minimum of the flow (location where the jet diameter is smaller than locations immediately upstream and downstream of that location). As JPR increases in the next three images, the jet then impinges near the third flow maximum, then the second flow minimum, and finally, just downstream of the second flow maximum. Figure 5 shows normalized pressure profiles from these four runs, as well as four additional runs with similar JPRs. As the JPR increases from about 1.7 to about 2.14, the pressure profile becomes narrower and single-peaked (that is, with a single location of the

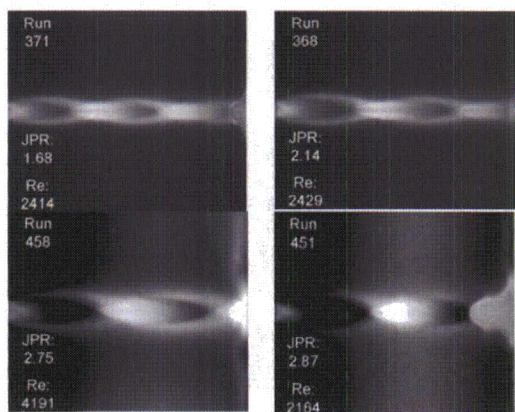


Figure 4 Sensitivity of impingement flow structures to jet pressure ratio (JPR). The chain-like flow structures seen here are reminiscent of the familiar diamond shock pattern seen in sonic jets. Note: the top images are from flow visualization runs; the bottom images are from "pressure" runs, in which the fluorescence intensity is primarily a function of pressure.

maximum pressure occurring along the centerline of the flow). Then the profiles broaden again, with a marked change around a JPR of about 2.7, including a sudden broadening and the reemergence of a double-peaked structure (with peak pressures occurring along the edges of the jet, and a flattened profile in the subsonic central region of the impingement).

Similar sensitivity was not seen for the sonic cases that were studied in these tests. This is likely due to the impingement distances that were chosen. The minimum impingement distance in the sonic nozzle cases was 1.0 inch. Whereas the low JPR supersonic nozzle flows (with JPRs less than about 5) exhibited repeating flow patterns (i.e. spatial frequencies) on the order of 0.5 to 1.25 inches, low JPR sonic nozzle flows had much smaller spatial frequencies—on the order of 0.2 inches. PLIF images show that diamond shock structures tended to dissipate within about 2 or 3 oscillations. Laminar impingement structures for the sonic cases were thus rather indistinct, with little sensitivity to changes in JPR.

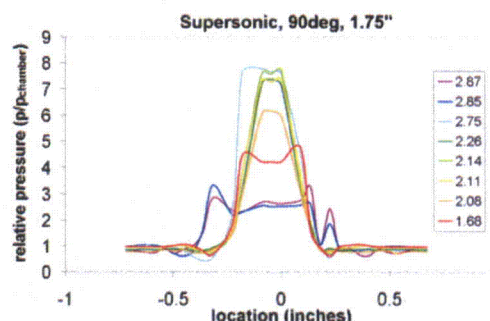


Figure 5 . Pressure profile sensitivity to JPR. These pressure profiles have been normalized by the chamber pressure of the corresponding run.

IV. CONCLUSIONS

PLIF images have been used to visualize free and impinging underexpanded jet flows. They have provided detailed information about flow structures and have allowed determination of the laminar, unsteady, or turbulent state of the flow (although the results reported in this paper will be restricted to laminar cases). The insights into flow structure characteristics provided by PLIF images have helped to elucidate the results of pressure measurements taken at the surface of a flat impingement target and have shed light on the features of the pressure distributions across the face of the target. Under certain conditions, the shape of these pressure distributions was seen to be a very sensitive function of jet

Extended abstract to be submitted to: 46th AIAA Aerospace Sciences Meeting and Exhibit,
Reno, NV, 7-10 January 2008

pressure ratio; under other conditions, the dependence was rather insensitive to JPR. In all cases, the absolute magnitude of the measured pressures was seen to be a linear function of plenum pressure, and therefore, of Reynolds number. The full paper will include more cases, it will delve into greater detail about the relationship between flow structures and characteristics of pressure profiles (e.g. width, single or double peaks, location of maximum pressure), and it will attempt to place this work in context with the literature on previous studies by others.

ACKNOWLEDGEMENTS

The authors wish to acknowledge the collaborative input of Scott Halloran and Don Picetti of The Boeing Company and Chris Glass of NASA Langley Research Center, as well as the technical assistance of David Alderfer, Stephen Jones, and Paul Tucker, also of NASA Langley Research Center. They also wish to acknowledge the image processing work done by Aiyana Garcia, a graduate physics student from The College of William and Mary and a NASA GSRP (Graduate Student Researchers Program) student. This work was funded as part of the Shuttle Return to Flight effort through Chuck Campbell of Johnson Space Center and Tom Horvath of NASA Langley Research Center.

REFERENCES

- [1] J. L. Palmer and R. K. Hanson, "Shock tunnel flow visualization using planar laser-induced fluorescence imaging of NO and OH," *Shock Waves*, vol. 4, pp. 313-323, 1995
- [2] J. A. Wilkes, P. M. Danehy, and R. J. Nowak "Fluorescence Imaging Study of Transition in Underexpanded Jets," *Proceedings of the 21st International Congress on Instrumentation in Aerospace Simulation Facilities (ICIASF)* [CD-ROM], Sendai, Japan, 29 August – 1 September 2005, pp. 1-8.
- [3] J. A. Wilkes, C. E. Glass, P. M. Danehy, and R. J. Nowak, "Fluorescence Imaging of Underexpanded Jets and Comparison with CFD," *44th AIAA Aerospace Sciences Meeting and Exhibit*, AIAA-2006-0910, Reno, NV, 9-12 January 2006.

SMiRT-5

Trans. 5th Int. Conf. on SMiRT Vol. F6/2 (1979)

F6/2

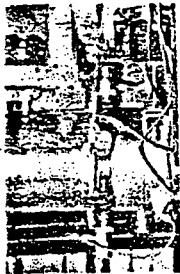
EXPERIMENTAL STUDY OF PIPE REACTION FORCE AND JET IMPINGEMENT LOAD AT THE PIPE BREAK

K. KITADE, T. NAKATOGAWA

MAPI Engineering Center, Mitsubishi Atomic Power Industries,
Inc., 2-1, Taito 1-chome, Taito-ku, Tokyo, Japan

H. NISHIKAWA, K. KAWANISHI, C. TSURUTO

Takasago Technical Institute, Mitsubishi Heavy Industries, Ltd.,
2-chome, Arai-cho, Takasago-City, Hyogo, Japan



PIPE BREAK - TEST

BER

SUMMARY

In the design of a light-water reactor nuclear power plant, the extreme loads which are caused as the result of hypothetical pipe break accident have recently become the most severe factors for the structure and equipment design of the plant.

In this paper, we describe the results of experiments about reaction forces and jet impingement loads in the pipe break accident conditions. Experiments were carried out for the kinds of jets, that is steam jet and subcooled water jet.

For the steam jet experiment, the steady state saturated steam was ejected at pressure range of 10 - 40 Kg/cm²G through the pipe of inner diameter of 9.4 mm. into the atmospheric condition. In the jet impingement experiments, the steam jet impinged vertically on the flat plate, varying the distance H in the range of 0.59 H/D to 6.6 H/D (D: pipe diameter).

The results are as follows:

- (1) The reaction forces T is proportional to the reservoir pressure P₀ and the area of the pipe opening, that is, T=KPA formula is applicable. The thrust coefficient K was 1.12 in our experiments, and this is slightly smaller than Moody's prediction.
- (2) The stagnation pressure P_s at the centre of the pressure distribution on the plate, is estimated by following formula.

$$\frac{P_s - P_\infty}{P_0 - P_\infty} = 0.65 \left(\frac{H}{D}\right)^{-2}$$

- (3) A configuration of the pressure distribution on the plate and the area of it depend mainly on H/D. We could classify the configurations of the pressure distribution to three types in this experiments.

The subcooled water jet experiments were carried out under the condition of initial pressure of 70 Kg/cm²G and 150 Kg/cm²G with subcooling temperature of 13 - 41°C. The diameters of the ejection opening were from 10.5 to 43.1 mm. The instantaneous guillotine breaks were simulated by means of the rupture disks. The jet was ejected upward into the atmosphere and impinged vertically on the plane board.

As results, it is clarified that the reaction forces have a maximum peak value just after the break and subsequently decreases gradually. A thrust coefficient slightly depends on a reservoir pressure transients after the break and is approximately between 1.2 and 1.4. The distribution of pressure on the plate spreads to it's maximum area just after the break. On the other hand, the stagnation pressure on the plate has it's maximum value after a some period of time from the rupture.

1. Introduction

In a design of a light-water reactor nuclear power plant, the extreme loads which are caused as the result of hypothetical pipe break accident, have recently become the most severe factors for the structure and equipment design of the plant. Especially the evaluation of these reaction force and jet impingement load is essential for the design of the piping systems and the structures.

In this paper, experimental results of the reaction force, the impingement load and the jet pressure distribution on the flat target on which the jet impinges vertically, are described. The experiments were performed for the two kinds of jet, that is steam jet and subcooled water jet.

For the steam jet experiment, the steady state saturated steam was ejected at the pressure range of 10 - 40 Kg/cm²G through the pipe of inner diameter of 9.4 mm. into the atmospheric condition. In the jet impingement experiments, the steam jet impinged vertically on the flat plate, varying the distance H in the range of 0.59 H/D to 6.6 H/D (D: pipe diameter).

The subcooled water jet experiments were carried out under the condition of the initial pressure of 70 Kg/cm²G and 150 Kg/cm²G with subcooling temperature of 13 - 21 °C. The diameters of the ejection opening were simulated by means of rupture disks. The jet was ejected upward into the atmosphere and impinged vertically on the plate.

Data about the impingement jet which is practically useful for the design of the piping systems and structures have been obtained.

2. Impingement Jet of Saturated Steam

2.1 Apparatus

A schematic of experimental apparatus is shown in Fig. 1. Saturated steam was ejected into the atmosphere through a straight nozzle as shown in Fig. 1. Inner diameter of the nozzle was 9.4 mm. The steam was supplied through a 1 inch pipe from a boiler. Quality of steam was more than 99 per cent. It is considered that the flow was choked and the exit Mach number was unity. The ejected steam impinged vertically on a flat target plate which had a pressure tap. The target was made to traverse vertically and horizontally in order to measure the pressure distribution on the target. The whole jet was intercepted by the target. Strain gauge type pressure transducers were used for pressure measurement. The experiment was carried out at the ejection pressure of steam of 10 - 40 Kg/cm²G and a distance between the nozzle opening and the target was from 5.5 mm to 62 mm.

2.2 Pressure Profile on a Target

Moody discussed about a jet expansion assuming a flat pressure profile. But it is not in such a simple manner. Results of the pressure profile on the target in the case of ejection pressure of 41 Kg/cm² are shown in Fig. 2 typically. H is a distance between the target and the nozzle exit and D is a diameter of the nozzle exit. In this case D is 9.4 mm. P and P₀ are the impingement pressure on the target and the ejection (total) pressure of steam, respectively. r is a radial distance on the target from the center of the impingement jet.

The configurations of the pressure profile on the target are not same at all the locations. Within the limit of this experiment, the pattern of the pressure profile could be classified to three types. They varies with the location H.

type 1; In a region that H/D is smaller than 1.5, the pressure profiles are similar and is expressed as eq. (2.1)

$$\frac{P - P_{\infty}}{P_S - P_{\infty}} = \text{sech}^2 \left(0.88 \frac{r}{r_{1/2}} \right) \quad (2.1)$$

where P_S is a stagnation pressure on the target at the center of impingement jet, P_{∞} is an ambient pressure, and $r_{1/2}$ is a half value radius.

type 2; In a region that H/D is about 4, the pressure profile becomes to the distorted configuration.

type 3; In a region that H/D is larger than about 6, the profile is concave and a position of the maximum pressure on the target is not center.

These types of pressure profile and the jet spread are related to each other as described in section 2.3.

The stagnation pressure on the target at the center of the impinging jet are shown in Fig. 3. In the region $H/D > 1$, the experimental results are summarized as correlation eq. (2.2)

$$\frac{P_S - P_{\infty}}{P_0 - P_{\infty}} = 0.65 \left(\frac{H}{D} \right)^{-2} \quad (2.2)$$

Assuming that normal shock wave occurs slightly upstream from the target and that the flow is isentropic upstream the shock wave, the righthand side of eq. (2.2) is approximately expressed as eq. (2.3) by using a relation for total pressure change across the normal shock wave for ideal gas [1].

$$\frac{P_S}{P_0} = \left[1 + \frac{2x}{x+1} (M^2 - 1) \right]^{-\frac{1}{x-1}} \left[\frac{(x+1)M^2}{(x-1)M^2 + 2} \right]^{\frac{x}{x-1}} \quad (2.3)$$

where x is a ratio of specific heats and M is a Mach number at the axial position of interest. Owen et.al. [4] calculated the axial profile of the Mach number in the center of highly under-expanded free jet of which a nozzle exit Mach number was 1.008. The calculated stagnation pressure on the target using eq. (2.3) and the Mach number calculated by Owen et.al. is shown by a broken line in Fig. 3. In addition, experimental result for air by Stitt [3] is shown in Fig. 3. Experimental values are in good agreement with the calculated results.

When the pressure profile is type 3, the pressure is maximum on a circular line on the target. This maximum pressure (the secondary stagnation pressure) seems to be independent upon the ejection pressure and H/D in this type.

2.3 Spread of Jet

As Moody described in his work, the jet expands rapidly near the exit to the atmospheric pressure surrounding it. After this initial expansion, the jet would remain at a constant diameter if there were no mixing or shear force interaction with the environment. Dependence of the spread of the pressure profile on the target upon the impingement distance would be in same manner. The experimental results of the spread of the pressure profile are shown in Fig. 4, where $r_{1/2}$ is a half value radius. The spread of the pressure profile is characterized by the half radius. The results are as follows.

- (1) The spread of the pressure profile can be divided into three regions.
- (2) Region 1 extends from the nozzle exit to the distance where H/D is 1.8. In this

region, the half value radius slightly increases as H/D increases and the pressure profile is type 1.

- (3) In the region 2, the half value radius increases in proportion to H/D and the pressure profile is type 2. It should be noted that the half value radius is independent on the ejection pressure in region 1 and 2.
- (4) In the region 3, the half value radius remains constant. The pressure profile is type 3. In this region, the half value radius increases in proportion to the square root of the ejection pressure P_0 as expressed by eq. (2.4)

$$\frac{r_{1/2}}{D} = 0.43 \left(\frac{P_0}{P_\infty} \right)^{0.5} \quad (2.4)$$

where D is the nozzle diameter and P_∞ is the ambient pressure.

2.4 Reaction Force

Generally, the reaction force is expressed in the form of eq. (2.5)

$$T = K P_0 A \quad (2.5)$$

where T is a reaction force and A is a discharge area. K is a coefficient which is called thrust coefficient. For calculating the reaction force, saturated steam is usually treated as an ideal gas. If the flow is further considered isentropic, the thrust coefficient is 1.26 when $P_0 \gg P_\infty$. [2]

The experimental results are shown in Fig. 5. The value of the thrust coefficient which has been obtained is 1.12 less than 1.26. Friction loss upstream from the exit would reduce the thrust coefficient.

An upstream restriction which limits flow reduces the reaction force, too. [6] In this apparatus, the length of the straight nozzle is 120 mm. The effect of the frictional loss would be small. But there is a sudden contraction with a sharp edge at the entrance of the nozzle. Therefore, there may be a possibility that the flow contraction occurred at the entrance of the nozzle. If the flow contraction occurs, the discharge flow and the pressure at the nozzle exit may decrease. Moreover, the pressure loss at the entrance decreases the reaction force. It is not clear from the results of this experiment about these two effects. It is necessary that the effects of the configuration of the nozzle entrance and the frictional loss are confirmed experimentally in future.

3. Blowdown of Pressurized Hot Water

3.1 Equipment

Equipment used in experiment is shown schematically in Fig. 6. Electric heater (1920 kW) is equipped in a heating vessel, which is used to heat water. Blowdown piping (i.d. 190 mm) is contained in a blowdown vessel (140 m³). A straight pipe nozzle is mounted at the end of the blowdown piping. Detail is shown in Fig. 7. Three different nozzles are used. The diameters of the nozzles are 12.3 mm, 21.2 mm and 43.1 mm respectively. They have the round inlets. Rupture disk is mounted at the exit of the nozzle. The rupture disk was broken by electric arc in order to simulate instantaneous guillotine break. The water is circulated until blowdown starts so that the temperature of the water in the nozzle may be kept as high as in the loop.

and the pres-

H/D and the
ue radius is

ssure profile
oportion to the

(2.4)

5)

which is called
s usually treated
coefficient is

t coefficient which
exit would reduce

too. [6]

t of the frictional
at the entrance of
on occurred at the
w and the pressure
nce decreases the
these two effects.
ce and the fric-

ric heater (1920 kW)
iping (i.d. 190 mm)
nted at the end of
are used. The
they have the round
disk was broken by
ter is circulated
may be kept as high

Jet is ejected upward and hits a target plate perpendicularly. There are seven pressure taps by which the pressure distribution on the target is measured. The locations of the pressure taps are as shown in Fig. 7. The target is supported by three rods with load cells. Impingement load and Reaction force are measured by load cells. Natural frequency of the system are 46 Hz.

3.2 Test Procedure

The test loop was initially filled with demineralized water and the water was heated to the starting conditions. When the initial condition was achieved, the circulation pump was then stopped and the valves VP-7 and VP-8 were closed and the rupture disk was broken.

Nine tests were conducted. The initial conditions and the diameters of the nozzles used in each run are shown in Table 1.

3.3 Experimental Results

Typical pressure history in the blowdown pipe after the break is shown in Fig. 8. As the initial temperature of water is subcooled, the pressure decreases rapidly to near the saturated condition. An undershoot is observed. This seems to be due to time delay of evaporation.

Examples of the reaction forces are shown in Fig. 9. The reaction force and the impingement load were measured simultaneously. These two forces are equal within the experimental error.

The reaction force has a maximum value just after the break and then decreases rapidly as the pressure in the blowdown pipe decreases. Such a peak of the reaction force is distinguished when the initial subcooling is large. Probably, such a peak may diminish if the initial subcooling is zero.

The experimental result of thrust coefficient defined by eq. (2.5) was nearly constant with respect to time. The thrust coefficient seems to depend slightly on the steam quality of the mixture in the blowdown pipe.

The steady state reaction force is given by eq. (3.1)

$$\frac{T}{A} = P_E - P_{\infty} + \frac{G^2 V_E}{g} \quad (3.1)$$

where A is an area of the break, P_E is a pressure at the exit (critical pressure), G is a discharge mass flow rate, V_E is a specific volume of discharge flow at the exit and g is gravitational acceleration. Assuming an isentropic flow, and substituting P_E , G and V_E calculated by Moody's method [5] into eq. (3.1), the steady state frictionless thrust coefficient can be obtained. The predictions for steady state saturated water are shown by a broken line in Fig. 10. The experimental results of the thrust coefficient is from 1.2 to 1.4 which is slightly greater than Moody's prediction as shown in Fig. 10.

A configuration of the pressure distribution on the target varies considerably with time. The typical history of the pressure distribution is shown in Fig. 11. In the early stage of the period of blowdown, the configuration of the pressure distribution is flat and the spread of jet is wide. The pressure at the center was rather low. As time goes on after break, the spread becomes narrow and the pressure at the center becomes high and then low. Therefore, the pressure on the target plate is maximum in a short time after the break. The spread of the pressure distribution on the target is shown in Fig. 12, where P is a pressure in the

blowdown pipe during blowdown. The dependence on the pressure at more than 40 Kg/cm² is different from one at less than 40 Kg/cm². It seems that the lower the steam quality of the discharge mixture is, the larger the spread of jet is. It is interesting that when the blowdown pressure becomes low (the steam quality is high), the spread of the pressure distribution is similar to one for the saturated steam.

4. Conclusion

[A] For the steady saturated steam jet, following results were obtained.

- (1) The configuration of the pressure distribution on the impinged plate depends strongly on the distance between the plate and the pipe exit. The configurations are divided into three types according to the distance. The stagnation pressure of the jet at the center of the pressure distribution can be estimated by eq. (2.2), which agrees well with the analytical results derived from the relation of the total pressures across the shock wave.
- (2) The value of reaction force for steam jet we obtained was smaller than that of Moody's prediction which assumed the frictionless isentropic flow. This disagreement seems to be due to the friction loss and/or flow contradiction at the entrance of the nozzle. Further investigation is necessary to clarify this effect. This result, however, shows that it is conservative to evaluate the reaction force by Moody's prediction.

[B] For the subcooled water jet, following results were obtained.

- (1) In the case of the initially subcooled water, the peak reaction force and the peak impingement load are observed just after the break of the rupture disk. These phenomena are considered to be due to the sudden decreasing of the system pressure.
- (2) The thrust coefficients obtained in this experiment kept constant value during blowdown. The values of the thrust coefficients were in the range of 1.2 to 1.4.
- (3) The spread of the jet is large at the early stage of the water phase blowdown. On the other hand, the pressure on the impinged plate takes maximum value after a some period of time. This phenomena seemed to be complex. The pressure on the target depends on the impingement distance, the steam quality and the system pressure.

References

- [1] Liepmann, H.W. and Roshko, A., "Elements of Gasdynamics," John Wiley & Sons, Inc.
- [2] Moody, F.J., "Prediction of Blowdown Thrust and Jet Force," ASME 69-HT-31, (1969)
- [3] Stitt, L.E., "Interaction of Highly Underexpanded Jet with Simulated Lunar Surfaces," NASA TN D-1095, (1961)
- [4] Owen, P.L., and Thornhill, C.K., "The Flow in an Axially - Symmetric Supersonic Jet from a Nearly Sonic Orifices into a Vacuum" Brit., A.R.C. Technical Report, R & M 2616 (1952)
- [5] Moody, F.J., "Maximum Flow Rate of a Single Component Two-Phase Mixture," Journal of Heat Transfer, ASME, Series C, Vol. 87, (1965)
- [6] Moody, F.J., "Time-Dependent Pipe Forces Caused by Blowdown and Flow Stoppage," Journal of Heat Transfer, Trans. ASME, Vol. 95, Series 1, No.3, (1973)

n 40 Kg/cm² is
 sam quality of the
 that when the blow-
 ressure distribu-

ned.
 late depends
 he configuration
 gnation pressure
 imated by eq.
 m the relation

r t at of
 w s dis-
 adiction at the
 larify this effect.
 the reaction

force and the
 rapture disk.
 ig of the system

it value during
 ge of 1.2 to 1.4.
 phase blowdown.
 mum value after a
 pressure on the
 id the system pres-

y & Sons, Inc.

HT-31, (1969)

id Lunar Sur-

ic Supersonic Jet
 Report, R & M

ture," Journal

w Stoppage,"
 173)

Table 1 Experimental condition

Run No.	Initial pressure P_0 kg/cm ²	Initial temperature T_0 °C	Subcooling ΔT_{sub} °C	Initial saturated pressure $P_{o sat}$ kg/cm ²	Break area D mm	Impingement distance H mm	H/D
MIKT 201	67	255	26	43	21.2	290	13.7
202	148	299	41	85	21.2	290	13.7
203	150	318	23	112	21.2	290	13.7
204	68	268	16	53	10.7	290	27.1
205	148	309	31	98	10.5	290	27.6
206	66	264	18	50	38.1	260	6.85
207	68	271	13	56	40.8	400	9.85
208	70	264	21	50	34.8	150	4.31
208-2	68	263	21	49	38.2	150	3.83

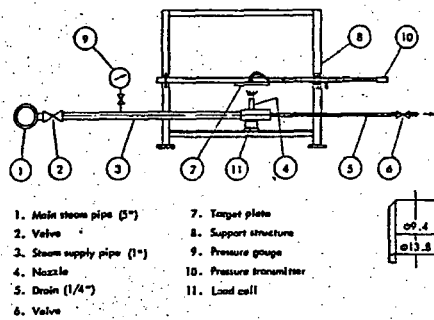


Fig. 1 Sketch of experimental apparatus (steam blowdown)

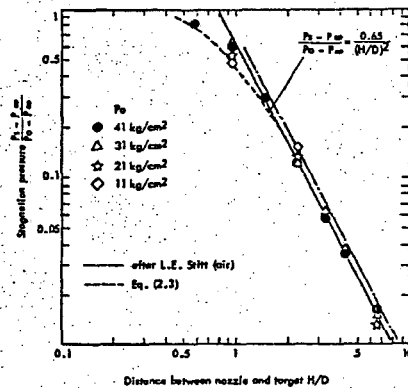


Fig. 3 Stagnation pressure of saturated steam jet on target

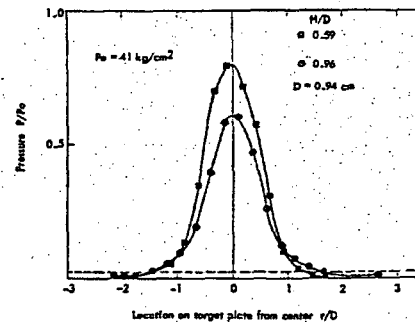
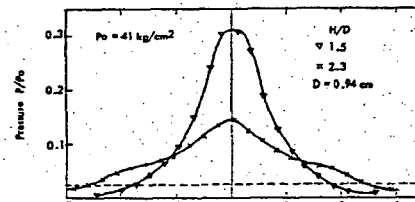
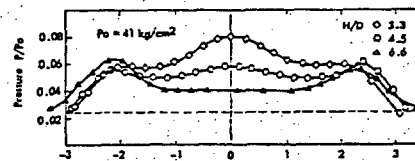


Fig. 2 Examples of radial pressure profile on target (steam)

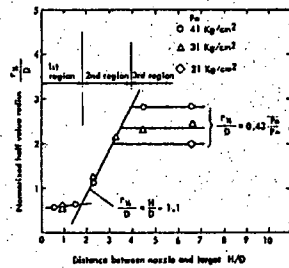


Fig. 4 Half value radius of pressure profile on target for steam jet.

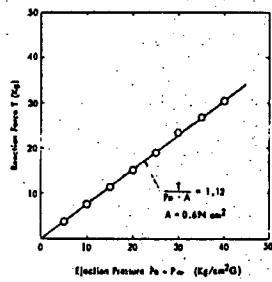


Fig. 5 Results of steam reaction force

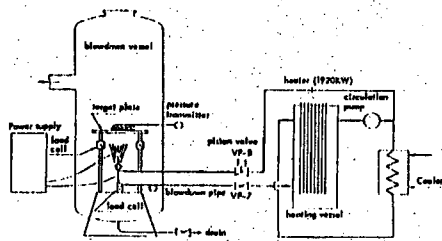


Fig. 6 Schematic diagram of water blowdown apparatus

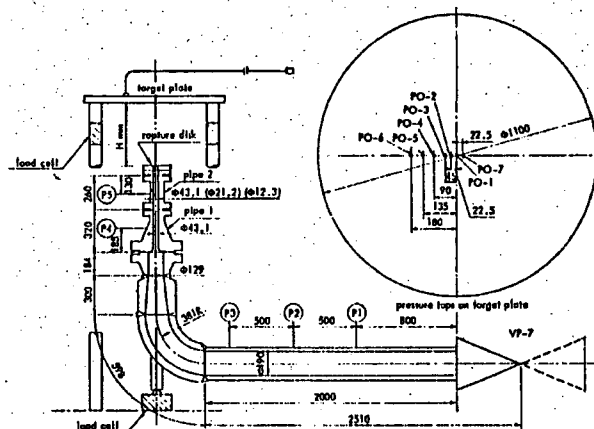
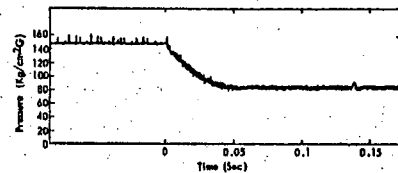
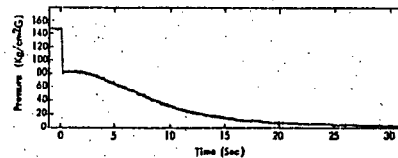


Fig. 7 Details of water blowdown piping



(a) Initial sudden depressurization after break, MIKT 202



(b) History of pressure after break, MIKT 202

Fig. 8 Typical history of pressure in blowdown pipe

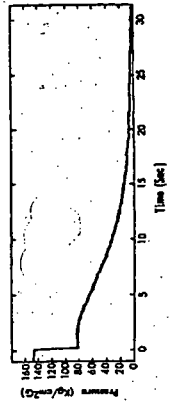


Fig. 8 Typical history of pressure in blowdown pipe
(*) History of pressure after break, MIKT202

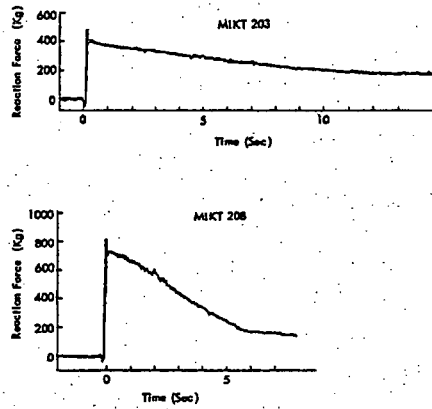


Fig. 9 Typical histories of reaction force during water blowdown

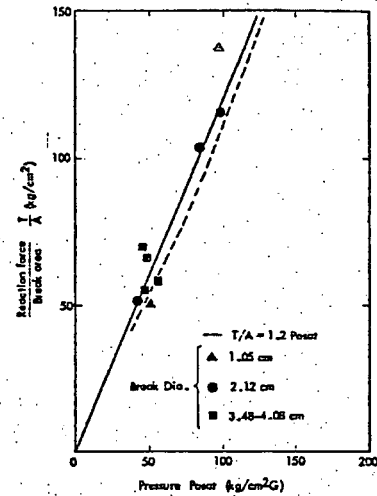


Fig. 10 Reaction force just after initial depressurization (water blowdown)

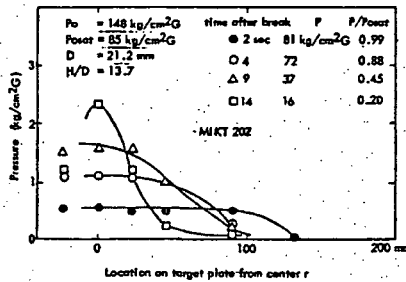


Fig. 11 Typical radial pressure profile of two-phase impingement jet

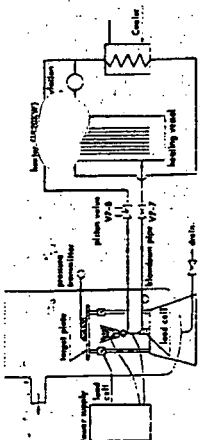


Fig. 6 Schematic diagram of water blowdown apparatus

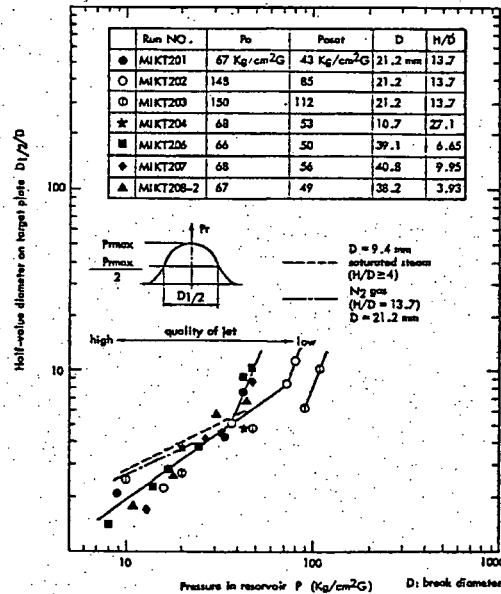


Fig. 12 Jet diameter at half-maximum pressure on target (water blowdown)

ATTACHMENT 1

FILES CONTAINED IN CDs

CD 1: Technical Report, MUAP-10017-P (R1) "Methodology of Pipe Break Hazard Analysis (Proprietary)"

Contents of CD

<u>File Name</u>	<u>Size</u>	<u>Sensitivity Level</u>
MUAP-10017-P_R1_PBHA.pdf	1,042KB	Proprietary

CD 2: Technical Report, MUAP-10017-NP (R1) "Methodology of Pipe Break Hazard Analysis (Non-Proprietary)"

Contents of CD

<u>File Name</u>	<u>Size</u>	<u>Sensitivity Level</u>
MUAP-10017-NP_R1_PBHA.pdf	136KB	Non-Proprietary